

**APPLICATION OF FT-IR SPECTROSCOPY TO STUDY HYDROCARBON REACTION CHEMISTRY**

Peter R. Solomon, David G. Hamblen, Robert M. Carangelo,  
James R. Markham and Michele R. Chaffee

Advanced Fuel Research, Inc., 87 Church Street, East Hartford, CT 06108, USA

Fourier Transform Infrared Spectroscopy (FT-IR) is one of the most versatile analytical techniques available for the study of fossil fuel structure and reaction chemistry. Among its advantages are: (i) its ability to study feedstocks and reaction products as solids, liquids and gases, since almost all have characteristic absorptions in the infrared; (ii) its sensitivity, allowing the study of highly absorbing materials such as coal and char and the use of difficult techniques such as photoacoustic or diffuse reflectance spectroscopy; (iii) its speed (instruments commercially available can obtain a complete spectrum every 20 milliseconds) allowing the possibility of following chemical reactions on-line; (iv) its inherent rejection of stray radiation, allowing transmission measurements at elevated temperatures to be made in-situ; (v) its ability to measure emission spectra to determine temperature as well as chemical changes of reactants at elevated temperature.

Because of these advantages, FT-IR spectroscopy has achieved increasing use in fuel science. This paper will review some of its applications. Recent progress has been made in the use of FT-IR for the quantitative determination of hydrogen functional groups in solid hydrocarbons. Developments in this area are important since uncertainties in the hydrogen distribution have hindered investigations of coal structure. The paper will discuss the present convergence being obtained in the determination of aliphatic hydrogen and the uncertainties remaining in the determination of aromatic hydrogen. A second area to be considered will be the application of the functional group determination to the study of coal pyrolysis. The paper will consider the changes in the functional group composition of coal during primary pyrolysis and its relationship to the pyrolysis products which are formed. Finally, recently developed methods employing both emission and transmission spectroscopy will be considered to monitor, in-situ, the coal particle temperature and chemical changes which occur during pyrolysis.

**DETERMINATION OF AROMATIC AND ALIPHATIC HYDROGEN IN COAL**

While several techniques are available for obtaining infrared spectra of coal, only the KBr pellet technique has been pursued extensively for quantitative analysis. Methods for quantitative preparation of samples have been described in a number of publications (1-7) and it appears that with a representative sample of coal and care in sample preparation, spectra can be repeated with less than 5% variation. Typical KBr pellet spectra for two bituminous coals and a lignite are illustrated in Fig. 1. They have peaks due to their functional groups and mineral components which are identified in the figure. In general, all coals have these absorption bands and the major variation with rank is in their relative magnitude. There are three features of the KBr spectra whose interpretation has been controversial. The first is the large peak at 1600 wavenumbers, which evidence now suggests is an aromatic ring stretch whose intensity is greatly enhanced by the presence of hydroxyl groups on the ring and nitrogen in the ring (2-4,6). The second is the sloping baseline which has generally been attributed to scattering (rather than absorption) of the transmitted radiation by the particles of coal in the KBr pellet. A straight line correction has sometimes been used to obtain a spectrum more "representative" of the absorption. Figure 2 compares a baseline corrected spectrum of coal (a) in Fig. 1. to a spectrum of the same coal obtained by photoacoustic absorption spectroscopy (PAS) (8,9). The PAS technique which is sensitive only to the absorption of energy does not have a sloping baseline and is quite similar in appearance to the baseline-corrected KBr pellet spectrum. The baseline correction appears to be accurate for coals and chars

up to about 90 percent carbon. At high carbon concentrations, a broad slopping absorption is also present. Comparison of the two spectra suggest some distortion of the aliphatic band in the KBr pellet spectrum may occur due to the Christiansen effect. This distortion could influence measurements of the aromatic hydrogen if the 3100 wavenumber band is used. PAS spectra also appear to exaggerate the mineral peaks. A third controversial feature is the hydroxyl band. Is it really as broad as it appears (due to hydrogen bonding) and can the band associated with water incorporated during the pellet preparation be eliminated by drying the pellet? Results of Ref. 1 suggest that drying removes almost all of the water and good results have been obtained using the optical density at 3200 wavenumbers to determine the hydroxyl content. Comparison of the dry KBr pellet spectrum with the PAS spectrum in Fig. 2. suggests that the broad absorption peak of the hydroxyl groups in the dried pellet is real.

To obtain aromatic and aliphatic hydrogen concentrations,  $H(ar)$  and  $H(al)$ , it is necessary to integrate the areas  $A(ar)$  and  $A(al)$  under the appropriate peaks (spectra are normalized to 1 mg per square cm) and divide by appropriate integral absorptivities  $a(ar)$  and  $a(al)$  (in abs. units  $\times$  wavenumbers/mg/cm<sup>2</sup>) to relate the areas to the hydrogen concentrations. The former task has been automated by employing a synthesis routine which uses a set of preselected peaks whose position and width are held fixed and whose amplitude is varied to reproduce the experimental spectrum (2-4). The technique has the advantage that integrated areas will be obtained in a consistent manner for all samples. Excellent fits have been obtained for hundreds of coal samples using one set of 45 Gaussian peaks (2). To obtain the absorptivities for coal samples, a method was derived (2-4) in which  $H(al) = A(al)/a(al)$  and  $H(ar) = A(ar)/a(ar)$  was equated to the total hydrogen,  $H$ , minus the hydroxyl hydrogen,  $H(OH)$  and rearranged to yield the following equation,

$$\frac{1}{a(al)} \left[ \frac{A(al)}{H - H(OH)} \right] = 1 - \frac{1}{a(ar)} \left[ \frac{A(ar)}{H - H(OH)} \right] \quad (1)$$

If the absorptivities are independent of coal composition, than the two unknowns,  $a(ar)$  and  $a(al)$  can be determined from  $A(al)$ ,  $A(ar)$ ,  $H$  and  $H(OH)$  for two samples.  $H(OH)$  can be determined chemically or by FT-IR (1,5).  $A(al)$  is usually obtained from the set of peaks near 2900 wavenumbers which are strong and do not have any interfering peaks nearby.  $A(ar)$  can be obtained from the peaks near 800 wavenumbers which are strong but have interference from mineral peaks (which must be subtracted) and long methylene chains (which are weak and can be subtracted) or from the peak near 3100 wavenumbers which are weak and have interference from the aliphatic and hydroxyl bands. The problem of determining the area for the 3100 wavenumber peak is substantial for low rank coals as will be discussed below.

In practice, coals do not have different enough ratios of  $H(al)$  and  $H(ar)$  to determine accurately the absorptivities from two samples, so large numbers of coals are used to define a straight line by plotting the two terms in brackets. But, even this method is not accurate because the coals tend to be tightly clustered. To alleviate this problem, coal derived chars and tars, which have related chemical structures were also included to provide a wider range of aliphatic to aromatic ratios (2-4). This will work only if the absorptivities for these additional samples are the same as for coals. A set of chars produced by heating a bituminous coal at 30°C/sec to different final temperatures is illustrated in Fig. 3. As can be seen  $A(ar)/A(al)$  increases continuously with pyrolysis temperature. The chars produced above 600°C have little aliphatic hydrogen and thus provide an excellent sample for determining  $a(ar)$ . Using the 800 wavenumber region for  $A(ar)$ , the bracketed terms in Eq. 1 are plotted in Fig. 4 with some additional chars and tars from a Pittsburgh Seam coal of similar carbon content. The chars form a regular series along a straight line with intercepts at  $a(ar) = 684$  and  $a(al) = 744$ . The results are in excellent agreement with previously derived values of 686 and 746 for all bituminous coals, chars and tars (2). Model compounds were also examined to provide guidance in the possible absorptivity values (2-4). The  $a(ar)$  value is 11% lower than the average value of  $a(ar) = 768$  for 25 model compounds containing C and H only. The same model compounds give an average value of

$a(ar) = 220$  for the 3100 wavenumber band. This corresponds to  $\epsilon(ar) = .60$  in good agreement with the value derived in Refs. 7 and 10.

Using these absorptivities, values of  $H(ar)$  and  $H(al)$  have been derived for a set of bituminous coals from the Exxon premium sample collection. The results are plotted as a function of rank in Fig. 5a. The values of  $H(ar)$  lie in a narrow band which shows a smooth variation with rank. Values of  $H(al)$  are more scattered. The scatter in the data appear to reflect real variations in  $H(al)$ , since  $H(al) + H(ar)$  is in good agreement with  $H - H(OH)$  as shown in Fig. 6a. The data form a band with a random variation of  $\pm 10\%$ . The slight slope in Fig. 6a suggests a variation of the absorptivity with carbon concentration.

The problem of obtaining absorptivities using coals alone (i.e., defining a line through data points clustered in a small region) was recently discussed extensively by researchers at Penn State University (7,10). They used an error minimization procedure (equivalent to the graphical method discussed above) to evaluate the absorptivities for a group of coals and lignites. The 3100 wavenumber region was chosen for  $H(ar)$  instead of the 800 wavenumber region. The same method was used on pyridine extracts (7) and it was determined that the absorptivities match reasonably with absorptivities derived from proton nmr. The absorptivity value derived for  $a(al)$  was 665, 11% lower than our value of 745. Note the conversion factor  $\epsilon(al) = .20$  in Ref. (10) is the reciprocal of  $a(al)$  multiplied by 100 (weight fraction to weight %) and by 1.33 (mg per pellet to  $mg/cm^2$ ). The results are shown in Fig. 5b. The  $H(al)$  values are about 10% higher than ours and are in agreement with the differences in  $a(al)$ . The 10% extra hydrogen in the  $H(al)$  values must be made up in the  $H(ar)$  values which are up to 30% to 50% lower than our values at low carbon concentration. A comparison of  $H(al) + H(ar)$  to  $H - H(OH)$  is made in Fig. 6b. The random variation is similar to our results ( $\pm 12\%$  vs.  $\pm 10\%$ ) but the dependence on carbon concentration is greater. While Reisser et al. (10) have attributed all the discrepancies between  $H(al) + H(ar)$  derived by FT-IR and  $H - H(OH)$  derived by elemental analysis and FT-IR to random errors in KBr pellet sample preparation, some of the variation is clearly a systematic rank dependence caused by variations in the absorptivities with rank. This variation was observed in our earlier work and we derived separate absorptivity values for lignites and subbituminous coals (2). The rank variation in the absorptivities using the 3100 wavenumber region appear to be greater than what we have obtained using the 800 wavenumber region. This observation will be discussed below. We believe that the values of  $H(ar)$  reported originally (3) were too high because of the influence of the rank variation when using rank independent absorptivities.

Considering the above results, how accurate is the FT-IR method for determining hydrogen functional group concentrations? Both sets of data derived by FT-IR (Figs. 5a and 5b) produce similar values of  $H(al)$ . Values of  $H(ar)$  are in reasonably narrow bands which agree above 85% carbon. The method in its current state of development (using rank independent absorptivities) can, therefore, determine  $H(al)$  to  $\pm 10\%$  and relative trends for  $H(ar)$ . The FT-IR technique appears capable of providing accurate absolute values for the hydrogen functional group distribution provided the proper absorptivity can be determined for  $H(ar)$  below 85% carbon. As guidance in determining the proper absorptivities, data for  $H(ar)$  in coal derived by dipolar dephasing (11) are presented in Fig. 5c and data for pyridine extracts (12,13), vacuum distillates (14) and coals (13) obtained by proton nmr and IR are presented in Fig. 5d. Among these data for  $H(ar)$  the dipolar dephasing data (Fig. 5c) are the highest. The data from this work (Fig. 5a) are similar to the data on coal like materials (Fig. 5d) and are within the range of the dipolar dephasing data. The data of Reisser et al. (10), (Fig. 5b) are the lowest and appear outside the range of the dipolar dephasing data.

Another comparison is made in Table I using the average values determined for the ratios of  $H(ar)$  to  $H(al)$  in the range of 80-85% carbon (10-16). The value of 0.35, determined by Reisser et al., (10) is 24% lower than the cumulative average of 0.46. The value of 0.52 from the present results is 13% too high. The value of 0.2 originally determined by Brown (15) is too low and the value of 0.70 determined by

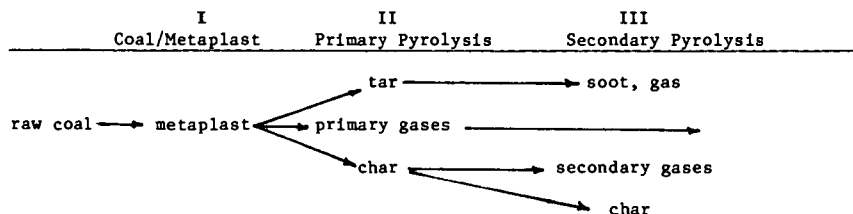
Wilson et al. (11) using dipolar dephasing appears too high.

Some of the discrepancy in the FT-IR values may be due to the choice by the Penn State group (7,10) of the 3100 wavenumber band for H(ar). This band appears to shrink more rapidly with decreasing rank than do the 800 wavenumber bands. A comparison is made in Fig. 7 between these two regions for a lignite, its tar and its char. These samples are low in mineral content. The spectra are presented without baseline or mineral corrections. While the coal shows a distinct band near 800 wavenumbers it is very difficult to distinguish a band at 3100 wavenumbers. The tar and char produced in pyrolysis show large peaks at 800 wavenumbers but only the char has a clearly defined peak at 3100 wavenumbers. The amplitude at 3100 wavenumbers is either weakened or partially hidden by the presence of the hydroxyl band. The ratio of areas of the 3100 to 800 wavenumber bands for the Exxon coals are plotted in Fig. 8a. The ratio goes to zero with increasing rank. A similar effect is observed for model compounds in Fig. 8b. The stretch region appears more sensitive to the oxygen concentration than the wag. For example, a(ar) goes from 220 (25 model compounds without oxygen) to an average value of 122 (8 model compounds with an average of 11% oxygen). For the same model compounds a(ar) for the 800 wavenumber region goes from 768 (no oxygen) to 889 (with oxygen). While this ratio depends on the way the bands are fit (i.e. integration limits and baseline) it is very difficult to avoid very small areas in the 3100 wavenumber region for low rank coals.

The decreasing 3100 wavenumber band intensities for low rank coals would explain the low values of H(ar) in Fig. 5b and the slope in Fig. 6b. Resolution of this issue and improved accuracy in the technique requires the following advances: i) an agreed upon procedure for obtaining peak areas, ii) use of rank dependent absorptivities, iii) a premium set of reproducible samples of coals, vacuum distillates and pyridine extracts for round robin tests at different laboratories using FT-IR, proton nmr and  $C^{13}$  nmr with dipolar dephasing. Even with its limitations, the present technique appears to be the best routine method to obtain hydrogen functional group concentrations.

#### THE VARIATIONS IN FUNCTIONAL GROUP COMPOSITION DURING COAL PYROLYSIS

An application of the analysis method described above was made in the study of coal pyrolysis where the evolution of pyrolysis products may be related to the chemical changes occurring in the coal as determined by FT-IR spectroscopy. Pyrolysis has been described in terms of the following stages:



During, stage I the coal may undergo some bond breaking reactions and reduction of hydrogen bonding which may lead to melting. Some light species which exist as guest molecules or are formed by the breaking of very weak bonds are released. During stage II, further bond breaking occurs leading to evolution of tar and gases and the formation of char. During stage III the products can continue to react. The char can evolve secondary gases, mainly CO and H<sub>2</sub> while undergoing ring condensations. The tars can crack to form soot, coke and gases and the gases can crack to form lighter gases and soot.

To demonstrate the relationship between the "extent of pyrolysis" and the functional group composition, we consider an experiment in which samples of a bituminous coal were heated at a constant rate of 30°C/min starting at 150°C and ending at a series of

temperatures between 350 and 950°C. Slow heating is useful in separating the stages of pyrolysis, which can overlap in rapid heating experiments. Figure 3 shows the infrared spectra obtained for the product chars (at several temperatures) by quantitative FT-IR spectroscopy. There are substantial changes in the spectra as the peak pyrolysis temperature is increased. To relate these changes to the stages of pyrolysis, the functional group compositions from these spectra are compared in Fig. 9 to the weight loss and evolution of tar and gases measured during the experiment.

Substantial changes occur during the primary pyrolysis, stage II. Figure 9a compares the weight loss with the rate of tar evolution. The maximum rate of weight loss at 470°C compares with the maximum rate of tar evolution. Figure 9b shows the rate of aliphatic gas evolution compared to the loss of aliphatic hydrogen, H(al), in the char. There is also an increase in H(ar), Fig. 9e, which occurs as the tar picks up hydrogen from hydroaromatic rings, converting them to aromatic sites. The loss of tar, aliphatic gases and H(ar) are closely coupled events which dominate the primary pyrolysis. The loss of H(al) indicates the end of stage II. The loss of H(al) also signals the loss of plasticity and swelling as described in (17).

At 30°C/min heating rate, secondary pyrolysis, stage III, began above 550°C. Figure 9c compares the evolution of methane with the concentration of methyl groups in the char. The methyl group concentration first increases during primary pyrolysis (due to bond breaking and stabilization) and then decreases as methane is formed. The events occurring during the later parts of stage III include the elimination of ether linkages coupled with the evolution of CO (Fig. 9d) and the elimination of aromatic hydrogen, H(ar), (Fig. 9e) which occurs during ring condensation coupled with evolution of hydrogen gas (not measured in this experiment). Since ring condensations also eliminate active sites for oxygen attack, H(al) should be a good parameter to correlate with intrinsic char reactivity. Figure 9f shows the evolution of CO<sub>2</sub> and H<sub>2</sub>O. The evolution of water appears to correlate with the increase in the ether oxygen suggesting that two hydroxyls may combine to form a water and an ether link.

For these experiments, the changes in the functional group composition as determined by FT-IR provide a good chemical description of the pyrolysis stages which are in turn correlated with the evolved products. It has been demonstrated that this relationship between the pyrolysis events and the functional group composition is quite general, being independent of coal rank and temperature (3,17-20). The sequence of functional group changes is the same in high heating rate experiments as for the slow heating case and corresponds in the same way to the pyrolysis events. FT-IR spectra provide a good method to determine the "extent of pyrolysis".

#### IN-SITU MONITORING OF COAL TEMPERATURE AND SPECTRAL EMITTANCE

As a final example of the FT-IR's versatility, we consider its application in the on-line, in-situ monitoring of coal conversion. In this application the sample volume is in the reacting stream rather than in a KBr pellet. Both emission and transmission measurements are made to provide data on the coal's temperature and spectral emittance (which is related to its chemical composition). As described in a previous publication (21), the transmittance measurement is used to determine the total emitting surface of the coal particles so that a normalized emission, (emission/(1-transmittance)) can be compared in both shape and amplitude to a theoretical black-body. In the work described below, the coal flow rate was monitored to insure that both measurements be made under the same conditions. Also, the emission from several phases (tar in particular) and diffraction effect required additional care in the computation of the normalized emission. Compared to other techniques for measuring temperature the FT-IR normalized emission measurement has the following advantages: 1) A complete spectrum is obtained, not just two or three colors; 2) Measurements are made in the infrared where the emission is strongest and where measurements of emission and optical properties are relevant to practical conversion processes; 3) Measurements are possible with mixed phase (particles, soot and gas); 4) For grey-bodies, the measurement of normalized emittance allows the use of the spectral shape to obtain temperature and the

amplitude, to obtain emissivity; 5) Measurements are fast. A complete spectrum can be obtained in 20 milliseconds using a commercial FT-IR. With this speed, tomographic techniques to obtain point measurements may be practical; 6) Determination of temperature distributions are possible; 7) The technique is applicable to measurements in process equipment.

The spectra which we consider were obtained for pyrolysis measurements made in a tube reactor described in another paper presented at this meeting (22) and combustion measurements made in an entrained flow reactor (17). Both reactors allow optical access to the high temperature products. For these experiments, the FT-IR measurement can provide a direct measurement of the coal particle temperature. The technique has been validated by making measurements under conditions where the particle temperatures are known. A simple case is illustrated in Fig. 10a. For this case, sufficient time was allowed for the coal to reach the asymptotic tube temperature of 935°C (1208 K) and for primary pyrolysis to have occurred. The normalized emission spectrum is in good agreement with a theoretical black-body at 1190 K with an amplitude corresponding to an emissivity of 0.9. The measured temperature is in excellent agreement with the tube temperature, as a 10°C drop in temperature is expected between the end of the tube, and the measuring point at 0.75 cm below the end.

The measurement of temperature before and during pyrolysis is not as simple, since for the size of coal particles used here, only specific bands (corresponding to the absorbing bands in coal) provide sufficient absorbance for the spectral emittance to reach 0.9. Then, only these regions can be used to compare to the black-body. Examples for a 200 x 325 mesh fraction of a Montana Lignite injected at 3 grams/min into the tube reactor at 800°C (1173 K) with a cold helium velocity of 4 m/sec are presented in Figs. 10b and 10c. The same coal with a cold velocity of 28 m/sec is shown in Fig. 10d. The spectrum is noisier due to the lower density of coal at the higher velocity, but has a shape similar to Fig. 10b where the coal is at a comparable temperature. The spectra are decidedly non-black or non-grey. Measurements show that the particle's emissivity is size, rank and temperature dependent. The result can be understood by remembering that a particle's emittance is related to its absorbance. Only the region between 1000 and 1600 wavenumbers has sufficient absorbance to fully attenuate the incident light over the particle thickness. It is only in this region that the normalized emission can be compared to the black-body. The aliphatic and hydroxyl bands are questionable.

Figures 10b to 10d contain the best fit grey-body curve ( $\epsilon = 0.9$ ) in the 1000 to 1600 wavenumber region and a grey-body curve ( $\epsilon = 0.9$ ) corresponding to the thermocouple measurement at the FT-IR focus. The grey-body curves are fit, excluding the region around 1500 wavenumbers where there is interference from water. The differences between the FT-IR and thermocouple measurements were 30°C, 40°C, and -13°C for measurements at 853 K, 953 K, and 913 K, respectively. The three cases are for transit distances of 10, 30 and 50 cm in the tube reactor. The spectra change with particle temperature and with changes in composition as ring condensation (which takes place during pyrolysis) makes the char more graphitic. The emission spectrum approaches a grey-body like Fig. 10a, only after sufficient time at elevated temperature (after primary pyrolysis is complete). The spectrum of Fig. 10c is almost a grey-body ( $\epsilon = 0.9$ ). The spectrum for the same coal at 935°C, Fig. 10a, is even closer. To determine the change under even more severe pyrolysis conditions, chars of the same coal were prepared at 1300°C and then injected into the tube reactor at 800°C. The spectrum in Fig. 10e shows a grey-body with an emissivity of  $\epsilon = 0.70$ , close to that expected for graphite.

The spectral emittance is also particle size dependent. Figure 10f shows a spectrum for a -400 mesh fraction of the same lignite. Except for the 1200 to 1600 wavenumber region, the spectral emittance is much lower than 0.9. As pyrolysis proceeded and particle mass was lost, the spectral emittance decreased even in the 1200 to 1600 region. These data show that raw coal of a size used for pulverized coal combustion does not have anywhere near the 90% absorption of radiation which is usually assumed in

calculating the particle heating rates. The average spectral emittance in the mid IR (where furnace radiation is a maximum) is about 0.5 for the 200 x 325 mesh fraction and 0.2 for the -400 mesh fraction.

Figure 10g shows that temperature was determined as low as 300°C. Figures 10h and 10i show temperature determinations during combustion. Under identical conditions, the lignite, at 1650 K is much more reactive than the bituminous coal at 1350 K. The particles spectral emittance have fallen to about 0.70 in agreement with the results of Fig. 10e.

#### ACKNOWLEDGMENT

The support of the Morgantown Energy Technology Center is gratefully acknowledged for the work on coal pyrolysis and on FT-IR emission/transmission spectroscopy. We wish to thank Dr. John McClelland of Ames Laboratory who obtained the photoacoustic spectrum in Fig. 2 and Richard Neavel, at the Exxon Corporation, for permitting the use of data on the Exxon samples.

#### REFERENCES

1. Solomon, P.R. and Carangelo, R.M., *Fuel*, **61**, 663, (1982).
2. Solomon, P.R., Hamblen, D.G., and Carangelo, R.M., "Applications of Fourier Transform IR Spectroscopy in Fuel Science", ACS Symposium Series **205**, pg. 77, (1982).
3. Solomon, P.R., *Advances in Chemistry Series*, Vol. **192**, "Coal Structure", 95, (1981).
4. Solomon, P.R. and Carangelo, R.M., "Characterization of Wyoming Subbituminous Coals and Liquefaction Products by Fourier Transform Infrared Spectrometry", EPRI Final Report, Project No. 1604-2, (1981).
5. Kuehn, D.W., Snyder R.W., Davis, A., and Painter, P.C., *Fuel*, **61**, 682, (1982).
6. Painter, P.C., Starsinic, M., Squires, E., and Davis, A.A., *Fuel*, **62**, 742, (1983).
7. Sobkowiak, M., Reisser, E., Given, R., and Painter, P., *Fuel*, **63**, 1245, (1984).
8. McClelland, J.F., *Anal. Chem.*, **55**, 89A, (1983).
9. Vidrine, D.W., *Fourier Transform Infrared Spectroscopy*, **3**, 125, (1982).
10. Reisser, B., Starsinic, M., Squires, E., Davis, A., and Painter, P.C., *Fuel*, **63**, 1253, (1984).
11. Wilson, M.A., Pugmire, R.J., Karas, J., Alemany, L.B., Woolfenden, W.R., Grant, D.M., and Given, P.H., *Analytical Chemistry*, **56**, 993, (1984).
12. Retcofsky, H.L., *Applied Spectroscopy*, **31**, 116, (1977).
13. Durie, R.A., Shewchuk, Y., and Sternhell, S., *Fuel*, **45**, 99, (1966).
14. Brown, J.K., Ladner, W.R., and Sheppard, N., *Fuel*, **39**, 79, (1960).
15. Brown, J.K., *J. Chem. Soc.*, 744, (1955).
16. Mazumdar, B.K., *Fuel*, **43**, 78, (1964).
17. Solomon, P.R., Hamblen, D.G., Carangelo, R.M., and Krause, J.L., 19th Symposium (Int.) on Combustion, The Combustion Institute, Pittsburgh, PA, pg. 1139 (1982).
18. Solomon, P.R. and Hamblen, D.G., *Finding Order in Coal Pyrolysis Kinetics*, Topical Report Submitted to the U.S. Department of Energy, under Contract #DE-AC21-FE05122 (1983).
19. Solomon, P.R. and Hamblen, D.G., *Measurement and Theory of Coal Pyrolysis Kinetics in an Entrained Flow Reactor*, EPRI Final Report for Project RP 1654-8 (1983).
20. Solomon, P.R., Hamblen, D.G., and Best, P.E., *Coal Gasification Reactions with On-Line In-Situ FT-IR/Analysis*, DOE Quarterly Reports, Contract #DE-AC21-81FE05122 (1981-1983).
21. Best, P.E., Carangelo, R.M. and Solomon, P.R. *ACS Division of Fuel Chem*, **29**, 249 (1984).
22. Solomon, P.R., Serio, M.A., Carangelo, R.M. and Markham, J.R., *Very Rapid Pyrolysis*, ACS Div. of Fuel Chemistry Preprints, **30** (1985).

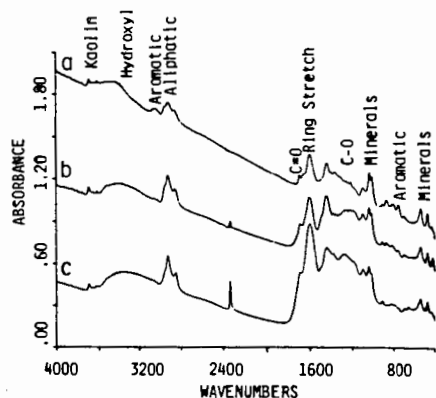


Figure 1. FT-IR Spectra for  
a) a Low Volatile Bituminous Coal,  
b) a High Volatile Bituminous Coal,  
and c) a Lignite.

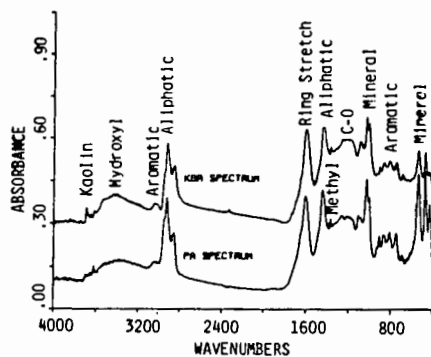


Figure 2. Comparison of KBr  
Pellet and Photoacoustic Spectra.

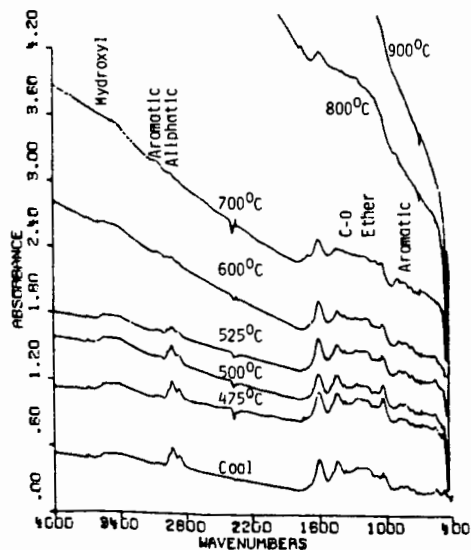


Figure 3. FT-IR Spectra for Chars Produced  
by Heating at 30°C/min to the Indicated  
Temperatures.

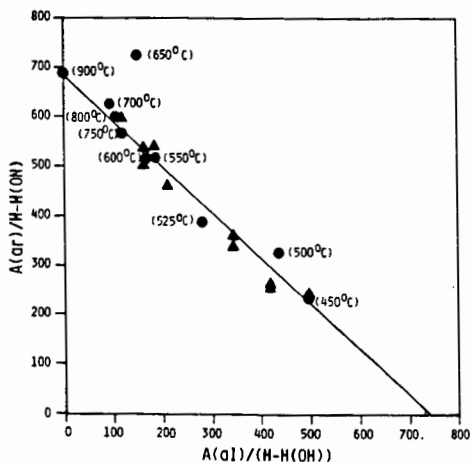


Figure 4. Regression Analysis to Determine  
Aromatic and Aliphatic Absorptivities for  
Bituminous Coals, Tars and Chars.



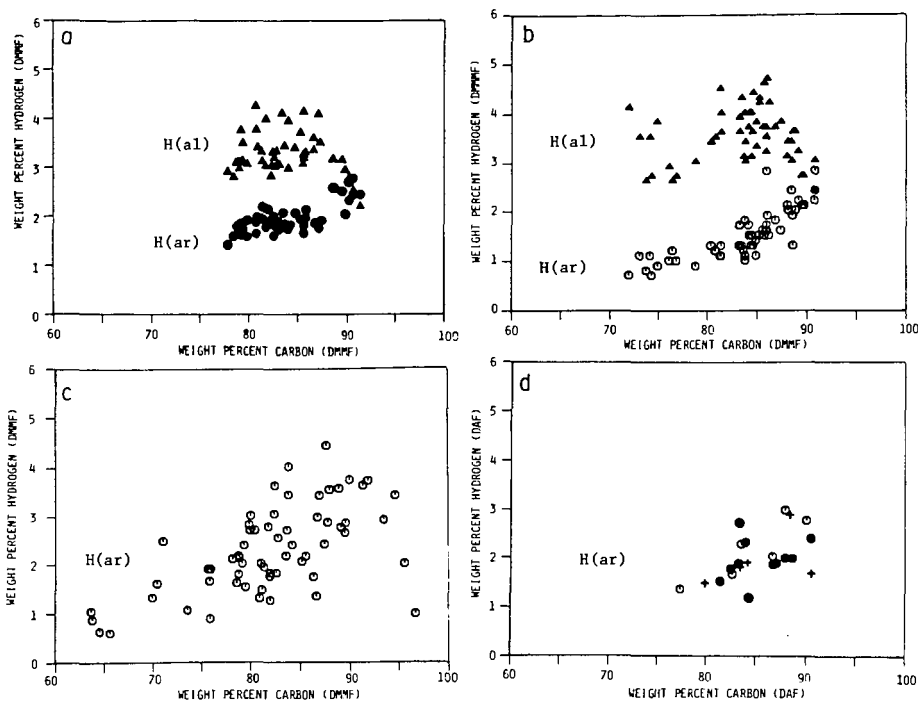


Figure 5. Aliphatic and Aromatic Hydrogen Concentration as a Function of Carbon Concentration. a) FT-IR, Present Results, b) FT-IR (10), c)  $^{13}\text{C}$ NMR with Dipolar Dephasing (11), and d) Proton NMR (12), (13), + (14).

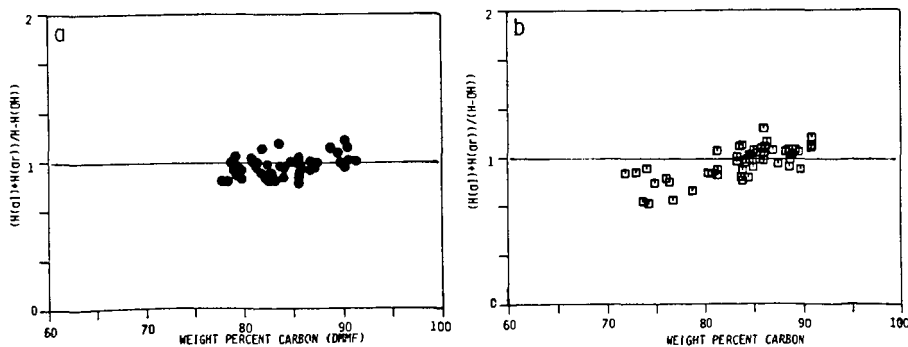


Figure 6. Hydrogen Balance,  $(\text{H(al)} + \text{H(ar)})/(\text{H} - \text{H(OH)})$  as a Function of Carbon Concentration a) FT-IR, Present Results and b) FT-IR (10).

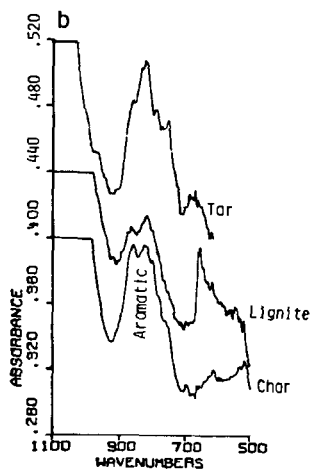
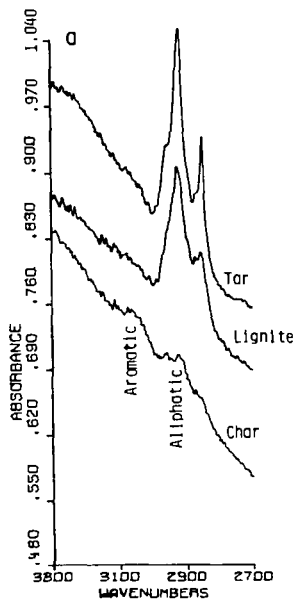


Figure 7. Comparison of Aromatic Hydrogen Stretch at 3100 Wavenumbers and Wag at 800 Wavenumbers.

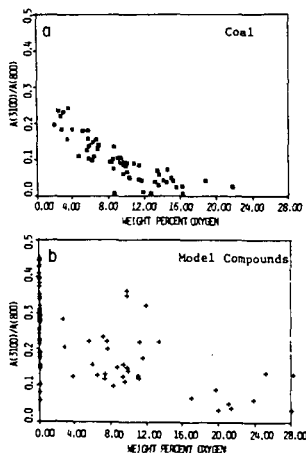


Figure 8. Ratio of Aromatic Stretch (3100 wavenumbers) to Aromatic Wag (800 wavenumbers) Absorption Bands as a Function of Oxygen Concentration.

TABLE I

Author	Ref.	H(al)/H(ar)
Brown	15	0.20
Brown et al.	14	0.33
Reisser et al.	10	0.35
Durie, et al.	13	0.38
Summary of other data		
Retcofsky	12	0.48
Present Results		0.52
Durie, et al.	13	0.56
Mazumdar	16	0.59
Summary of data		
Wilson et al.	11	0.70
Coals and Vitrinities		
Average		0.46

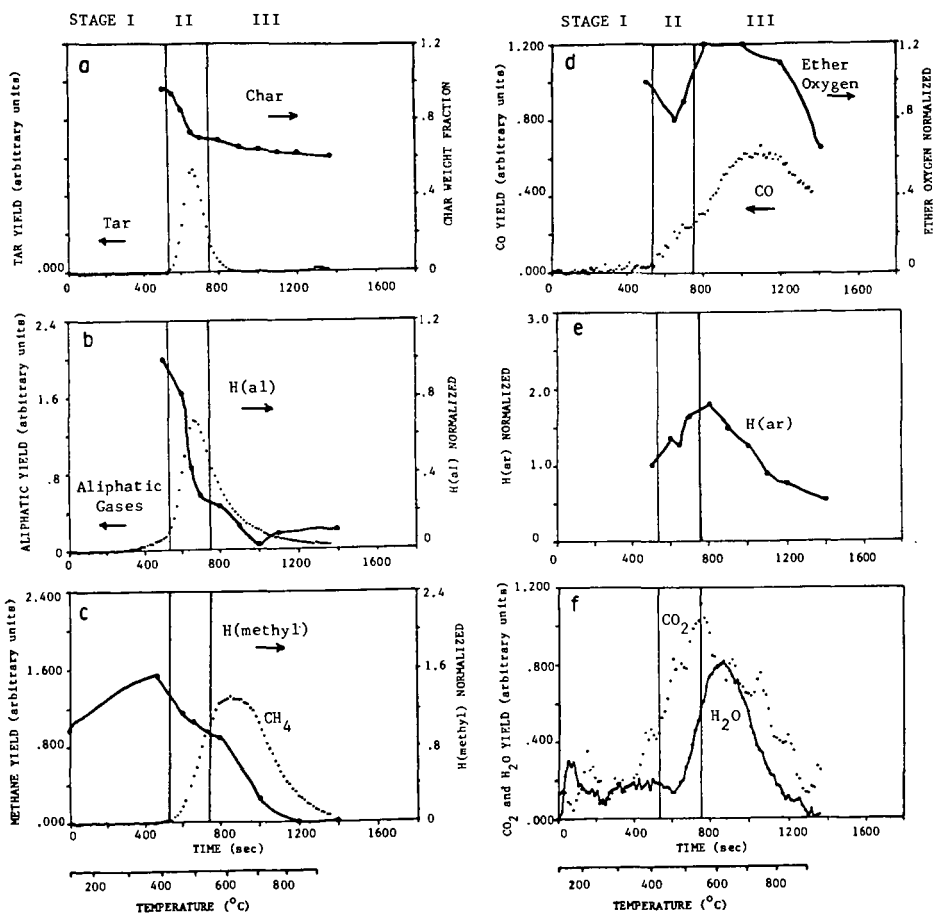


Figure 9. Comparison of Functional Group Composition and Evolved Gases in Slow Pyrolysis.

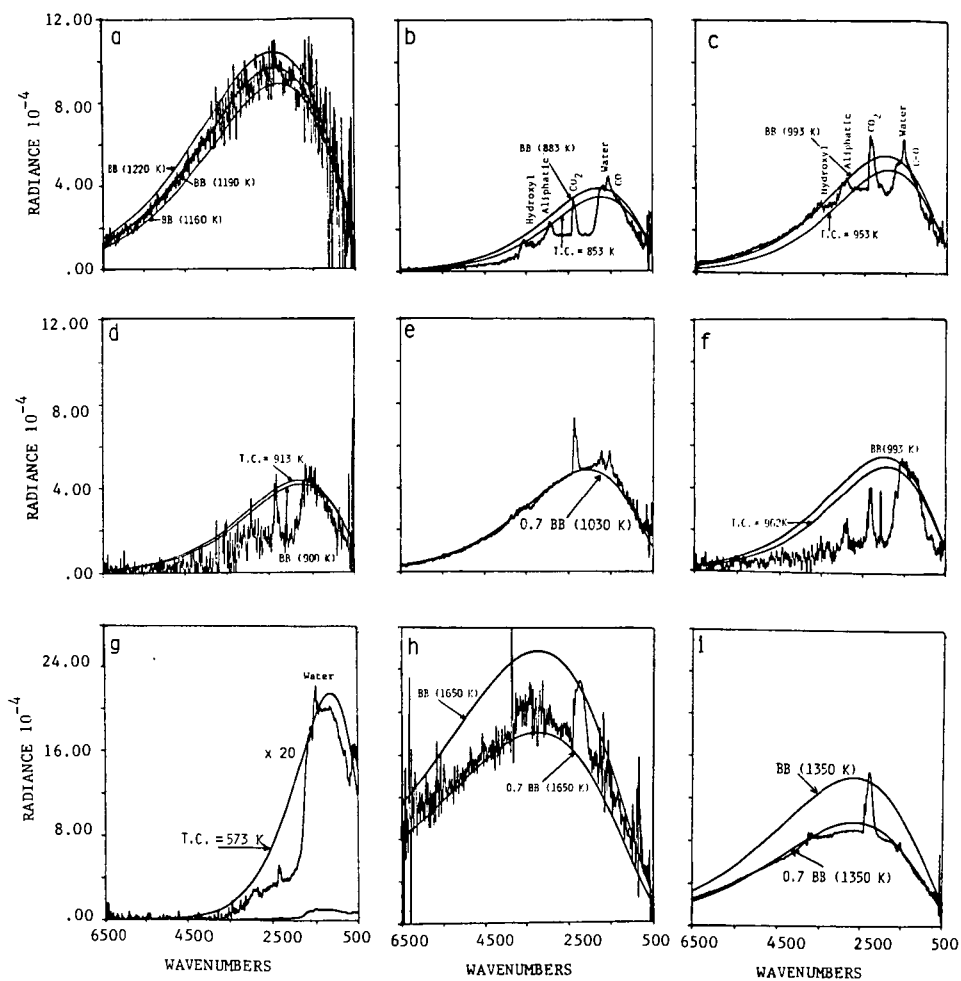


Figure 10. Normalized Emission Spectra for Coal and Char. a) Char in Stage III, b) Coal, c) and d) Char During Stage II, e) Char after Stage III, f) Char During Stage II, g) Coal, h) Lignite Char During Combustion, and i) Bituminous Char During Combustion.

# COMPARISON OF FOURIER TRANSFORM INFRARED-PHOTOACOUSTIC SPECTROSCOPY (FTIR-PAS) AND CONVENTIONAL METHODS FOR ANALYSIS OF COAL OXIDATION

P.-L. Chien, R. Markuszewski, J. F. McClelland

Ames Laboratory\*, US DOE, Iowa State University, Ames, Iowa 50011

## ABSTRACT

Fourier Transform Infrared-Photoacoustic Spectroscopy (FTIR-PAS) has been used to study variations in coal oxidation produced under laboratory-controlled conditions (temperatures of 140 and 150°C and exposure times up to 72 hours). Prominent oxidation-induced spectral changes were monitored by the peak heights of carbonyl (1690  $\text{cm}^{-1}$ ) and carboxylate (1575  $\text{cm}^{-1}$ ) bands. Changes in these peak heights have been plotted against conventional test data which are sensitive to the oxidation level of coal. Good linearity was observed for comparisons with the U.S. Steel oxidation test by alkali extraction and with measurements of the heating value. Advantages demonstrated for the FTIR-PAS method of monitoring coal oxidation include speed of analysis (several minutes), non-destructive character, minimal sample preparation (coarse powder), insensitivity to sample mass, and flat spectral baselines without hydroxyl band interference common to KBr-pellet IR transmission spectroscopy.

## INTRODUCTION

It is well known that exposure of fresh coal to air will deteriorate its coking propensity as well as heating value, floatability, and other properties. The oxidation of coal begins with adsorption (physical adsorption and chemisorption) of oxygen on accessible aromatic and aliphatic surface sites to form acidic functional groups, in particular,  $-\text{COOH}$ ,  $=\text{CO}$ , and phenolic  $-\text{OH}$  (1). If moisture is generated from chemically combined hydrogen in coal, some chemisorbed oxygen will produce peroxide or hydroperoxide complexes. The breaking down of these hydroperoxide groups at higher oxidation temperature (140°C) is responsible for the loss of CH groups (2). At later stages of oxidation, the acids produced combine with phenol to generate esters or anhydrides (2,3,4). Conventional oxidation testing methods (including free swelling, Gieseler plasticity, U. S. Steel oxidation transmission, and heating values) not only need a considerable time to complete a single measurement but also offer no information about the detailed chemical changes of coal. For instance, the U. S. Steel oxidation transmission test can only indicate whether or not coal is good for metallurgical use (5) while heating values provide only caloric data.

Methods based on diffuse reflectance (4,7,8), transmission (2,3,6), and photoacoustic (7,8) Fourier Transform Infrared (FTIR) spectroscopy have been used extensively in recent years in studies of oxidation associated coal beneficiation products. These methods can help reveal the detailed mechanisms of coal oxidation. Painter et al. (2,3,6) applied the transmission FTIR method to study oxidation mechanisms. They attributed the formation of ester links as responsible for the loss of free swelling characteristics and suggested that loss of aliphatic CH groups during oxidation is responsible for reduction of Gieseler plasticity. The groups of Hamza (7) and Lynch (8) have deduced that coal oxidation is initiated at aliphatic carbon adjacent to aromatic rings and that the initial generation of hydroperoxides and cyclic peroxides precedes the formation of carbonyl functionality which can reduce the hydrophobicity of coal surfaces, resulting in decreased floatability. On the contrary, Spitzer (9) believes that the decrease of floatability of coal after oxidation is associated with decreasing alkyl content and not with increasing oxygen content.

\* Ames Laboratory is operated for the U. S. Department of Energy by Iowa State University under Contract No. W-7405-Eng-82.

Although there are controversies in explaining the oxidation results characterized by FTIR methods, the information provided enables insights into detailed reaction mechanisms. However, there are several inherent disadvantages in diffuse reflectance and transmission methods including difficulty in obtaining a suitable reference spectrum in diffuse reflectance measurements, variable moisture content in KBr-pellet transmission spectroscopy, tedious sample preparation, severe background scattering, difficulty in selection of correct scaling factors for spectral subtraction, and uncertainty of pressure effects in making KBr pellets. The FTIR-PAS method is able to provide the same quality of results as the other FTIR methods in analyzing coal beneficiation products but with fewer problems. In this paper, capabilities of the FTIR-PAS method for characterizing coal oxidation are demonstrated with comparisons of FTIR-PAS results to those of conventional coal analysis data.

#### EXPERIMENTAL

FTIR-PAS spectra were measured with an IBM Instruments IR-98 FTIR system (8 cm<sup>-1</sup> resolution, 128 scans) and a photoacoustic cell designed and constructed at the Ames Laboratory. The cell sample cup volume was less than 0.1 cm<sup>3</sup> and contained helium gas during measurements to enhance the signal amplitude. The photoacoustic interferogram signal was detected in the frequency range 90 to 900 Hz by a model 4176 pre-polarized Bruel and Kjaer microphone with 50 mV/Pa sensitivity. Signals were amplified by a thousand gain preamplifier before being fed into the FTIR instrument for processing. After the interferogram was Fourier transformed, spectra were subtracted using the IR-98 software and difference spectra plotted, usually without spectral smoothing.

The Illinois No. 6 coal used in this oxidation study was obtained from the Ames Laboratory Coal Library (11). It came from the Captain Mine in Randolph County, IL. The description of the coal is given in Table 1.

Table 1. Analysis of Illinois No. 6 Coal Performed at Ames Laboratory

Proximate Analysis, (%):	Sulfur Forms (dry)						Heating Value (Btu/lb) Dry	
	Moisture	Volatile Matter	Ash	Total Sulfur	Pyritic Sulfur	Sulfate Sulfur		Organic Sulfur (by diff.)
	8.14	33.65	13.12	3.45	2.03	0.14	1.28	12,189
Ultimate Analysis, (%):	C	H	S(total)		N	O(by diff.)		
	62.17	4.13	3.45		1.60	15.53		

Controlled oxidation of the Illinois coal was performed at Ames Laboratory by placing samples in an oven at either 140 or 150°C for varying times up to 72 hours with an air flow rate of 42 ml per second. The particle size ranged from 44 to 125 micrometers (120 to 325 mesh). FTIR-PAS spectra, heating value measurements, and U. S. Steel oxidation transmission tests on the Illinois #6 coal were also completed in this Laboratory. The amount of sample needed for acquiring FTIR-PAS spectra was roughly 15 mg. No sample preparation after sieving was required for this measurement. Raw or oxidized coal was poured directly into the photoacoustic cell's sample holder and the spectra were measured. Since the photoacoustic signal is rather insensitive to the amount of sample used for measurements, volume sampling is adequate.

and it is unnecessary either to weigh out samples for analysis or to adjust the spectrum weighting factor during spectral subtraction. The FTIR-PAS spectral acquisition time is typically three minutes (128 scans) per sample. The degree of oxidation as characterized by this method is determined by the changes in peak heights of carbonyl ( $1690\text{ cm}^{-1}$ ) and ionized carboxyl ( $1575\text{ cm}^{-1}$ ) bands which can be quantitatively measured by spectral subtraction.

Measurements for the U. S. Steel oxidation transmission test (5) were performed by: adding 1g of coal sample to 100 ml of 1 N NaOH; adding one drop of Tergitol to the caustic-coal slurry; boiling the caustic-coal slurry for 3 minutes; cooling and filtering the slurry through a 45 micrometer Whatman filter paper; diluting the filtrate with distilled water to a total volume of 80 ml; and measuring the percent transmission of the solution with a spectrophotometer set at 520 nm. The heating values were determined using the standard ASTM method (D2015).

## RESULTS AND DISCUSSION

Spectra 1a and 1b of Figure 1 are for raw Illinois #6 coal acquired by conventional transmission FTIR and FTIR-PAS methods, respectively. Besides the problems of background scattering and uncertainty of hydroxyl bonds ( $1600$  and  $3400\text{ cm}^{-1}$ ) in spectrum 1a, these two methods give qualitatively similar results. Spectrum 1c was acquired by the FTIR-PAS method on the same Illinois #6 coal after oxidation in air at  $140^{\circ}\text{C}$  for 24 hours. Spectrum 1d shows the spectral differences between the oxidized and the raw coal after spectral subtraction. No weighting factor adjustment was used or was necessary because scaling of the FTIR-PAS spectrum is insensitive to sample mass.

Besides the increases of carbonyl ( $1690\text{ cm}^{-1}$ ) and carboxylate ( $1575\text{ cm}^{-1}$ ) bands as well as the decrease of aliphatic CH groups ( $\sim 2900\text{ cm}^{-1}$ ), there also appear to be slight losses in aromatic CH ( $\sim 3050\text{ cm}^{-1}$ ) and in hydroxyl OH ( $\sim 3550\text{ cm}^{-1}$ ) groups. The observations at  $1690$ ,  $1575$ , and  $2900\text{ cm}^{-1}$  are consistent with Painter's results (3,6), while all of the features observed are in agreement with Smyrl's results (4). Apparently Painter's failure to see the features near  $3050$  and  $3550\text{ cm}^{-1}$  is due to the moisture interference and subtraction factor selection problems associated with transmission. Smyrl applied an in-situ diffuse reflectance method to characterize coal oxidation which, like the present work, is free from worries of moisture interference and subtraction factor selection.

Although there is controversy about which portions of coal are consumed during oxidation, the carbonyl, carboxylate and ester groups produced by the reaction have never been doubted. Therefore, these functional groups were selected to correlate with the results from conventional characterization methods. For instance, Figure 2 shows the increase of carbonyl and ionized carboxyl peak heights measured by the FTIR-PAS method and the variations of percent transmission measured by the U. S. Steel oxidation transmission test versus time of oxidation for Illinois #6 coal samples at  $140^{\circ}\text{C}$ . Similar saturation trends for FTIR-PAS and U. S. Steel tests are evident for oxidation conducted at both  $140$  and  $150^{\circ}\text{C}$ , resulting in the asymptotic behavior of carbonyl and carboxylate group changes. Figure 3 shows that the FTIR-PAS and U. S. Steel test data are linearly correlated. Data for coal oxidized at  $140^{\circ}\text{C}$  and  $150^{\circ}\text{C}$  are plotted in this figure to show that linearity is maintained for two different oxidation conditions. The linear correlation was found for both temperatures to better than 6% transmission units.

Two hypotheses regarding coal oxidation behavior are suggested by the linear correlation observed. First, the loss of coking properties of coal during oxidation is due to the formation of oxygen functional groups. Since the U. S. Steel test is a measurement of coking properties, the linear relationship of these two methods

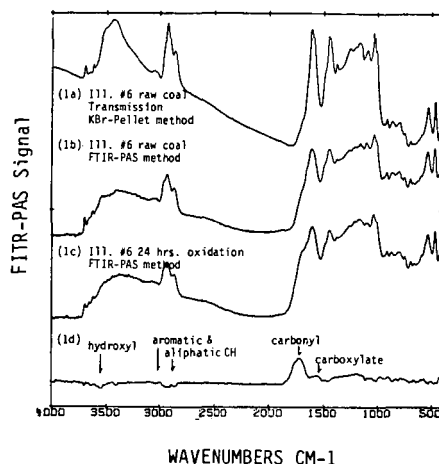


Figure 1. Comparison of Illinois #6 coal spectra, measured by transmission and photoacoustic methods and an example of a spectral subtraction result using photoacoustic spectra to show oxidation induced spectra changes.

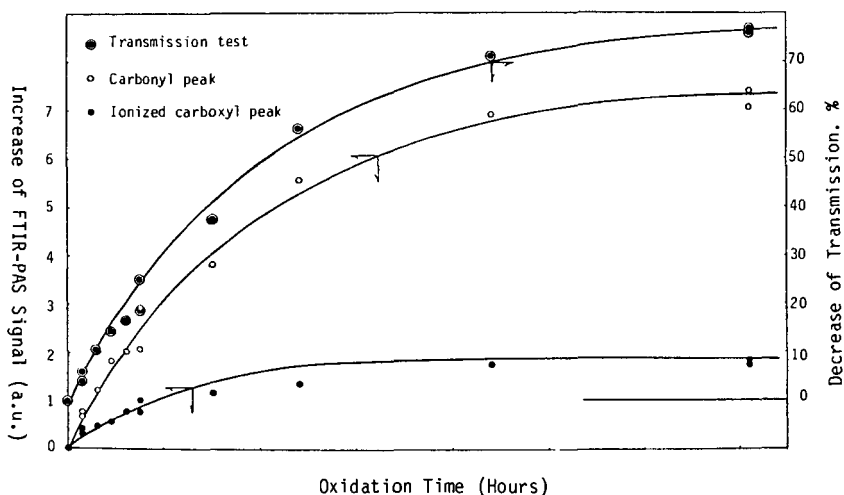


Figure 2. Progress of oxidation measured by the FTIR-PAS method and U. S. Steel alkali extraction transmission test (a.u.=arbitrary units).



suggests that both the degradation of coal in coking ability and the U. S. Steel transmission value are due to the formation of oxygen functional groups. Second, the coal particles in the size range explored appear to be oxidizing uniformly throughout their volume rather than to a decreasing degree with depth as would be the case for a diffusion limited process. The hypothesis is based on the fact that for this size coal sample, particles are opaque and the FTIR-PAS measurement senses a surface layer whereas the U. S. Steel test is a bulk determination. Since the data of the two methods have a linear correlation, the surface and bulk regions appear to be uniformly oxidized. To test this hypothesis further, the coal samples oxidized at 140°C were ground to the micrometer size range to permit the FTIR-PAS measurement of the bulk material oxidation changes since the particles are no longer opaque. To prevent additional coal oxidation during the grinding process, the grinder capsule which contained coal was cooled by liquid nitrogen. The results obtained from the FTIR-PAS spectra of ground, oxidized coal are plotted in Figure 4 against the results before grinding. The linear relation found in this plot indicates the same time evolution for oxidation of surface and bulk regions of the samples. Hence, the oxidation processes do not appear to be either separate surface-bulk processes or diffusion-limited processes but rather processes occurring uniformly throughout the bulk for the experimental conditions used.

There are two heating value estimating formulas available for coal, the Dulong and the Dulong-Berthelot formulas (Ref. 1, p. 35). In these two formulas the heating value decreases linearly with increasing oxygen content of coal. This implies that the decrease of heating value during oxidation can be correlated linearly with the amount of oxygen functional groups produced. Figure 5 is a plot of the decrease in the ASTM heating value versus increase in coal oxidation as monitored by changes in the sum of peak amplitudes associated with carbonyl and carboxylate bands of Illinois #6 coal. A common linear relation was found between these two methods for both 140 and 150°C oxidation conditions. This linear relationship between heating value degradation and FTIR-PAS data may enable optimization of coal beneficiation processes when coal oxidation occurs during the process. Since the beneficiation process includes demineralization, the decrease of mineral contents of coal can also be monitored by the same FTIR-PAS spectrum. Hence, the trade-off between mineral removal and loss of heating value can be evaluated based on one sample and a single data acquisition effort. Furthermore, the correlation between the U. S. Steel test and FTIR-PAS data can also be used to determine whether or not demineralized coal still has coking properties for metallurgical use.

Samples of coal oxidized by natural weathering, which were provided by the Koppers Company, were also studied and the FTIR-PAS spectra were measured. Linear correlations were found between our FTIR-PAS results and results obtained previously (10) for the U. S. Steel oxidation transmission, free swelling index, and Gieseler plasticity tests. These findings, which will be reported fully elsewhere, suggest that FTIR-PAS data can be correlated and substituted for data from these conventional coal tests which demand more time.

In the above discussions, only spectral changes of oxygen-containing functional groups generated during oxidation of coal were used to correlate with conventional testing method results. If the other features of FTIR-PAS subtraction spectrum 1d (as shown in Figure 1) are also involved in the data manipulation, more relations may be found that will provide a better understanding of the oxidation process.

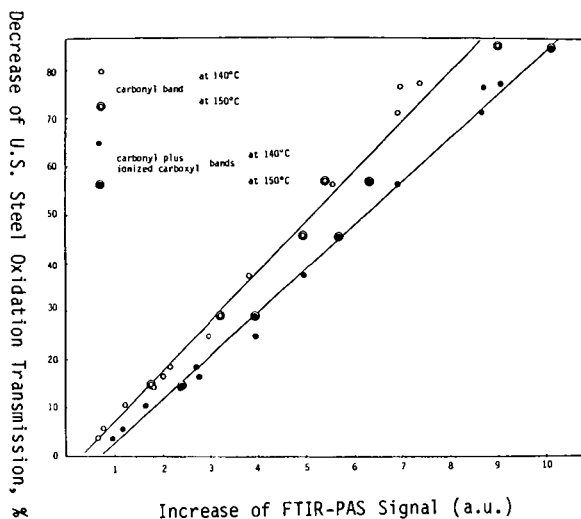


Figure 3. Comparison of FTIR-PAS signal to U. S. Steel oxidation transmission tests at the oxidation temperatures of 140 and 150°C (a.u.=arbitrary units).

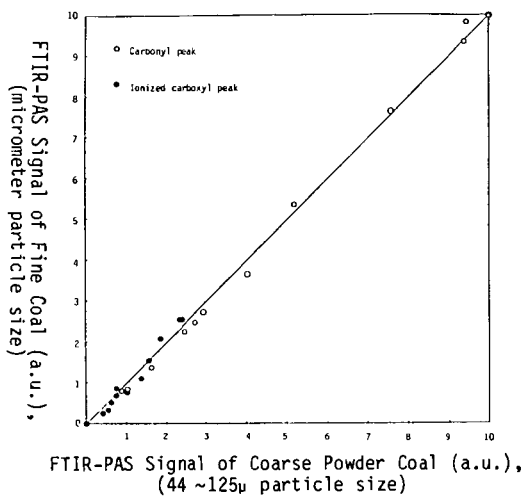


Figure 4. Plot of the photoacoustic signal for coarse opaque versus signal for fine non-opaque coal powders showing that oxidation has occurred uniformly through the coarse powder volume (a.u.=arbitrary units).

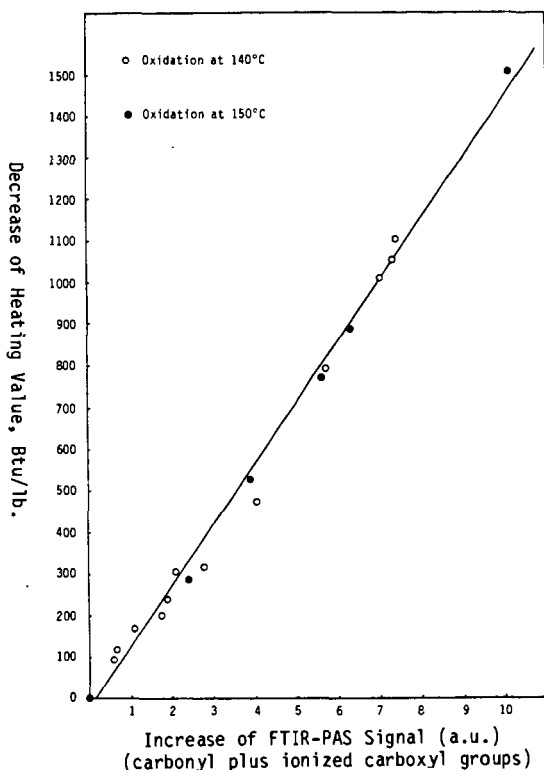


Figure 5. Comparison of FTIR-PAS signal to heating value measurement at the oxidation temperatures of 140 and 150°C (a.u.=arbitrary units).

#### CONCLUSIONS

FTIR-PAS spectral changes induced by coal oxidation have been found to correlate linearly with results of conventional coal analysis methods that are sensitive to coal oxidation. Advantages demonstrated for the FTIR-PAS method of monitoring coal oxidation include speed of analysis (several minutes), non-destructive character, minimal sample preparation (coarse powder), insensitivity to sample mass, and flat spectral baselines without hydroxyl band interference common to KBr-pellet IR transmission spectroscopy.

## REFERENCES

1. N. Berkowitz, "An Introduction to Coal Technology", Academic Press, New York, 1979, pp. 95-104.
2. C. A. Rhoads, J. T. Senftle, M. M. Coleman, A. Davis, and P. C. Painter, Fuel, **62**, 1387 (1983).
3. P. C. Painter, R. W. Snyder, D. E. Pearson, and J. Kwong, Fuel, **59**, 282 (1980).
4. N. R. Smyrl and E. L. Fuller, "Chemistry and Structure of Coals - Diffuse Reflectance IR Fourier Transform (DRIFT) Spectroscopy of Air Oxidation," in Coal and Coal Products: Analytical Characterization Techniques, ACS Symposium Series 205, E.L. Fuller, ed., 1982, pp. 133-145.
5. D. E. Lowenhaupt and R. J. Gray, International J. of Coal Geology, **1**, 63 (1980).
6. P. Painter and C. Rhoads, ACS Division of Fuel Chemistry Preprints, **26**(1), 35 (1981).
7. H. A. Hamza, K. H. Michaelian, and N. E. Andersen, Proc. 1983 International Conference on Coal Science, Pittsburgh, PA, pp. 248-251.
8. B. M. Lynch and A. M. MacEachern, Proc. 1983 International Conference on Coal Science, Pittsburgh, PA, pp. 653-654.
9. D. P. Spitzer, Proc. Pittsburgh Coal Conference, 1984, Pittsburgh, PA, pp. 858-872.
10. J. Markiewicz and R.J. Gray, Task Group Report on Alkali Extraction Test for Oxidized Coal, ASTM Meeting, Louisville, KY, May 9-11, 1983.
11. D.L. Biggs, D.H. Birlingmair, R.W. Fisher, R.T. Greer, R.A. Kaelin, R. Markuszewski, B.F. Smith, T.G. Squires, C.G. Venier, and T.D. Wheelock, "Status Report on the Collection and Preparation of Coal Samples for the Ames Laboratory Coal Library," presented at the Coal Sample Bank Workshop at the Am. Chem. Soc. Meeting, Atlanta, GA, March 27-28, 1981.

## ACKNOWLEDGEMENTS

This work was performed for the Ames Laboratory, operated for the U. S. Department of Energy by Iowa State University under Contract No. W-7405-Eng-82, and was supported by the Assistant Secretary of Fossil Energy, Division of Coal Utilization, through the Pittsburgh Energy Technology Center, Coal Preparation Branch. The authors would like to express gratitude to Dr. John Markiewicz at the Koppers Company for providing naturally weathered coal samples and test results, as well as to N. Adams, G. Norton, and R. Bachman at Ames Laboratory for conducting coal oxidation, heating value, and U. S. Steel oxidation tests.

# A SPECTROSCOPIC STUDY OF THE PRODUCTS OF REDUCTIVE ALKYLATION OF AN ILLINOIS COAL

Leon M. Stock and Reid S. Willis

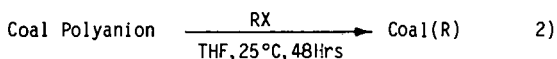
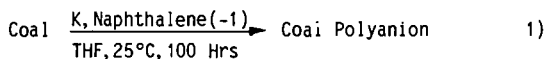
Department of Chemistry, University of Chicago, Chicago, IL 60637

## INTRODUCTION

Mild chemical reactions such as alkylation and reductive alkylation provide techniques for the conversion of coal macromolecules into substances that are soluble. The soluble products of such reactions can be investigated by one and two dimensional, high resolution NMR spectroscopy to obtain structural information that is often difficult to obtain by the investigation of solids. Moreover, the soluble products can be subjected to selective chemical transformations to obtain additional information to guide the interpretation of the spectroscopic results. This article concerns the use of a selected series of chemical reactions and nuclear magnetic resonance spectroscopy for the definition of the structural characteristics of the reactive carbanions and oxygen anions formed during the reductive alkylation of an Illinois No. 6 coal.

## RESULTS AND DISCUSSION

The reductive alkylation (1,2) of a representative Illinois No. 6 coal,  $C_{100}H_{87.0}O_{13.1}S_{1.9}N_{0.75}$ , with 8.2 % ash, was carried out as shown.



The reactions were performed and the products were isolated as described previously (3) using methyl, methyl- $d_3$ , methyl- $^{13}C$ , and ethyl iodide as the alkylating agents. The yield of tetrahydrofuran-soluble products ranged from 48 to 68% in 15 experiments. Infrared spectroscopy established that the alkylation reaction was complete. In particular, the very typical, broad oxygen-hydrogen stretching frequency was absent in the spectra of the products. The molecular weight distribution of the soluble, alkylated coal was examined by vapor pressure osmometry (4). The results imply that the number average molecular weight of the material obtained after filtration and gel permeation chromatography is about 2000 in pyridine solution.

Several different measurements indicate that about 22 equivalents of potassium are consumed per 100 carbon atoms of this coal during reductive alkylation (3). Analyses of the soluble reaction products obtained in the reaction with methyl- $d_3$  iodide for deuterium by deuterium nuclear magnetic resonance spectroscopy and by combustion mass spectroscopy (5) indicate that the most soluble products contain  $11 \pm 1.5$  alkyl groups per 100 carbon atoms. The difference between the amount of potassium consumed in the reduction and the degree of alkylation arises, in part, because the reactive

intermediates generated in the reduction reaction abstract hydrogen from tetrahydrofuran. The occurrence of this reaction was demonstrated by conducting the reduction in the presence of labeled tetrahydrofuran and quenching the reaction in water. We estimate that not less than 5 hydrogen atoms are incorporated into the coal macromolecules from the solvent on the basis of the degree of incorporation of deuterium in the experiment and the anticipated primary kinetic isotope effect.

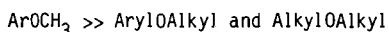
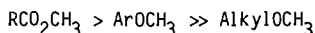
**C-Alkylation.**--Quantitative analyses of the reaction products obtained using methyl- $^{13}\text{C}$  iodide by carbon NMR spectroscopy indicate that about equal quantities of C- and O-alkylation products are formed (3). Following a leading observation by Ignasiak and his coworkers (6), we also examined the carbon NMR spectrum of the products obtained in a reductive ethylation reaction. There were 5 prominent absorption bands in the spectrum as outlined in Table 1. The resonance at 8.5 ppm is surprisingly intense and implies that the concentration of ethyl groups at saturated, quaternary carbon atoms is quite high. Indeed, quantitative analysis of the spectral data suggest that the carbon alkylation reactions occur preferentially at highly substituted positions and at primary benzylic positions and are compatible with the idea that this coal contains three distinct structures--reactive aryl methyl groups, activated trisubstituted methane fragments, and aromatic structures--that may be alkylated.

**O-Alkylation.**--The assignments of the resonances of the O-methylation products observed in regions 1, 2, and 3 obtained in the reactions with methyl- $^{13}\text{C}$  iodide, Figure 1, are summarized in Table 2. The assignments presented in column A are based upon chemical shift data exclusively. To obtain more definite information about the structures of the compounds responsible for these resonances, we carried out a series of selective chemical transformations.

First, the soluble reaction products were hydrolyzed using tetrabutylammonium hydroxide in aqueous tetrahydrofuran for 24 hours at room temperature. The solution was acidified with dilute hydrochloric acid and the product was isolated and dried prior to the reexamination of its carbon spectrum. Quantitative measurements of the absorption at 51 ppm revealed that over 98% of the intensity was removed. Hence, the resonances in region 3 arise, virtually exclusively, from alkyl and aryl carboxylic acid esters.

Second, acid hydrolysis was carried out to examine the proposal of Hanel and coworkers (7) that enol methyl ethers may, in part, be responsible for the resonance signals in region 1. The reaction was carried out with 2N hydrochloric acid in aqueous tetrahydrofuran for 48 hours at room temperature. The product was recovered and the NMR spectrum recorded. There was no change in the absolute intensities of the resonance signals in regions 1 and 2. Thus, methyl vinyl ethers are not formed to a measurable degree in the reductive alkylation of the Illinois coal.

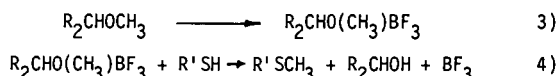
Third, a selective displacement reaction was used to distinguish the methyl alkyl ethers from the methyl aryl ethers. The reaction of the soluble coal with lithium iodide in collidine at 170°C for 24 to 48 hours was used for this purpose. The chemical literature indicates that this reaction is highly selective for the displacement of methyl groups (8).



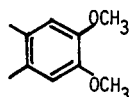
Appropriate control experiments with collidine indicated that the alkylated coal could be recovered unchanged from the reaction medium in the absence of lithium io-

dide. However, when the reaction was carried out with in the presence of the iodide there was a 70% decrease in solubility in tetrahydrofuran. The product was alkylated with unlabeled ethyl iodide to yield a material that was more than 80% soluble in pyridine. The carbon NMR spectrum of this product is greatly altered, Figure 2A. Specifically, the areas of regions 1, 2, and 3 are decreased by 96, 89, and 100%, respectively.

Fourth, it is known (9) that primary and secondary alkyl methyl ethers and benzyl methyl ethers can be cleaved selectively by boron trifluoride-etherate and a thiol, equations 3) and 4).



This reaction was performed with the  $^{13}\text{C}$  enriched demethylated coal using 1,2-ethanedithiol at room temperature. The product of the reaction was quite soluble in organic solvents. The changes in the intensities of the resonances at 55 and 58 ppm, Figure 2B, are particularly informative. The signal at 58 ppm has disappeared from the spectrum but the signal at 55 ppm is unaltered. These results imply that the compounds responsible for the residual signal at 58 ppm in Figure 2A are aliphatic methyl ethers and that the compounds responsible for the residual signal at 55 ppm in Figures 2A and 2B are aryl methyl ethers that resist dealkylation by both lithium iodide and borontrifluoride-ethanedithiol. The observations are most consistent with the presence of dimethoxyaryl compounds.



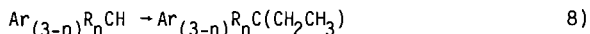
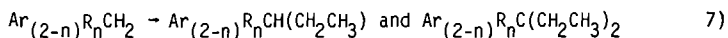
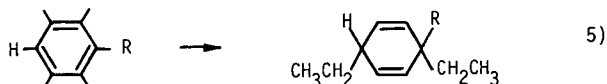
These compounds are known to resist demethylation with lithium iodide and to be inert toward acid-catalyzed cleavage. Thus, we infer that about 4% of the methyl groups added to this coal appear in such structures. The existence of compounds of this type may also be inferred from the differences observed in the nuclear Overhauser effect for the compounds in region 2 relative to the NOE for the other O-alkylation products.

The fact that the acid-catalyzed ether cleavage reaction eliminates the resonance at 58 ppm confirms the assignment of this weak signal to an aliphatic methyl ether. The chemical shift observed for this resonance is in accord with the resonance expected for the carbon atom of the methyl group in a primary alkyl methyl ether, but is incompatible with the signal expected for a simple primary benzyl methyl ether.

#### CONCLUSION

Reductive alkylation adds about 12.5 alkyl groups/100 carbon atoms to the Illinois No. 6 coal. Broadly speaking 5.5 of these groups are bonded to carbon atoms and 7 are bonded to oxygen atoms. Only very small quantities of nitrogen and sulfur alkylation products can be detected. The spectroscopic results for the reductively

ethylated coal suggest that the C-alkylation reactions proceed via reductive alkylation to yield substituted dihydroaromatic compounds, equation 5), and via base-catalyzed alkylation to yield substituted arylmethanes as shown in equations 6) - 8).



The occurrence of the latter reactions strongly suggests that this Illinois coal contains three or four reasonably strong carbon acids per 100 carbon atoms. The existence of these reaction sites offers new opportunities for other selective transformation reactions.

The results obtained in the spectroscopic investigations of the chemically transformed O-alkylation products provide a reasonable basis for the definition of the relative abundances of the different O-alkylation products. The outcome of the analysis is shown in Column B of Table 2. The new observations provide definite information regarding the occurrence of low, but observable, quantities of alkyl methyl ethers, the presence of significant amounts of highly hindered aryl methyl ethers and dimethoxyaryl compounds and carboxylic acid esters. Our results also exclude several types of compounds. Thus, primary benzylic methyl ethers, secondary and tertiary alkyl methyl ethers as well as vinyl methyl ethers are not present in detectable amounts. We infer that the observed distribution of products in the alkylated coal is comparable to the distribution of these functional groups in the original coal. As a consequence, the new results provide a more secure basis for the discussion of the structure and reactivity of this coal.

#### REFERENCES

- 1) H.W. Sternberg, C.L. Delle Donne, P. Pantages, E.C. Moroni, and R.E. Markby, Fuel, **50**, 432 (1971).
- 2) The subject has been reviewed, L.M. Stock, Coal Science, **1**, 161 (1982).
- 3) L.B. Alemany and L.M. Stock, Fuel, **61**, 250 (1982).
- 4.) This determination was performed by J.W. Larsen and his students.
- 5) The combustion mass pectral analysis was carried out by Gollob Laboratories.
- 6) N. Cyr, M. Gawlak, D.W. Carson, and B.S. Ignasiak, Fuel, **62**, 412 (1983).
- 7) M.W. Haelnel, R. Mynott, K. Niemann, U.-B. Richter and L. Schanne, Angew. Chem. Int. Ed. Eng. **19**, 636 (1980).
- 8) J.E. McMurry, Org. Reactions, **24**, 187 (1976).



- 9) M. Node, H. Hari, and E. Fujita, J. Chem. Soc. Perkin Trans. I, 2237 (1976).

ACKNOWLEDGEMENT

It is a pleasure to acknowledge the support of this research by the United States Department of Energy and by the Illinois Department of Energy and Natural Resources.

Table 1. The Assignment of Resonances in the Carbon NMR Spectrum of Reductively Ethylated Coal.

Chemical Shift (ppm)	Assignment Resonance of Ethyl Group, Reaction
8.5	Methyl, ethylation at tertiary carbanionic center to form quaternary product, $R_3C(CH_2CH_3)$
12.5	Methyl, ethylation at secondary carbanionic center to form tertiary product, $R_2CH(CH_2CH_3)$
15	Methyl, ethylation at primary carbanionic center to form secondary product, $RCH_2(CH_2CH_3)$ Methyl, ethylation at oxygen, $ArO(CH_2CH_3)$
65	Methylene, ethylation at unhindered aryl oxygen, $ArO(CH_2CH_3)$
69	Methylene, ethylation at hindered aryl oxygen, $R_2ArO(CH_2CH_3)$

Table 2. Column A. The Assignments of the Resonances in the O-Alkylation Region of the Carbon NMR Spectrum of Reductively Methylated Illinois No. 6 Coal. Column B. The Relative Abundances of the O-Alkylation Products Defined by Chemical Conversions and Carbon NMR Spectroscopy.

Column A Possible NMR Assignments	Column B Relative Abundance <sup>a</sup>
1. Region Centered at 61 ppm	Region Centered at 61 ppm
Vinyl ethers	
Primary alkyl ethers	Primary alkyl ethers 0.1
Primary benzyl ethers	
Hindered aryl ethers	Hindered aryl ethers 2.2
2. Region Centered at 55 ppm	Region Centered at 55 ppm
Secondary alkyl ethers	
Unhindered aryl ethers	Unhindered aryl ethers
Dihydroxyaryl compounds	Dihydroxyaryl compounds 0.6
Simple aryl ethers	Simple aryl ethers 3.3
3. Region Centered at 51 ppm	Region Centered at 51 ppm
Tertiary alkyl ethers	
Aryl- and Alkylcarboxylic acid esters	Aryl- and Alkylcarboxylic acid esters 0.8

<sup>a</sup>The results have been normalized on the basis of the analytical results which suggest that there are 7 O-methyl groups per 100 carbon atoms in the alkylated products.

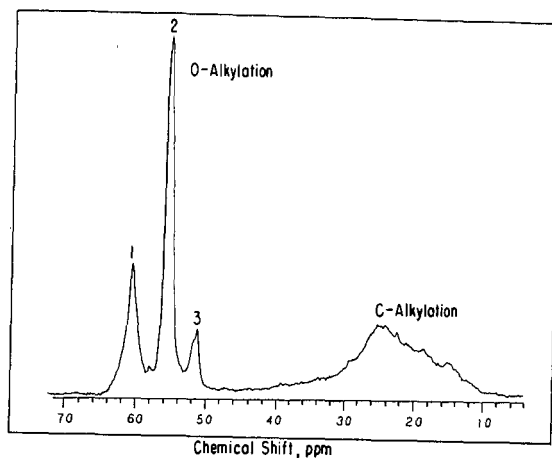


Figure 1.--The carbon nuclear magnetic resonance spectrum of an intermediate molecular weight, gel permeation chromatography fraction of the product of reductive methylation of Illinois No. 6 coal.

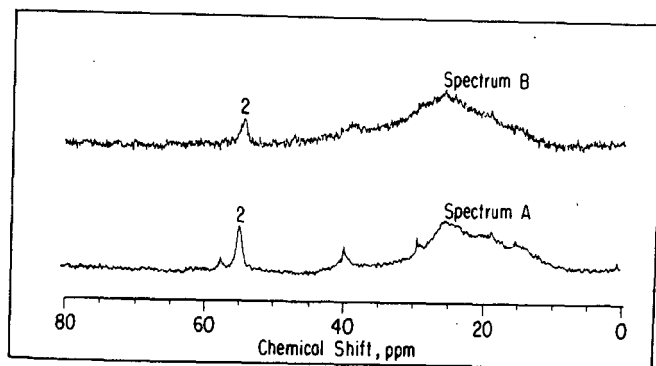


Figure 2.--The carbon nuclear magnetic resonance spectrum of the material shown in Figure 1 (A) after treatment with lithium iodide in collidine and (B) after subsequent treatment with boron trifluoride and ethanedithiol.

A DETAILED STRUCTURAL CHARACTERIZATION OF HEAVY CRUDE  
ATMOSPHERIC TOWER BOTTOMS

by

D. W. Grandy, D. A. Danner, T. L. Youngless,  
G. P. Feulmer, D. C. Young, and L. Petrakis

As the petroleum industry finds itself faced with increasing proportions of heavy sour crude, researchers must address the problem of how to upgrade this material to be compatible with existing refinery processes and product slates. The first problem to be faced in upgrading a heavy crude or residue is how to characterize the material well enough to understand the chemistry of the upgrading process. Crude residues are far more complex than coal liquids for they not only contain a variety of aromatic and heterocyclic units, but they also contain naphthenic and alkyl substituents of almost infinite variety on these simpler units as well as heavy alkanes.

The samples that will be discussed here were derived from a Maya (Mexico) crude (API gravity 19.1°). Since we are primarily interested in the chemistry of the residue, the crude was distilled at 680°F (360°C) to obtain an atmospheric tower bottom (ATB). The Maya ATB is 61% of the crude and has an API gravity of 7.7° and a sulfur content of 4.7%.

In order to simplify the characterization and upgrading chemistry, the Maya ATB was separated chromatographically into asphaltene, three acid, three base, neutral oil and neutral resin fractions on a preparative scale (1 kg) (1, 2). The separation yields and elemental analysis of the fractions are shown in Table I. A wide variety of characterization techniques were then applied to many of these fractions, including <sup>1</sup>H NMR, <sup>13</sup>C NMR (conventional and INEPT (3)), high resolution mass spectrometry (4) (HRMS), GC-MS (5), and atom specific GC (6).

Flame ionization detector (FID) and flame photometric detector (FPD) gas chromatograms of the Maya ATB neutral oil are shown in Figure 1 (5). The chromatograms were obtained on a Varian 3700 using a 10 ft long, 1/8 inch OD column packed with 10% OV-1 on acid-washed Chromasorb W. The FID trace shows an alkane series from n-C<sub>17</sub> to n-C<sub>34</sub> superimposed on a broad unresolved hump. The sulfur specific FPD trace shows some resolution of a few peaks at the low boiling end of the chromatogram and a similar unresolved hump. Other than the normal alkane series, no specific compounds were identified in the chromatogram. In spite of the rather small amount of information obtained on this sample, gas chromatographic techniques were found to be useful in monitoring changes in the hydrocarbon and sulfur species upon upgrading.

In order to eliminate interferences from saturates, the neutral oil was further separated into saturates, aromatics and polars by HPLC. This was done on a Waters HPLC using a dry silica (22-47 mesh) column.

The aromatic fraction was analyzed using a Kratos MS 50 high resolution mass spectrometer (HRMS) operated with an ionizing voltage of 70 eV, to obtain quantitative information on the aromatic and heterocyclic compounds in the neutral oil (4). Table II is a summary of the HRMS results, giving the weight percentage of the various species by Z number and the average number of carbon atoms in each Z class. For example, dibenzothiophenes were 3.32% of the sample and had an average of about six carbon atoms attached to the basic dibenzothiophene unit. Searching through the list of specific compounds in the sample reveals that dibenzothiophene accounts for 0.19% of the sample, methyl dibenzothiophene 0.43%, etc., through the series of alkyl dibenzothiophenes up to mass 408, C<sub>10</sub> dibenzothiophenes. Several hundred individual mass peaks are identified by carbon number, Z class, heteroatom content and weight percentage. This specific information allows the monitoring of the reactivity of particular molecules or molecular types.

GC-MS was also applied to the aromatic cut of the Maya ATB neutral oil. A Finnigan 4500 system with a 60-meter DB-5 fused silica capillary column was used. Due to the poor GC separation (see Figure 1), few GC peaks could be identified. However, knowing the masses of the sulfur species in the sample from HRMS, specific ion chromatograms were generated to obtain isomer number information and to observe the relative reactivity of these isomers in hydroprocessing (6). Figure 2 shows the mass chromatograms for dibenzothiophene (DBT) (m/z = 184) and substituted DBT through C<sub>7</sub>.

Proton and <sup>13</sup>C NMR spectra were obtained on most of the fractions from the Maya ATB on a Varian XL-200 FT NMR instrument. Table III gives some of the results from the <sup>13</sup>C NMR data on the fractions. Note that the neutral oils are the least aromatic fraction, being comprised of aromatics and "polars," which are only about one third aromatic, and 25% saturates, which gave no detectable signal in the aromatic region. Figures 3 and 4 show the normal <sup>13</sup>C NMR and INEPT spectra of the aromatic cut of the neutral oil (3). The INEPT technique causes the NMR signals due to CH and CH<sub>3</sub> to be inverted and virtually eliminates the signals due to carbons with no protons attached, such as those with a chemical shift around 140 ppm in the normal <sup>13</sup>C NMR spectra. A complete analysis of the spectrum gives much more structural detail.

The <sup>1</sup>H NMR spectrum of the Maya ATB neutral oil aromatics is shown in Figure 5. Although the spectrum is not rich in detail, due to the complex mixture in the sample, it can be analyzed by the technique of Clutter, Petrakis et al. to give average molecule information (7). These data are presented in Table IV. Compared to the <sup>13</sup>C NMR technique, the proton data give a somewhat lower aromaticity (0.27 versus 0.34) and a much lower (15.6% versus 28%) naphthenic carbon content. <sup>13</sup>C NMR techniques are believed to give the more reliable data. <sup>1</sup>H NMR, however, is better for determining the number of alkyl substituents.

While some of these types of data can be formally integrated to produce concentrations of functional groups (8), the general picture of the Maya ATB neutral oils that can be synthesized from the data is that the material is a very complex mixture of hydrocarbons and sulfur heterocycles. It contains about 25% saturates with alkanes from C<sub>17</sub> to about C<sub>40</sub>, alkyl

naphthenes, and very few isoprenoids. About 75% of the neutral oil is alkyl aromatics and thiophene-based compounds that are mostly from 1 to 5 rings, have some naphthene substituents, and are substituted, on the average in three to four positions with alkyl groups that range from methyl to about C<sub>16</sub>. The ratio of methyl to longer chains is 1.5:1 and the average length of the alkyl chain is about 5. Qian et al. give data from an aromatic cut of a petroleum pitch which has similar aromaticity, but a higher molecular weight and longer alkyl chains (9).

Due to their very complex nature, these petroleum residues require extensive separation and as many analyses as are available and affordable. While their absolute accuracy in describing the molecules in the mixture may be subject to a variety of errors, the strength of the analytical techniques described here is in measuring changes in the molecular structures upon hydroprocessing.

#### References

- (1) L. Petrakis, R. G. Ruberto, D. C. Young, and B. C. Gates, Ind. Eng. Chem. Process Des. Dev., 22, 292 (1983).
- (2) D. M. Jewell, E. W. Albaugh, B. E. Davis, and R. G. Ruberto, Ind. Eng. Chem. Fundam., 13, 278 (1974).
- (3) "<sup>13</sup>C NMR Multi-Pulse Sequences for the Analysis of Coal and Petroleum Products," R. Gerhards, in "Magnetic Resonance. Introduction, Advanced Topics and Applications to Fossil Energy," L. Petrakis and J. P. Fraissard, eds., D. Reilel Publishing Co., Dordrecht, The Netherlands, 1984, pp. 377-407.
- (4) I. P. Fisher and P. Fischer, Talanta, 21 (8), 867 (1974).
- (5) "Detectors," M. J. O'Brien, in "Modern Practice of Gas Chromatography," R. L. Grob, ed., John Wiley and Sons, New York, 1977, pp. 266-269.
- (6) "Techniques of Combined Gas Chromatography/Mass Spectrometry: Applications in Organic Analysis," W. H. McFadden, John Wiley and Sons, New York, 1973, p. 252.
- (7) D. R. Clutter, L. Petrakis, R. L. Stenger, and R. K. Jensen, Anal. Chem., 44, 1395 (1972).
- (8) L. Petrakis, D. T. Allen, G. R. Gavalas, and B. C. Gates, Anal. Chem., 54, 1557 (1983).
- (9) S. A. Qian, C. F. Li, and P. Z. Zhang, Fuel, 63, 268 (1984).

TABLE I  
Yield and Elemental Composition of Maya ATB Fractions

<u>Yield %</u>	<u>C %</u>	<u>H %</u>	<u>O %</u>	<u>N %</u>	<u>S %</u>	<u>Total</u>	
Maya ATB	-	84.26	10.40	0.47	0.51	4.70	100.34
Stral Oil	69.68	84.30	11.31	0.82	1.53	3.79	101.75
Asphaltene	24.14	82.65	7.83	1.41	1.12	6.97	99.98
Very Weak Base	0.86	81.78	9.42	2.48	0.15	5.00	98.83
Weak Base	0.07	49.49	6.32	18.95	0.30	6.04	81.10
Strong Base	0.01	53.98	6.86	12.87	3.34	7.55	84.60
Very Weak Acid	0.17	80.32	8.02	4.93	1.60	4.02	98.89
Weak Acid	0.04	61.81	6.65	14.13	0.85	1.72	85.16
Strong Acid	1.23	58.39	6.97	16.79	3.74	0.20	86.09
Neutral Resin	<u>2.39</u>	76.28	8.43	3.14	0.81	5.08	93.74
Total Recovery %	98.58						



TABLE II

High Resolution Mass Spectrometry Data on Maya ATB Neutral Oil Aromatics

<u>Z # Hydrocarbon Type</u>	<u>AV C #</u>	<u>Wt%</u>	<u>Total Wt</u>
Monoaromatics			28.01
-6 Alkylbenzenes	14.03	12.75	
-8 Indans	15.37	7.08	
-10 Indenes	15.16	8.18	
Diaromatics			19.88
-12 Naphthalenes	15.96	7.79	
-14 Biphenyls	18.08	5.29	
-16 Fluorenes	18.80	6.81	
Triaromatics			10.61
-18 Phenanthrenes	19.86	4.48	
-20 Phenanthrocyloparaffins	20.78	6.13	
Tetraaromatics			7.48
-22 Pyrenes	21.50	3.54	
-24 Chrysenes	22.92	3.94	
Pentaaromatics			10.04
-26 Chrysocycloparaffins	24.48	3.77	
-28 Benzpyrenes	25.20	2.75	
-30 Dibenzanthracenes	26.48	3.52	
Polyaromatics			8.03
-32	25.73	3.53	
-34	27.07	2.29	
-36	28.40	2.21	
Thiophenes			15.35
-10S Benzothiophenes	20.38	2.52	
-12S	20.41	2.59	
-14S	20.22	0.58	
-16S Dibenzothiophenes	18.14	3.32	
-18S	20.47	1.28	
-20S	18.28	1.03	
-22S Benzonaphthothiophenes	21.05	1.36	
-24S	22.65	1.15	
-26S	22.00	0.90	
-28S	23.97	0.62	
Phenols/Furans			0.60
-60 Phenols	6.00	0.04	
-160 Dibenzofurans	15.28	0.18	
-180	16.36	0.13	
-220 Benzonaphthofurans	18.56	0.25	

AV C NO 19.33

AV Z NO -16.88

C/H = 1/1.127

TABLE III  
Carbon Distribution in Fractions by  $^{13}\text{C}$  NMR

	<u>% Aromatic</u>	<u>% Naphthenic</u>	<u>% Saturate</u>	
Neutral Oils		25% (calc)		
Aromatics	60.0*	34%	28%	38%
Saturates	25.7*	0%	34%	66
Polars	14.3*	32%	ND	ND
Very Weak Acid		62%	12	26
Weak Acid		54%	17%	29%
Strong Acid				
Very Weak Base		45%	22	33
Weak Base		44%	23%	33%
Strong Base		52%	ND	ND

\*Percentage of neutral oil.

TABLE IV  
Average Molecule Data on Maya ATB Neutral Oil Aromatics from  $^1\text{H}$  NMR

Aromaticity:	0.27	% Monoaromatics:	43.8
Aromatic Rings/Molecule:	1.7	% Diaromatics:	46.9
Aromatic Ring Carbons/Molecule:	8.6	% Triaromatics:	9.3
Average Molecular Formula:	C31.7 H43.4	Average Molecular Weight:	423.9
% Alkyl Carbon:	72.8	Nonbridge Aromatic Carbons/Molecule:	7.3
Alkyl Substituents/Molecule:	3.6	% Subst. of Nonbridge Arom. Carbons:	57.8
Carbons/Alkyl Substituent:	6.4	Naphthene Rings/Molecule:	1.4
% Nonbridge Aromatic Ring Carbons:	23.1	% Naphthenic Carbon	15.6

NOTE: Average mol wt is based only on C and H and does not account for O, S, N, etc.

FIGURE 1  
FID and FPD Chromatograms  
of Maya ATB Neutral Oil

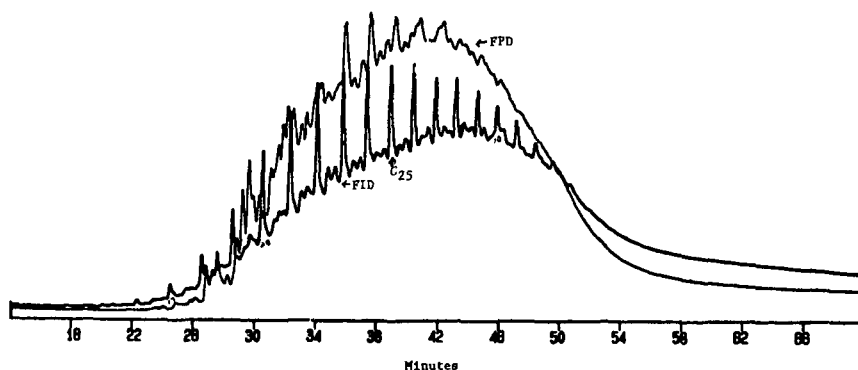
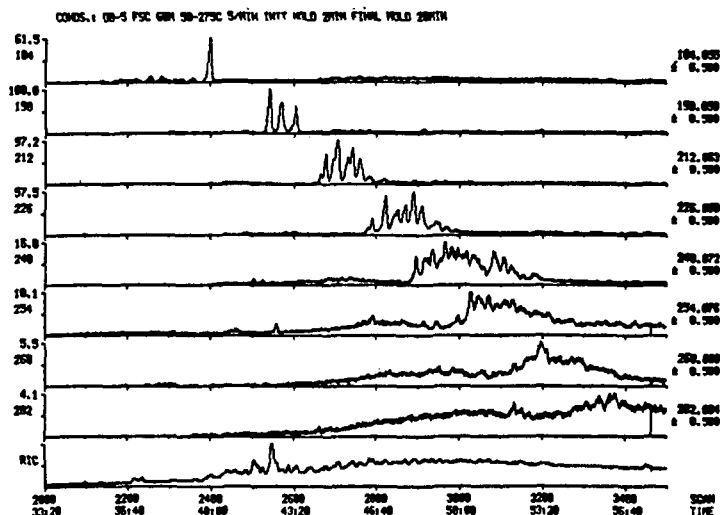


FIGURE 2  
Specific Ion Chromatograms for Dibenzothiophene and  
Substituted Dibenzothiophenes in Maya ATB Neutral Oil, Aromatic Fraction



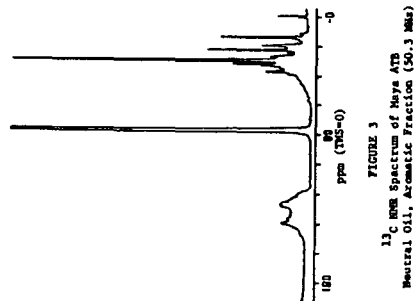


FIGURE 3  
 $^{13}\text{C}$  NMR Spectrum of Maya ATB  
Neutral Oil, Aromatic Fraction (50.3 Mhz)

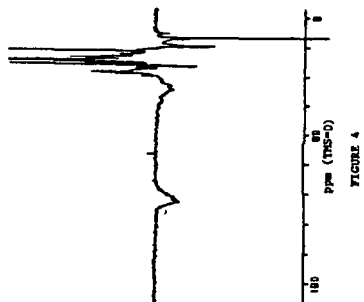


FIGURE 4  
 $^{13}\text{C}$  INEPT Spectrum of Maya ATB  
Neutral Oil, Aromatic Fraction (50.3 Mhz)

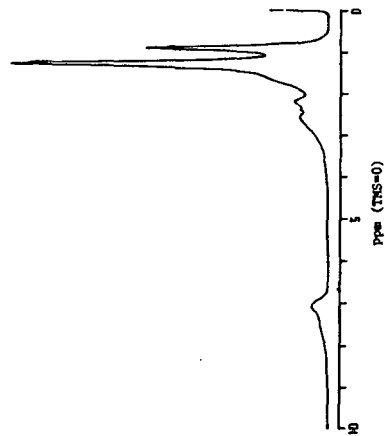


FIGURE 5  
200 MHz  $^1\text{H}$  NMR Spectrum of Maya ATB  
Neutral Oil, Aromatic Fraction

## MEASUREMENT OF ORGANIC SULFUR IN FOSSIL FUELS

K.C. Hsieh, B.T. Tseng, M. Buckentin and C.A. Wert  
Materials Research Laboratory and Department of Metallurgy and Mining  
Engineering, University of Illinois, Urbana, IL 61801  
and

Gary Dyrkacz  
Chemistry Division, Argonne National Laboratory  
Argonne, IL 60439

### ABSTRACT

A method of direct determination of the organic sulfur content of solid fossil fuels has been developed using the transmission electron microscope. The technique uses the detection of the  $K\alpha$  line of sulfur to measure the presence of sulfur and the volume from which this radiation comes is measured using the bremsstrahlung radiation counted simultaneously with the sulfur line. Applications have been made to the organic sulfur content of whole and treated coals, to amber and to kerogen in oil shale. The greatest value of the method is its ability to measure the variation of organic sulfur content over extremely fine distances.

### INTRODUCTION

Sulfur is found in coal in two principal forms: mineral sulfur (principally pyrites) and organic sulfur distributed through the carbonaceous matter. The conventional method of determination of the organic sulfur content is a two step process (1). First, total sulfur is measured. Then the pyritic and sulfatic sulfur is determined after selective dissolution of the minerals with acids. The organic sulfur is calculated as the difference between the total sulfur and the mineral sulfur. This commonly used ASTM procedure (method D 2492) is apparently sound when applied to raw coals, but there may be problems with analysis of chemically processed coals (2,3). Furthermore, this method provides only an average sulfur concentration and is unable to distinguish among possible variations either spatially or among the maceral types.

A number of investigators have examined the possibility of direct measurement of organic sulfur in coal which does not depend upon this difference technique. These methods have commonly utilized the x-ray emission lines of sulfur to detect its presence and have used a variety of standardization techniques to provide numerical data and to differentiate among the variety of sulfur forms which may be present. Several earlier papers have described these techniques (4-11). Among them, the extensive work of Raymond and Gooley and of Straszheim and Greer should be especially noted. The resolution of these techniques using either the electron microprobe or the SEM is about  $5\mu$ , so the volume of each measurement is immensely less than that of the standard ASTM technique. Determination of average values using the microprobe or SEM instruments does require the averaging over a number of individual observations to take account of possibility of variability in organic sulfur content from place to place in the coal.

We have extended this electron-optical technique to even finer spatial resolution using the transmission electron microscope. The specimens are either finely divided powders or foils of coal which are thin enough to be practically transparent to the electron beam. The technique has been adapted from methods developed by Hall and his collaborators for measurement of organically dispersed elements in biological tissue (12-15). We have developed applications of the technique, standardized the method for our microscope and have presented first results in a publication in Fuel (16). We refer only briefly to the chief features of the technique here.

## THE TEM METHOD

The geometry of the measurement is sketched in Fig. 1. An electron beam is incident upon a coal foil which is less than  $1\ \mu$  thick. Ionizing collisions with atoms in the irradiated volume cause the emission of characteristic x-ray lines which can be counted by an appropriate detector. At the same time, the background radiation is counted from the same volume. The  $K\alpha$  line of sulfur has an energy of about 2300 eV and we measure the bremsstrahlung radiation over the range 10-18 keV; a typical spectrum is sketched in Fig. 2. The organic sulfur concentration of the volume being irradiated by the electrons is simply related to the ratio of these two count rates:

$$S(\text{wt}\%) = A C_S / C_b \quad 1)$$

We have found this equation to be well satisfied for thin specimens and have determined the proportionality constant A using known sulfur standards. For our instrument and the geometry of our detector, A has the value 1.6. This number varies slightly among the coals because the bremsstrahlung radiation is somewhat dependent on the C/O ratio in the hydrocarbon matrix. This variation is slight however, being only a few percent for coals from the sub-bituminous to anthracite range.

We emphasize that success of the method is achieved only if the coal foil is thin enough that the electron beam is essentially undiminished in passing through the foil so that the intensity of ionization of the elements in the coal is uniform throughout the irradiated volume. Furthermore no absorption of either the sulfur line or the bremsstrahlung radiation should occur in the specimen. For coal foils less than  $1\ \mu$  in thickness, these conditions are amply met.

## APPLICATIONS TO COAL

### Measurement of the Average Organic Sulfur Content

We have tested the technique using a high organic sulfur bituminous coal and a low organic sulfur anthracite. Ten thin foils from each coal were prepared and five measurements were made on each foil. The total of fifty measurements for each coal is averaged to give the organic sulfur content. The organic sulfur content of a third coal, a low sulfur bituminous, was determined by examining the sulfur content of powdered macerals. The graph in Fig. 3 shows that results from this method compare very well with those from the standard ASTM method for these three coals. We could make additional measurements of this type, but we have elected to utilize the most valuable feature of this technique, namely the spatial variation.

### Spatial Variation of the Organic Sulfur Content

A measurement was made over a coal maceral (presumably vitrinite) in an Illinois #5 coal. That variation is sketched in Fig. 4. The average value is about 2.6 wt% organic sulfur with a variation of about 25% about this mean. At one point in the maceral a slight excursion away from the edge showed a much higher organic sulfur content locally, some 3.5%.

We have made additional measurements of variation of sulfur concentration around mineral particles in coal, and find some variation. We were not completely sure that that variation was not a function of the maceral type in which the mineral was located, rather than being due to the mere presence of a mineral. Consequently, we need to carry out additional work to show the factors on which this variation depends. In particular, we are interested to see whether the organic sulfur varies as one approaches closely to a sulfide particle or whether it remains constant right up to the edge of the particle. Further, we would like to see whether the organic sulfur concentration in the vicinity of a sulfide is

altered as the coal is heated into the temperature range where sulfides are known to decompose (some 700 K). Measurements of both types are in progress.

#### Variation of Organic Sulfur Between Submaceral Types

We wished to see whether the variation we observed in organic sulfur content in repeated measurements on some coals was due to random spatial variation or whether it might be due to variation in sulfur content of maceral types. It is known that the organic sulfur content of coals varies in the order  $S(\text{exinite}) > S(\text{vitrinite}) > S(\text{inertinite})$ . Our technique seems to have the capability of determining this on a fine scale. We have made measurements on a coal which had been separated into maceral fractions. We used an Indiana bituminous coal, PSOC 106, which had been separated into maceral fractions by the gradient-centrifuge method employed at the Argonne National Laboratory (17,18). Our first measurements on the gross maceral types showed the expected general trend. For the inertinite the average was 0.428 wt%, for the vitrinite, 0.61 wt% and for the exinite 1.2 wt%. Multiplying these numbers by the known fractions of the maceral types gave an average value of 0.64 wt% S, observations made by Dyrkacz independently gave an average value of 0.57 wt%. His measurements are discussed further in more detail (19).

The most significant feature of these measurements was not the average values, but the range of organic sulfur content for the three maceral types. In particular, the exinites gave wide variation, from 0.03 to 2.31 wt% for the fifty-five observations made on that maceral type.

We then took maceral fractions separated on an even finer scale so that the organic sulfur content of submaceral types could be determined independently of each other. We took 12 density fractions of this coal, 5 exinites, 3 vitrinites and 4 inertinites. Each was measured independently. Data for these three vitrinites are displayed in Fig. 5. These graphs show the organic sulfur content measured over many micron size particles of particular density fractions. The averages are listed on the graphs and the spread about the averages is evident.

A plot of the average organic sulfur content of all 12 maceral fractions is shown in Fig. 6. One sees a gradual curve, rising from the dense inertinites toward the lighter vitrinites into the exinite. Then the curve goes through a high value at a density around 1.18, and falls off toward the lighter fractions.

The peak value of organic sulfur content about the density 1.18 is striking. Since it is believed that the maceral sporinite has about this density, we elected to measure the organic sulfur content of an individual sporinite maceral embedded in whole coal, not separated from its surrounding by fine grinding. A specimen of Illinois #5 coal was examined by reflectance microscopy until a sporinite maceral was observed embedded in surrounding vitrinite macerals. A hole appropriate for electron microscope observation was milled at this point. The organic sulfur content of this area was measured from one vitrinite maceral through the sporinite into the other vitrinite maceral. As was expected, the organic sulfur content of the sporinite maceral was much higher than that of the surrounding vitrinite macerals, see Fig. 7. Furthermore, the organic sulfur content rises sharply at the boundary between the vitrinite and sporinite macerals.

This poses an interesting question. Is the high organic sulfur of sporinite a function of high organic sulfur in the initial spore and would it be true for pollens as well? We are examining these questions.

## AMBER

Amber is a fossilized resin from either deciduous trees or needle trees. It is akin to the resinite maceral type in coal. Therefore we desired to measure the organic sulfur content of amber to see how it would fit in this scheme. A measurement on an amber of Dominican origin showed that the organic sulfur content was low, much less than 1%, and that it varied from about 0.14 to 0.3 with an average value over six measurements of 0.2 wt% sulfur. Similar measurements for a Baltic amber gave an average value of about 0.33% organic sulfur with only a small variation about this mean. These measurements are consistent with the data in Fig. 6 which indicate that resinite, a low density maceral, should be on the lower end of a curve such as that in Fig. 6. We are now examining resinite maceral fractions taken from whole coals to determine the validity of this observation.

Amber also has other lines in the x-ray emission spectrum showing that other elements may be present in organically distributed form, see Fig. 8. In addition to the  $K\alpha$  line of sulfur, lines for Cl, K and Ca are present. We believe that these elements too are organically distributed, although one cannot rule out the possibility of there being tiny precipitates below the limits of resolution of the electron microscope (some 20 Å or so). Since lines for Al, Si and heavy metals are absent, precipitates of a clay-like nature or of minerals containing iron, copper and other heavy metals are not to be seen. The measurement does show that organic elements other than sulfur might be detected and measured using the electron microscope technique, with appropriate standardization of the constant A in Equation 1.

## OIL SHALE

Oil shale contains carbonaceous matter distributed in pores in the massive mineral crystals and also as an interparticle film between the mineral crystals. An electron microscope observation of a thin foil of a Green River shale from the mahogany zone is shown in Fig. 9. The kerogen is the light material between the dark mineral blocks. One also sees that smaller minerals are also embedded within the kerogen film; in this particular specimen they are a phosphate. We have measured the organic sulfur content along a line in a kerogen film over a distance of about 100  $\mu\text{m}$ . Six observations were made; they range in value from 0.2 wt% to 1.3 wt% with an average value over 6 randomly spaced points of about 0.4 wt% sulfur.

We emphasize that this technique is a valuable method of measuring the organic sulfur content of the carbonaceous matter in oil shale in situ. Furthermore, the variation over different regions in the kerogen could readily be determined.

## SUMMARY

The technique we have described measures the organic sulfur content of fuel materials directly. It must be standardized to a particular microscope and detecting system. Small variations in the proportionality constant A exist among the various carbonaceous matrices, but these are at most 5-10%. The technique is probably not valuable for measuring the average organic sulfur content of coals where the standard ASTM method might be employed, since the electron microscope is expensive to use and demands careful specimen preparation. However, it has high potential for measuring the organic sulfur content of kerogen, tar sands and other carbonaceous material in situ. Its greatest value, though, seems to lie in its ability to measure small spatial variations in organic sulfur content and in determining the variation of organic sulfur concentration among maceral types in either whole or treated coals. Finally it has promise in determination of changes in organic sulfur content which accompany heat treatments or chemical treatments.



#### ACKNOWLEDGEMENTS

Support for staff of the University of Illinois were supported by the Division of Materials Research, DoE, under contract DE-AC02-76ER01198. Part of the support for K.C. Hsieh and M. Buckentin also came from the Center for Research on Sulfur and Coal through the State of Illinois affiliated with the University of Illinois.

#### REFERENCES

1. Annual Book of ASTM Standards, ASTM D2492, Standard Test Method for Forms of Sulfur in Coal, 347 (1983)
2. Suhr, N. and Given, P.H., Fuel, 60, 541 (1981)
3. Gladfelter, W.L., and Dickerhoof, D.W., Fuel, 55, 355 (1976)
4. Raymond, R. Jr., and Gooley, R., Scanning Electron Microscopy/1978/I, 93 (1978)
5. Raymond, R. Jr., Gregory, T.G., and Gooley, R., Proc. Annual Conf. Microbeam Analytical Soc., 12, 177A (1977)
6. Raymond, R. Jr., Proc. Annual Conf. Microbeam Analytical Soc., 14, 93 (1979)
7. Raymond, Robert, Jr., ACS Symposium Series, No. 205, COAL AND COAL PRODUCTS: ANALYTICAL CHARACTERIZATION TECHNIQUES. Ed. Fuller, E.L. Amer. Chem. Soc. Washington, DC (1982)
8. Sutherland, J.K., Fuel, 54, 132 (1975)
9. Solomon, P.R., and Manzione, A.V., Fuel, 56, 393 (1977)
10. Straszheim, W.E., and Greer, R.T., Scanning Electron Microscopy/1982/III, 1013 (1982)
11. Clark, C.P., Freeman, G.B. and Hower, J.C., Scanning Electron Microscopy/1984/II, 537 (1984)
12. Hall, T.A., Physical Techniques in Biological Research: Optical Techniques, 2nd Ed., Vol. 1A, Ed. G. Oster, 157 (1971)
13. Hall, T.A., Anderson, H.C., and Appleton, T., Jour. of Microscopy, 99, Pt. 2, 177 (1973)
14. Hall, T.A., Jour. of Microscopy, 117, Pt. 1, 145 (1979)
15. Hall, T.A., Microbeam Analysis in Biology, Ed: Lechene, C.P. and Warner, R.R., Academic Press, NY, 185 (1979)
16. Hsieh, K.C., and Wert, C.A., Fuel, in press
17. Dyrkacz, G.R., and Horwitz, E.D., Fuel, 61, 3 (1982)
18. Dyrkacz, G.R., Bloomquist, C.A.A., Ruscio, L., and Horwitz, E.P., 1983 International Conference on Coal Science, International Energy Agency, Pittsburgh, August, 1983, p. 393-396
19. Dyrkacz, G.R., Bloomquist, C.A.A., and Ruscio, L., Fuel, in press

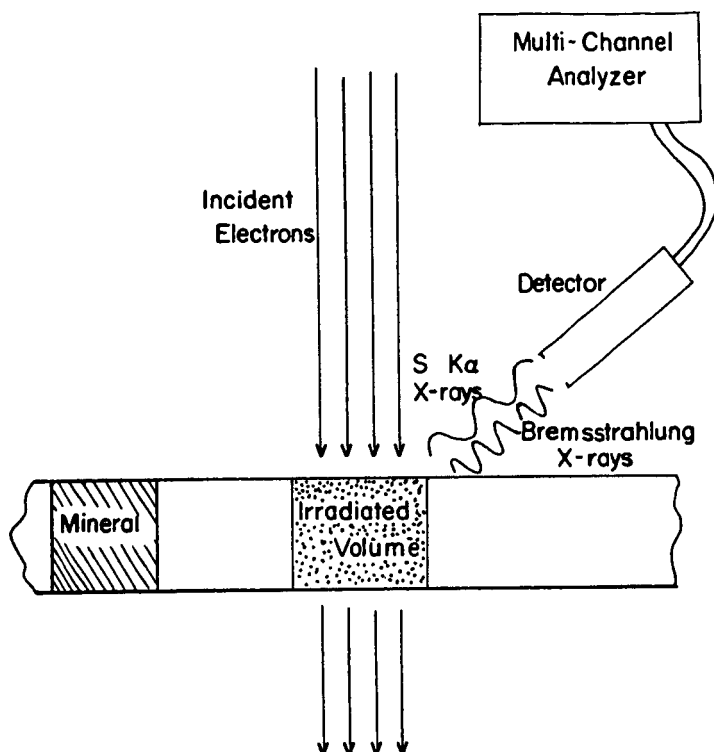


Figure 1. Sketch of x-ray detection system.

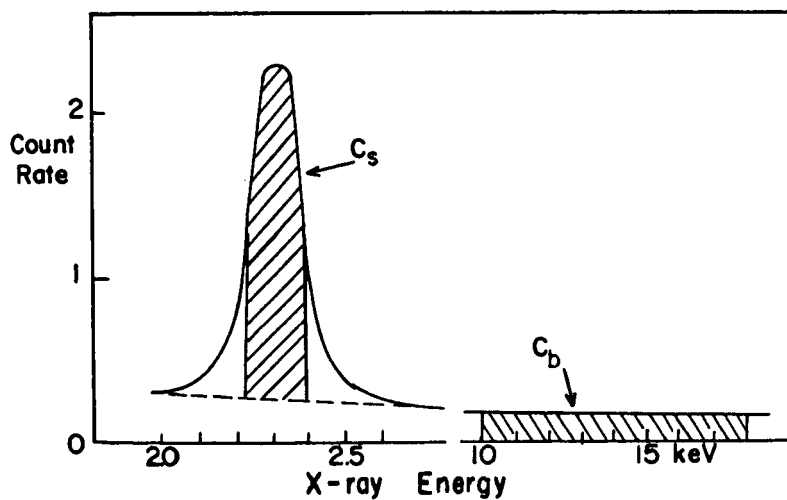


Figure 2. Schematic of counting signals.

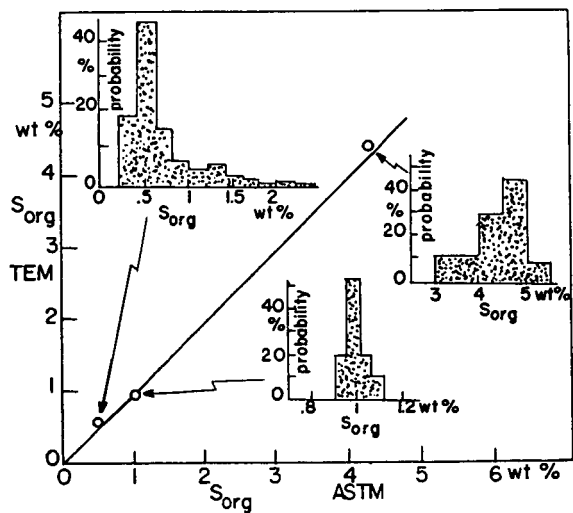


Figure 3. Correlation of measuring techniques.

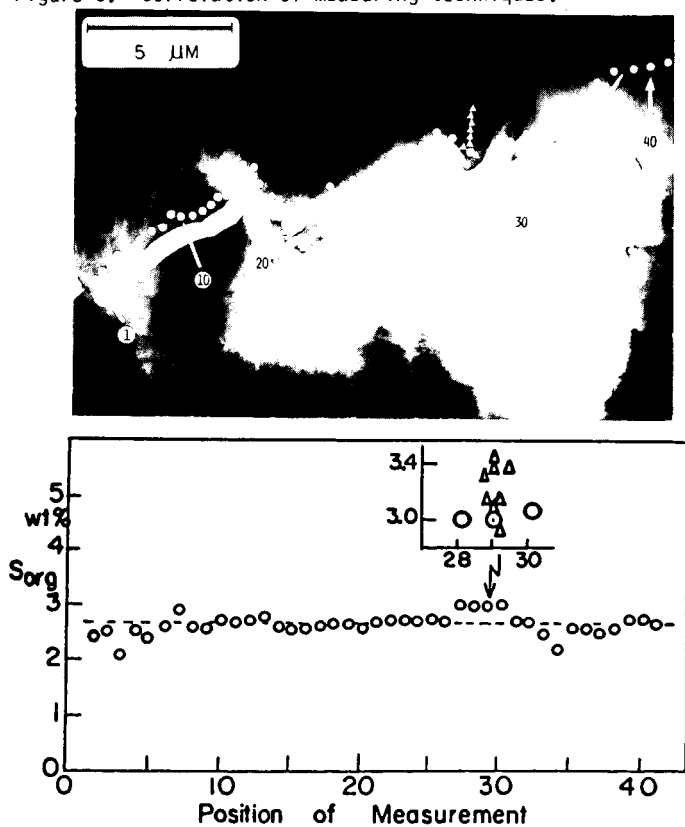


Figure 4. Spatial variation of organic sulfur.

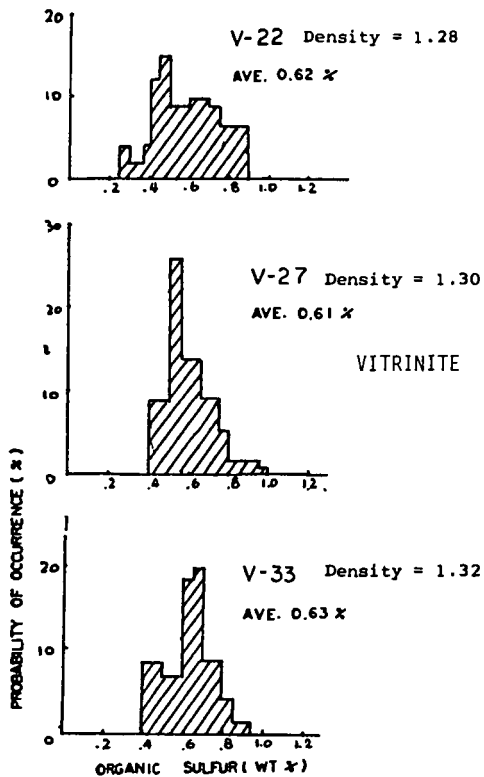


Figure 5. Distribution of  $S_{org}$  concentration.

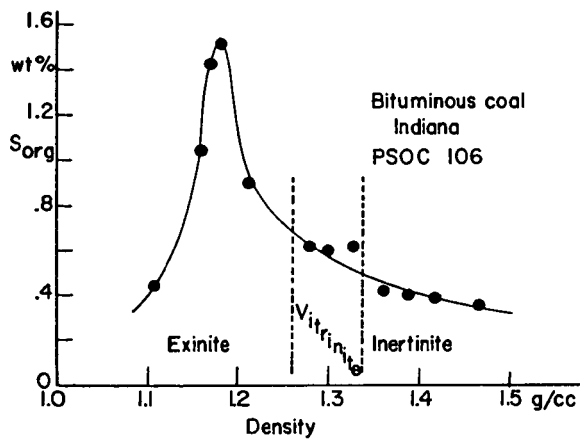


Figure 6. Variation of  $S_{org}$  by maceral type.

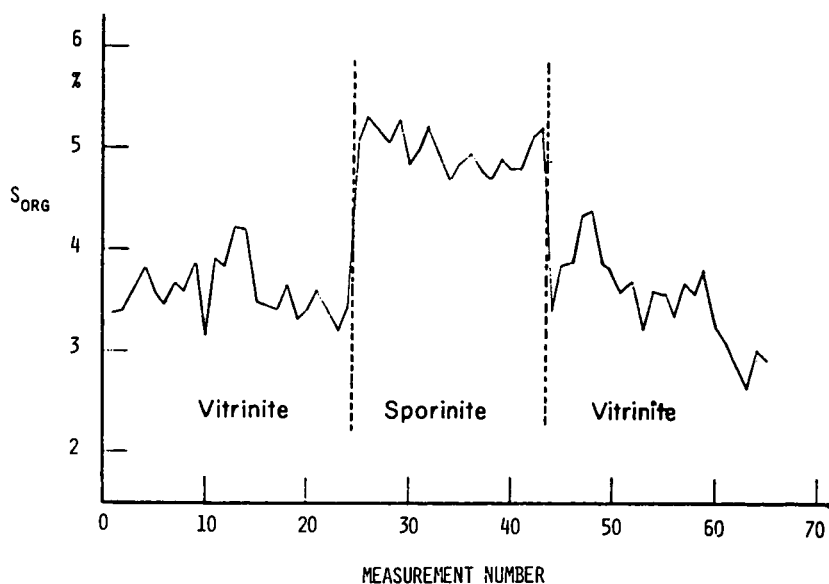
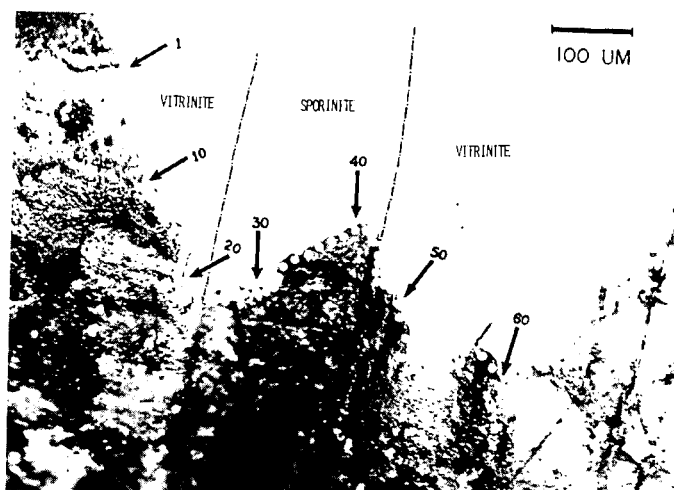


Figure 7. Variation of  $S_{org}$  across a sporinite maceral.

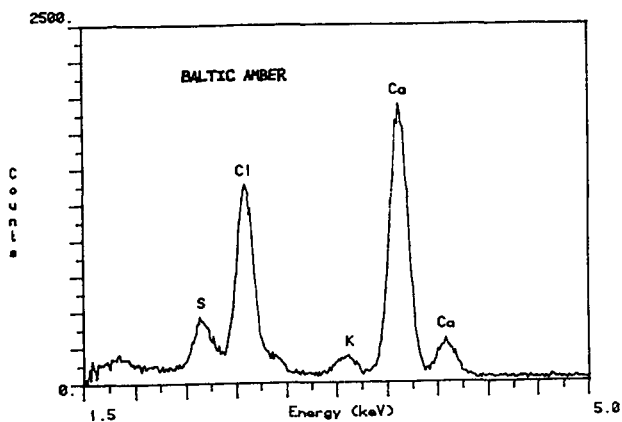


Figure 8. X-ray emission spectrum for amber.



Figure 9. Electron micrograph of oil shale.

# APPLICATION OF SCANNING ELECTRON MICROSCOPY AND AUTOMATED IMAGE ANALYSIS FOR CHARACTERIZATION OF MINERAL MATTER IN COAL

Warren E. Straszheim and Richard Markuszewski

Ames Laboratory\* and Department of Engineering Science and Mechanics  
Iowa State University, Ames, IA 50011

## INTRODUCTION

The value of the scanning electron microscopy in providing in-situ information on the microstructure of materials such as coal is well known. It is particularly suited for examining the finely distributed mineral particles found in finely-ground coal. In polished cross section, a wealth of size, shape, roughness, and association data can be provided. Addition of an energy-dispersive x-ray analyzer permits chemical analysis to be performed on these minute features, thus allowing a tentative identification of the mineral phase.

The use of automated image analysis (AIA) in conjunction with scanning electron microscopy (SEM) and energy-dispersive x-ray analysis (EDX) is gaining ever wider acceptance as a powerful tool for the in-situ characterization of mineral matter in coal (1). The SEM-AIA technique is able to combine data from SEM and EDX measurements to provide detailed information on sample character that is not available from other analytical methods. The unique features of AIA include information generated for size, shape, composition, and association of mineral phases with the coal matrix.

The SEM-AIA technique is applicable to a wide variety of characterization problems. Because the in-situ nature of this capability can provide quantitative information on the distribution of the mineral species present in coal, it lends itself particularly well to the characterization of minerals in raw and processed coals. Distribution of minerals by both phase and particle size is of great importance to almost any work on coal, but it is especially useful to coal plant operators in determining the steps necessary for effective and efficient removal of undesirable mineral phases during cleaning (2). It is not adequate to know only the relative amounts of the mineral phases present; such information is available from x-ray diffraction or infra-red spectroscopy. But the size of the minerals and their relation to the coal matrix is just as important. Such information was provided in a recent publication of our studies (3). In that work, the mineral matter distribution in raw coals and coals supercleaned by float-sink techniques was described.

In this work, the SEM-AIA technique as an analytical method for coal will be described. The discussion will include particle detection and measurement, mineral phase identification by x-ray analysis using a file of chemical definitions, and the number of particles needed to develop reliable results and adequate reproducibility between samples. In addition, attention will be given to problems in the application of AIA techniques to coal, including difficulties arising from a wide spread in the minimum and maximum particle sizes, problems in the apparent enrichment of pyrite content due to instrumental factors, and the special case of characterizing chemically treated coals.

\* Ames Laboratory is operated for the U. S. Department of Energy by Iowa State University under Contract No. W-7405-Eng-82.

The SEM-AIA techniques have been applied at the Ames Laboratory to many samples of bituminous and sub-bituminous coals to characterize their mineral content for studies of cleanability. Results from some of those studies will be used to illustrate the application and limitations of this technique.

#### BACKGROUND

Combined SEM-EDX techniques have been able to provide much information with manual operation, but results were qualitative and subject to operator judgment. The development of automated control for the SEM has permitted the same information to be extracted objectively, quantitatively and less tediously. The main limitation of the manual techniques is the human factor, since the analysis of particles for size and elemental composition is tedious. Human operators are severely limited in the rate and amount of data that they can reasonably produce. There is also a possibility of operator bias in not treating all particles alike. The intelligence of a human operator is a fantastic advantage, but the limitations on the operator are also significant.

The task of the automated image analyzer is to assume the repetitive duties of the SEM operator in such a way that statistically significant number of particles can be analyzed in a reasonable amount of time and to tabulate the data in a meaningful format. The following paragraphs describe the operations involved.

The first requirement of particle characterization is feature identification and sizing. A human operator is able to work with gross signal contrast and rather subtle edge effects to determine feature outline. As a rule, the microcomputers and electronics used in image analysis in the lab are presently restricted to determining particle boundaries, or extents, from the rather gross measure of contrast in the signal level. Therefore, sufficient contrast is required in the video signal between two phases of interest to permit differentiation of the phases. Backscattered electron imaging is very sensitive to the average atomic number of a phase and, therefore, provides high contrast between minerals of relatively high atomic number and lower atomic number coal and mounting material. A specialized analog-to-digital converter, called a "threshold selector," is used to inform the computer which pixels are above threshold and belong to a phase of interest, and which pixels are below threshold and therefore indicate background phase. The computer is thus able to discern which picture elements belong to coal, mineral, or background.

The mode of extracting information on the particle extents is complicated. In many image analysis systems built around optical microscopes and TV cameras, the whole image is digitized for processing. For SEM operations this is often not practical. Often the signal from an SEM exhibits a relatively low signal-to-noise ratio requiring that several frames be averaged to provide an adequate signal. Also, some older SEM instruments do not respond well to the scanning speed demands of TV imaging rates. In addition, it is only recently that backscattered electron detectors have become available that can operate at TV-rates. Therefore, it has been common for SEM-based image analyzers to employ some form of digital beam control to direct the beam on the sample in such a fashion as to extract the most information in the least time. A number of software algorithms are available with our AIA system to discern particle extents.

Once the particle extents have been determined, the chemical identity of a particle is determined. The image analyzer directs the SEM beam to the center



of the particle of interest and directs the EDX analyzer to collect an x-ray spectrum. Whereas a human operator can quickly scan the entire x-ray spectrum to locate and identify the significant x-ray peaks, the image analyzer must monitor regions of interest defined about x-ray lines of interest. For many mineral analyses, only 11 common elements are necessary. They are, in increasing atomic number: Na, Mg, Al, Si, P, S, Cl, K, Ca, Ti, and Fe. Additional elements can be also monitored if they are suspected to occur in trace quantities. Based on the relative intensities of the x-ray signals, particles are classified into one of several mineral categories according to definitions such as those given in Table 1. For many AIA applications, including coal mineral analyses, it is reasonable to define the chemical categories rather loosely and still to discern the various mineral components. In fact, for many minerals, it is necessary only to define the elements that must be present to define a mineral. Quartz and calcite are examples for which only a single element is needed (Si and Ca, respectively). However, for the clay minerals, more sophisticated definitions are necessary to differentiate the phases.

Table 1. Ranges of Elemental Compositions, Ratios, and Other Features for mineral phase definitions.<sup>a</sup>

Mineral Phase	Chemical Definition in % Range <sup>b</sup>	Density
Pyrite	S 10-80, Fe 10-70	5.00
Kaolinite	Al 15-80, Si 15-85 Al/Si ratio 0.4-2.5	2.65
Illite	Al 15-80, Si 20-85, Fe 0-40, K 2.5-35, Na 0-20	2.75
Montmorillonite	Al 10-75, Si 19-80, Na 0-30, Ca 0-30	2.30
Quartz	Si 60-100	2.65
Calcite	Ca 70-100	2.80
Minors (included are the following categories)		
Gypsum	S 10-80, Ca 10-70	2.30
Dolomite	Mg 5-60, Ca 60-100	2.90
Iron-rich (e.g. siderite)	Fe 90-100	3.90
Chlorite	Al 10-75, Si 10-80, Mg 0-30, Fe 0-30 (Mg or Fe required)	3.00
Rutile	Ti 70-100	4.50
Al-Rich	Al 75-100	4.00
Apatite	P 10-40, Ca 30-100	3.20
Silicates	Si 40-100	2.70
Miscellaneous	All other elemental compositions not specifically defined	2.00
Not included	Signals with <1000 total x-ray count	

<sup>a</sup> Modified after Reference 3.

<sup>b</sup> Additional specifications are often given for other elements that are allowed to be present. Although such specifications allow the presence of minor elements not specifically listed in the chemical definition, they place an upper limit on the allowable amount.

# EXPERIMENTAL

The AIA-SEM system at Iowa State University consists of a JEOL (Japan Electron Optics Laboratory) model JSM-U3 scanning electron microscope, a LeMont Scientific B-10 image analyzer, and a Tracor Northern TN-2000 energy-dispersive x-ray spectrometer. The software-based AIA system contains associated electronics for SEM beam

control, image amplification, and thresholding. For AIA, the software base allows selection of the appropriate analysis algorithm for the particular sample and image conditions encountered.

Actual analyses were performed on pellets of coal mounted in an epoxy or polyethylene matrix according to standard petrographic procedures. The pellets were polished to a cross section and coated with carbon to render the surface electrically conductive for SEM examination. Samples were analyzed in the SEM under 50-500x magnification, using 25 kV beam voltage, 1-2 nA sample currents, and backscattered electron imaging. A point density of 1024 pixels across the screen was used to provide  $\pm 10\%$  accuracy on measurements as small as 1% of the field of view. X-ray data were collected for four seconds per particle at a typical rate of 1000 counts per second. The intensities of 30 elements were set to be monitored in regions of interest. Approximately 4000 particles were analyzed per sample, at a rate of 200 particles per hour.

The AIA procedures classify mineral particles into both size and chemical classes. Area-equivalent diameter was used as the size parameter for data presentation. This measurement is the diameter of a circle with the same area as that measured for the mineral particle. Area-equivalent diameter was used instead of a simple length or width measurement because the outline of mineral particles in coal is often complex enough to render such measurements meaningless. The equivalent diameter measurement allows particles to be classified by the area of the particle and yet reported in terms of a linear dimension. Using available literature values for the specific gravity of the individual minerals, the data were then expressed as the weight fraction of the mineral matter within a given mineral/size category. The weight fraction data could then be normalized according to the mineral matter content calculated from ash values by using a modified Parr formula (4) to present mineralogical estimates on a dry coal basis. Such a presentation provides a common base for comparing the coals before and after processing.

#### DISCUSSION OF RESULTS AND PROBLEMS

A major problem encountered in the analysis of coal samples arose from the wide size range of particles present. The weight distribution is heavily influenced by the particles in the largest size categories. However, most of the particles are found in the smallest categories. This problem is especially troublesome for relatively coarse samples of where the particle diameter can range from 1 to 1000  $\mu\text{m}$ . As an example, Table 2 presents actual data for such a case, using an Illinois No. 6 coal characterized more fully elsewhere (3).

Since analysis time per particle is dominated by the time of x-ray acquisition which is independent of particle size, it becomes necessary to allocate analysis time among the size categories in order to include a significant number of particles of all sizes. Therefore, analyses were conducted at several magnifications for restricted ranges of particle sizes. A relatively small area was analyzed at high magnification to collect data on small particles, and a much larger area was then analyzed at lower magnification to collect data on large particles. Data were then combined by correcting the weight of particles analyzed in each size range for the area of sample analyzed for that size range. The table of weight fractions was then normalized to 100%. For samples with particularly wide size ranges, three or more size partitions were required to obtain a representative size distribution. As can be seen from Table 2, the actual number of particles counted parallels the weight distribution much closer than does the unadjusted count fraction.

Table 2. Weight and Count Distribution for an Illinois No. 6 Coal  
(Nominally 70-80% less than 200 mesh or 75  $\mu\text{m}$ )

	Area Equivalent Diameter (in $\mu\text{m}$ )					
	0-4	4-7	7-12	12-20	20-36	>36
Count fraction	16.3	51.1	23.3	7.1	1.7	0.6
Weight fraction	2.5	15.3	20.4	21.0	14.4	26.3
% of particles counted	13.6	42.6	25.3	7.8	7.9	2.8
Number of particles counted	654	2055	1221	374	382	136

The statistical distribution involved in AIA analysis is a multinomial distribution, for which the standard deviation of the counts measured for a category is equal to the square root of the count. Thus a count of 100 particles would yield to a relative standard deviation of 10%. Relative error in the weight distribution results can be calculated from the number of particles collected in each category. For a system of four predominant minerals with approximately equal particle abundances, and six size categories, approximately  $4 \times 6 \times 100 = 2400$  particles would be needed for a relative standard deviation of 10% in the data.

This assumption has been borne out in analyses of multiple pellets of the same coal. Five pellets each of three coals were analyzed by AIA. A total of 1500 particles was characterized for each pellet. Standard deviations were calculated from the five estimates of weight fraction in each size/chemical category and compared with the relative error expected from the particle count. Agreement was excellent for categories containing more than ~30 particles.

A problem of artificial enrichment of one phase relative to the others arises when one phase appears much brighter in the image being analyzed than do the remaining phases. In our work with coal minerals (3,5) and in the work of others (6) such a problem was experienced with the mineral pyrite. Typically the pyrite content found by SEM-AIA is substantially higher than what is estimated by the ASTM wet chemical technique (see Table 3). The problem arises in our AIA system since it employs what is known as "global thresholding". In it, a threshold level is established against which image signal levels are compared to determine whether a pixel is part of a particle or part of the background. The recommended procedure is that the threshold be set midway between background and full signal brightness to allocate equally any noise on the particle edges between particle and background. For coal minerals this is strictly not possible. The intensity of backscattered electron image used for analysis is highly dependent on the average atomic number of the material in view. Pyrite is so much heavier than the other mineral phases that the threshold, set at a level at which the clays can be consistently detected, crosses pyrite particles at the 20-30% level and increases the possibility that individual pyrite particles will be measured larger than they are. To compensate for this bias, the U.S. Steel workers (6) recommended an empirical factor of 0.75 for scaling down the pyrite values.

Another possible explanation is that the brighter signal for pyrite causes small particles of the mineral to have a better chance of rising above threshold as opposed to the signal being diminished to a level below the threshold by the fact that a large percentage of the electrons pass completely through the particle before backscattering, causing the signal brightness to be lower than the signal from a massive particle. However, this explanation does not account for much of the error

observed since only a relatively small amount of the pyrite is found in the smallest size ranges.

Table 3. Comparisons of ASTM and SEM-AIA Estimates of Pyrite and Pyritic Sulfur Sulfur Content for Raw and Supercleaned Coals (recalculated from data of Reference 3)

	Illinois No. 6		Pittsburgh No. 8	
	Raw	Cleaned	Raw	Cleaned
<u>Pyritic Sulfur</u>				
ASTM	2.37	0.22	1.35	0.03
AIA	4.22	0.63	2.50	0.52
<u>Pyrite/Mineral Matter<sup>a</sup> Ratio</u>				
ASTM	22.93	13.48	30.55	1.66
AIA	40.86	38.53	56.54	28.59
Fe by XRF (%)	2.01	0.38	1.64	0.44
Total S (ASTM)	5.10	2.54	3.17	1.82
Organic S (ASTM)	2.36	2.27	1.42	1.67
Mineral Matter <sup>a</sup>	19.32	3.05	8.26	3.37

<sup>a</sup> Mineral matter = 1.13 (ash) + 0.47 (pyritic sulfur), as in reference 4.

For chemically processed coals, problems arise with the chemistry definitions. New mineral phases may be formed during processing that bear little resemblance to the original minerals. It may become necessary to analyze the material with alternate techniques, such as x-ray diffraction, in order to determine what phases are present. Then the necessary chemical definition can be built into the file knowing the chemistry of the new phases. Alternatively, an automatic classification option can be employed to sort particles routinely based on the relative amounts of the elements present.

Some of our work with the direct determination of organic sulfur in raw and chemically treated coal by an SEM-EDX technique (7) and additional analysis of mineral matter in those samples by FTIR spectroscopy (8) indicate that the AIA values for pyrite may be correct for at least some samples. The analyses were performed on samples of Illinois No. 6 coal, raw and chemically cleaned by the Gravimelt Process at TRW Inc., in California (8). The samples were analyzed by ASTM techniques for moisture, ash, and sulfur forms; by SEM-AIA for mineral phases; by SEM-EDX for organic sulfur; and by FTIR for mineral phases. The results are presented in Tables 4 and 5.

For the raw coal, the pyritic sulfur values obtained by AIA agreed well with those obtained at TRW. However, they were somewhat higher than the ASTM values obtained at Ames. For the cleaned coal, the pyrite values obtained by AIA and the organic sulfur values obtained by SEM agreed very well with the Ames ASTM results.

The comparison of FTIR data with AIA results in Table 5 shows good agreement for all components except kaolinite. Since the coal had to be low-temperature ashed for the FTIR analyses, and the cleaned coal did not have much ash left, the FTIR results on the cleaned coal are not as informative as the AIA results. The FTIR techniques could not identify much of the mineral matter in the cleaned coal, adding most of it

to the miscellaneous category. Since AIA does not require mineral standards and is not particularly dependent on crystal structure, more particles could be categorized by the chemical definition file.

Table 4. Analysis of Illinois No. 6 Treated by the Gravimelt Process at TRW  
(Values reported as wt. % on a dry basis, except for moisture)

	RAW COAL			TREATED COAL		
	TRW Results	ASTM At Ames Lab	SEM/AIA Results	TRW Results	ASTM At Ames Lab	SEM/AIA Results
Moisture	15.81	1.84	----	----	6.33	-----
Ash	9.97	9.23	----	0.51	0.53	-----
Mineral Matter <sup>a</sup>	-----	10.92	----	----	0.61	-----
Total S	4.21	4.03	----	0.57	0.59	-----
Pyritic S	1.36	1.04	1.46	----	0.02	0.026
Sulfate S	0.05	0.09	----	----	0.02	-----
Organic S	2.80	2.90	2.13	----	0.35	0.32

<sup>a</sup> Mineral Matter = 1.13 (ash) + 0.47 (pyritic sulfur), as in reference 4.

Table 5. FTIR and AIA Results of Raw and Chemically Treated Illinois No. 6 Coal  
(values expressed as wt. % of total mineral matter present)

	RAW		TREATED	
	FTIR	AIA	FTIR	AIA
Kaolinite	12.0	7.4	4.0	8.4
Illite	31.5	29.8	----	10.2
Quartz	19.0	20.0	10.0	13.9
Calcite	1.5	1.3	----	3.7
Pyrite	----	23.3	----	8.4
Miscellaneous	36.0	18.1	86.0	46.0

In addition, the AIA technique provided information on particle size distribution as well as mineral phase identification (see Table 6). Such information, of course, cannot be provided by the FTIR technique.

#### CONCLUSIONS

The SEM-AIA technique has been shown to be a useful tool in characterizing the mineral matter of coal by chemical composition as well as particle size distribution. The fundamental aspects of this analytical technique have been described, including the method of defining mineral phases by chemical composition, requirements for the number and size of particles to be samples for reliable and reproducible results, comparison of this technique with other methods of characterizing coal mineral matter, and some problems associated with the application of this technique to measurements of pyrite and analysis of chemically treated coals.

TABLE 6. AIA Classification of Mineral Matter in Illinois No. 6 Coal by Chemistry and Area-Equivalent Diameter of Particles (in  $\mu\text{m}$ ), Expressed as Weight Percent of the Total Mineral Matter Only.

Mineral Phase	<u>Raw Coal</u> Particle size ( $\mu\text{m}$ )						Total <sup>a</sup>
	< 6.3	6.3-19	20-62	63-199	200-632	>632	
Pyrite	2.16	7.97	7.02	6.14	0.00	0.00	23.29
Kaolinite	1.34	3.81	1.52	0.70	0.00	0.00	7.37
Illite	4.27	7.29	4.90	5.08	8.28	0.00	29.82
Quartz	4.47	9.15	3.95	1.98	0.51	0.00	20.06
Iron-rich	0.04	0.22	0.49	1.16	0.00	0.00	1.91
Calcite	0.05	0.06	0.08	0.21	0.92	0.00	1.32
Silicates	1.57	2.19	1.38	1.47	0.98	0.00	7.59
Miscellaneous	1.64	4.13	0.70	0.40	1.73	0.00	8.60
Total <sup>a</sup>	15.54	34.83	20.04	17.15	12.42	0.00	100.00

Mineral Phase	<u>Clean Coal</u> Particle size ( $\mu\text{m}$ )						Total <sup>a</sup>
	< 6.3	6.3-19	20-62	63-199	200-632	>632	
Pyrite	2.74	4.54	1.09	0.00	0.00	0.00	8.37
Kaolinite	4.20	3.35	0.89	0.00	0.00	0.00	8.43
Illite	5.78	4.41	0.00	0.00	0.00	0.00	10.19
Quartz	6.82	6.42	0.67	0.00	0.00	0.00	13.91
Iron-rich	1.93	2.66	0.00	0.00	0.00	0.00	4.59
Calcite	1.63	2.06	0.00	0.00	0.00	0.00	3.69
Silicates	1.71	2.50	0.64	0.00	0.00	0.00	4.85
Miscellaneous	14.34	21.60	10.03	0.00	0.00	0.00	45.97
Total <sup>a</sup>	39.15	47.53	13.32	0.00	0.00	0.00	100.00

<sup>a</sup> Totals may be slightly off due to rounding.

#### ACKNOWLEDGEMENT

This work was supported by the Assistant Secretary for Fossil Energy, Division of Coal Utilization, through the Pittsburgh Energy Technology Center Coal Preparation Branch. The authors wish to thank Drs. R.A. Meyers and W.D. Hart from TRW, Inc., for supplying the Gravimelt-treat coal samples, Dr. P. Painter at Pennsylvania State University for obtaining the FTIR data, and G. Norton from Ames Laboratory for supplying the ASTM analyses.

REFERENCES

1. F.E. Huggins, G.P. Huffman, and R.J. Lee, in Coal and Coal Products: Analytical Characterization Techniques, E.L. Fuller, Jr., ed., ACS Symp. Series 205, Am. Chem. Soc., Washington, D.C., 1982, pp. 239-258.
2. T.D. Wheelock and R. Markuszewski, in The Science and Technology of Coal and Coal Utilization, B.R. Cooper and W.A. Ellingson, eds., Plenum Press, New York, 1984, pp. 47-123.
3. W.E. Straszheim and R. Markuszewski, Am. Chem. Soc. Div. of Fuel Chem. Preprints 29(4), 310-318, (1984).
4. P.H. Given and R.F. Yarzab, in Analytical Methods for Coal and Coal Products, Vol. II, C. Karr, Jr., ed., Academic Press, New York, 1978, pp. 3-41.
5. R. Markuszewski, G. Norton, and W. Straszheim, in Fossil Energy Quarterly Report (April 1, 1983 - June 30, 1983), IS-4548, Ames Laboratory, Iowa State University, Ames, IA, 50011, pp. 35-47.
6. F.E. Huggins, D.A. Kosmack, G.P. Huffman, and R.J. Lee, Scanning Electron Microscopy/1980, Vol. I, pp. 531-540.
7. W.E. Straszheim, R.T. Greer, and R. Markuszewski, Fuel 62(9), 1070-1075 (1983).
8. R. Markuszewski and W. Straszheim, in Fossil Energy Quarterly Report (January 1 - March 31, 1983), IS-4835, Ames Laboratory, Iowa State University, Ames, IA, 50011, pp. 43-50.

# CHARACTERIZATION OF COAL MORPHOLOGY BY SMALL ANGLE X-RAY SCATTERING (SAXS)

Mark Foster and Klavs F. Jensen

Department of Chemical Engineering and Materials Science  
University of Minnesota, Minneapolis, MN 55455

## INTRODUCTION

To fully understand heterogeneous reactions involving porous substances such as coal, one must have a good picture of the pore structure. This picture must reflect characteristic dimensions of the pores, their connectedness, and the surface area available for reaction on the pore walls. While the chemical structure of the coal determines the kinetics of fluid-coal reactions at the surface, the porous structure dictates how much surface is available for reaction, and what role mass transfer will play in the overall rate of reaction.

Conventional techniques for investigating pore structure, e.g. gas adsorption and Hg porosimetry, have played important roles in providing our present understanding of this structure. However, data from these methods often lead to incomplete and contradictory conclusions. Adsorption works well when measuring surface areas of nonporous or macroporous substances with chemically homogeneous surfaces. However, porosity of size scale less than 30Å is difficult to characterize with adsorption. Chemically inhomogeneous surfaces are also difficult to study. The adsorption probe molecule may adsorb preferentially on specific sites and these sites may or may not be active sites in a fluid-solid heterogeneous reaction of interest. Mercury porosimetry also works best with macroporosity. Depending on the compressibility of the sample matrix, the lower limit of pore diameter one probes may vary from 200Å to 40Å for coals (1).

Small angle x-ray scattering (SAXS) is an attractive alternative characterization technique because, above all, it is nonintrusive. Since x-rays readily penetrate the entire sample, all pores are accessible to investigation including isolated pores, i.e. those not connected to a pore leading to the particle surface. Furthermore, SAXS can study micropores as small as 10Å in diameter as well as macropores of up to 500Å in diameter. These limits may be extended using x-ray cameras designed for studying high angles or very low angles. The most exciting characteristic of SAXS is its potential for in-situ studies where the sample structure may be continually probed as it is subjected to reaction conditions.

## EXPERIMENTAL METHODS

The objectives of the present SAXS studies are 1) to measure the specific surface area of the sample and 2) to infer a pore size distribution. In pursuing these objectives three types of samples are used; a model microporous carbon, three coals, and a porous  $\gamma$ -alumina. The model carbon is Carbosieve-S, a pure carbon molecular sieve distributed by Supelco, Inc. The manufacturer quotes a surface area of 860 m<sup>2</sup>/g for this product, but does not specify the measurement technique. Conventional N<sub>2</sub> BET analysis yields a value of 1100 m<sup>2</sup>/g. The carbon's highly homogeneous microporosity has been imaged with transmission electron microscopy by Fryer (2).

Basic data on the three coal samples is summarized in Table I. The anthracite coal, with its low mineral matter content and high carbon content provides the best approximation to a true two phase system of carbon and void. Anthracite, more than lower rank coal, also has microporosity similar to that in Carbosieve. The first scattering experiments with coal were therefore performed with anthracite. The other two coals were used in a study of pore change with pyrolysis due to their higher volatile matter content.

The Carbosieve and coal samples were gasified in pure CO<sub>2</sub> at 825°C and 1 atm in a thermogravimetric apparatus (TGA). The proper precautions were taken to ensure



Table I. PSOC Coal Samples

Type	PSOC #	Name	% C	% Mineral
Anthracite	870	Primrose	93.05	2.90
Low Volatile Bituminous	127	Lower Kittanning	84.45	5.16
High Volatile Bituminous	980	Gentry	80.40	3.97

that this reaction proceeded without mass transfer limitations. The coal samples were slowly pyrolyzed in  $N_2$  in the TGA at a heating rate of  $8^\circ C/sec$  before beginning gasification. A pyrolysis reactor containing a heated wire mesh was used for preparing samples at higher heating rates (up to  $260^\circ C/sec$ ) for the study of varying pyrolysis conditions.

The third type of sample studied here is a porous alumina powder provided by W.R. Grace, Davison Chemical Division. Pore distributions from both  $N_2$  adsorption and Hg porosimetry are provided by the manufacturer. The maximum of the adsorption pore volume distribution lies at a pore radius of  $32\text{\AA}$ , and the pore volume median radius is  $41\text{\AA}$ . The  $N_2$  BET surface area is  $339\text{ m}^2/g$ . Traditional analysis of the porosimetry data yields a radius of  $35\text{\AA}$  for the maximum of the pore volume distribution.

#### SMALL ANGLE X-RAY SCATTERING

X-ray diffraction or "scattering" results from boundaries between phases of sufficiently different electron densities. The large electron density difference between carbon and void generates strong scattering. Figure 1 shows schematically how the x-rays are collimated, diffracted, and detected in the University of Minnesota's modified Kratky camera (3). This configuration allows simultaneous collection of scattering data for values of the scattering vector,  $h$  from 0.015 to 0.43, where

$$h = 4\pi \sin\theta/\lambda \quad 2\theta = \text{scattering angle}$$

The data, once corrected for sample transmission coefficient and parasitic scattering, is most profitably plotted as log intensity against  $\log(h)$ , as in Figure 4. Scattering from small inhomogeneities appear at large values of  $h$ .

All the data presented here were collected with the sample at room temperature. However, a high temperature sample cell, shown in Figure 2, has been designed and constructed for in-situ studies of coal gasification. A carbon sample may be gasified in the reaction chamber while x-rays directed through the boron nitride windows probe the change in pore structure.

Two quantities characteristic of the sample may be obtained from SAXS data without assuming a model of the pore geometry. The first is an estimate of the surface per unit volume and the second is the radius of gyration,  $R_g$ . The specific surface may be estimated from the behavior of the scattering curve for values of  $h$  such that

$$hd_m > 5.0 \quad 1)$$

where  $d_m$  is the minimum dimension of the inhomogeneity. The relationship between the scattering intensity in this region and the sample's specific surface is known as Porod's law (4). Invoking this relationship assumes that the boundaries between phases in the sample are sharp. In practice this calculation is difficult because accurate data are required for a sizeable range of  $h$  where condition 1) is met and the scattering intensity must be accurately measured to small angles also.

The radius of gyration,  $R_g$ , is more widely used and may be calculated by fitting the experimental curve with the Guinier approximation at the lowest angles (5). However, a meaningful  $R_g$  is found only for systems with nearly monodisperse inhomogeneities. Also, in order to relate  $R_g$  to a precise dimension (e.g. radius) of the inhomogeneities one must assume a model for their geometry. In general, it is best to regard  $R_g$  as a persistence length characteristic of the structure.

A great deal of information lies in the middle region of the scattering curve, but it is neglected by a Porod or Guinier analysis alone. When the system under study is polydisperse, the Guinier approximation should not be used. Information about sizes of the inhomogeneities may be derived from fitting the entire curve with a reasonable model of the structure. We have considered two models for analysis of SAXS curves from coal and chars, the Voronoi model (6) and the Fully Penetrable Polydisperse Spheres (FPPS) model. We believe this is the first application of FPPS to the modelling of small angle scattering. Thus this work represents an extension of the work of Chiew and Glandt (7) and Torquato and Stell (8).

The most convenient model for deriving a pore size distribution is one which assumes the pores are discrete spheres (9). Such a model is obviously not consistent with the interconnected nature of coal porosity. The geometric regularity of these models and cylindrical pore models used by engineers studying gasification is inconsistent with the irregularity of actual char structure. Both the Voronoi and FPPS models correspond to interconnected, random porous structures with irregular pore sizes and shapes.

The theoretical scattering from the Voronoi model is completely determined by the measurement of  $\phi_v$ , the void fraction of the sample and the choice of  $c$ , the Poisson point density (6). Empirically,  $c$  may be related to an apparent  $R_g$  of the model which reflects a mean size of cells in the structure. To fit our curve one varies  $R_g$ . Though the Voronoi model contains a distribution of cell sizes, a choice of two characteristic  $R_g$ 's, one for macropores, one for micropores, becomes necessary for a bimodal porous sample (10).

The pores in coal char are so polydisperse that several Voronoi cell sizes would have to be used to represent the experimental scattering curves. However, the Voronoi model no longer seems applicable in this case, so the FPPS is used. A two-dimensional representation of one possible combination of pore sizes and shapes constructed by the FPPS model is shown in Figure 3. For a single mode in the pore size distribution the theoretical scattering from the FPPS model is completely specified by three quantities, the void fraction  $\phi_v$ , and two parameters defining the distribution of sphere sizes. In this work we consider the Schulz distribution

$$f(r) = \frac{1}{\Gamma(b)} \left(\frac{b}{r_0}\right)^b r^{b-1} \exp\left(-\frac{br}{r_0}\right) \quad (2)$$

where  $r_0$  is a mean sphere radius, and  $b$  is a parameter that measures the sharpness of the distribution. Chiew and Glandt (7) discuss the use of this distribution with FPPS to model the surface area of a porous medium.

Considering  $\phi_v$  as a measurable quantity we see that two parameters,  $r_0$  and  $b$ , are required to fit experimental data with a unimodal FPPS model, while only one parameter is required with the unimodal Voronoi model. Thus, greater flexibility in fitting the curves is obtained at the price of one new parameter. The parameters  $r_0$  and  $b$  are determined by performing a least squares fit of the model to the data. Given the values of  $r_0$  and  $b$  which minimize the error in approximating the curve, the total surface area, complete pore size distribution, and surface area distribution are obtained analytically (7).

## RESULTS

Scattering curves for three samples of Carbosieve-S are shown in Figure 4 along with parametric fits of the Voronoi model to the data. The curve for untreated Carbosieve and the curve for the sample gasified to 16.6% conversion exhibit similar behavior. Both have distinct regions reflecting scattering from micropores and macropores. The scattering intensity attributable to a particular size of pore,  $d$  should fall off sharply for values of  $hd > 5.0$ . The sharp decrease in intensity for  $0.015 < h < 0.025$  is therefore due to macropores and the drop-off for  $h > 0.2$  is due to micropores. Consequently, two Voronoi cell sizes are required to represent curves 1 and 2. At a conversion of 80% the scattering due to macropores has become much

Table II. Voronoi Model Surface Areas: Change with Conversion

Conversion	Porosity	$R_{g,micro}$ (Å)	$R_{g,macro}$ (Å)	S(m <sup>2</sup> /g)
0.00	0.375	4.5	250	1730
0.166	0.479	4.0	250	2080
0.30	0.563	4.0	250	1820
0.41	0.631	4.5	250	1720
0.68	0.80	5.0	-	1070
0.80	0.875	5.5	-	660

less important relative to that from the growing micropores, so only a micropore cell size is needed. The parameters used in fitting the curves and surface areas calculated from the Voronoi model are given in Table II. The surface areas attain a maximum at about 16% conversion.

The surface areas are greater than those previously reported (14). However, the earlier values were determined by Porod's law at insufficiently large angles. The present technique is more accurate and the values compare favorably with the large microporosity and surface areas reported by János and Stoeckli (15).

The effect of pyrolysis heating rates on char structure have been studied for two coals, Gentry and Lower Kittanning. Final results of that work will be presented at the meeting. Preliminary results for both coals suggest a small decrease in macroporosity following pyrolysis independent of heating rate over the range studied (0.8-260°C/sec). However, samples of both coals pyrolyzed slowly at 0.8°C/sec and 5°C/sec all showed similar increases in microporosity. No change was seen in the microporosity of the fast pyrolysis samples.

Scattering data collected for the anthracite coal, PSOC 870, are shown in Figure 5. The raw coal shows a more gradual decrease in intensity at low values of  $h$  than does the Carbosieve. This reflects the presence of significantly more mesoporosity. Microporosity is present here, as indicated by the scattering persisting to high values of  $h$ , but there is no drop-off in intensity for the micropore region. A small amount of conversion seems to create a large change in the curve. However, some of this change occurs with pyrolysis. The further increase in intensity at middle values of  $h$  for the 50% conversion sample demonstrates a continued growth in mean pore size.

The FPPS model was used to fit the experimental scattering curve of our characterized porous alumina sample. Figure 6 presents the comparison of experimental and theoretical scattering curves. The FPPS approximation yields values of 15Å for  $r_0$ , and 2 for  $b$ , which corresponds to a broad distribution. These results indicate a surface area of 350 (m<sup>2</sup>/cm<sup>3</sup> particle volume) or 440 m<sup>2</sup>/g compared to 339 m<sup>2</sup>/g from N<sub>2</sub> BET analysis. Further refinement of the FPPS model allowing for noninteger values of  $b$  should improve the approximation.

#### DISCUSSION AND CONCLUSIONS

Changes in the porous structure with conversion are clearly evident in scattering data from both the model carbon and anthracite coal. Growth of the micropores in Carbosieve and of both micro- and mesopores in the coal is seen in the increasing intensity at intermediate values of  $h$ . Also, the intensity drop-off at high values of  $h$  moves in toward the mesopore scattering.

Scattering from microporosity lies at the highest values of  $h$  available with most SAXS cameras, but the microporosity contains the vast majority of surface area and must be followed. Equipment for obtaining data at still higher values of  $h$  would be very helpful. Another challenge in collecting data in the micropore region is the appearance of a broad, weak intensity maximum at  $h = 0.25$  for some coal and vitrain samples (11,12). This feature may be caused by interactions between scat-

tering units made up of layers of aromatic ring structure (11,13). The models presented here do not account for this phenomena and it has not been observed in our samples.

The Voronoi and FPPS models are better for analyzing SAXS than traditional discrete models since they correspond to interconnected, random porous structures with irregular pore sizes and shapes. The Voronoi model can be used with the model carbon which appears to have a bimodal distribution with pore sizes closely grouped about the modes. However, the FPPS model, which allows for broad distributions, is more widely applicable. The FPPS model closely approximates the scattering from a characterized sample with polydisperse porosity. However, there is a marked difference between the pore size distributions derived from SAXS and those derived from N<sub>2</sub> adsorption and Hg porosimetry. This could be explained in terms of the inability of the two conventional techniques to appropriately characterize microporosity. However, more comparative studies of the techniques are needed.

#### REFERENCES

1. Nelson, J.R., Ph.D. Thesis, The Pennsylvania State University (1979).
2. Fryer, J.R., Characterization of Porous Solids, Proc. of Symposium, S.J. Gregg, D.S.W. Sing and H.F. Stoeckli, Eds., London: Society of Chemical Industry, 41 (1979).
3. Kaler, E.W., Ph.D. Thesis, University of Minnesota (1982).
4. Porod, F., Kolloid Zeitschrift 124, 83 (1951).
5. Guinier, A. and G. Fournet, Small-Angle Scattering of X-Rays, John Wiley and Sons, Inc., New York (1955).
6. Kaler, E.W. and S. Prager, J. Coll. Int. Sci. 86, 357 (1982).
7. Chiew, Y.C. and E.D. Glandt, J. Coll. Int. Sci. 99, 86 (1984).
8. Torquato, S. and G. Stell, J. Chem. Phys. 79, 1505 (1983).
9. Lin, J.S., R.W. Hendricks, L.S. Harris and C.S. Yust, J. Appl. Cryst. 11, 621 (1978).
10. Brumburger, H. and J. Goodisman, J. Appl. Cryst. 16, 83 (1983).
11. Kalliat, M., C.Y. Kwak and P.W. Schmidt, New Approaches in Coal Chemistry, ACS Symposium Series, 169, B.D. Blaustein, B.C. Bockrath and S. Friedman, Eds., ACS: Washington, D.C., 3 (1981).
12. Chiche, P., S. Durif and S. Pregermain, J. Chim. Phys. 60, 825 (1963).
13. Hirsch, P.B., Proc. Roy. Soc. A226, 143 (1954).
14. Foster, M.D. and K.F. Jensen, Proc. Int. Conf. Coal Science, Aug. 1983, 464 (1983).
15. János, A. and H.F. Stoeckli, Carbon 17, 465 (1979).

#### ACKNOWLEDGEMENT

The work was supported by DOE (DE-FG22-82PL 50806).

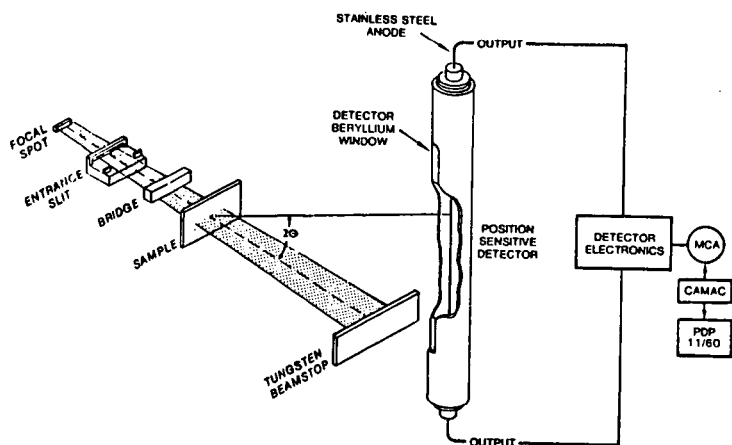


FIGURE 1. Kratky SAXS camera collimation system and detector. (From Kaler (3))

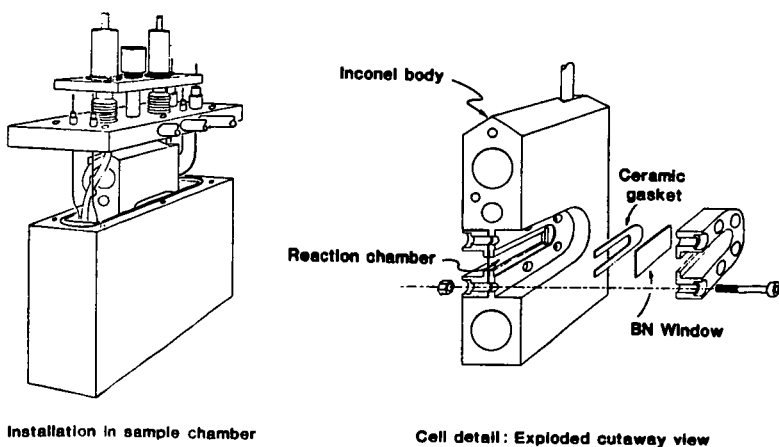


FIGURE 2. High temperature cell for in situ SAXS.

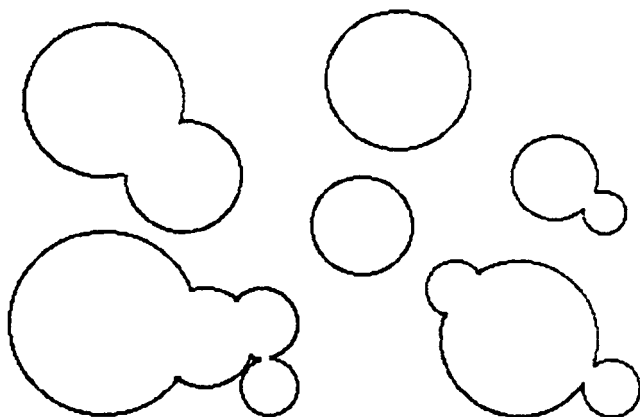


FIGURE 3. Two dimensional representation of FPPS model porous structure.

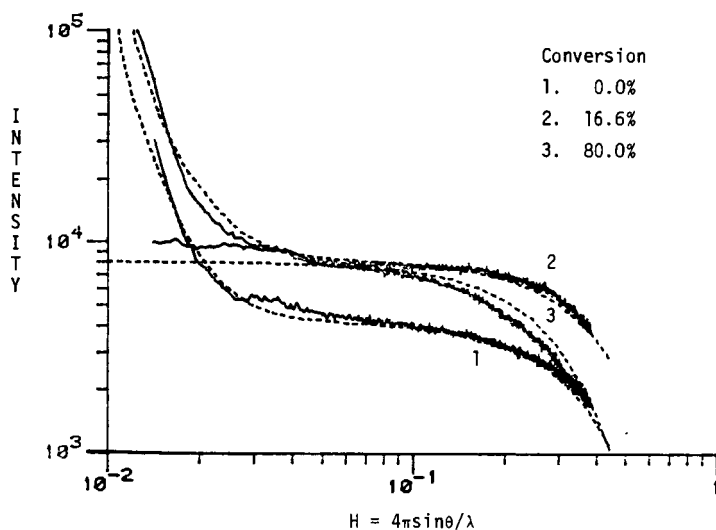


FIGURE 4. Comparison of Voronoi model approximation (----) with experimental SAXS curves (—) for Carbosieve gasified in  $\text{CO}_2$  at  $825^\circ\text{C}$ .

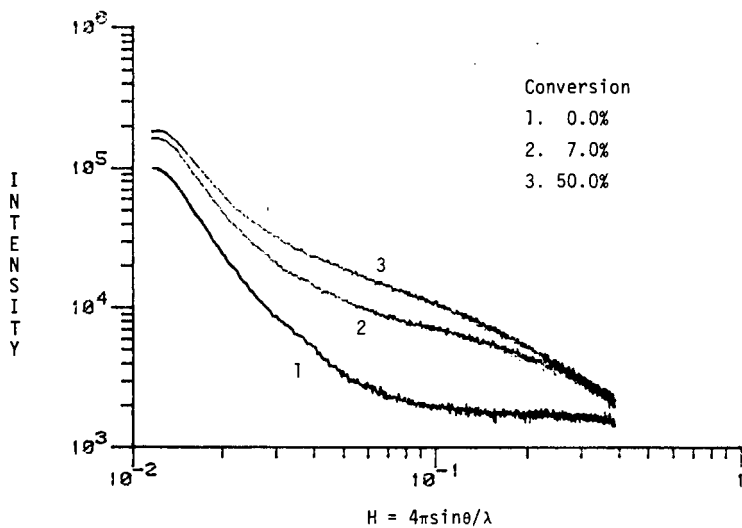


FIGURE 5. SAXS curves for Primrose anthracite (PSOC 870).

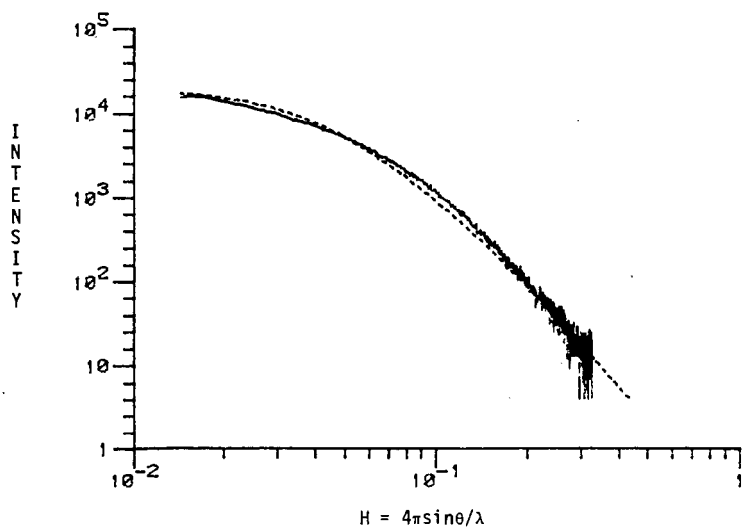


FIGURE 6. Comparison of FPPS model approximation (----) with experimental SAXS curve (—) for porous  $\gamma$ -alumina.

## THERMOPLASTIC AND VISCOELASTIC PROPERTIES OF COALS

Barbara D. Barr-Howell, John M. Howell, and Nikolaos A. Peppas

School of Chemical Engineering  
Purdue University  
West Lafayette, IN 47907

### INTRODUCTION

The modern structural view of the organic phase of bituminous and other coals is one of a crosslinked network structure (Larsen and Kovac, 1978; Lucht and Peppas, 1981 a, b; Lucht and Peppas, 1984a; Peppas and Lucht, 1984). In a recent publication (Peppas and Lucht, 1984) we have presented experimental evidence of the crosslinked structure using equilibrium swelling studies and we have offered a model that can be used to analyze it. Dynamic swelling studies using penetrants (Peppas *et al.*, 1983; Lucht and Peppas, 1984b; Peppas *et al.*, 1984; Barr-Howell and Peppas, 1985) have contributed to our understanding of this macromolecular structure.

If coal is a macromolecular network it should be possible to analyze it using theories and experiments widely applicable to polymers, basically theories of viscoelastic and rheological behavior. Since coal is a more complex and inhomogeneous structure, rheological and other analyses can give only an approximate picture of the coal structure, one that will not satisfy the purists, but still one that can offer important new insight.

Of particular importance is any information that can be obtained of the coal structure at temperatures approaching the liquefaction temperatures (300–350°C). It is known (Peppas, 1983) that coal exhibits a glass transition temperature in this range depending on its carbon content and other characteristics. The process of liquefaction is one that involves diffusive, reactive and thermal degradative phenomena; exact molecular information becomes quite difficult to obtain at high temperature. However, by using thermal analysis techniques or a combination of thermal analysis and diffusive techniques it is possible to investigate the relative importance of diffusion and degradation in the overall process. In addition, the associated viscoelastic changes of the coal network, which are expected to occur even significantly below  $T_g$  can be quantified by use of simple or sophisticated mechanical experiments (Howell and Peppas, 1984).

It is known that coal at high temperatures, close to the liquefaction temperature of 300–350°C, softens and behaves as a highly viscoelastic material. Its viscosity becomes dependent on the conditions of application of stress or strain. For example, Nazem (1980) studied the non-Newtonian behavior of carbonaceous mesophase pitch at high temperatures using a Haake viscometer and established the non-Newtonian behavior in terms of the viscosity as a function of the shear rate. Briggs investigated the viscosity of coal tar pitch as a function of temperature. Covey and Stanmore (1980) attempted to present a constitutive equation for the rheological behavior of Victorian brown coals of Australia.

An alternative approach of investigation of the viscoelastic behavior of coals is through thermal analysis at high temperatures. The early work of Bangham and Franklin (1946) established characteristics of the change and expansion of the coal structure at high temperatures. Sanada and Honda (1963) used creep deformation of various Japanese coals to establish their mechanical behavior at high temperatures. Gryaznov *et al.* (1977) and Lazarov (1983) examined the thermoplastic behavior of coals and discussed the results of several thermal analysis techniques. They examined the plasticizing phenomena of coals at high temperatures, their anisotropic liquid crystalline formations and their rheological behavior.

Thermogravimetric studies for the purpose of elucidating the thermoplastic behavior has been presented by Rovenskii and Melnik (1975), Ciuryla *et al.* (1979) and Elder and Harris (1984). Probably the most interesting recent studies on this subject are those of the group of Jenkins (Jenkins and Khan, 1982; Khan and Jenkins, 1984 a,b) who used a microdilatometer to investigate changes in the stress-strain behavior of certain coals.

### EXPERIMENTAL PART

Coal samples, packed under nitrogen, were supplied by the Pennsylvania State University Coal Bank. They were sieved to the desired mesh size and stored under nitrogen until use.



For the pyridine sorption studies at high temperatures, a thermogravimetric analyzer (Perkin Elmer, model TGA-2, Norwalk, Conn.) and an associated sorption system were used. Approximately 5 mg of the coal sample was placed in a platinum pan which was suspended from a lever arm balance. The system was then emerged in a microfurnace and purged with nitrogen. After one hour pyridine was allowed to bubble through the system and over the coal sample. Changes in weight due to sorption were recorded. The sorption experiments were carried out at constant temperature of 50 °C, 100 °C, 150 °C, 250 °C, 300 °C, and 350 °C.

For the creep experiments a thermomechanical analyzer was used. The flat coal samples for these studies were prepared under nitrogen by slicing coal chunks along their fault lines, and grinding the resulting slabs smooth with a diamond wheel (Peppas *et al.*, 1984). The size of each sample was approximately 2.5 mm<sup>2</sup> in surface area, by 0.6 to 0.9 mm in thickness. The flat samples were cut to the size of the TMA probe and tested using the thermomechanical analyzer (Perkin Elmer, model TMS-2) in the penetration mode under continuous purging with nitrogen. The initial temperature was 35 °C and a scanning rate of 10 °C/min was used. The surface area of the cylindrical probe tip used was 0.6207 mm<sup>2</sup>. Each sample was tested using applied loads of 10, 20, 30 and 40 g with corresponding stresses of 0.158, 0.316, 0.474 and 0.632 MPa. Changes due to deformation were recorded.

## RESULTS AND DISCUSSION

### *Dynamic Swelling at High Temperatures*

Dynamic swelling experiments with coal particles were performed at various temperatures to establish the transport mechanism in the presence of a solvent and the degradation reaction of coal. The studies presented here were performed with PSOC 312 coal particles of 20-30 mesh at 35, 50, 100, 150, 200, 250 and 300 °C.

The results of these studies are presented in Figures 1 and 2. At low temperatures, 35 and 50 °C, significant pyridine uptake is observed with minimum degradation. At 100 °C degradation is prominent, and the overall change of weight is smaller than at lower temperatures. Above 150 °C the degradation is significant. To further investigate this phenomenon similar coal samples were run in the TGA equipment in the absence of pyridine vapors and the degradation was recorded as shown in Figure 3. Experiments at 35 °C, 50 °C, 100 °C and 150 °C showed no measurable degradation over a period of 15 hours. Then, the data of Figure 1 and 2 were corrected for the loss of weight due to degradation and the corrected values are reported in Figure 4.

The overall penetrant uptake does not, and should not be expected to, correlate with temperature, since, due to the degradation process, the coal structure changes radically, leading to significant changes of the thermodynamic interactions between pyridine and coal network as well as, most probably, the porous structure. However, the inflection points and overshoots observed especially at 200 °C, 250 °C, and 300 °C are "real" observations, since the experimental error of the technique was determined to be less than 0.1 %. The data of 150 °C show that at this temperature the degradation is more significant than the pyridine uptake.

In general we may conclude that the pyridine transport through the significantly altered coal network at temperatures approaching its glass transition temperature is highly non-Fickian, that macromolecular relaxations become extremely important (as exhibited by the strong overshoots observed), and that the affinity of pyridine for the network is dramatically altered at high temperatures. Obviously, more detailed studies are needed to quantitatively elucidate this very fascinating phenomenon.

In the presence of 70-150 % pyridine in coal particles at 250-350 °C the coal network is in the rubbery state, only slightly above its  $T_g$  values (Peppas, 1983) and the highly anomalous transport mechanism should be expected, due to the value of the Deborah number which is of the order of one (Peppas *et al.*, 1984). The macromolecular relaxation, and the associated anomalous transport, lead to a drastically increased penetrant flux in the coal network, since the pseudo-convective contribution to anomalous transport becomes extremely important. In fact, no experimental data have been observed before, where at equilibrium the pyridine uptake is as high as 2.3 times the weight of coal, when Fickian diffusion predominates.

### *Viscoelastic Behavior at Low and High Temperatures*

Figures 5 and 6 present the compressive strain versus temperature (and time, since the scanning speed was 10 °C/min) curves for samples of PSOC-312 with 78.33 % C and PSOC-853 with 80.15 % C, for different applied stresses.

Each curve on Figure 5 shows an induction period, followed by a change of the strain, usually starting at about 115-150 °C. At about 350 °C, where the sample is near its glass transition temperature, the compressive strain is only about 3-3.5 % of the total thickness, a typical value of compressive strain for porous, glassy polymers. Almost all the samples show that at low applied stresses and up to 300 °C a significant "negative strain" (namely expansion) of the coal samples is exhibited, which is, of course, characteristic of the traditional "swelling" of coals when heated in an inert atmosphere. With higher applied stress, the overall effect is compression and therefore an increase in compressive strain.

To further understand the viscoelastic behavior of coal below and near  $T_g$ , one may have to further examine Figure 6 which shows the strain versus temperature behavior up to the glass transition region. All the curves are smooth (a minor inflection point of unknown origin appears at about 250 °C) and quite typical of the similar behavior of glassy polymers. The porous structure should not be of major concern in this analysis. Since coal is glassy in most of the range of temperatures studied here, major pore compression would be unlikely to occur.

At a specific temperature, the creep behavior is highly similar to that of conventional macromolecular structures (Figure 7). A smooth increase in compressive strain is observed, which at 250 °C (for PSOC-853) seems to level off at about 20 %, whereas at 300 °C it reaches 65 %. It should be noted that the  $T_g$  value for this coal is 305 °C.

Figure 7 shows also the effect of repeated loadings (or creep experiments) on the compressive strain at constant temperature. For example, at 300 °C the creep behavior was followed for 200 hours at which time (point A) the load was removed and the recovery process was followed. The sample attained a certain compressive strain of 0.50 (permanent plastic deformation). Upon reapplication of the same stress at 260 hours (point B) a very fast creep behavior was observed. It must be noted that the new values of the compressive strain were on the extrapolated curve of the first creep experiment (see dashed line of Figure 7). A similar behavior is obtained at 250 °C, although of much smaller magnitude since the coal network is still glassy at this temperature.

One important comment must be made here. In a previous note (Howell and Peppas, 1984) we had discussed our first data with this technique, using coal samples which were bigger than the probe size of the TMA and we had concluded that some coal samples exhibit unusual "plateau" regions during their temperature-dependent creep behavior. In a private communication, Dr. D. Brenner of Exxon pointed out that the phenomenon studied before was that of "squeezing flow" in a viscoelastic matrix. The new studies reported here are with TMA probe-size coal samples (and with much improved preparation techniques which provide samples of truly uniform thickness (Ritger, 1985)), and they truly represented a creep behavior. The plateau region observed in the "squeezing flow" type studies has disappeared here, although a weak inflection point can be seen in some of the samples in the same region where the plateau was before. Obviously, studies towards this direction will continue.

## REFERENCES

- D.H. Bangham and R.E. Franklin, *Trans. Faraday Soc.*, **42B**, 289 (1946).
- B.D. Barr-Howell and N.A. Peppas, *Fuel Chem. Prepr.*, this volume (1985).
- V.T. Ciuryla, R.F. Weimer, D.A. Bivans and S.A. Motika, *Fuel*, **58**, 748 (1979).
- G.H. Covey and B.R. Stanmore, *Fuel*, **59**, 124 (1980).
- J.P. Elder and M.B. Harris, *Fuel*, **63**, 262 (1984).
- N.S. Gryaznov, L.V. Kopeliovich and Y.A. Nechaev, *Khim. Tverd. Topl.*, **11** (3), 104 (1977).
- J.M. Howell and N.A. Peppas, *Fuel Chem. Prepr.*, **29** (1), 207 (1984).
- R.G. Jenkins and M.R. Khan, EPRI Report AP-2337, Palo Alto, CA 1982.
- M.R. Khan and R.G. Jenkins, *Fuel Process. Techn.*, **8**, 307 (1984a).
- M.R. Khan and R.G. Jenkins, *Fuel*, **63**, 109 (1984b).
- J.W. Larsen and J. Kovac, in *Organic Chemistry of Coal*, J.W. Larsen, ed., ACS Symposium Series, Vol. 71, 36, Washington, D.C., 1978.
- L. Lazarov, *Koks i Khimiya*, (2), 13 (1983).
- L.M. Lucht and N.A. Peppas, in *New Approaches in Coal Chemistry*, B.D. Blaustein, B.C. Bockrath and S. Friedman, eds., ACS Symposium Series, Vol. 169, 43, Washington, D.C., 1981a.
- L.M. Lucht and N.A. Peppas, in *Chemistry and Physics of Coal Utilization*, B.R. Cooper and L. Petrakis, eds., Amer. Inst. Physics, Vol. 17, 18, New York, N.Y., 1981b.
- L.M. Lucht and N.A. Peppas, *Fuel Chem. Prepr.*, **29**, (1), 213 (1984).
- L.M. Lucht and N.A. Peppas, in *Advances in Rheology: Fluids*, B. Mena, A. Garcia-Rejon and C. Rangel-Nafaile, eds., Vol. 2, 631, UNAM, Mexico City, 1984b.
- F.F. Nazem, *Fuel*, **59**, 851 (1980).
- N.A. Peppas, Final Report to DOE, FG-28-80PC30222, Lafayette, IN, 1983.
- N.A. Peppas, L.M. Lucht, J.M. Larson and G.W. Sinclair, *Procecd. Intern. Coal Confer.*, **2**, 280 (1983).
- N.A. Peppas, B.D. Barr-Howell, J.M. Howell and P.L. Ritger, Annual Report to DOE, FG-22-83PC60792, Lafayette, IN, 1984.
- N.A. Peppas and L.M. Lucht, *Chem. Eng. Commun.*, **30**, 291 (1984).
- P.L. Ritger, M.S. Thesis, Chem. Engineering, Purdue University, 1985.
- V.I. Rovenskii and N.A. Melnik, *Khim. Tverd. Topl.*, **9** (4), 36 (1975).
- Y. Sanada and H. Honda, *Fuel*, **42**, 479 (1983).

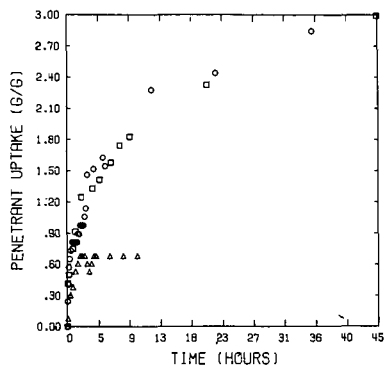


Figure 1: Effect of Swelling Temperature on Pyridine Uptake on Coal Particles of PSOC-312. Temperatures: 35 °C (○), 50 °C (□) and 100 °C (Δ).

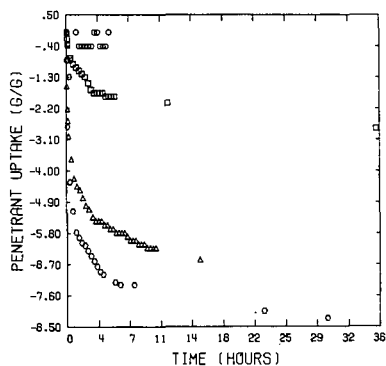


Figure 2: Effect of Swelling Temperature on Pyridine Uptake on Coal Particles of PSOC-312. Temperatures: 150 °C (○), 200 °C (□), 250 °C (Δ), and 300 °C (◇).

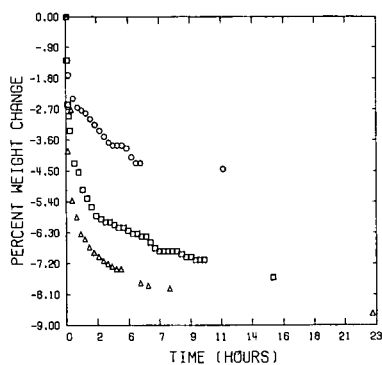


Figure 3: Coal Weight Loss as a Function of Time for PSOC-312. Temperatures: 200 °C (○), 250 °C (□), 300 °C (△).

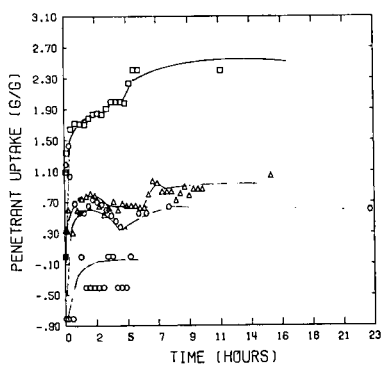


Figure 4: Corrected Pyridine Uptake of PSOC-312. Temperatures: 150 °C (○), 200 °C (□), 250 °C (△), 300 °C (◊).

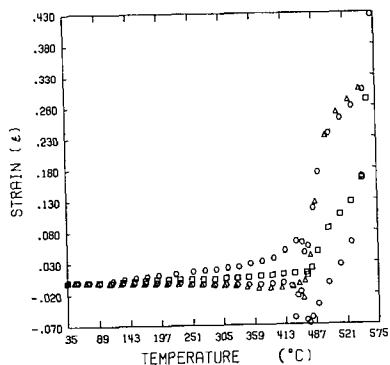


Figure 5: Compressive Strain as a Function of Temperature for Flat Coal Section of PSOC-312 with Applied Stress of 0.158 (○), 0.316 (□), 0.474 (Δ), and 0.632 (◇) MPa.

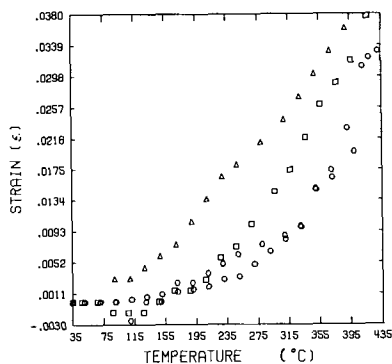


Figure 6: Compressive Strain as a Function of Temperature for Flat Coal Section of PSOC-853 with Applied Stress of 0.158 (○), 0.316 (□), 0.474 (Δ), and 0.632 (◇) MPa.

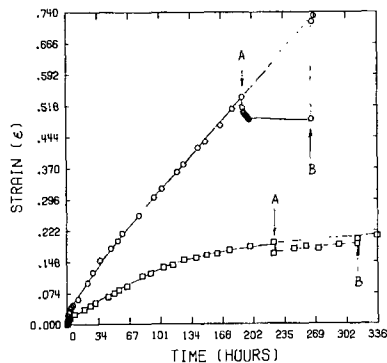


Figure 7: Compressive Strain as a Function of Time for PSOC-853 Coal Samples under Applied Stress of 0.474 MPa at 250 °C (□) and 300 °C (○). Creep period (from 0 to point A); recovery period (from A to B); second creep period (after point B).

## DIFFUSIVE UPTAKE OF FLUIDS BY COAL PARTICLES -- EFFECTS OF PARTICLE SHAPE AND PARTICLE SIZE DISTRIBUTION

D. Brenner and P. S. Hagan

Corporate Research Science Laboratories  
Exxon Research and Engineering Company  
Annandale, NJ 08801

### INTRODUCTION

Diffusion into coals is of considerable technological importance since many coal modification processes, such as direct liquefaction, desulfurization, demineralization, and chemical modification, involve diffusion of liquids or gasses into the coal. Additionally, much of the fundamental chemical research on coals requires diffusion of liquids or dissolved reagents into the coal so that reactions can occur. Precise interpretation of these experiments often requires an understanding of the diffusional behavior. The rate that reactants diffuse into the particles is often a rate-limiting step. The variety of shapes and sizes of particles in the coal slurry greatly complicates the overall diffusion kinetics, and unless this heterogeneity is properly taken into account it can lead to erroneous analyses of the process. There is information in the literature on the diffusive uptake of fluids by differently shaped single particles for various concentration-dependent diffusion coefficients (1), and there is some literature on diffusion into coals (2,3). However, no information concerning the effect of the particle size distribution on the diffusive uptake of coals in a slurry is available. The objective of this paper is to determine the range of diffusive uptake behaviors which can result from the different particle shapes and the particle size distribution.

Coal samples are commonly prepared by breaking down the coal until it is below a selected mesh size. This procedure results in a wide distribution of particle sizes. Sometimes mesh cuts of the coal are taken in which only that coal which passes through a selected larger mesh size, but not through a selected smaller mesh size, is utilized. This reduces the breadth of the size distribution, but even in the limit of an infinitely narrow mesh cut there will still be considerable variations in the diffusive uptake of the various particles due to the wide range of shapes that result from the breakdown or fracture process, and also due to the cracks and heterogeneity of the coal's microstructure.

To assess the effects of the different particle shapes and of the particle size distribution, we adopted the following strategy. First, since typical distributions of particle shapes present in coal samples are unknown, to determine the range of diffusive uptake behavior caused by having different particle shapes in the slurry, we calculate diffusive uptakes for both slab-shaped particles (with infinite height-to-width ratios) and spherical particles. Most other particle shapes can be considered to be intermediate between these two shapes, so their uptakes can be expected to fall in between these two extreme cases. Thus, these pairs of uptake calculations bracket the range of diffusive uptakes for most particle shapes, and therefore bracket the uptakes for most distributions of particle shapes.

To determine the effects of the distribution of particle sizes, for each particle shape (slab or sphere) we calculate the diffusive uptakes of both a single particle and a slurry of differently sized particles with that shape. The particle size distribution used was obtained from an experimental study of ball milling of coal by P. Luckie, *et al.* at Pennsylvania State University (4), so the distribution is relevant to actual coal slurries. While these investigators found that there were some variations in the measured particle size distribution depending on the experimental conditions, a typical distribution is approximated by

$$(1) \quad W(R) = 1 \text{ for } 0 \leq R \leq R_0, \\ = 0 \text{ for } R > R_0,$$

where  $W(R)dR$  is the weight fraction (or volume fraction) of particles whose size  $R$  is between  $R$  and  $R + dR$ .  $R_0$ , of course, gives the upper limit on the sizes of the particles. For spherical particles  $R$  is the particle radius. For slab-shaped particles,  $R$  is the half-thickness of the particle. The particle size distribution given by Eq. 1 is the distribution we use for all slurry calculations in this paper.

Besides the variations in particle shapes and sizes, there are a number of other factors which complicate diffusion in coal. These factors include the cracks and holes through the coal, the variety of macerals having different chemical and physical properties which make up the coal, the heterogeneity of the structure even within individual macerals, and the effects of intermaceral interfaces and mineral matter (5). These heterogeneities of the coal structures will not be explicitly treated in this paper, but they may cause substantial deviations from the usual diffusional behavior. The effects of particle shape and particle size distributions which are treated here should give a qualitative indication of the sorts of deviations which might result from these heterogeneities.

#### FORMULATION OF THE MODELS

In this section the diffusion models being considered are discussed briefly, and the mathematics describing the models is formulated. Two distinct modes of diffusion are treated, Fickian diffusion (6) and Case II diffusion (7). Fickian diffusion is the common form of diffusion in which the rate of flow of the penetrant is related to the concentration gradient by a proportionality factor,  $D(c)$ , which is called the diffusion coefficient. For Fickian diffusion, the concentration  $c(t,x)$  of the penetrant within a particle obeys the following equation:

$$(2) \quad \frac{\partial c}{\partial t} = \nabla \cdot D(c) \nabla c$$

For Fickian diffusion,  $D$  is either a constant or is an explicit function of the concentration  $c$ . Diffusion coefficients which are non-decreasing functions of concentration can be expected for the diffusion of most penetrants into coal, so only these are considered in this paper.

We impose the boundary and initial conditions

$$(3.1) \quad c = c^* \quad \text{at the particle's surface} \\ (3.2) \quad c = 0 \quad \text{at time } t = 0 \text{ within the particle.}$$

Here the (fixed) concentration  $c^*$  is the concentration of penetrant within the coal particle which would be in equilibrium with the concentration of penetrant in the solution; i.e.,  $c^*$  is the saturation concentration of the penetrant within the coal. By using Eq. 3.1, we are assuming that the external surface of the particle is in equilibrium with the solution. By taking  $c^*$  to be constant in time, we are assuming that the slurry is well-stirred and that the depletion of the penetrant in the solution is negligible. (Maintaining the proper boundary conditions in experiments we wish to interpret is crucial. For example, a frequent experimental procedure is to allow a penetrant to diffuse from a liquid reservoir through an inert gas to reach the particles. However, this procedure generally will not maintain the boundary condition (Eq. 3.1) sufficiently accurately, which may greatly perturb the results). The initial condition, Eq. 3.2 simply states that the particles contain no penetrant at the start of the experiment. Once the penetrant concentration  $c(t,x)$  within a particle has been determined from Eqs. 2, 3.1 and 3.2, the particle's uptake of penetrant at time  $t$ ,  $m(t)$ , is found by integrating over the particle's volume:

$$(4) \quad m(t) = \iiint c(t, \vec{x}) dV.$$



For the conditions of Eqs. 3, the uptake will be proportional to  $\sqrt{t}$  for a semi-infinite medium so for any reasonably shaped particle it will be proportional to  $\sqrt{t}$  at small enough times.

There is an important class of problems which do not involve pure diffusion, but which are also governed by Eqs. 2-4. If a substance undergoes both Fickian diffusion and chemical reaction within the particles, and if the reaction proceeds much more rapidly than the diffusion (so diffusion is the rate-limiting step), then the diffusive uptake of the substance by a particle is again given by Eqs. 2-4.

Among all non-decreasing diffusion coefficients  $D(c)$ , there are two cases which represent extremes in the concentration dependence. One extreme case is simply a constant diffusion coefficient

$$(5.1) \quad D(c) = D_0 \quad \text{for all } c.$$

The other extreme case is found by considering a diffusion coefficient which is zero up to nearly the saturation concentration  $c^*$ , but just short of this concentration the coefficient jumps to a large value and remains fixed until saturation. Mathematically, this diffusion coefficient is

$$(5.2) \quad \begin{aligned} D(c) &= 0 & \text{for } c < c^* - \epsilon \\ &= \frac{A}{\epsilon} & \text{for } c^* - \epsilon < c < c^* \end{aligned}$$

where  $A$  is a constant, and  $\epsilon/c^* < 1$ . This second extreme case is obtained by letting  $\epsilon$  become arbitrarily small and thereby take the limit as  $\epsilon \rightarrow 0$ .

We assert that the normalized uptake curve  $m(t)$  for any non-decreasing diffusion coefficient  $D(c)$  always lies in between the normalized uptake curves calculated for the two extreme cases given by Eq. 5.1 and Eq. 5.2 (in the limit of  $\epsilon \rightarrow 0$ ). (The normalization of the uptake curves is discussed in the next section.) Thus, the uptake curves calculated using the two extreme diffusion coefficients bracket the range of uptake curves for all non-decreasing diffusion coefficients  $D(c)$ . We have tested this assertion with a very large number of different concentration dependent diffusion coefficients including, for example, diffusion coefficients which increase exponentially with concentration. In all cases the uptake curves remained between the two extremes. As we shall see, for slurry systems these two extreme cases yield normalized uptake curves which lie surprisingly close together. So the curves for all non-decreasing diffusion coefficients lie close together.

Case II diffusion is distinctly different from Fickian diffusion and cannot be described by similar equations. In Case II diffusion there is a sharp penetration front that propagates into the matrix material at a constant velocity, so the initial uptake of penetrant is linear in time. Ahead of the front the concentration is nearly zero, and behind the front the concentration is nearly constant. Then for Case II diffusion, the concentration  $c(t, x)$  of penetrant at position  $x$  in a particle is given by

$$(6) \quad \begin{aligned} c(t, x) &= c^* & \text{if } s < vt \\ &= 0 & \text{if } s > vt \end{aligned}$$

where  $s$  is the distance from the point  $x$  to the particle's surface, and  $v$  is the velocity of the penetration front. Case II diffusion often occurs where the absorption of the penetrant results in a transition of the matrix material from a plastic to a rubbery or viscous state. Since some liquids are known to transform some coals from a plastic to a rubbery state (8,9), Case II diffusion or behavior intermediate between Case II and Fickian diffusion is a possibility for coals.

One of the most common and easiest methods of characterizing the diffusional behavior of a system is to expose the material to the fluid at  $t = 0$ , and to monitor the uptake as a function of time. This is the approach taken in this study. For this approach there are two aspects of these diffusional systems

that we are particularly interested in: (1) given the uptake behavior, what can be learned about the diffusion coefficient  $D(c)$ ; and (2) how well can the uptake be predicted without having detailed knowledge of the diffusion coefficient. To address these issues, the uptakes were calculated for the systems that were described above.

The uptakes were calculated from Eqs. 1-6 using numerical methods on a digital computer. The method used was the Crank-Nicolson scheme (10). The results were calculated to an accuracy of better than 0.1%, so any residual deviations from the exact results would not be observable in the figures.

#### METHOD OF PRESENTATION OF DATA

Results for each of the models with the conditions discussed in the Formulation Section are presented in this paper in graphical form. A few words are needed to describe the mode of presentation of the graphical data. The approach taken in this study is that the experimenter does not know anything a priori about the diffusive behavior of his system; rather he measures the penetrant uptake as a function of time and then attempts to determine such characteristics as the type of diffusion (e.g. Fickian, or Case II, or an intermediate behavior), and the concentration dependence of the diffusion coefficient. Our procedure, then, is to compute theoretical curves based on various models to which the experimenter can compare his data and attempt to determine the diffusive character of his system. The data computed for the different hypothetical models are conveniently displayed as normalized graphs or curves. The vertical axis measures the fraction of penetrant taken up by the medium, where 1.0 is the maximum value which occurs at saturation (i.e., equilibrium). The horizontal axis is the time axis. For Fickian diffusion having the boundary condition of constant concentration of penetrant at the fluid-solid interface, the uptake curve for any reasonably shaped particle will be proportional to  $\sqrt{t}$  at small enough times. Since a linear curve (initially) is easy to evaluate visually, the time axis in the figures is scaled as  $\sqrt{t}$ . What remains is to scale the absolute magnitude of time along the time axis. We have found that a convenient criterion is to match the slopes of the various curves in a figure at zero time. Then the curves start off together and it is easy to observe how they deviate from the original slopes as time progresses. For the single particle data for Fickian diffusion, the scaling of the system is arbitrarily chosen to produce initial slopes of  $45^\circ$ . The uptake curves produced by plotting fractional uptake versus the square root of time, where the initial slopes are scaled to be  $45^\circ$ , will be referred to as "normalized uptake curves".

#### RESULTS

##### Fickian Diffusion

###### a. Fickian diffusion in a single slab-shaped particle

Figure 1 shows the normalized uptake curves for Fickian diffusion in a slab, for a constant diffusion coefficient and for the diffusion coefficient defined in Eqs. 5.2. (Recall that the normalized uptake curve for any non-decreasing diffusion coefficient lies in between these two curves). The lower curve is for the constant diffusion coefficient and the upper curve is for the coefficient which is zero except for concentrations very near saturation. The curves are straight and virtually indistinguishable up to an uptake of roughly 0.6. This behavior is not surprising since it is well known that for Fickian diffusion in a semi-infinite medium with the boundary condition described in Eq. 3.1, the curves would be straight for all time for any concentration dependence of the diffusion coefficient. A deviation from the straight line can only occur when there is an appreciable overlap of fluid diffusing in from one side of the slab with fluid which diffused in through the other side. That is, only when the fluid achieves an appreciable concentration at the center plane of the slab do differences occur between the finite thickness slab and a semi-infinite slab.

The diffusional behavior for the diffusion coefficient defined by Eqs. 5.2 is readily pictured physically. Since for this diffusion coefficient there can be no diffusion unless the fluid concentration is essentially at saturation, the fluid propagates into the medium as a sharp front with concentration zero ahead of the front, and it is essentially at its saturation value behind the front. The front propagates with a decreasing velocity which is proportional to  $1/\sqrt{t}$ . Only when the fronts propagating in from opposite sides of the slab meet, does the system recognize that the slab is not semi-infinite. Since Fickian uptake curves for non decreasing diffusion coefficients always remain concave towards the  $\sqrt{t}$  axis (11), it is clear that the diffusion coefficient of Eqs. 5.2, which maintains the  $45^\circ$  straight line all the way to saturation gives an upper bound to the cumulative uptake at any time.

#### b. Fickian diffusion in a single spherical particle

In Figure 2, the same two diffusion coefficients used in Figure 1 are again utilized, but this time for a spherical particle. In addition, an intermediate concentration dependence is included -- the exponential concentration dependence  $D(c) = e^{2c}$ . The exponential diffusion coefficient gives the intermediate curve in Figure 2, which illustrates our general finding that the normalized uptake curve for any diffusion coefficient (that is non-decreasing with concentration) always lies in between the normalized uptake curves obtained from the extreme diffusion coefficients in Eq. 5.1 and Eqs. 5.2. For spherical particles the difference in the normalized uptake curves for the two diffusion coefficients which give the upper and lower bounds is much less evident than for the slab case. In fact, unless an experimental uptake curve had a very high accuracy, it would be difficult to determine whether the observed behaviour was produced by the most strongly concentration dependent diffusion coefficient possible (the upper curve) or by a constant diffusion coefficient (the lower curve), much less some intermediate concentration dependence.

It is seen in Figure 2, that the uptake curves depart from the initial straight line much earlier than for the slab. The deviation from the straight line by the upper curve, for which the penetrant propagates into the material as a sharp front, is caused by the smaller and smaller area of the surface defined by the front as it propagates towards the center of the sphere.

#### c. Fickian diffusion in a slurry of slab-shaped particles

Figure 3 shows the effect of the particle size distribution on the uptake behavior of slab-shaped particles. The curves in this slurry graph are scaled such that if all of the volume of the sample was used in making up particles of the same size as the largest particle in this distribution, then the curves would start out at  $45^\circ$  on this plot. Of course the presence of the smaller particles in the distribution results in a larger surface area than if the same volume resided in larger particles, so the initial slope for the slurry is considerably greater than  $45^\circ$ .

The top and bottom curves in Figure 3 are for the same diffusion coefficients as in Figure 1. It is immediately obvious by comparing Figures 1 and 3 that the particle size distribution dramatically changes the behavior of the normalized uptake curves. For example, for this slurry of slab-shaped particles there is significantly less difference between the uptake curves for the two extreme concentration dependencies shown than for the single particle case. In fact, the curves for the slurry of slab-like particles in Figure 3 are significantly closer together than the curves for the single spherical particle in Figure 2.

It is seen that the uptake curves in Figure 3 fall well below the initial slope at a much lower uptake value than even for the single spherical particle case. Qualitatively the reason for this early deviation is clear. The smaller particles in the distribution approach saturation quickly and then contribute little to the uptake. The close correspondence of the two curves at all times and the

dramatic differences between the curve shapes in Figures 1 and 3 suggest that the particle size distribution is the dominant factor in the uptake behavior.

#### d. Fickian diffusion in a slurry of spherical particles

Figure 4 presents slurry data for spherical particles calculated using the diffusion coefficients described previously. This figure should be compared with the single spherical particle curves of Figure 2. The uptake curves in Figure 4 lie very close together, even though the curves represent the two extreme cases of concentration dependence for (monotonically increasing) Fickian diffusion coefficients. It is clear from these results that for the sort of particle distribution used, it is extremely difficult, if not impossible, to get reliable concentration dependence information for the diffusion coefficient from the shape of the uptake curve.

#### Case II Diffusion and Comparison with Fickian Diffusion

As described previously, Case II diffusion exhibits behavior which is fundamentally different from Fickian diffusion, regardless of the concentration dependence of the Fickian diffusion coefficient. Case II diffusion is easy to visualize since it involves the propagation of a sharp front into the medium, with zero concentration ahead of the front and saturation behind the front. In this respect it is similar to the Fickian diffusion described by Eqs. 5.2, and discussed previously. However, physically and mathematically these two modes of diffusion are fundamentally different. For example, whereas (regardless of the concentration dependence) a Fickian front propagates into a semi-infinite medium at a velocity proportional to  $1/\sqrt{t}$  (assuming the usual fixed concentration of penetrant at the surface), the Case II front propagates at a constant velocity.

#### a. Case II diffusion in a single slab-shaped particle

Figure 5 shows the penetrant uptake curve for Case II diffusion in a single slab-like particle. In this figure the Case II diffusion is compared to the two extremes of Fickian diffusion previously shown in Figure 1. The curve which starts off lowest in Figure 5 is from Case II diffusion, the other two curves are identical to the ones in Figure 1. The Case II uptake curve can not be conveniently normalized to a initial slope of  $45^\circ$  on this graph because of its initial linear-in-t time dependence. Therefore, the Case II curves were normalized in a different manner. In all of the remaining figures, the Case II curve is scaled along the square-root-of-t horizontal axis by requiring that the area under its curve be equal to the area under the curve for the constant Fickian diffusion coefficient. The dramatic difference in behavior between Case II diffusion and Fickian diffusion for any monotonically increasing concentration dependence is obvious from Figure 5. Presumably uptake curves for Fickian diffusion coefficients having any concentration dependence which is a non-decreasing function of concentration will fall between the two Fickian curves in Figure 5, whereas the Case II curve is far out of this range. While the Case II curve appears to be highly curved in this  $\sqrt{t}$  plot, actually the Case II curve would be a straight line if the graph utilized a linear-in-t horizontal axis.

#### b. Case II diffusion in a slurry of slab-shaped particles

Figure 6 shows the uptake curve for Case II diffusion for a slurry of slab-like particles. The particle size distribution is given by Eqs. 1. The corresponding Fickian uptake curves for this particle shape and particle size distribution, which were shown in Figure 3, are displayed in Figure 6 for comparison. It is seen that there is slightly closer correspondence between the Fickian and Case II curves for the slurry than in Figure 5 for the individual particles, but the curves are still quite different. Comparing the Case II curve for the individual slab of Figure 5 with the Case II curve for the slurry of Figure

6, it is seen that in the region up to an uptake of about 0.8 the curve in Figure 6 has much less curvature than in Figure 5. In fact, over more than half of the entire uptake curve, from below 0.2 up to nearly 0.8, the Case II uptake curve in Figure 6 is very nearly straight. This is surprising since with our boundary conditions a straight line plot of uptake versus square root of time is commonly taken as the signature of Fickian diffusion. To add to the confusion, the Fickian curves in Figure 6 have much more curvature than the Case II curve. So, if the very early time curvature of the Case II curve were neglected (for example, there are frequently experimental difficulties or uncertainties at small times), it is possible that an experimenter would misinterpret the Case II curve as signifying Fickian diffusion, and would misinterpret the Fickian curves as signifying a non-Fickian type of diffusion. Recall also that the particle size distribution used for these calculations is not an arbitrary one, but is a fit to an experimentally derived curve from the ball milling of a coal. Therefore, it is crucial that an experimenter understand the effective particle size distribution of his sample before attempting to interpret diffusional data from uptake curves. A particle's effective size will be affected by the exact shape of the particle, and in fact, the effective particle size may be quite different from the particle's geometrical size. This distinction can be especially important for heterogeneous, crack-containing, and porous materials, such as coals, for which the geometrical surface and the region rapidly penetrated by fluids may differ substantially (5).

The change in shape of the Case II uptake curve for the slurry in Figure 6, as compared to the single particle uptake in Figure 5, is caused by the saturation of the smaller particles so that they no longer contribute to fluid uptake.

#### c. Case II diffusion in a single spherical particle

Figure 7 shows the Case II uptake curve for a single spherical particle. Also shown on the graph are the Fickian uptake curves for the corresponding system. The Case II uptake curve for the sphere differs from the linear-in-time behavior for the slab, because as the diffusion front propagates into the sphere towards the center, the position of the front describes a smaller and smaller sphere. It is noteworthy that for the single spherical particle, the Case II uptake curve has a long, relatively straight region from about 0.2 to 0.8 on the square-root-of-time plot. This is a longer (approximately) straight region than for the corresponding Fickian curves. Of course, the large curvature in the region below an uptake of 0.2 gives away the non-Fickian behavior of the Case II curve for this system.

#### d. Case II diffusion in a slurry of spherical particles

Figure 8 shows the uptake curve for Case II diffusion in a slurry of spherical particles whose size distribution is again given by Eqs. 1. The Fickian curves for the corresponding systems (i.e. Figure 4) are also shown. What is remarkable about this Case II curve is that it is nearly straight all the way from an uptake of about 0.05 to 0.7 uptake. If the particle size distribution was not taken into consideration one could very easily conclude (mistakenly) that this uptake curve is the result of Fickian diffusion.

It is clear from the above results that for slurry systems it is very difficult to determine the concentration dependence of the diffusion coefficient, or even the type of diffusion, from the usual continuous fluid uptake curve. If concentration dependent diffusional information is desired for a system, more effective, though less convenient, methods must be used, such as equilibrating the sample at various concentrations and making differential uptake measurements.

#### CONCLUSIONS

This study has shown that the fluid uptake behavior of particles in slurries can differ drastically from the uptake behavior of individual particles. Therefore, fluid uptake profiles for single particles must not be utilized to

interpret diffusional data on slurries without taking into consideration the particle size distribution. For a particle size distribution produced by the ball mill grinding of coal, it was found that the effect on the penetrant uptake was sufficiently severe that the initial uptake rate for Fickian diffusion was highly non-linear on a square-root-of-time plot. However, surprisingly, with this same particle size distribution, Case II diffusion gave a nearly linear graph on a square-root-of-time plot. So Case II diffusion might easily be mistaken for Fickian diffusion for this system. Thus faulty analysis of the diffusional system can readily occur.

This study also brought to light an unexpected similarity in the shape of fluid uptake curves for diffusion coefficients having drastically different concentration dependencies. For a coal slurry having a typical particle size distribution, the fluid uptake profiles for diffusion coefficients having extremes in concentration dependence are quite similar for slab-shaped particles, and for spherical particles the curve shapes are almost indistinguishable. These results show that the concentration dependence of diffusion coefficients can not be readily determined for slurry systems using continuous fluid uptake measurements. Other less convenient methods must be used, such as differential uptake measurements.

For coals and other micro-heterogeneous and micro-cracked materials, the problem of determining diffusional behavior is particularly complex because the external surface geometry may not satisfactorily indicate the rate of penetration of the fluid into the particles. In coal, for example, the uptake of fluid through holes, cracks, along maceral interfaces and along regions of mineral matter may contribute substantially to the diffusion process. In addition, the various macerals or microcomponents of the coal will have different diffusional characteristics. Even within the vitrinite classification different pieces of material may exhibit substantially different diffusion characteristics.

#### REFERENCE

1. Crank, J., "The Mathematics of Diffusion", Second Edition, Clarendon Press, Oxford (1975).
2. Walker, P. L. Jr., and Mahajan, O. P., in "Analytical Methods for Coal and Coal Products", Edited by C. Karr, Jr., Vol. I, Chapt. 5, Academic Press, NY (1978).
3. Larsen, J. W., Lee, D., Fuel, 62, 1351-1354 (1983).
4. Luckie, P. T., Annual Progress Report for Sept. '76-Sept. '77, ERDA Contract EX-76-C-01-2475, NTIS Report # FE-2475-13 (1977).
5. Brenner, D., "Thin Section Microscopic Studies of the Diffusion of Oxygen into Coal at Elevated Temperatures", Corporate Research Report CR.25BN.84 (1984).
6. Crank, J., "The Mathematics of Diffusion", Second Edition, Chp. 1, Clarendon Press, Oxford (1975).
7. Alfrey, A., Gurnee, E. F., and Lloyd, W. G., J. Polym. Sci., C12, 249 (1966).
8. Brenner, D., "The Macromolecular Nature of Bituminous Coal", Corporate Research Report CR.22BN.82 (1982).
9. Brenner, D., Nature, 306, No. 5945, 772 (1983).
10. Crank, J., and Nicolson, P., Proc. Camb. Phil. Soc. Math. Phys. Sci., 43, 50, (1947).
11. Crank, J., "The Mathematics of Diffusion", Second Edition, p. 180, Clarendon Press, Oxford (1975).

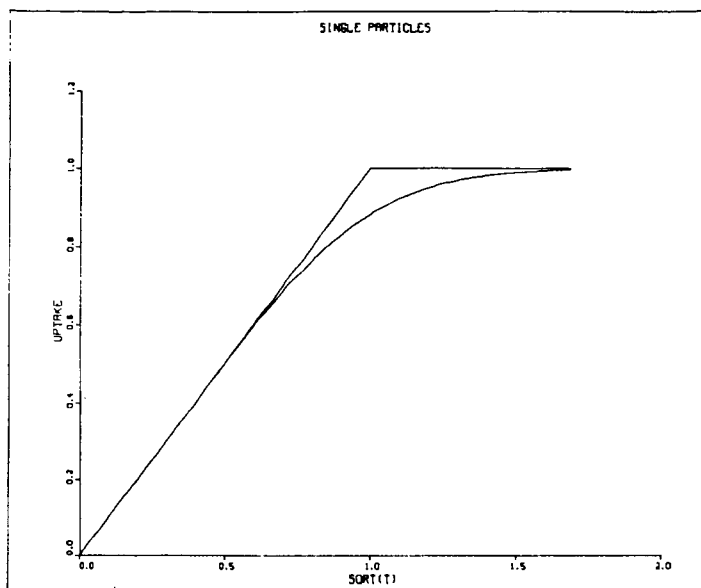


Figure 1. Solvent uptake for a single slab-shaped particle  
a) Lower curve is for constant diffusion coefficient (concentration independent)  
b) Upper curve is for extreme concentration dependent Fickian diffusion

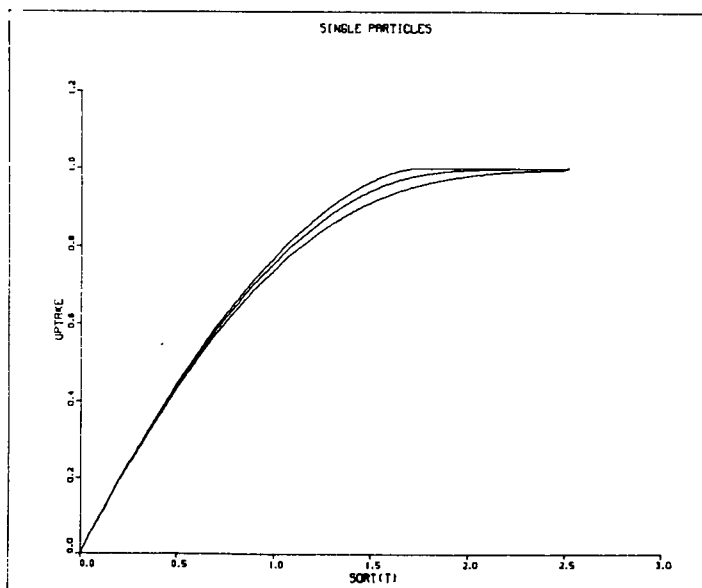


Figure 2. Solvent uptake for a single spherical particle  
a) Lower curve is for constant diffusion coefficient (concentration independent)  
b) Middle curve is for exponentially concentration dependent diffusion coefficient  
c) Upper curve is for extreme concentration dependent Fickian diffusion

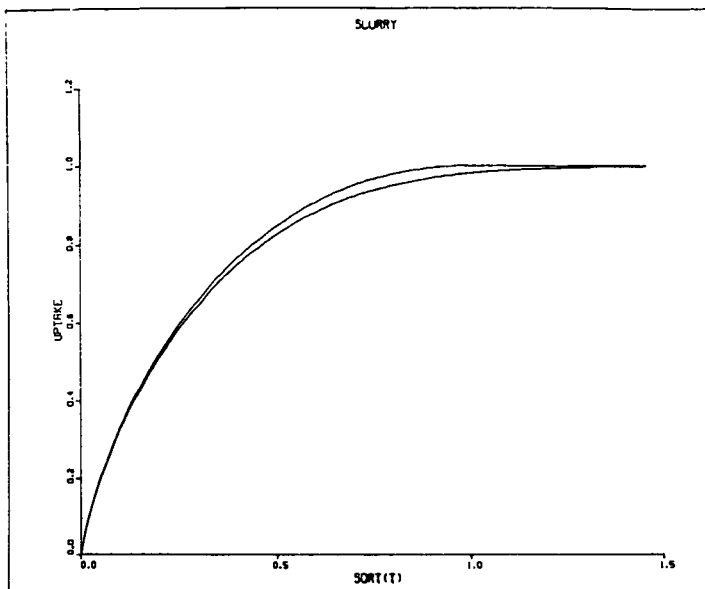


Figure 3. Solvent uptake for a slurry of slab-shaped particles

- a) Lower curve is for constant diffusion coefficient (concentration independent)
- b) Upper curve is for extreme concentration dependent Fickian diffusion

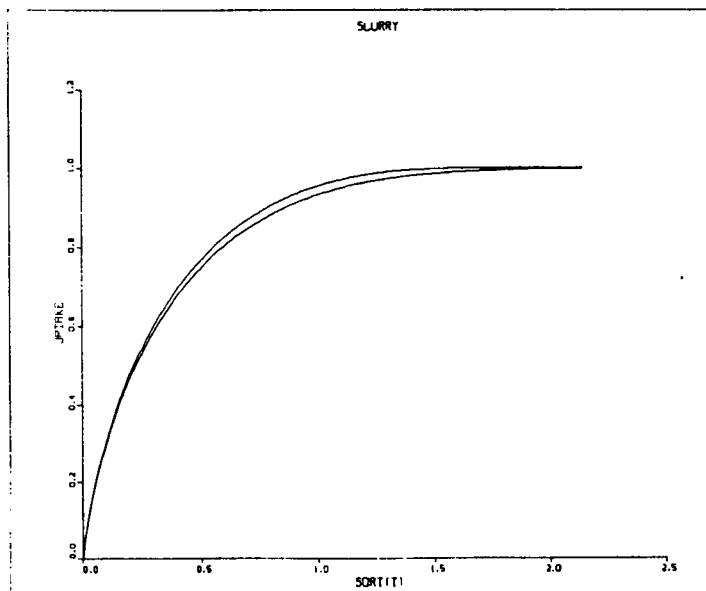


Figure 4. Solvent uptake for a slurry of spherical particles

- a) Lower curve is for constant diffusion coefficient (concentration independent)
- b) Upper curve is for extreme concentration dependent Fickian diffusion



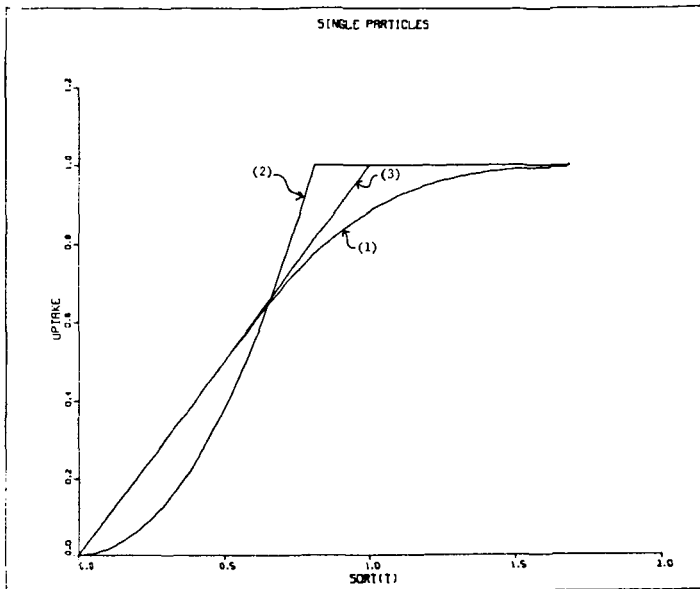


Figure 5. Solvent uptake for a single slab-shaped particle  
 a) Curve 1 is for constant diffusion coefficient (concentration independent)  
 b) Curve 2 is for extreme concentration dependent Fickian diffusion  
 c) Curve 3 is for Case II diffusion (constant velocity)

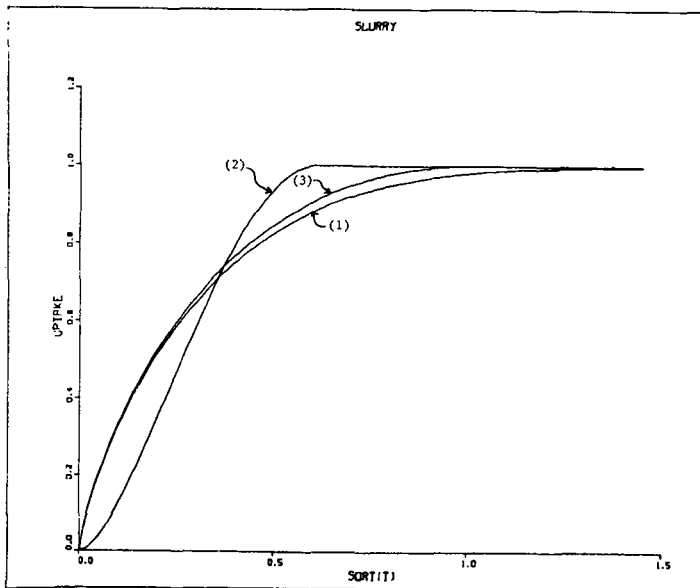


Figure 6. Solvent uptake for a slurry of slab-shaped particles  
 a) Curve 1 is for constant diffusion coefficient (concentration independent)  
 b) Curve 2 is for extreme concentration dependent Fickian diffusion  
 c) Curve 3 is for Case II diffusion (constant velocity)

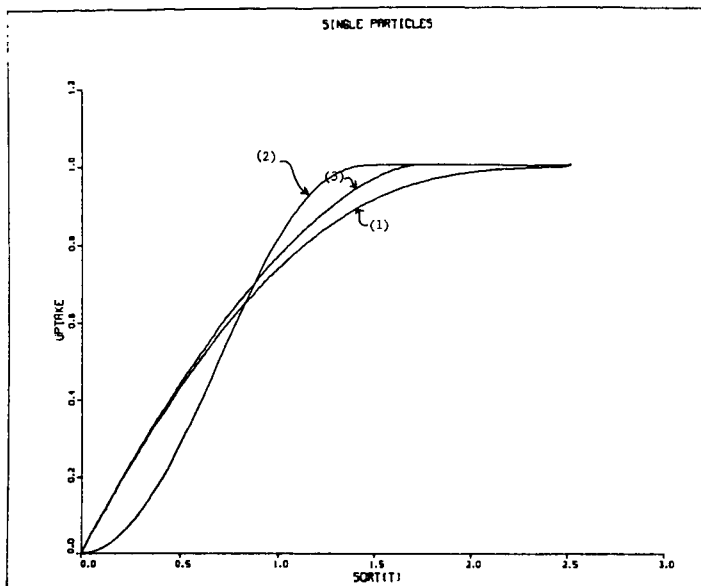


Figure 7. Solvent uptake for a single spherical particle  
 a) Curve 1 is for constant diffusion coefficient (concentration independent)  
 b) Curve 2 is for extreme concentration dependent Fickian diffusion  
 c) Curve 3 is for Case II diffusion (constant velocity)

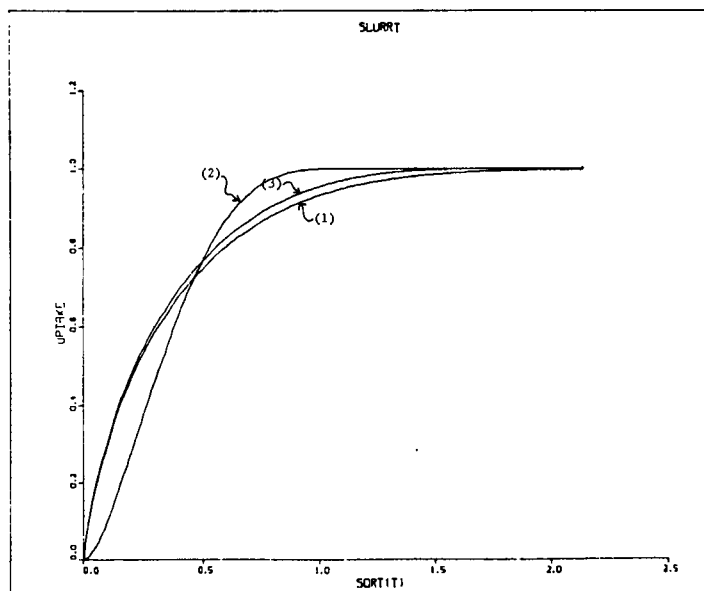


Figure 8. Solvent uptake for a slurry of spherical particles  
 a) Curve 1 is for constant diffusion coefficient (concentration independent)  
 b) Curve 2 is for extreme concentration dependent Fickian diffusion  
 c) Curve 3 is for Case II diffusion (constant velocity)

## "IN SITU" OBSERVATIONS OF LIQUID DIFFUSION IN THIN SECTIONS OF COAL

D. Brenner

Corporate Research Science Laboratories  
Exxon Research and Engineering Company  
Annandale, NJ 08801

### INTRODUCTION

The objectives of this study are to advance our understanding of how liquids penetrate through the microstructure of coals and to use diffusion to probe the macromolecular and microstructure of coals. Diffusion of liquids and of solids dissolved in liquids is of considerable importance in many areas of coal technology and science. Many coal liquefaction processes involve the penetration of a liquid into coal; in particular, this is the case for many slurry-based liquefaction processes. There are a number of coal beneficiation processes actively being investigated which rely on diffusion of reagents into the coal to modify its structure or to remove undesired mineral or organic components. Similarly, many chemical pretreatments of coals depend on diffusion for the reagents to reach the reactive sites in the coal. Mass transfer is crucial to many fundamental chemical investigations of coal structure which utilize wet chemical techniques since reagents must diffuse to reactive sites within the structure. From a fundamental viewpoint a better understanding of diffusion in coal will advance our overall comprehension of the underlying macromolecular structure and microstructure of coals.

The escape of reaction products, mobile coal molecules, or molecular fragments from the coal structure are other diffusional processes in coal which are of substantial technological importance. For example, they occur in most conversion processes. In liquefaction, liquids or gases produced within the coal or molecular fragments of the coal dissolved in the liquids must escape from within the coal particles. In gasification molecular fragments from the degraded coal structure must diffuse to the surface of the particle before they can evaporate into the surrounding gas.

In this study we focus on a reasonably well-defined system in order to better understand diffusion phenomenon. We investigate the diffusion of good liquid swelling agents into a high volatile bituminous coal. Since the diffusing swelling agents greatly enhance the mobility of the macromolecular chain segments within the coal, this system is particularly well suited for probing macromolecular aspects of the coal structure.

The diffusion of liquids in materials is commonly studied by fluid uptake and/or desorption as a function of time. For simple or well-behaved materials this approach is effective, but for coal which is highly heterogeneous varying markedly from sample to sample and from micro-region to micro-region within each sample, this approach can give only averaged and incomplete information. A technique utilized with polymers is to characterize diffusion by observing the movement of colored solvents, liquids colored with dyes, or index of refraction gradients in the material. These methods have not been successfully applied to coals because of the high opacity of coals and the difficulty in fabricating satisfactory samples.

In this study we report the first successful "in situ" microscopic observations of diffusion in coals. The techniques involved first producing uncontaminated thin section specimens of coals using methods developed in our laboratory. Then special procedures were developed for securing the specimen, shielding the top and bottom surfaces from the penetrant and exposing the edge of the thin section to the selected solvent. This technique enables one to follow the kinetics of the diffusion in detail under the microscope in transmitted light as the solvent penetrates the coal. In this manner the maceral composition, mineral matter, and other aspects of the microstructure are observed directly during the diffusion process, and the heterogeneity of the coal can be accounted for

explicitly. This is crucial to the understanding of the diffusion phenomenon in coals since for adequate evaluation it is necessary to be able to measure the progress of the solvent into each of the micro-components which are being penetrated within the coal.

## EXPERIMENTAL

The coal used in these studies was Illinois No. 6 from the Monterey No. 1 mine which is of high volatile C bituminous rank. Because coal is so highly absorbing in the visible region of the spectrum, transmitted light optical microscopy can only be done with very thin specimens. Unfortunately, coal is a fragile material in thin pieces and it readily breaks into small fragments. For this reason special techniques must be used to prepare the thin section specimens. To avoid fragmentation of the thin slivers of coal, the specimens are normally embedded in an adhesive cement such as an epoxy adhesive. However, the diffusional characteristics of such embedded specimens are affected by the adhesives, so they are not satisfactory for diffusion studies. Canada Balsam has been used by many investigators as a securing agent for the coal. It can be mostly removed, but it leaves behind residues which are undesirable contaminants in the coal and may affect diffusion in unpredictable ways. The sample preparation procedure used to prepare the samples for this study utilized an adhesive which is completely soluble. The adhesive is a paraffin-based embedding wax (1). It is soluble in hexane which has a minimal effect on the coal. This sample preparation procedure has been described previously (2) and will not be described further here. The samples were cut perpendicular to the bedding plane. The thin sections were about 15 micrometers thick and roughly 0.5 mm across.

All of the experiments described in this paper were at room temperature and atmospheric pressure. The diffusing liquid used in this study was reagent grade pyridine.

Once satisfactory thin section specimens have been prepared they cannot simply be immersed in the solvent. If the whole surface of the sample were exposed to the solvent, then penetration would occur from all sides and the specimen would be rapidly penetrated in its thin direction from solvent coming through the top and bottom. The kinetics of this process would be difficult to interpret and even more difficult to quantify. Rather, it is desirable to prevent the solvent from penetrating through the top or bottom of the thin section and to allow it to penetrate only from one edge. Unfortunately, because of the tiny size and delicate character of the specimens one can not simply dip one edge of the sample in the solvent.

Two different techniques for holding the thin section samples and exposing them to the penetrating liquid were developed. Each of the techniques has advantages and disadvantages depending on the particular type of information which most interests the investigator. In the "grease-immersion" technique the solvent is prevented from contacting most of the top and bottom surfaces of the thin section by coating most of these surfaces with a grease. The grease must itself be an adequate barrier to the solvent. Some of the materials which were found usable were fluorinated greases (3) and a low molecular weight uncrosslinked butyl rubber (4). A small area of the top and bottom surfaces is left uncoated to avoid getting grease on the edge. The thin section is then placed between two glass slides. A schematic diagram of the grease-immersion setup is shown in Figure 1. At the start of the experiment a drop of liquid solvent is placed in contact with the uncoated edge of the thin section. The liquid then penetrates through one edge and propagates into the thin section of coal parallel to the surface.

In the weighted coverglass method the thin section of coal is sandwiched between a 1 mm thick glass slide on the bottom and a No. 1-1/2 glass coverslip on top. Weights are put along the edges of the coverslip so that good contact between the coal and the glass surfaces is insured. While it might be thought that the solvent would very rapidly wick along the glass surfaces and thereby quickly penetrate the coal from the top and bottom surfaces, this did not tend to occur in practice. Apparently, where the solvent does penetrate in between the glass and the

top or bottom of the thin section, the coal swells. This swelling effectively plugs up the channels where the solvent was penetrating -- right where the plug was needed. Additionally, where the solvent penetrated along the surface of the coal, it transformed the surface coal material into a rubbery state. The rubbery surface-coal acted as a gasket preventing any appreciable further penetration by the solvent.

During a diffusion experiment the solvent can not be directly observed within the coal because it is transparent. Rather, the swelling caused by imbibition of the solvent renders the diffusion observable. When the solvent swells the coal it appears to be a lighter color. This lighter color occurs primarily because for the swollen coal there is less material per unit cross sectional area of the coal in the path of the light passing through the sample. There may also be an effect caused by the change in index of refraction of the pore space as it becomes filled with fluid, but this effect is far less than from swelling for the pyridine-Illinois No. 6 coal system.

An "in situ" diffusion experiment was started by bringing a drop of solvent into contact with the edge of the coal thin section which was properly set-up as described in the previous section. The time of liquid contact was recorded and the sample was observed on the microscope stage in transmitted light. Periodically photomicrographs were taken and the time was noted in order to record the kinetics of the process. The liquid was kept in contact with the edge of the coal throughout the experiment.

## RESULTS AND DISCUSSION

### Diffusion of Pyridine in relatively homogeneous vitrinite

A thin section sample of Illinois No. 6 coal consisting of relatively homogeneous vitrinite was used for a diffusion experiment. The sample was placed in the grease-immersion setup. Liquid pyridine was brought into contact with the exposed edge of the sample. The thin section was then observed in the microscope as the liquid penetrated into the edge of the sample and diffused into the coal parallel to the surface of the thin section. Figure 2 shows the sample after 50 minutes exposure to the pyridine. The circle of light on the sample is caused by the field diaphragm of the microscope which is partially closed to keep light from passing around the sides of the sample. Illuminator light which does not pass through the coal is very bright and the haze caused by it tends to obscure the more dimly illuminated structural features of the coal. In Figure 2 a very abrupt change in coloration at the diffusion front is evident. Just ahead of the diffusion front the coal is the dark red color of the unchanged coal whereas just behind the front the coal is a much lighter orange-yellow color. This sharp diffusion front having an abrupt change in penetrant concentration demonstrates that the diffusion of the liquid in the coal is highly concentration dependent. A strong concentration dependence is characteristic of many macromolecular materials, especially in cases where the imbibition of the liquid transforms the macromolecular substance from a glassy material to a rubbery or viscous state and/or where the solvent swells the sample. In the coal behind the diffusion front where the solvent has already penetrated to an appreciable concentration there is relatively little change in the color of the coal. Since the color of the coal is related to its degree of swelling or the concentration of imbibed solvent, it is seen that there is relatively little change in the concentration of the solvent in the coal behind the diffusion front.

There are several particular modes of diffusion which could cause the very abrupt change in solvent concentration at the diffusion front along with the small change in solvent concentration behind the front. For example, a system where some of the penetrant can react with the matrix and the reaction is faster than the diffusion, can exhibit a relatively sharp front. Also, a relatively sharp front will result from a Fickian diffusion coefficient which is small at low concentrations of penetrant, but which abruptly jumps up to a much larger value at some concentration.

We had demonstrated previously (5) that swelling of this coal with pyridine depresses the glass transition temperature of the coal below room temperature and transforms it into a rubbery state. For polymers, when a liquid plasticizes it to above its glass transition, the diffusion is sometimes of Case II type (6). Case II is the name given to diffusion which has the following characteristics (7). There is a very sharp diffusion front. The diffusion front propagates into the material at constant velocity. And, there is extremely small variation in the concentration of the penetrant in the region behind the diffusion front. We have shown that the diffusion of pyridine into vitrinite in Illinois No. 6 coal has the first and last of these characteristics. The velocity of movement of the diffusion front will be discussed later.

The diffusion front in Figure 2 has substantial curvature and is somewhat irregular. The curvature may be caused by the exterior geometry of the sample and/or the shape of the region where the liquid pyridine contacts the coal. The irregularity of the diffusion front is caused by the micro-heterogeneity of the vitrinite -- even though it appeared relatively homogeneous under the microscope.

Large regions of variable coloration are seen trailing behind the diffusion front in Figure 2. The pattern of the coloration suggests that it is caused by strains in these flexible regions of the sample behind the diffusion front which are restricting solvent uptake. Such strains might be caused by stresses resulting from the swelling, which is highly anisotropic in the vicinity of the diffusion front. Strains could also have been caused by deformation of the coal at some earlier stage in its evolution. Another possibility is that this coloration comes from regions having variable composition which results in a variable rate of swelling. However, the relationship between these regions of variable color and the position of the diffusion front makes it most likely that this behavior is a direct consequence of the diffusion and/or the resultant swelling.

The diffusion front is somewhat ragged, but it is not grossly irregular. There are bits of unswollen vitrinite just behind the front. There is a prominent "finger" of vitrinite which has not yet been swollen by the pyridine; however, there are some channels of swollen material in it which have been penetrated by the pyridine. This finger of vitrinite clearly must be appreciably different from the surrounding vitrinite.

Figure 3 shows the sample after 78 minutes exposure to the pyridine. The shape of the diffusion front has changed considerably. It is seen that the finger of Figure 2 has been completely penetrated by the pyridine and is now indistinguishable from the surrounding vitrinite. It is also seen that the small bits of unpenetrated vitrinite behind the front in Figure 2 have been penetrated and swollen. It was observed that when these small regions begin to change to a lighter color in one part they then tend to change relatively quickly to the lighter color overall. It appears as if there is some sort of barrier to the solvent surrounding these small regions, perhaps a membrane or coating. Then, once the barrier becomes penetrated by the solvent the whole inside is relatively rapidly penetrated. It is clear from these photographs that the "homogeneous-appearing" vitrinite is far from homogeneous, but rather there is considerable variation from region to region within it.

A potential difficulty with the grease-immersion technique used in this experiment is that transfer of solvent either into or out of the top or bottom surfaces of the thin section may occur via the grease. The greases utilized were selected to minimize this effect. In addition, during the "in situ" experiment the sample was carefully monitored for evidence of appreciable solvent transfer through the grease. For example, appreciable direct transfer of solvent from the liquid reservoir through the grease to the coal would be expected to produce thin solvent-swollen regions along the edges of the sample, or at least to perturb the solvent concentration at the junction of the diffusion front with the edge of the sample. No evidence of either of these effects was observed. However, an estimate of the magnitude of loss or gain of solvent through the grease would be desirable to reliably evaluate its effect on the kinetics of the diffusion process.

When the sample was observed through the optical microscope in transmitted light between crossed polarizers, a thin, orange-colored line stood out against the

darkened thin section. With time, this thin line moved further into the sample. When the polarizers were removed, it was seen that the thin orange line corresponded to the position of the diffusion front; that is, it occurred at the position where the color of the coal changed from the dark red color of the unswollen coal to the light orange color of the expanded coal. The thin orange-colored line which is observed between crossed polarizers at the position of the diffusion front is apparently caused by the orientation of the coal structure in this region. The expanding coal behind the diffusion front is constrained by the unswollen coal ahead of the diffusion front. This can be expected to stretch and align the macromolecular network in this region. Such partially oriented macromolecular chains cause a significant difference in the index of refraction parallel and perpendicular to the direction of orientation. This causes a rotation in the direction of polarization of light passing through the specimen. The result is that some light passes through the second of the crossed polarizers. A short distance behind the diffusion front there is enough flexibility that the macromolecular orientation is diminished and the orange line is no longer seen. The orientation of the structure in the region of the diffusion front and the relaxation of the orientation behind the front are further evidence for the macromolecular nature of the coal and the transition of the coal from a rigid to a rubbery material.

#### Diffusion of pyridine in coal having a heterogeneous striated structure

A thin section of Illinois No. 6 coal having a heterogeneous striated structure was used in a diffusion experiment. The sample was about 15 micrometers thick and, as in the other samples, its surface was perpendicular to the bedding plane. Figure 4 shows the sample after its edge has been in contact with liquid pyridine for 4 minutes. The dark gray material seen in the photomicrograph is the vitrinite or wood-derived component of the coal. In this sample it is seen to occur as strands which are approximately parallel to the bedding plane. The bedding plane is seen edge-on in the photograph. The lighter bits of material are the liptinite which is the more hydrocarbon-rich waxy component. This component is derived from non-woody parts of plants such as spores, pollen, and stem and leaf coatings.

A sharp diffusion front is seen in Figure 4. The front is similar to that seen in the homogeneous vitrinite sample of Figure 2. The front here, though, is more ragged because of the different macerals present in the sample. It is also seen that some of the vitrinite strands behind the diffusion front are far more darkly colored than the other vitrinite behind the front. Apparently these particular vitrinite macerals are more slowly penetrated by the pyridine. In time, though, these macerals are penetrated and swollen and become light-colored.

Figure 5 shows the sample after 52 minutes exposure to pyridine. Although the coal specimen in Figure 5 is quite heterogeneous, the diffusion front is not far from being straight. There are, however, a number of small fragments of vitrinite behind the front which appear to be very slightly, if at all, penetrated by the pyridine. These bits of vitrinite may have a coating or membrane surrounding them which retards penetration by the pyridine, or this material may have a less permeable structure which the pyridine penetrates more slowly. However, with time almost all of these darker fragments behind the diffusion front are swollen and become light-colored. It is also evident from comparing Figures 4 and 5 that there has been substantial swelling in the pyridine of the large liptinite maceral in the left center of the photomicrograph.

#### Diffusion rates parallel and perpendicular to the bedding plane

In order to compare the diffusion rates of the solvent parallel and perpendicular to the bedding plane of the coal all four edges of a thin section were simultaneously exposed to the pyridine. This sample had a striated structure. Its surface was perpendicular to the bedding plane; the bands of material ran parallel to the bedding plane and the direction perpendicular to the bands was perpendicular to the bedding plane. Figure 6 shows this thin section after 15 minutes in contact

with the liquid pyridine. It is seen that the penetration rates of the pyridine in the directions parallel and perpendicular to the bedding plane are comparable.

Some investigators have reported that the diffusion rates of various fluids in coals is much faster parallel to the bedding plane than perpendicular (8,9). An important difference between these prior investigations and our current studies is that we are observing primarily intra-maceral diffusion whereas earlier work was more effected by larger scale diffusion. We showed earlier (9) that major routes for rapid penetration of the coal structure included intermaceral interfaces, cracks, holes, and regions containing mineral matter accumulations. These types of irregular regions within the coal tend to extend along the bedding plane. Therefore, on a large scale faster diffusion can be expected parallel to the bedding plane. Our studies however, are more concerned with the finer structures of the coal. We have focused on the diffusional behavior within individual vitrinite macerals within the coal. Within the individual macerals or for groups of macerals which are in intimate contact with each other and which do not contain substantial irregular regions, the diffusion rates parallel and perpendicular to the bedding plane are comparable.

#### Self-sealing in coal undergoing solvent-swelling

A thin section sample of vitrinite was exposed to pyridine using the weighted coverglass method. In Figure 7, the sample is shown after 60 seconds contact with the pyridine. Note the lightened areas indicating solvent penetration and solvent swelling along the edges of the large crack in the sample as well as along the edges of the sample. The sample is shown in Figure 8 after 100 seconds exposure to the pyridine. Note that the large crack has fully closed. Also, whereas the diffusion front has moved substantially in from the outer edges of the sample there has been relatively little movement of the diffusion front along the edges of what was the large crack. Figure 9 shows the sample after a total of 210 seconds exposure to the pyridine. There has been considerable additional movement of the diffusion front into the coal from the edges. However, along what was the large crack there has been little change in the coal.

These observations illustrate one important mechanism which can occur during the diffusion of good swelling solvents into coals. The swelling of the coal may seal-off cracks and holes in the coal and thereby stop or diminish penetration of the solvent through these routes. Although such routes may constitute a very small volume of the coal, if they were not sealed by the swelling they can be major routes for uptake of the solvent. For example, our prior work on diffusion of oxygen into coals (9) has shown that the cracks and holes provide paths for rapid penetration of oxygen into the interior of the coal.

The self-sealing effect may also have important consequences on the sub-microscopic scale. Pores within the coal, or inter-maceral interfaces in the coal which have previously been shown can be routes for rapid penetration by fluids (9) may be sealed by swelling if the solvent starts to penetrate them. On the other hand, porosity within mineral matter accumulations is less likely to be plugged by swelling (unless there is a substantial concentration of swellable organic matter within the region of mineral matter. Note, however, that the sealing mechanism is only expected to be operable in localized regions which swell in advance of surrounding materials. If all of a region swells isotropically, then cracks and holes in the region will also swell and sealing will not occur. It should be kept in mind, however, that the converse of self-sealing frequently occurs; that is, stresses produced during solvent swelling often produce cracks in coal particles (10).

#### Kinetics of Diffusion and Re-diffusion

The movement of diffusion fronts as they penetrated into thin section specimens was quantified for several samples. For each sample the rate of propagation of the diffusion front into the sample was quantified. The results were somewhat variable, probably because of the heterogeneous nature of the coal. For



all samples measured, though, there was a pronounced slowing down of the velocity of the diffusion front with increasing time, as the front penetrated deeper into the sample. This would suggest that the diffusion is not Case II. However, because the amount of solvent penetrating through the grease, or between the glass slide and the coal into the top and bottom surfaces of the coal has not been accurately quantified (though qualitative checks were made -- see earlier in this section), it would be desirable to corroborate these results either through an accurate evaluation of this contribution to solvent uptake or by using alternate techniques.

After the diffusion front had propagated well into the thin section, the pyridine was removed and the sample was allowed to dry at room temperature in nitrogen gas for several days. Then the same diffusion experiment as before was repeated. Figure 10 shows graphically the results for both the original diffusion and the second exposure after drying. It is evident that the movement of the diffusion front is much more rapid for the second run, after the sample has previously been swollen by the pyridine and dried. This faster diffusion in the second run had been observed in our previous work where thin sections were fully immersed in liquid pyridine and penetration occurred primarily through the top and bottom surfaces (11).

There are several possible contributions to the more rapid penetration of the pyridine the second time. When the sample is dried after the initial swelling, some of the pyridine remains in the coal (12). So, less pyridine diffuses into the coal the second time. In addition, the residual pyridine probably weakens some of the inter-molecular interactions so that the new pyridine diffusing in encounters a looser structure and can therefore swell the coal more readily. Another possibility is that the initial swelling and drying causes microcracks in the structure so that subsequent diffusion can utilize these new routes. However, in the regions where the diffusion rate was measured, no diffusion via microcracks was observable in the optical microscope. There may also have been some effect on the diffusion rate from some bitumen being extracted from the coal during the first diffusion run.

## CONCLUSIONS

Diffusion into coal has been observed "in situ" at the microscopic level for the first time. This technique which utilizes uncontaminated thin sections of coal enabled the study of true intra-maceral diffusion as distinguished from the usual concurrent diffusion in a variety of maceral structures, or diffusion via cracks, mineral matter, macropores, or maceral interfaces. For diffusion of a good solvent into a high volatile bituminous coal, a sharply defined front occurred, and the diffusive flow was highly concentration dependent. The movement of the front slowed with depth of penetration into the coal. When the sample was placed between crossed polars, a thin light line was seen along the diffusion front against the dark background. This indicates that orientation of the macromolecular network occurs as a result of the stresses in the vicinity of the front. For intra-maceral diffusion in vitrinite there was no obvious difference between the rates of movement of the front parallel versus perpendicular to the bedding plane. When the liquid was desorbed and then reabsorbed, the diffusion rate was considerably faster the second time. Liquid penetration into cracks in vitrinite was initially rapid, but the swelling which resulted often sealed the cracks, greatly reducing further penetration.

## ACKNOWLEDGEMENTS

The encouragement and support of M. Siskin and M. L. Gorbaty in this investigation is gratefully acknowledged. The technical assistance of M. S. Beam in the preparation of the thin section samples is greatly appreciated.

## REFERENCES

1. Paraplast is a paraffin-based embedding wax having a melting point of 57°C. It is manufactured by the Lancer Co., St. Louis, MO, USA.
2. Brenner, D. in "Coal Structure" (Ed. R. A. Meyers), Academic Press, New York, 1982, pp 254-263.
3. Some usable fluorinated greases are Krytox, manufactured by DuPont and Fomblin manufactured by Montedison.
4. LM Butyl, manufactured by Exxon Chemical Company.
5. Brenner, D., Nature, 306, No. 5945, 772 (1983).
6. Crank, J., "The Mathematics of Diffusion", Second Edition, Chapter 11, Clarendon Press. Oxford (1975).
7. Alfrey A., Gurnee, E. F., and Lloyd, W. G., J. Polym. Sci., C12, 249 (1966).
8. Attar, A., and Warren, D., "Division of Fuel Chemistry Preprints", 26, No. 3, pp. 172-177, Am. Chem. Soc. National Meeting, New York, New York (1981).
9. Brenner, D., "Division of Fuel Chemistry Preprints", 26, No.1, pp. 42-49, Am. Chem. Soc. National Meeting, Atlanta, Georgia (1981).
10. Brenner, D., Fuel, 62, 1347, (1983).
11. Brenner, D., Fuel, 63 pp 1324-1328, (1984).
12. Collins, C. J., Hagaman, E. W., Jones, R. M. and Raaen, V. F. Fuel, 60, 359 (1981).

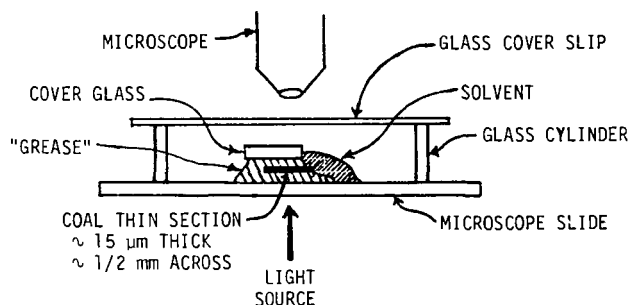


Figure 1. Grease-immersion setup for "in situ" microscopic observations of solvent diffusion in coals.



Figure 2. Diffusion of pyridine in relatively homogeneous vitrinite, after 50 minutes contact of edge with liquid pyridine.



Figure 3. Diffusion of pyridine in relatively homogeneous vitrinite, after 78 minutes contact of edge with liquid pyridine.



Figure 4. Diffusion of pyridine in a heterogeneous striated coal structure, after 4 minutes contact of edge with liquid pyridine.



Figure 5. Diffusion of pyridine in a heterogeneous striated coal structure, after 52 minutes contact of edge with liquid pyridine.



Figure 6. Comparison of diffusion rates parallel versus perpendicular to the bedding plane.

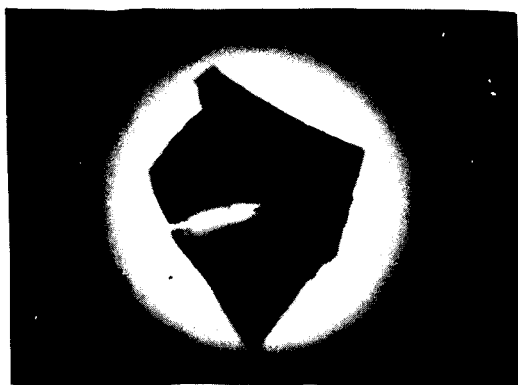


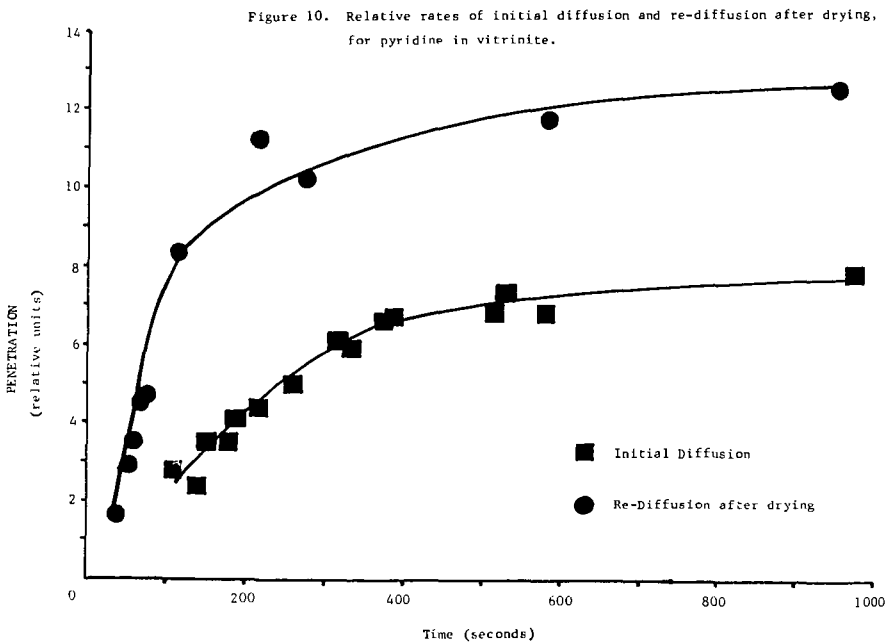
Figure 7. Thin section with crack, after 60 seconds exposure to pyridine.



Figure 8. Crack in thin section sealed by swelling, after 100 seconds exposure to pyridine.



Figure 9. Thin section with sealed crack, after 210 seconds exposure to pyridine.



## SOLVENT SWELLING OF COAL 1. DEVELOPMENT OF AN IMPROVED METHOD FOR MEASURING SWELLING PHENOMENA

Tetsuo Aida and Thomas G. Squires

Ames Laboratory\*  
Iowa State University  
Ames, Iowa 50010

### INTRODUCTION

Although the polymeric nature of coal was established over a quarter of a century ago (1), many phenomena which derive from its cross-linked, macromolecular structure are still not well understood. This includes one of the most important aspects of coal chemistry, the accessibility of solvents and/or chemical reagents to sites buried within the solid coal matrix (2). Thus, the rate and extent of chemical conversion and/or solubilization of these interior sites are governed by penetration of the macromolecular structure by an appropriate chemical agent. Generally, penetration of cross-linked, macromolecular solids by organic chemicals has been investigated using swelling techniques.

The swelling induced by contacting coal with organic solvents has been investigated intensively in recent years; and several convenient methods using both liquids and saturated vapors have been developed for measuring coal swelling properties (3). The liquid phase swelling behavior is particularly interesting because it is a reasonable measure of a solvent's ability to penetrate the coal matrix. Previously, investigators of this phenomenon have utilized some variation of the test tube technique developed by Dryden (4). In this method, the initial height of a dry coal bed,  $h_i$ , is compared to the final swollen height,  $h_f$ , after equilibration with solvent. These values are used to compute the equilibrium swelling ratio,  $Q = h_f/h_i$ , for each solvent.

However, the accuracy of this method is not satisfactory, particularly at lower ( $Q < 1.3$ ) and higher ( $Q > 3.0$ ) swelling ratios; and it is also quite difficult to investigate dynamic swelling behavior. Moreover, the  $Q$ -value reflects not only interactions between solvent and coal, but is also grossly affected by complicated elastic restoring forces in the coal network due to covalent bond cross-linking, hydrogen bonding, or  $\pi$ - $\pi$  interactions between condensed aromatics. On the other hand, initial swelling rates may isolate interactions between solvent and coal by minimizing the involvement of such complicated restoring forces.

On the basis of these considerations, we have developed a new method for the dynamic measurement of liquid phase solvent swelling phenomena which is 100 times more accurate than conventional methods. We have used this technique to determine  $Q$ -values and initial swelling rates for Illinois No. 6 Coal with a variety of solvents. Here we present our initial experimental results and compare these findings with those obtained using conventional methods.

---

\* Operated for the U.S. Department of Energy by Iowa State University under Contract No. W-7405-Eng-82.

## EXPERIMENTAL

### Materials

Illinois No. 6 Coal from the Ames Laboratory Coal Library was used in these studies. This coal has the following ultimate analysis (dmmf basis): 78.82% C; 5.50% H; 1.59% N; 2.29% S<sub>org</sub>; and 10.05% ash. Prior to use, this coal was ground, sized, and dried at 110°C overnight under vacuum. Except for commercial "Gold Label Grade" reagents (Aldrich Co.) which were used without further purification, solvents were distilled by ordinary procedures before use.

### Apparatus

As shown in Figure 1, this apparatus is similar in principle to an osmotic pressure measurement device, except that coal and solvent are separated by 10  $\mu$  stainless steel filter. In each experiment, the movement of the piston as a function of time was recorded; and the initial swelling rate ( $V_i$ ) was determined graphically as shown in Figure 1. The Q-value was calculated by dividing the final volume,  $S_0 + \Delta S$ , by the initial volume,  $S_0$ .

### General Procedure

In a typical experiment, 500 mg. of Illinois No. 6 Coal was placed in the cylinder bottom and covered by the piston. The pressure on the piston was adjusted to 5.0 g/cm<sup>2</sup> and was maintained at this level throughout the experiment. After positioning the piston, the entire system was evacuated to 0.20 - 0.15 mm Hg for 10 minutes. The valve of the solvent container was then opened allowing the solvent to contact the coal; and the movement of the piston was recorded as a function of time.

## RESULTS AND DISCUSSION

### Comparison of New Method and Conventional Method

Conventional swelling measurements were carried out using a 10 mm x 75 mm test tube, 2.0 g of Illinois No. 6 Coal, and 8.0 ml. of THF. The height of coal bed was read at five minute intervals after shaking the mixture vigorously each time. As shown in Figure 2, there is an interesting contrast in swelling behavior as measured by the two methods. In the case of the conventional method, the rate is retarded in the early stages of swelling, possibly because many pores are filled with air and the solvent cannot achieve intimate contact with the coal surface during this initial stage.

For the more interactive solvents, a higher Q-value was observed using the new method. This is probably because, in contrast to the conventional method, there is no mechanical agitation of the coal bed; and the integrity of the coal bed is thus maintained throughout the swelling measurement. In support of this hypothesis, the new apparatus was found to be quite sensitive to mechanical shock which usually resulted in an instant drop in the reading.



### Sensitivity of New Method

In a 500 mg. experiment, our new apparatus can detect a volume change of  $10^{-4}$  ml, that is the Q-value can be determined to  $\pm 0.0001$ . However, for practical reasons, we prefer to report the data to  $\pm 0.01$  Q-value units. Typical Q-values measured by this method are included in Table I along with data obtained by conventional measurements.

Table I. Comparison of Methods for Measuring Q-values<sup>a</sup>

SOLVENT	Benzene	Toluene	p-Xylene	Methanol	THF	0.5N <sup>b</sup> Bu <sub>4</sub> NOH
Q <sub>N</sub> <sup>c</sup>	1.04	1.06	1.06	1.24	2.20	4.15
Q <sub>C</sub> <sup>d</sup>	~1.3	~1.3	~1.3	1.4	1.8	--

a. Illinois No.6 Coal measured at 21.0°C

b. Solution in pyridine/methanol (1:1 vol.)

c. Present method

d. Conventional method

Our new method exhibits some obvious advantages, both at lower and higher swelling conditions, which will allow us to examine subtle differences in swelling behavior. An interesting contrast in the two methods is found in the relative Q-values for methanol and hydrocarbons. The reason for the difference is not clear at the present time, but may involve non-swelling volume increase processes like particle-particle repulsions. In the new method such forces are apparently overcome by the pressure of the piston. At the other extreme, Q = 4.15 for the tetrabutyl ammonium hydroxide solution is the highest swelling ratio which we have ever measured for Illinois No. 6 Coal.

### Determination of Initial Swelling Rate

In order to evaluate the capability of this method for investigating kinetic phenomena, several experiments were conducted. The effect of particle size on coal swelling rates was first examined. As expected, swelling rates are very sensitive to particle size. As shown in Figure 3, 200 x 400 mesh Illinois No. 6 Coal swells in THF at approximately 10 times the rate of 25 x 60 mesh coal. The temperature dependence of the THF-coal interaction in the range of 20 to 40°C was also examined. Interestingly, the Q-value was not affected by temperature, while the initial swelling rate increased by 15% for each 10°C increase (see Figure 4).

Although the actual penetration of the solvent and/or chemical reagent will not always be reflected by the Q-value or initial swelling rate, we believe that they provide a quite useful basis for designing chemical conversions or extractions of coal. One such basis for evaluating solvents is presented in Table II. Here, the swelling rates of common solvents, including some hydrogen donor solvents, are compared using a new parameter,  $\tau_{10}$ , which is defined as the time which would be necessary to swell the initial volume by 10%. This value is calculated on the basis of the initial swelling rate.

Table II. Comparison of Swelling Rates Using  $\tau_{10}^a$ 

Solvent	$\tau_{10}$	Solvent	$\tau_{10}$
n-Propylamine	10 sec.	Benzene	1.7 hrs.
Pyridine	48 sec.	Quinoline	5.0 hrs.
DMSO <sup>b</sup>	1.8 min.	Indoline	16.6 hrs.
THF <sup>c</sup>	1.6 min.	THQ <sup>d</sup>	2.0 mos.
Acetone	2.7 min.	Tetralin	>1.0 year
Methanol	3.1 min.		
Dichloromethane	4.7 min.		

a. Illinois No.6 Coal, 60 x 100 mesh, measured at 21°C.

b. Dimethylsulfoxide

c. Tetrahydrofuran

d. 1,2,3,4-Tetrahydroquinoline

#### Relation Between Initial Swelling Rate ( $V_i$ ) and Q-Value

Prior to undertaking these experiments, we expected a direct relationship between Q-values and  $V_i$ 's because we understood that both are a measure of the relative affinity of solvent for coal. The results obtained are presented in Table III.

Table III. Comparison of Q-Value and  $V_i^a$ 

SOLVENT	Q-Value	$V_i \times 10^2$
Methanol	1.24	3.2
CH <sub>2</sub> Cl <sub>2</sub>	1.23	2.1
Acetone	1.50	3.7
THF	2.20	6.2
Quinoline	2.35	0.03
n-Propylamine	2.45	58.6
NH <sub>2</sub> CH <sub>2</sub> CH <sub>2</sub> NH <sub>2</sub>	2.60	46.4
DMSO	2.80	4.8
Pyridine	2.90	12.5

a. Illinois No.6 Coal, 60 x 100 mesh, measured at 21°C.

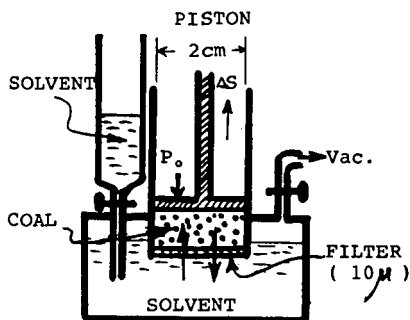
We are puzzled by the lack of correlation between  $V_i$  and Q-value. However, two possible explanations come to mind. Initial swelling rates could be more sensitive than Q-values to solvent viscosities and steric requirements. A more detailed study of these factors, especially steric requirements for solvent swelling of coal, will be presented in the next paper.

#### ACKNOWLEDGEMENTS

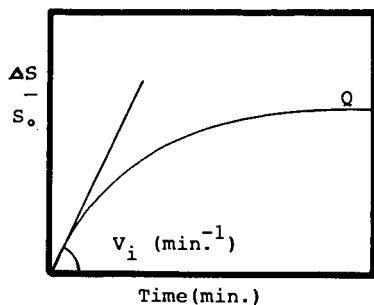
We wish to thank Professors R. S. Hansen and D. K. Finnemore for their useful discussion and encouragement. We are grateful for support from The State of Iowa, and from the U. S. Department of Energy through the Ames Laboratory under Contract No. W-7405-ENG-82. The opinions, findings, and conclusion expressed herein are those of the authors, and do not necessarily reflect the views of DOE or the State of Iowa.

#### REFERENCES

1. van Krevelen, D. W., "Coal" Elsevier Publishing Co., Amsterdam, 1961, pp. 433-452.
2. Larsen, J. W.; Green, T. K.; Choudhury, P.; Kuemmerle, E. W. Adv. Chem. Series 1981, 192, 277.
3. Key references are cited in a recent paper by Green, T. K.; Larsen, J. W. Fuel 1984, 63, 1539.
4. Dryden, I. G. C. Fuel 1951, 30, 145.



$P_0$ : Initial Pressure  
 $\Delta S$ : Increased Volume



$S_0$ : Initial volume of coal  
 $V_i$ : Initial swelling rate

Figure 1. Method for Measuring Liquid Phase Solvent Swelling of Coal.

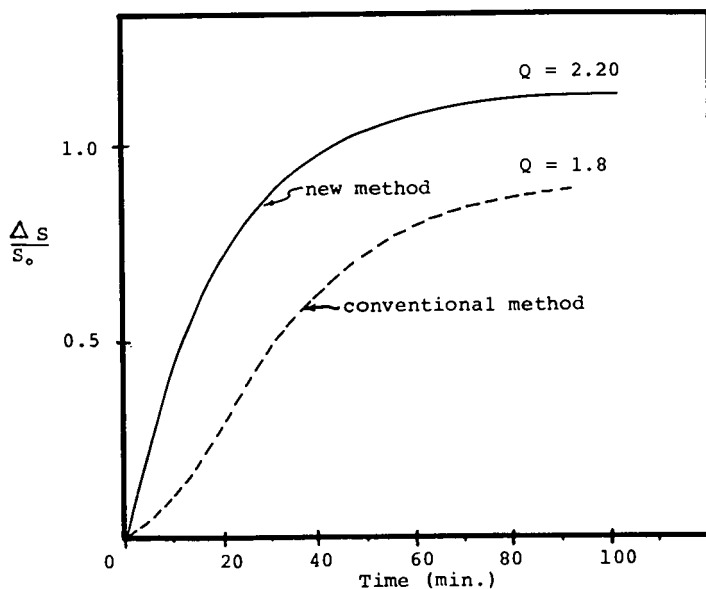


Figure 2. Comparison of THF Swelling Patterns for Illinois No. 6 Coal at 21.0°C.

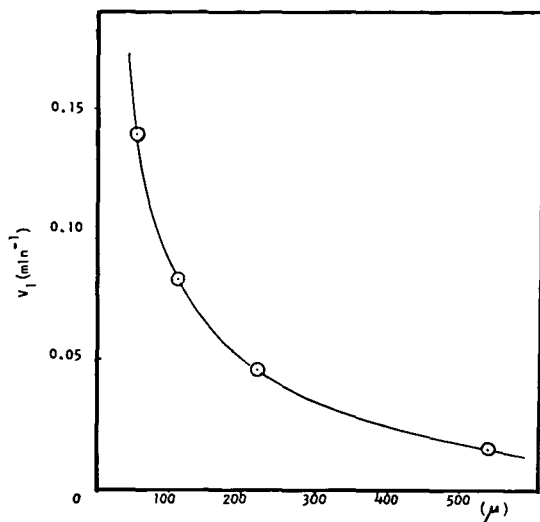


Figure 3. Effect of Particle Size on Initial THF Swelling Rate of Illinois No. 6 Coal (21.0°C).

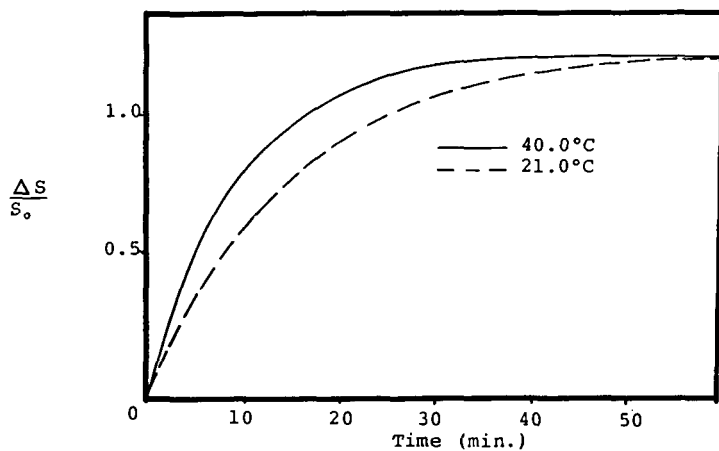


Figure 4. Temperature Effect on THF Swelling Behavior of 60 x 100 mesh Illinois No. 6 Coal

## SOLVENT SWELLING OF COAL 2. INVESTIGATION OF STERIC REQUIREMENTS

Tetsuo Aida and Thomas G. Squires

Ames Laboratory\*  
Iowa State University  
Ames, Iowa 50011

### INTRODUCTION

Some time ago it was established that, as a solid, microporous material, coal behaves as a molecular sieve (1), i.e. it discriminates among molecules diffusing into the pore system on the basis of size, shape, and functionality. It seems to us that the process by which solvent molecules penetrate the solid coal matrix should be similarly selective. The investigation of such phenomena is important, not only from the perspective of understanding the accessibility of chemical agents to sites within the coal matrix (2), but for the rational design of chemical conversion processes.

Recently, we developed a new method for accurately measuring both the dynamic and equilibrium solvent swelling behavior of coal (3). Here, we report the initial application of these techniques to the investigation of accessibility phenomena. From this study, which examines the steric interactions between solvent and coal, we expect to obtain a better understanding of the mechanism by which chemical agents penetrate the coal matrix.

### EXPERIMENTAL

The swelling measurements were carried out as described in the previous paper (3); and the initial swelling rates were determined graphically. All coals used in these studies were from the Ames Laboratory Coal Library. Prior to use, the coals were ground, sized to 100 x 200 mesh, and dried at 110°C overnight under vacuum. Except for commercial "Gold Label Grade" reagents (Aldrich Co.) which were used without further purification, solvents were distilled by ordinary procedures before use.

### RESULTS AND DISCUSSION


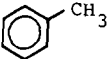
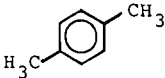
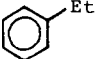
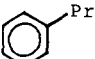
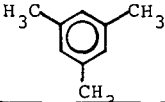
#### Swelling of Illinois No. 6 Coal in Hydrocarbon Solvents

The swelling data obtained with hydrocarbon solvents are shown in Table I. There apparently is no simple relationship between the initial swelling rate,  $V_i$ , and the equilibrium swelling ratio,  $Q$ , for this series of solvents. Neither is there an obvious relationship between viscosity and swelling behavior. However, with the exception

---

\*Operated for the U.S. Department of Energy by Iowa State University under Contract No. W-7405-Eng-82.

Table I. Swelling Behavior of Illinois No. 6 Coal in Hydrocarbons<sup>a</sup>

Hydrocarbon	Q	$V_{Ret}^b$	$\eta_{20}$
	1.04	1.00 <sup>c</sup>	0.65
	1.06	0.40	0.59
	1.06	1.18	0.65
	--	4.00	0.69
	--	16.7	--
	--	30	--

a. 100-200 mesh, measured at 21.0°C

b. Rate Retardation Factor:  $V_i(\text{benzene})/V_i(\text{hydrocarbon})$ c.  $V_i = 2.73 \times 10^{-4} \text{ min.}^{-1}$ 

of toluene which initially swells about 2.5 times as fast as benzene, the sharp decrease in  $V_i$  from benzene to mesitylene suggests that there is a steric component to the rate constant for solvent penetration of the coal matrix.

#### Solvent Swelling Behavior of Illinois No. 6 Coal in Alcohols

The initial swelling rates ( $V_i$ ) and equilibrium swelling ratios (Q) were measured for  $C_1$  through  $C_4$  alcohols, and the results are summarized in Table II.<sup>1</sup> Except for methanol, Q-values for the unbranched primary alcohols were almost identical, while, with increasing chain length, a twelve-fold decrease in initial swelling rates was noted for this series. Although the latter behavior is consistent with that predicted on the basis of steric considerations, it is also consistent with the trend in solvent viscosities.

However, comparison of the initial swelling rates of *n*-propyl and isopropyl alcohol reveals a rate retardation factor ( $V_{Ret}$ ) of 4 for the branched isomer despite almost identical viscosities. Similar behavior is exhibited by the butyl alcohol series: compared to *n*-butyl alcohol, the initial swelling rates of isobutyl and *sec*-butyl alcohol are retarded by factors of 9 and 40, respectively. These large effects cannot be rationalized on the basis of viscosities.

Table II. Swelling Behavior of Illinois No. 6 Coal in Alcohols<sup>a</sup>

Alcohol	Q	V <sub>Ret</sub> <sup>b</sup>	$\eta_{20}$
MeOH	1.23	1.00 <sup>c</sup>	0.60
EtOH	1.34	1.92	1.2
n-PrOH	1.36	3.96	2.3
i-PrOH	--	14.18	2.3
n-BuOH	1.34	12.17	2.9
i-BuOH	--	103.4	4.2
s-BuOH	--	499.0	3.9

a. 100-200 mesh, measured at 20.0°C

b. Rate Retardation Factor:  $V_i(\text{methanol})/V_i(\text{alcohol})$ c.  $V_i = 3.18 \times 10^{-2} \text{ min.}^{-1}$ Solvent Swelling Behavior of Illinois No. 6 Coal in Amines

The swelling behavior of Illinois No. 6 Coal in various aliphatic amines was also examined. Once again, we can ascertain no significant differences among the Q-values for the entire series of amines. On the other hand, initial swelling rates for this series vary over a range of  $10^6$  and provide an unambiguous basis for establishing the importance of steric requirements. In fact, the evidence is so compelling that the results are simply reported, with minimum discussion, in Tables III-VI.

Table III. Swelling Behavior in Primary Amines.<sup>a</sup> Effect of Chain Length.

Structure	Q	V <sub>Ret</sub> <sup>b</sup>
CH <sub>3</sub> CH <sub>2</sub> CH <sub>2</sub> NH <sub>2</sub>	2.45	1.00 <sup>c</sup>
CH <sub>3</sub> (CH <sub>2</sub> ) <sub>2</sub> CH <sub>2</sub> NH <sub>2</sub>	2.64	2.05
CH <sub>3</sub> (CH <sub>2</sub> ) <sub>4</sub> CH <sub>2</sub> NH <sub>2</sub>	2.19	9.31

a. Illinois No. 6 Coal (100 x 200 mesh), measured at 21.0°C

b. Rate Retardation Factor:  $V_i(\text{n-Propylamine})/V_i(\text{amine})$ c.  $V_i = 5.86 \times 10^{-1} \text{ min.}^{-1}$ Table IV. Swelling Behavior in Primary Butyl Amines.<sup>a</sup> Effect of Chain Branching

Structure	Q	V <sub>Ret</sub> <sup>b</sup>
CH <sub>3</sub> (CH <sub>2</sub> ) <sub>2</sub> CH <sub>2</sub> NH <sub>2</sub>	2.64	1.00
(CH <sub>3</sub> ) <sub>2</sub> CHCH <sub>2</sub> NH <sub>2</sub>	2.46	4.38
(CH <sub>3</sub> ) <sub>3</sub> CNH <sub>2</sub>	1.95	732

a. Illinois No. 6 Coal (100 x 200 mesh), measured at 21.0°C

b. Rate Retardation Factor:  $V_i(\text{n-Butylamine})/V_i(\text{amine})$



Table V. Swelling Behavior in C<sub>6</sub>H<sub>13</sub>N Amines.<sup>a</sup> Comparison of Primary, Secondary and Tertiary Isomers

Structure	Q	V <sub>Ret</sub> <sup>b</sup>
CH <sub>3</sub> (CH <sub>2</sub> ) <sub>4</sub> CH <sub>2</sub> NH <sub>2</sub>	2.19	1.00
(CH <sub>3</sub> CH <sub>2</sub> CH <sub>2</sub> ) <sub>2</sub> NH	2.05	15.4
(CH <sub>3</sub> CH <sub>2</sub> ) <sub>3</sub> N	--	1.5 x 10 <sup>5</sup>

a. Illinois No. 6 Coal (100 x 200 mesh), measured at 21.0°C

b. Rate Retardation Factor: V<sub>i</sub>(n-Hexylamine)/V<sub>i</sub>(amine)

Table VI. Swelling Behavior in Secondary C<sub>6</sub>H<sub>13</sub>N Amines.<sup>a</sup> Effect of Chain Branching.

Structure	Q	V <sub>Ret</sub> <sup>b</sup>
(CH <sub>3</sub> CH <sub>2</sub> CH <sub>2</sub> ) <sub>2</sub> NH	2.05	1.00
[(CH <sub>3</sub> ) <sub>2</sub> CH] <sub>2</sub> NH	--	1830

a. Illinois No. 6 Coal (100 x 200 mesh), measured at 21.0°C

b. Rate Retardation Factor: V<sub>i</sub>(Di-n-Propylamine)/V<sub>i</sub>(amine)

The nature and divergency of these comparisons leave little doubt that steric factors play an important role in coal accessibility phenomena and can provide answers to a number of troublesome questions. For example, the lack of coal solubility in solvents such as triethyl amine and hexamethyl phosphoramide (HMPA), which (because of their "solubility parameters") should be good solvents (4), is clearly consistent with steric inhibition of coal matrix penetration by these hindered solvents.

#### Effect of Coal Rank on Solvent Swelling Behavior

In a final series of experiments, the rank dependent solvent swelling behavior of coals in three isomers of primary butyl amine was investigated. While we found small differences in the equilibrium swelling ratios for various coal/amine systems, we can detect no systematic relationship between rank and Q-values; and we have focused our attention on initial swelling rates. In order to correlate this data, we have defined two swelling parameters,

$$\theta_s = V_n/V_s \quad \text{and} \quad \theta_t = V_n/V_t$$

where  $\theta_s$  and  $\theta_t$  represent the steric sensitivity of coal toward secondary and tertiary branching in the butylamine isomers, and  $V_n$ ,  $V_s$ , and  $V_t$  are the initial swelling rates of coal in n-butylamine, sec-butylamine, and t-butylamine, respectively. These rate parameters, analogous equilibrium parameters, and carbon contents of the coals used in these studies are presented in Table VII.

Table VII. The Effect of Coal Rank on Steric Sensitivity.

Coal <sup>a,b</sup>	C(% dmmf) <sup>c</sup>	$\theta_s$	$\theta_t \times 10^3$	$Q_n/Q_s^d$
A	72.2	18.8	--	1.136
B	72.2	17.3	60.8	1.120
C	74.8	10.3	0.83	1.078
D	80.4	4.5	0.62	1.073
E	82.4	10.89	4.7	1.083
F	84.9	19.16	--	1.040

a. 100-200 mesh, measured at 21.0°C

b. A: Hanna No. 80; B: Dietz No. 1 & 2; C: Adaville No. 11;  
D: Illinois No. 6; E: West Kentucky No. 9; F: Pittsburgh No. 8

c. mm = 1.08 Ash + 0.55 S

d.  $Q_n$ : Q-value in n-butylamine;  $Q_s$ : Q-value in sec-butylamine

We have plotted  $\theta_s$  versus carbon content for the six coals used in this investigation. There appears to be some relaxation of steric requirements around 80% carbon content. While it is too early to speculate about the underlying basis for this behavior, we believe that it is related to the balance between covalent and non-covalent (hydrogen bonded) crosslinking (4). Investigation of these phenomena will be the target of future efforts.

#### ACKNOWLEDGEMENTS

We wish to thank Professors R. S. Hansen and D. K. Finnemore for their useful discussion and encouragement. We are grateful for support from The State of Iowa, and from the U. S. Department of Energy through the Ames Laboratory under Contract No. W-7405-ENG-82. The opinions, findings, and conclusion expressed herein are those of the authors, and do not necessarily reflect the views of DOE or the State of Iowa.

#### REFERENCES

1. van Krevelen, D. W., "Coal" Elsevier Publishing Co., Amsterdam, 1961, pp. 139-143.
2. Aida, T.; Squires, T. G., "Solvent Swelling of Coal. 1. Development of an Improved Method for Measuring Swelling Phenomena," Prepr. Pap.-Am. Chem. Soc., Div. Fuel Chem. Previous paper presented at this meeting (1985).
3. Key references are cited in a recent paper by Green, T. K.; Larsen, J. W. Fuel 1984, 63, 1539.
4. Green, T. K.; Brenner, D.; Kovac, J.; Larsen, J. W., "Coal Structure" (Ed. R. A. Meyers), Academic Press, New York, 1982.

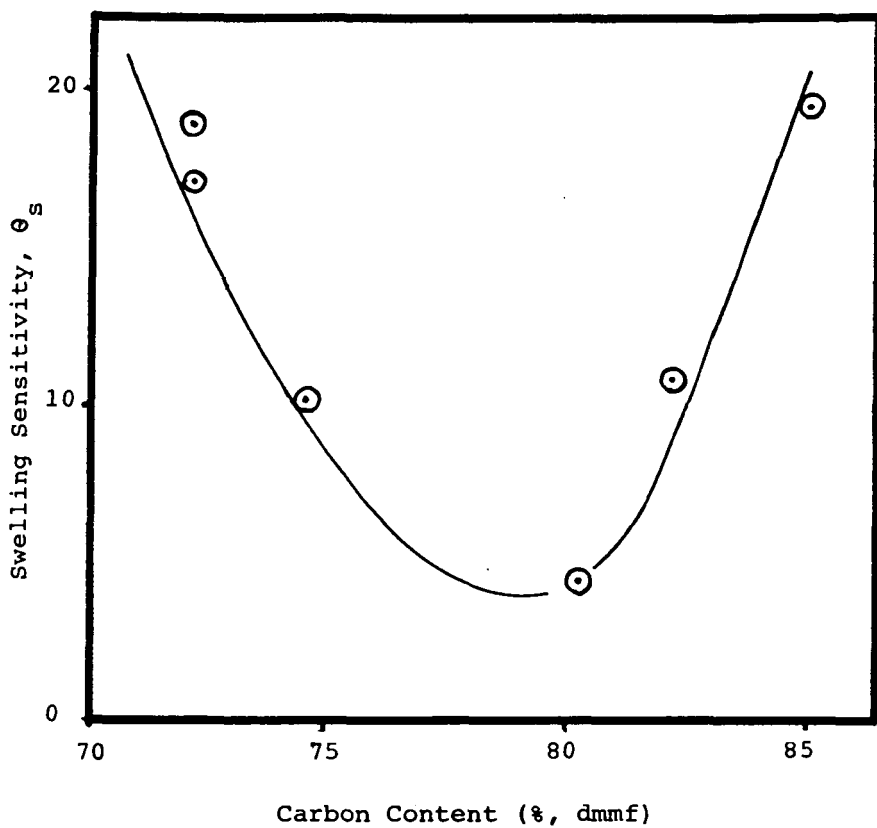


Figure 1. Dependence of Swelling Sensitivity on Coal Rank.

## MECHANISMS OF AMINE TRANSPORT IN COAL PARTICLES

Barbara D. Barr-Howell and Nikolaos A. Peppas

School of Chemical Engineering  
Purdue University  
West Lafayette, Indiana 47907

### INTRODUCTION

There exists considerable evidence in the literature which suggests that the organic phase of coal is a highly crosslinked macromolecular network. This analysis is supported by the fact that the organic phase of coals can swell in thermodynamically compatible solvents to twice its original volume without complete dissolution (Larsen and Kovac, 1978; Lucht and Peppas, 1981 a,b; Lucht, 1983). To aid in the study of the highly crosslinked coal network, Lucht and Peppas (1981a) proposed a simplified description of the organic phase, containing tetrafunctional and multifunctional crosslinks, unreacted functionalities, chain ends, entanglements, chain loops, and effective network chains. Physical crosslinks occur because the system is highly entangled. The chains have limited mobility and therefore are unlikely to disentangle. Chemical crosslinks result from chemical reactions and are stable under a variety of conditions.

Analysis of dynamic swelling results from macromolecular coal networks swollen by good solvents yields important information about solvent-network interactions and the structure of the network. Diffusion studies can be used to determine the thermodynamic state of the network, i.e., whether the network exists in the glassy or rubbery state. It is also possible to determine the type of solvent uptake which occurs in the network. The solvent uptake can occur by Fickian diffusion, anomalous transport, Case-II transport, or Super Case-II transport.

When a macromolecular network such as coal exists in the thermodynamic glassy state all large molecular chain motions are restricted, but the segmental motions are not necessarily limited. As the temperature of the network is increased to the glass transition temperature, large molecular chain motions become important and the network shifts to its thermodynamic rubbery state. The exact glass transition temperature of the macromolecular network is dependent on its chemical and physical nature. The presence of solvent can increase large molecular chain motions at lower temperatures thereby effectively lowering the glass transition temperature of the network. Anomalous diffusion occurs only below the glass transition temperature and at fairly high penetrant activities. Fickian diffusion occurs both in the glassy state and the rubbery state. Concentration-independent Fickian diffusion occurs generally at low penetrant activities or low temperatures.

A convenient method used in the analysis of sorption data employs fitting the sorption data to equation (1).

$$\frac{M_t}{M_\infty} = kt^n \quad (1)$$

Here  $M_t$  is defined as the mass of solvent uptake at time  $t$ ,  $M_\infty$  is the mass of solvent uptake as time approaches infinity,  $k$  is a constant dependent on the structural characteristics of the network, and  $n$  is the exponent which indicates the type of solvent uptake. Table 1 relates the exponent  $n$  to the various types of diffusion.

Table 1.  
Analysis of diffusional behavior using equation (1)

Exponent $n$	Type of diffusion
0.5	Fickian diffusion
$0.5 < n < 1.0$	Anomalous transport
1.0	Case-II transport
$> 1.0$	Super Case-II transport

Equation (1) is valid only in the analysis of the first 60% of the final mass of solvent uptake. It also cannot be used to analyze inflections or overshoots.

For Fickian diffusion with constant boundary conditions and a constant diffusion coefficient, the sorption and desorption kinetics in spheres is given by equation (2) (Crank, 1975).

$$\frac{M_t}{M_\infty} = 1 - \frac{6}{\pi^2} \sum_{n=1}^{\infty} \frac{1}{n^2} \exp(-Dn^2\pi^2t/r^2) \quad (2)$$

Here  $M_t$  is the mass of solvent uptake at time  $t$ ,  $M_\infty$  is the mass of solvent uptake as time approaches infinity,  $r$  is the radius of the sphere, and  $D$  is the concentration-independent diffusion coefficient. An important approximate solution to equation (2) at  $M_t/M_\infty = 0.5$  is given by equation (3).

$$D = \frac{0.00766d^2}{t_{1/2}} \quad (3)$$

Here  $t_{1/2}$  is the diffusional half-time in seconds and  $d$  is the sphere diameter in centimeters. Equation (3) gives a useful relationship for the calculation of the diffusion coefficient in  $\text{cm}^2/\text{sec}$ .

For Case-II transport which usually occurs at high penetrant activity and is relaxation-controlled, the desorption and sorption data in a sphere are expressed by equation (4) (Ensore *et al.*, 1977).

$$\frac{M_t}{M_\infty} = 1 - \left(1 - \frac{k_0 t}{C_0 r}\right)^3 \quad (4)$$

Here  $k_0$  is defined as the Case-II relaxation constant in  $\text{mg}/\text{cm}^2 \text{ min}$  and is assumed to be a constant;  $C_0$  is the equilibrium concentration of the penetrant and  $r$  is the radius of the sphere.

Most diffusion data do not follow Fickian diffusion or Case-II transport kinetics but are explained by a combination of the two kinetic models. Anomalous transport may be described by coupling of the relaxation process with the diffusion process. This idea of coupling led Berens and Hopfenberg (1978) to propose a model to describe this process; the model is given in equation (5).

$$1 - \frac{M_t}{M_\infty} = \phi_F \left[ \frac{6}{\pi^2} \sum_{n=1}^{\infty} \frac{1}{n^2} \exp(-4\pi^2 n^2 D t / d^2) \right] + \phi_R \exp(-kt) \quad (5)$$

Here  $\phi_F$  and  $\phi_R$  are the fractions of sorption contributed by Fickian diffusion and the relaxation process respectively,  $D$  is the diffusion coefficient for the Fickian portion of the transport, and  $k$  is the first-order relaxation constant. If diffusion occurs rapidly in comparison to the relaxation, both  $D$  and  $k$  can be determined from the sorption data (Ensore *et al.*, 1977).

## EXPERIMENTAL PART

The coal samples, packed under nitrogen, were supplied by the Pennsylvania State University Coal Bank. The samples were sieved to the desired mesh size and stored in nitrogen until use.

Untreated coal samples of 1-2 g were dried and weighed to  $\pm 0.005$  g on a Mettler top loading balance. The samples were then placed in 10 ml beakers which were suspended in a desiccator over a pool of solvent. The solvents used in the studies were n-propylamine, butylamine, diethylamine, and dipropylamine. The desiccator was sealed and suspended in a water bath to maintain a constant temperature of  $35 \pm 0.5^\circ\text{C}$ . At set time intervals, the coal samples were removed, weighed, and then returned to the desiccator.

## RESULTS AND DISCUSSION

Dynamic swelling studies were performed on seven untreated coal samples. In the first set of experiments, the effect of carbon content on the sorption of n-propylamine vapor was studied. The samples were prepared for experimentation by drying, and then exposed to n-propylamine vapor at  $35^\circ\text{C}$  until equilibrium swelling had been reached. The mass of solvent uptake per mass of coal sample (dmmf) was calculated as a function of time. The results for PSOC 418 with 69.94%C (dmmf), PSOC 312 with 78.38%C (dmmf), and PSOC 9129 with 88.19%C (dmmf) are shown in Figure 1. The results for PSOC 791 with 72.25%C (dmmf), PSOC 853 with 80.12%C (dmmf), and PSOC 402 with 82.48%C (dmmf) are shown in Figure 2.

The first major observation from this set of experiments was the dramatic effect of carbon content on the final solvent uptake per mass of coal sample (dmmf). This is shown graphically in Figure 3. The solvent uptake is shown to decrease with increasing carbon content.

The mathematical analysis of the sorption data initially involved fitting the data to equation (3) for the first 60% of the final solvent mass uptake. The results from this analysis are tabulated in Table 2. The results show no direct correlation between carbon content and exponent  $n$ ; however, all the values fall between 0.5 and 1.0 and therefore all the sorption processes may be classified as anomalous transport.

Table 2.

Analysis of the Sorption Data from Dynamic Swelling Studies for n-Propylamine using Equation (1)

PSOC	%C (dmmf)	k	Exponent n	r
418	69.94	.07	.74	.998
791	72.25	.05	.83	.999
247	75.53	.024	.981	.993
312	78.38	.05	.79	.993
853	80.23	.04	.79	.996
402	82.48	.05	.68	.994

The model of Berens and Hopfenberg given in equation (1.10) was used to determine diffusion coefficients and relaxation constants. The results from this analysis are tabulated in Table 3. Here both the relaxation constants and the diffusion coefficients are found to decrease with increasing carbon content.

Table 3.

Diffusion Coefficients and Relaxation Constants  
from the n-Propylamine Studies

PSOC	%C (dmmf)	k (sec <sup>-1</sup> )	D(cm <sup>2</sup> /sec)
418	69.94	$1.1 \times 10^{-6}$	$7.5 \times 10^{-9}$
791	72.25	$5.5 \times 10^{-6}$	$2.8 \times 10^{-9}$
247	75.53	$6.2 \times 10^{-6}$	$2.2 \times 10^{-9}$
312	78.38	$7.9 \times 10^{-6}$	$3.2 \times 10^{-9}$
853	80.12	$5.8 \times 10^{-6}$	$2.2 \times 10^{-9}$
402	82.48	$4.3 \times 10^{-6}$	$5.6 \times 10^{-9}$

The final mathematical analysis of this data involved calculating the Case-II relaxation constant using the relaxation controlled model given by equation (4). The results from this analysis are tabulated in Table 4. Here the calculated relaxation constants show a decrease as the carbon content increases.

Table 4.

Case-II Relaxation Constants for  
n-Propylamine Studies Using Equation (4)

PSOC	%C (dmmf)	$k_0$ (g/cm <sup>2</sup> sec)
418	69.94	$5.1 \times 10^{-7}$
791	72.25	$3.0 \times 10^{-7}$
247	75.53	$3.1 \times 10^{-7}$
312	78.38	$2.7 \times 10^{-7}$
853	80.12	$2.8 \times 10^{-7}$
402	82.48	$1.6 \times 10^{-7}$

The second set of experiments were designed to determine the effect of particle size on solvent transport. Again the samples were pre-dried and then exposed to n-propylamine vapor at 35°C until equilibrium swelling had been reached. The results from these experiments were plotted as the mass of solvent uptake per mass of coal sample (dmmf) as a function of time; these results are given in Figure 4, for PSOC 312 with 78.38%C (dmmf) with sizes of 850-600  $\mu$ m, 600-425  $\mu$ m, 425-250  $\mu$ m, 250-180  $\mu$ m, and 180-150  $\mu$ m.

The results from the analysis of exponent n using equation (1) are tabulated in Table 5. A decrease in particle size has a resulting decrease in the value of the exponent n; there is a shift from anomalous transport in the larger particles to Fickian diffusion in the smaller particles.

Table 5

Analysis of the Sorption Data for Varying Particles (PSOC 312)  
Sizes Using Equation (1)

Particle Size	k	Exponent n	r
850-600 $\mu$ m	.05	.79	.993
600-425 $\mu$ m	.07	.72	.997
425-250 $\mu$ m	.10	.67	.997
250-180 $\mu$ m	.12	.62	.999
180-150 $\mu$ m	.13	.54	.998

#### Acknowledgements

This work was supported by DOE grant No. DE-PG22-83PC 60792.

#### REFERENCES

- Berens, A.R. and H.B. Hopfenberg, *Polymer*, **19**, 490 (1978).
- Crank, J., *The Mathematics of Diffusion*, 2nd ed., Oxford Press, London, 1975.
- Ensore, D.J., H.B. Hopfenburg, and V.T. Stannett, *Polymer*, **18**, 793 (1977).
- Larsen, J.W. and J. Kovac, in J.W. Larsen, (ed.) *Organic Chemistry of Coal*, ACS Symposium, **71**, 36, Washington, D.C., 1978.
- Lucht, L.M. and N.A. Peppas, in B.D. Blaustein, B.C. Bockrath, and S. Friedman, eds., in *New Approaches in Coal Chemistry*, ACS Symposium, **169**, 43, Washington, DC (1981a).
- Lucht, L.M. and N.A. Peppas, in B.R. Cooper and L. Petrakis, eds., *Chemistry and Physics of Coal Utilization*, American Institute of Physics, New York, NY, 18 (1981b).
- Lucht, L.M., "Macromolecular Network Structure of Coals: Interpretation of Equilibrium and Dynamic Swelling Experiments," Ph.D. Thesis, School of Chemical Engineering, Purdue University, West Lafayette, IN, 1983.

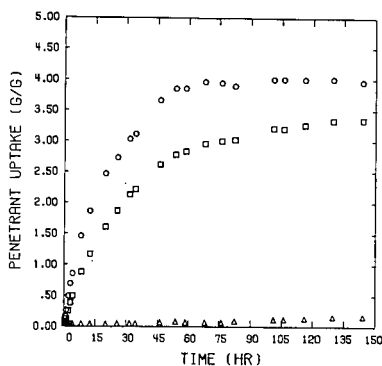


Figure 1: Uptake of n-Propylamine Vapor at 35°C a Function of Time for PSOC 418 (69.94%C, ○), PSOC 312 (78.38%C, □) and PSOC 989 (88.19%C, △).



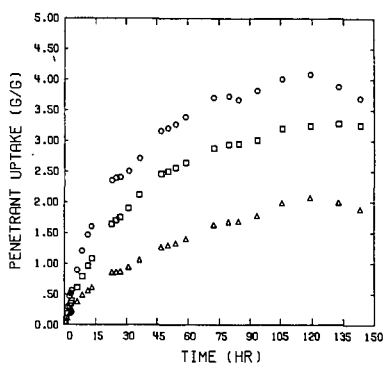


Figure 2: Uptake of *n*-Propylamine Vapor at 35° as a Function of Time for PSOC 791 (72.25%C, ○), PSOC 853 (10.12%C, □) and PSOC 402 (81.48%C, Δ).

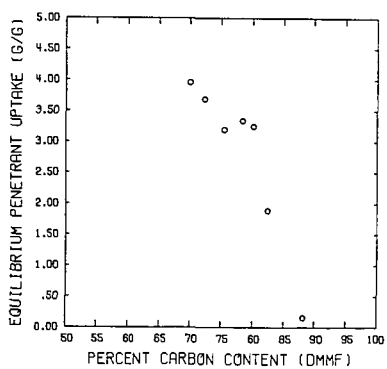


Figure 3: Final Solvent Uptake as a Function of Carbon Content for *n*-Propylamine Studies.

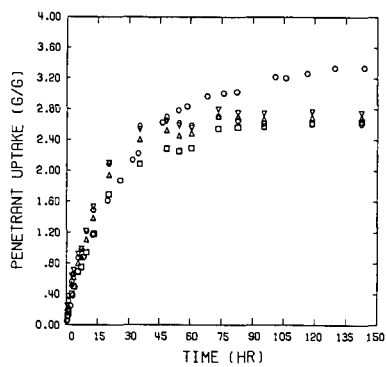


Figure 4: Uptake of n-Propylamine Vapors by Coal Particles as a Function of Time. Studies with PSOC 312 (78.38%C) and with Particles Sizes of 850-600  $\mu\text{m}$  (○), 600-425  $\mu\text{m}$  (□), 425-250  $\mu\text{m}$  (Δ), 250-180  $\mu\text{m}$  (◊), and 180-150  $\mu\text{m}$  (▽).

## Plastic Behavior of Coal Under Rapid-Heating High-Temperature Conditions

William S. Fong, Yehia F. Khalil, William A. Peters, and Jack B. Howard

Department of Chemical Engineering and Energy Laboratory  
Massachusetts Institute of Technology  
Cambridge, Massachusetts 02139

### Introduction

Bituminous coals upon heating undergo a number of physical and chemical changes. The solid coal passes through a transient plastic (fluid) phase before it resolidifies to form coke. This transient fluidity results in caking and agglomeration of the coal particles in the processing of many bituminous coals. Industrially, these phenomena may contribute to desirable process performance such as a strong and reactive product in metallurgical coke manufacture, or to undesirable operating behavior such as bed bogging in fixed or fluidized bed gasifiers. More fundamentally, the presence of the fluid phase can influence the pyrolysis rate process. A basic understanding of the plastic behavior of coal is therefore essential in the development of quantitative understanding of modern coal conversion and combustion processes.

The mechanism of coal plasticity is poorly understood. One picture is that softening is initiated by a superposition of physical melting and pyrolysis of the coal. A plasticizing agent (metaplast) generated by these processes maintains fluidity until evaporation, repolymerization, and thermal cracking reduce its concentration to a subcritical value causing resolidification (1-3). Previous studies of coal plasticity have mainly been performed under conditions pertinent to metallurgical coke making; i.e., low heating rate carbonization of packed bed samples. A standard instrument is the Gieseler plastometer which operates at a heating rate of  $5 \times 10^{-2} \text{ K s}^{-1}$  to final temperatures around 800 K. Plasticity data are needed at the high heating rates and temperatures (up to  $15,000 \text{ K s}^{-1}$  and 700 - 1300 K, respectively), and elevated hydrogen pressures (up to 10 MPa) of interest in coal conversion.

A new apparatus (4) has been developed that allows the rapidly changing plasticity of softening coal to be measured as a function of the following operating conditions, each varied independently over the stated range: heating rates 40 -  $800 \text{ K s}^{-1}$ , temperatures 600 - 1250 K, particle diameters less than 100  $\mu\text{m}$  and pressures of inert or reactive gases from vacuum to 10 MPa. This paper presents the findings of a detailed study of the plasticity of a high volatile Pittsburgh No. 8 seam bituminous coal using this instrument. Typical results are presented and compared to predictions of a preliminary mathematical model of coal plasticity. The inventory of fusible material within the coal was independently determined by pyridine extraction of rapidly quenched flash-pyrolyzed chars and correlated with the plastic behavior. The effect of the time-temperature history of the coal on the molecular weight of this extract was determined by gel permeation chromatography.

### Experimental

#### (a) Plastometer

The plastometer is described in detail elsewhere (4). Briefly, the technique involves measuring the torque required to rotate at constant speed, a thin shearing disk embedded in a thin layer of coal initially packed as fine particles, and confined between two heated metal plates. The unit is enclosed in a high-pressure vessel that can be evacuated or charged with hydrogen or inert gas. One end of the torque transducer is joined to the shaft of the shearing disk, while the other end is driven by a gear motor. Response time of the piezoelectric transducer is less than 10 ms.

The details of the coal shearing device are illustrated in Figure 1. The shearing chamber consists of a 0.50 mm thick shearing disk of 3.75 mm radius in a 38.1 mm x 0.76 mm slot formed by upper and lower bounding plates held together by a pair of stainless steel/ceramic clamps. The thin coal layer between the disk and each bounding plate is thus 0.13 mm (or about two particle diameters for the size of particles tested). The shearing disk and bounding plates are machined from a nickel superalloy for high-temperature strength, corrosion resistance, and high electrical resistivity. Measurement of temperature is by a thin-foil thermocouple of 0.013 mm thickness (response time 2 - 5 ms) attached to the outside surface of the upper metal plate of the shearing chamber. Heating is by sequentially passing two constant pulses of current of pre-selected magnitude and duration through the metal plates for heating up and holding the sample temperature, respectively. Currents as high as a few hundred A are drawn from the 12 volt DC source for sample heatup. A loading device (not shown here) (4) is used to permit reproducible loading of the coal particles into the shearing chamber and alignment of the rotating disk with the axis of the transducer shaft. The assembled and loaded shearing chamber is placed between the two electrodes in the viscometer before the experiment, and the couplings to the transducer are then connected. To protect the transducer against overload during startup, the shearing disk is rotated manually one or two turns until a torque in a measurable range of  $4 - 5 \times 10^{-2}$  Nm is attained. The unit is then evacuated to approximately 5 Pa and flushed twice with helium at 0.1 MPa. Then the test gas is admitted until the desired test pressure is established. The drive motor is started 0.5 s before the heating circuits are activated. The torque vs time, and temperature vs time profiles throughout the entire run are each recorded on an electronic recorder at a rate of 200 points/s, digitized, and stored for subsequent data processing.

#### (b) Screen Heater Reactor

The weight loss and extract yield data are obtained from an enlarged and modified version of the screen heater reactor described by Anthony (5). Coal particles (~30 mg) of the same size used in the plastometer study (63 - 75  $\mu$ m) are spread in a thin layer between two faces of 425 mesh stainless screen of 14 cm x 7 cm size. The screen is mounted between two electrode blocks and heated by the same high-current circuits used for the plastometer. One of the electrodes is spring-loaded so that the screen is held tight throughout the entire run. Volatiles readily escape the immediate neighborhood of the screen and are diluted by the ambient reactor gas (usually helium). At the end of the preset heating interval, a cooling valve is automatically activated, and sprays pressurized liquid nitrogen onto the screen, resulting in a substrate quenching rate exceeding  $1100 \text{ K s}^{-1}$ . The weight loss of coal is determined by weighing the loaded screen before and after the run. The extract yield is then determined by Soxhlet extracting the screen and char with pyridine, drying the extracted screen and char in a vacuum oven at 120°C for 4 hours, and reweighing.

### Results and Discussion

The objectives of this work are to determine the separate effects of temperature, heating rate, pressure, reactive gaseous atmosphere, inorganic additives and pretreatment on coal plastic behavior and to formulate kinetic models for coal plasticity. Experiments to date have employed a Pittsburgh seam bituminous coal of 39% volatile matter and 63-75  $\mu$ m particle diameter. The coal, which was from the same mine as the samples used previously in this laboratory, was freshly ground under nitrogen, washed, sieved and then vacuum dried at 383 K for 4 hours.

#### (a) Typical Plastometer Results

Figures 2 and 3 present typical data obtained under 0.1 MPa and 3.5 MPa of helium, respectively, at a disk rotational speed of 0.67 rpm (corresponding to an average shear

rate of  $1.32 \text{ s}^{-1}$ ). In Fig. 2 the sample was heated at  $461 \text{ K s}^{-1}$  to a final temperature of  $874 \text{ K}$  and then held at this temperature for  $6.0 \text{ s}$ . As the temperature increases, the torque decreases to a low value due to liquid formation. After a period of low viscosity, the viscosity of the molten coal rises to a high value due to progressive resolidification of the melt. However, continued rotation of the disk breaks up the resultant coke formed by resolidification, and the torque vs time curve gradually decreases thereafter.

The stages of physical change of the coal are illustrated in Fig. 3. For the given shear rate, the torque is related to the absolute viscosity by  $1.0 \times 10^{-2} \text{ Nm} \equiv 2.6 \times 10^4 \text{ Pa s}$ , obtained by calibrating the instrument with viscous liquid standards at room temperature using a method described elsewhere (4). Essentially, the shearing geometry is regarded as two sets of concentric parallel disks. A calibration factor is introduced to account for the slight deviation of the actual instrument geometry from the parallel disk geometry. The apparent Newtonian viscosity is then obtained using the standard equation for a concentric rotating disk viscometer and the calibration factor.

To show how different types of particles behave when heated in the plastometer, samples of Montana lignite (dried,  $53\text{--}88 \mu\text{m}$ ), quartz ( $<106 \mu\text{m}$ ), Pittsburgh No. 8 coal (dried,  $63\text{--}75 \mu\text{m}$ ) and the same Pittsburgh coal pre-extracted with pyridine (dried,  $63\text{--}75 \mu\text{m}$ ) were separately tested. Fig. 4 compares these results. In the case of quartz, which does not change its physical form when heated, there is an initial drop in torque due to the slight thermal expansion of the shearing chamber when heated. A high but fluctuating torque signal reflects shearing of particles with rigid edges. Montana lignite, which undergoes pyrolysis without softening under these conditions, retains its solid form but experiences a decrease in volume due to weight loss. Its torque curve thus shows a gentle decrease to a steady value. The Pittsburgh coal shows a plastic behavior very different from the above solids. A low minimum torque value and a distinct plastic period are clearly present. Finally, the pyridine pre-extracted coal shows a delayed softening. Resolidification is faster and the plastic interval is shorter as compared with the untreated coal, presumably due to the prior removal of some metaplast precursor by pyridine.

#### (b) Typical Screen Heater Results

Information on the time-resolved kinetics of devolatilization, the amount of extractables formed within the coal and on the molecular weight distribution and chemical makeup of these extracts provides independent but complementary information about the mechanism of plasticity. Fig. 5 is a time resolved plot of yields of volatiles (i.e. weight loss), pyridine extractables from char, and the pyridine insoluble material in the char, for a heating rate of  $448 \text{ K s}^{-1}$  to a holding temperature of  $858 \text{ K}$ . After different holding times, the sample is rapidly quenched with liquid nitrogen (dotted line). The weight average molecular weight  $M_w$  of the extract is determined by a Waters Associates ALC/GPC 201 system using two series-connected  $100 \text{ \AA}$  and  $500 \text{ \AA}$  Microstyragel columns. Fig. 6 is a similar plot for a higher holding temperature. The quantity  $M_w$  is found to increase in both cases. Pre-extraction of the coal removes part of the liquid precursor, and less extract would be expected upon subsequent pyrolysis as was observed. This behavior can significantly affect the plastic behavior of coal. Fig. 7 compares the yields of pyrolysis-derived extracts from raw coal samples with those from pyridine pre-extracted samples, subjected to identical temperature-time histories. A second set of comparisons, for a different heating history, are also shown.

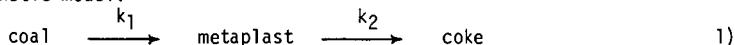
#### (c) Discussion of Results

The mechanism of plasticity in coals is not well understood for rapid heating and high temperature conditions. Plasticity and related phenomena such as swelling

and agglomeration are direct consequences of liquid formation by heating. Physical melting of part of the coal first occurs when the temperature is sufficiently high. Subsequent pyrolytic bond breaking generates additional liquid. The initial liquid generated by physical melting may also dissolve part of the solid coal material. At the same time, liquid is lost through evaporation of its lighter molecules (volatiles) from the particle, and through repolymerization and cracking reactions. This picture is supported by our present data. The kinetics of extract generation and destruction as inferred from the screen heater experiments correlates well with the plasticity data, as shown in Fig. 8. It seems reasonable to assume that the amount of extract is an indication of the instantaneous liquid metaplast content of the coal. Initially, we can extract 27% of pyridine solubles from the unheated raw coal. This amount would correspond to the material that is solid at low temperature but undergoes physical melting as temperature exceeds the 'melting' point. Our observation with the plastometer, that initial softening occurs around 580 K independent of heating rate ( $50 - 700 \text{ K s}^{-1}$ ), is consistent with the above observation as seen from Fig. 9. If this initial 27% of material is pre-extracted, and afterwards the coal is subjected to pyrolysis, the metaplast (extract) formed by pyrolysis alone is much less as seen from Fig. 7. The pre-extracted coal is expected to soften at a later time (higher temperature) and the duration of plasticity is shorter, as is observed (Fig. 4d).

The relation of extract inventory to the duration of plasticity and to resolidification rate is illustrated from the pyridine insoluble curves in Figs. 5 and 6. The amount of insolubles reaches a minimum and then rises to an asymptotic value determined by the competition of devolatilization and resolidification rates. The rising portion of the curves indicates either repolymerization reaction or cracking of metaplast to a light gas and a solid, or both. Repolymerization seems likely since the molecular weight of the metaplast increases with heating time (Figs. 5, 6). However, this can also be caused by selective evaporation of light molecules from the metaplast. The devolatilization rate also seems to be proportional to the instantaneous amount of metaplast in coal. At higher holding temperatures ( $\geq 973 \text{ K}$  for heating rates around  $500 \text{ K s}^{-1}$ ) the plasticity and extract curves do not correlate well. The extract curve has shorter width than the plasticity curve. This behavior may in part reflect an apparatus artifact since the mass transfer resistance for volatiles escape in the plastometer is much greater than in the screen heater.

The duration of plasticity and the resolidification rate are quite sensitive to temperature-time history (Figs. 9, 10). Fig. 10 shows how these vary for plastometer runs at  $450 \text{ K s}^{-1}$  to four different holding temperatures. This behavior leads to the conceptually simple mathematical model based in part on Fitzgerald's metaplast theory (6). He considered the formation and destruction of metaplast to be described by a first order kinetic model.



To simplify its implementation here, equivalent component densities and negligible weight loss are assumed. To relate metaplast concentration to the apparent viscosity of the melt, an expression for concentrated suspensions by Frankel and Acrivos (7) is employed. The relative viscosity  $\mu$  of a suspension at high solids concentration is given by,

$$\mu = \frac{\mu^*}{\mu} = \frac{9}{8} \left[ \frac{(\phi/\phi_m)^{1/3}}{1 - (\phi/\phi_m)^{1/3}} \right] \quad (2)$$

where  $\mu^*$  is the viscosity of a suspension with a solids volume fraction  $\phi$ ,  $\phi_m$  being the maximum value of  $\phi$  possible, and  $\mu$  is the viscosity of the continuous (solids-free) phase. We approximate  $\phi = 1 - M$  where  $M$  is the metaplast weight fraction. Since the sample is initially a packed bed of solids,  $\phi_m$  is assumed to be unity. This condition is possible if the solid elements of the suspension are thin slabs

(lamellae) which is a reasonable representation of the layered structure of vitrinite. Solving Equation 1 for metaplast concentration with the given temperature profile (constant linear heating followed by a constant holding temperature) and using Equation 2 allows  $\bar{\mu}$  to be calculated if the rate constants  $k_1$  ( $=k_{01} \exp[-E_{A1}/RT]$ ) and  $k_2$  ( $k_{02} \exp[-E_{A2}/RT]$ ) are known. These quantities can be estimated from laboratory data. At a late stage of resolidification, the metaplast formation rate is very small, so

$$\frac{dM}{dt} = -k_2 M \quad (3)$$

At small values of  $M$  ( $M < 0.1$ ), Equation 2 with the approximation  $\phi_m = 1.0$  is reduced to

$$\bar{\mu} = \frac{27}{8} \left( \frac{1}{M} \right) \quad (4)$$

It then follows that

$$\frac{d \ln \bar{\mu}}{dt} = k_2 = k_{02} \exp[-E_{A2}/RT] \quad (5)$$

The holding temperature is a good approximation for  $T$  when resolidification occurs well after the holding temperature is reached (such as in Fig. 2). The experimental rate of increase of the logarithm of torque is identical to the left-hand term of Equation 5. A plot of the logarithm of this quantity vs reciprocal holding temperature gives a straight line corresponding to an activation energy  $E_{A2}$  of  $133 \text{ kJ mole}^{-1}$  and  $k_{02}$  of  $2.0 \times 10^8 \text{ s}^{-1}$ . Actual viscosities are measured in the range  $1 \times 10^3 -$

$1 \times 10^5 \text{ Pa s}$ . Nazem (8) measured the viscosities of carbonaceous mesophase pitch at around  $623 \text{ K}$  and found them to be between  $30 - 200 \text{ Pa s}$ . Hence  $\bar{\mu}$  would be of order  $10 - 1,000$  if we assume the solids free metaplast has a similar viscosity. For illustration purpose,  $\mu$  is taken to be  $120 \text{ Pa s}$ . Values of  $k_{01} = 245 \text{ s}^{-1}$  and  $E_{A1} = 40.7 \text{ kJ mole}^{-1}$  are found to fit the plastic period of the experiments at  $450 \text{ K s}^{-1}$  heating rate (4). The temperature dependence of viscosity of the solids-free metaplast is not considered here. Calculated plasticity curve in Fig. 11 shows the same form of dependence of viscosity on reaction time as the observed data in Fig. 10. Fig. 12 shows that the calculated plastic period (smooth curve), defined as the time interval when  $\mu^* < 3.6 \times 10^4 \text{ Pa s}$ , fits the laboratory data well.

The above model is of preliminary nature and offers opportunities for improvement. Weight loss has not been considered in defining metaplast concentration. Generation of metaplast is described only by a first order chemical reaction, i.e. physical melting is neglected. This seems particularly suspect since curve fitting the present data with this model gave a low value of  $E_{A1}$  more suggestive, in the present context, of kinetics dominated by physical transport or phase change. Further, Equation 2 relating metaplast concentration to relative viscosity was derived for the highly simplistic case of solid spheres.

The plastic behavior under vacuum and high inert gas pressure was also investigated. For both vacuum and  $3.5 \text{ MPa}$  ambient helium pressure, the plastic period is shorter ( $4.5$  and  $4.2 \text{ s}$  respectively, compared to  $6.4 \text{ s}$  at  $0.1 \text{ MPa}$  helium pressure). The resolidification rates for both cases are faster than under  $0.1 \text{ MPa}$  helium. Under vacuum, the metaplast may escape faster from the particle, resulting in shorter plasticity duration. High pressure may favor repolymerization reactions, hence the resolidification rate. The effect of high pressure on fluidity agrees with inferences by Halchuk et al. (9) based on analyses of char particles from screen heater pyrolysis. They found that the fluidity of a HVA Pittsburgh No. 9 seam coal during rapid pyrolysis at  $760^\circ\text{C}$  was lower at pressures above  $0.45 \text{ MPa}$ , than that at  $0.1 \text{ MPa}$ .

## Conclusions

A new plastometer for measuring the apparent viscosity of plastic coals under rapid-heating, high temperature conditions has been developed and found to give reproducible data that are generally consistent with expected plasticity behavior. Under rapid heating conditions ( $40 - 800 \text{ K s}^{-1}$ ) the duration of plasticity and its rate of disappearance for a Pittsburgh No. 8 bituminous coal depended strongly on pressure, temperature, and heating rate. However, the initial softening temperature was insensitive to heating rate. Pre-extraction of the coal with pyridine at 389 K, typically yielded 25 - 30 wt% organic matter and strongly retarded plasticity on subsequent heating by delaying its onset and shortening its duration.

The effects of temperature on the duration of plasticity were correlated by a preliminary mathematical model relating viscosity of solid-liquid suspensions to the transient concentration of a plasticizing agent generated and depleted by single first-order chemical reactions in series. This simple kinetic picture is also in qualitative accord with the other observations described above. However, quantitative prediction of metaplast molecular weights, effects of pressure and particle size on plasticity, and of softening temperatures will require that transport processes and physical melting be included in the modelling. More detailed modelling will also be needed to describe other softening related phenomena, such as swelling and agglomeration of particles in coal conversion processes and the role of plasticity in liquefaction kinetics.

## Acknowledgements

Financial support of this work is provided by the United States Department of Energy under Contract No. DE-AC21-82MC-19207, and is gratefully acknowledged.

## References

1. Habermehl, D., F. Orywal, and H. D. Beyer, "Plastic Properties of Coal" in Chemistry of Coal Utilization, 2nd Suppl. Vol., M. A. Elliott, ed., J. Wiley & Sons, New York, 1981.
2. Loison, R., A. Peytavy, H. F. Boyer, and R. Grillo, "The Plastic Properties of Coal" in Chemistry of Coal Utilization, Suppl. Vol., H. H. Lowry, ed., J. Wiley & Sons, New York, 1963.
3. Kirov, N. Y. and J. N. Stephens, "Physical Aspects of Coal Carbonization" Kingsway Printers, Caringbah, Australia, 1967.
4. Fong, W. S., W. A. Peters, and J. B. Howard, submitted for Review for Publication, Rev. Sci. Instrum., 1984.
5. Anthony, D. B., J. B. Howard, H. P. Meissner, and H. C. Hottel, Rev. Sci. Instrum. 45, 992 (1974).
6. Fitzgerald, D., Fuel 36, 389 (1957).
7. Frankel, N. A. and A. Acrivos, Chem. Eng. Sci. 22, 847 (1976).
8. Nazem, F. F., Fuel 59, 851 (1980).
9. Halchuk, R. A., W. B. Russel, and D. A. Saville, Proc., Int. Conf. on Coal Science, Pittsburgh, 1983, pp. 491-3.



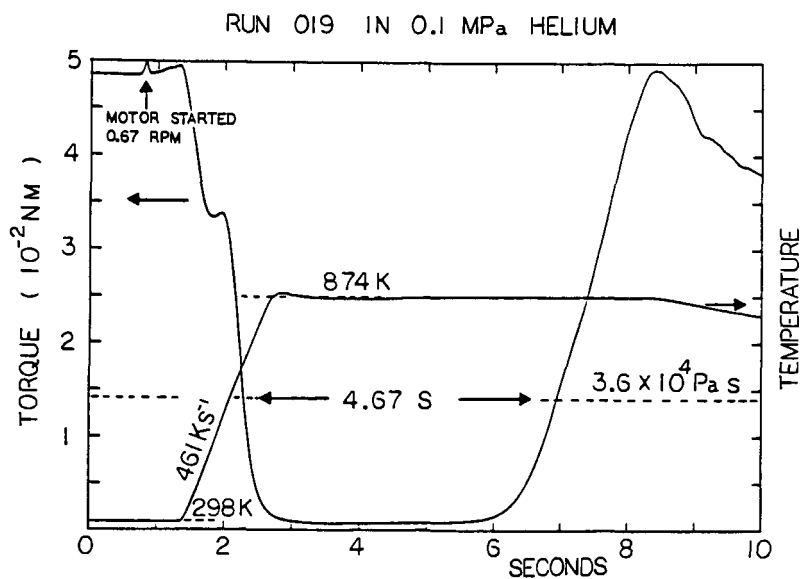


Figure 2 Typical Raw Data from Plastometer. Total Pressure = 0.1 MPa

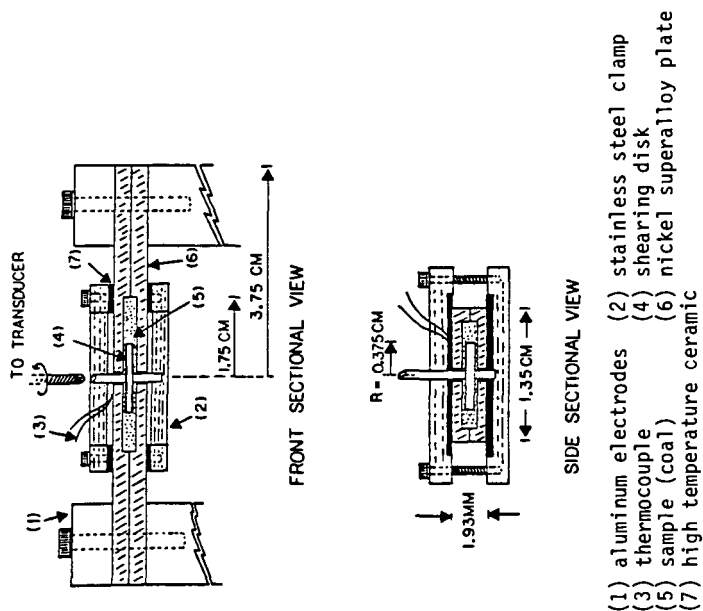


Figure 1 Details of Shearing Chamber

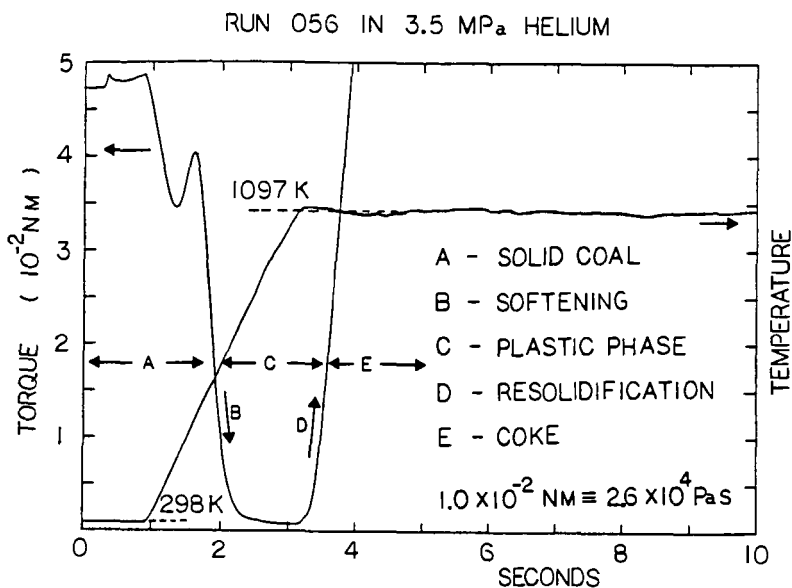


Figure 3 Typical Raw Data from Plastometer. Total Pressure = 3.5 MPa

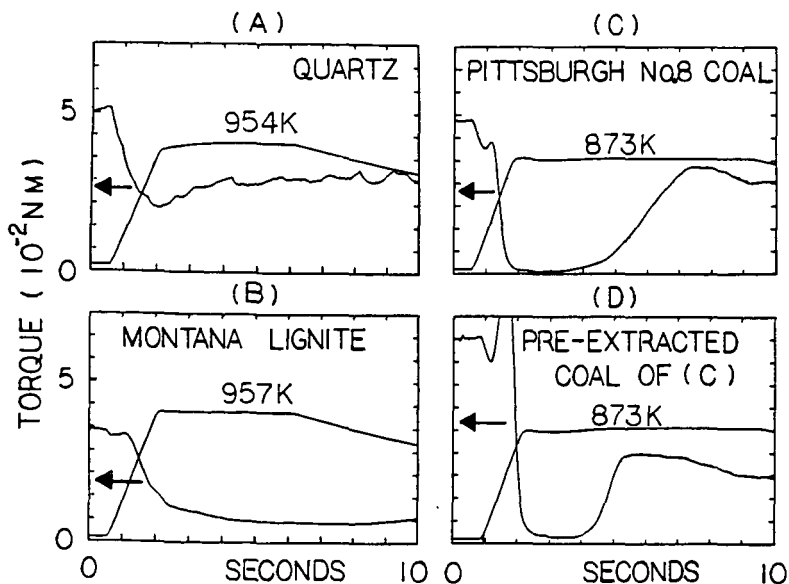


Figure 4 Behavior of Different Particles in the Plastometer

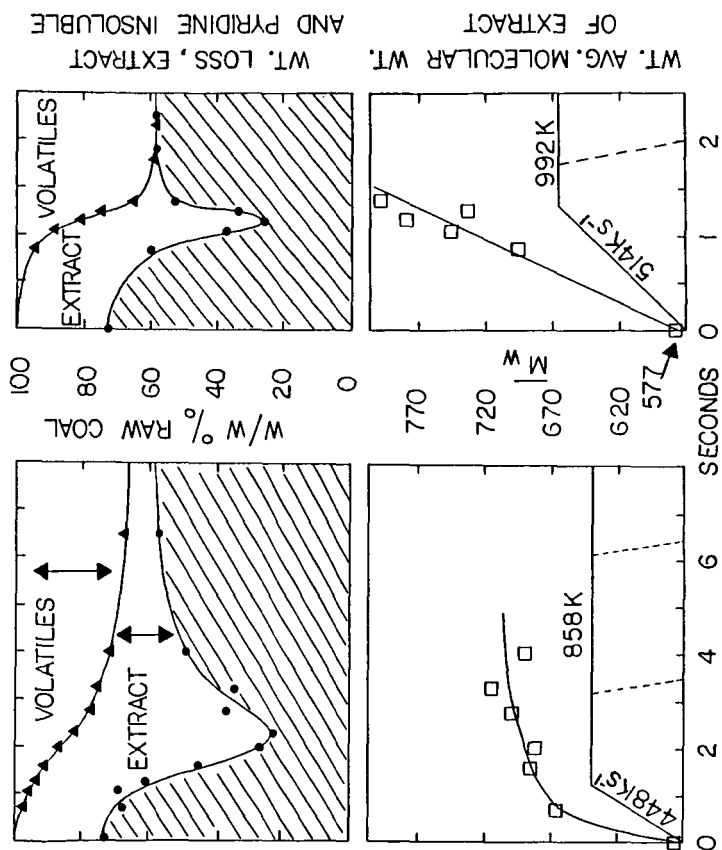


Figure 5

Figure 6

Figures 5,6 Weight Loss of Raw Coal, Pyridine Extract and Insoluble from Char and Weight Average Molecular Weight of Extract from Screen Heater Experiments. Temperature-time histories indicated.

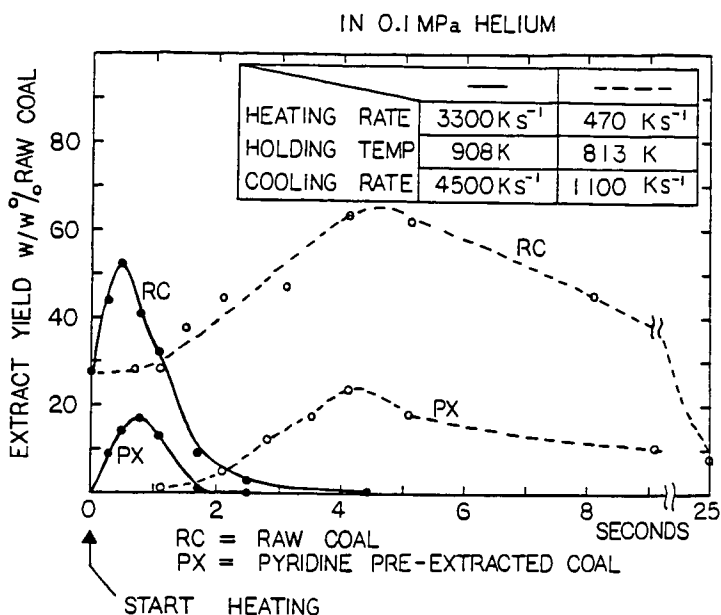


Figure 7 Comparison of Extract Yields for Raw Coal and Pre-extracted Coal

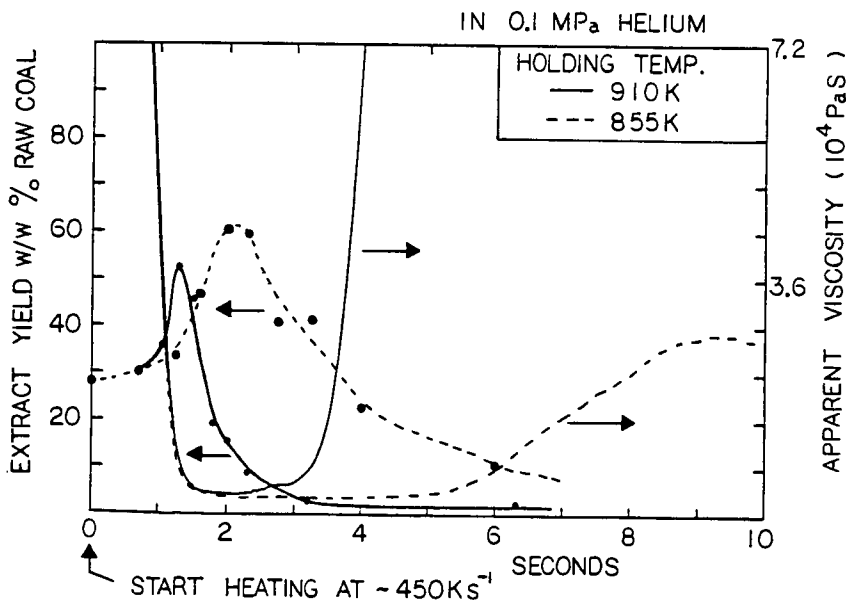


Figure 8 Comparison of Plastic Behavior and Extract Formation/destruction

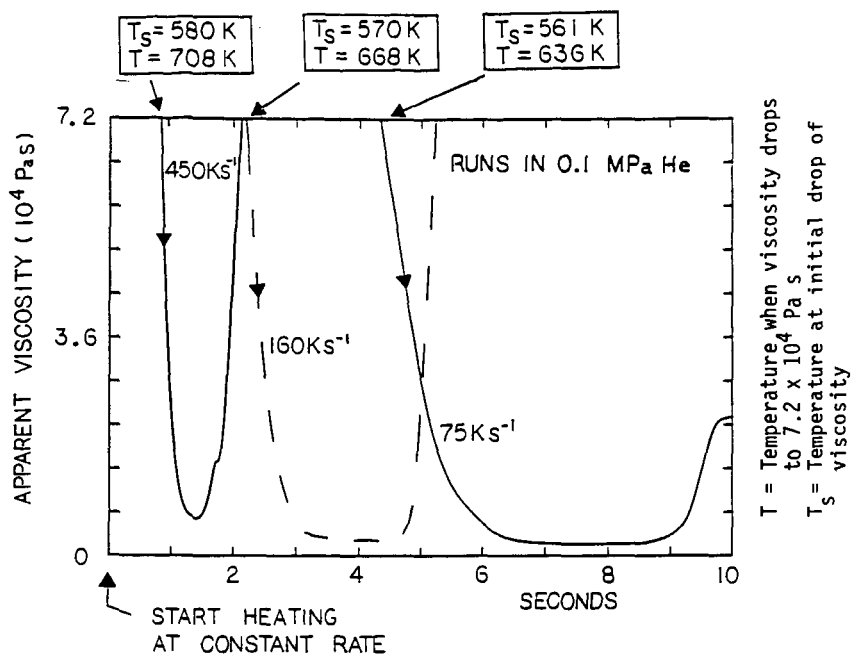


Figure 9 Plasticity Data for Constant Heating Rate Runs

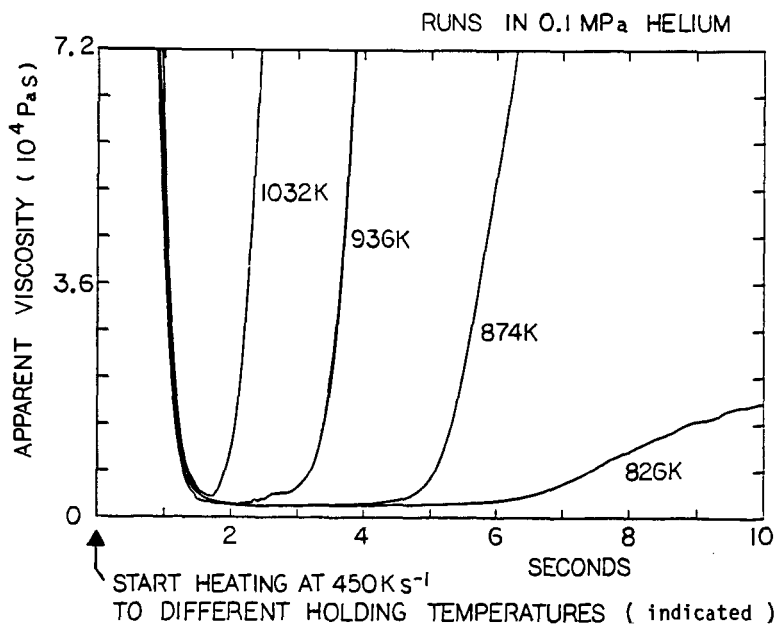


Figure 10 Plasticity Data for Holding Temperature Runs

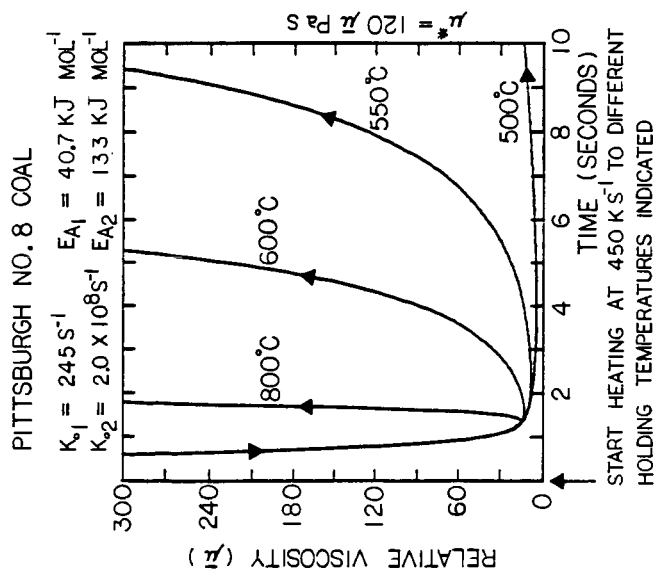


Figure 11 Calculated Viscosity Curve according to Single First Order Reaction Model

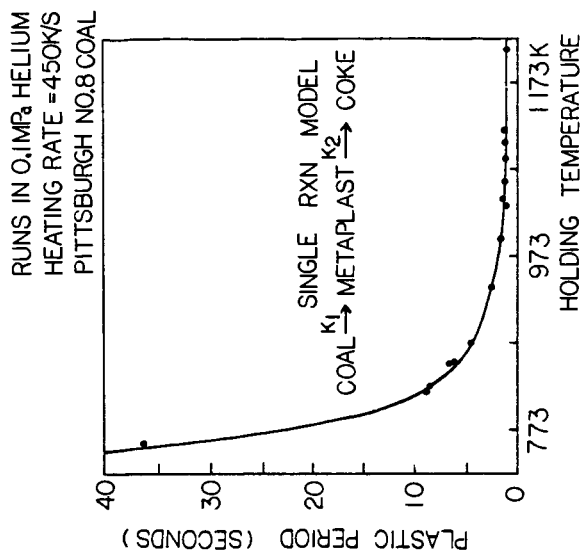


Figure 12 Calculated Plastic Period (curve) and experimental data (solid circles)

## INTERNAL FRICTION AND DYNAMIC YOUNG MODULUS OF A BITUMINOUS COAL

H. M. Ledbetter and M. W. Austin

Fracture and Deformation Division, Center for Materials  
Science, National Bureau of Standards

J. E. Callanan

Chemical Engineering Science Division, Center for Chemical  
Engineering, National Bureau of Standards,  
Boulder, Colorado 80303

### INTRODUCTION

Elastic properties of coal provide three types of information. First, elastic constants such as Young modulus and Poisson ratio provide essential engineering-design parameters. These parameters enter calculations for load-deflection, thermo-elastic stress, buckling instability, and crack propagation. Second, elastic constants provide valuable material characterization. They reflect differences in thermal-mechanical history, in void and crack content, and in chemical composition. Third, elastic constants relate closely to interatomic arrangements and interatomic forces. From interatomic force constants ("spring constants"), one can specify the complete set of elastic constants (two for isotropic symmetry, nine for orthotropic symmetry). Because coal exhibits three macroscopic orthogonal mirror planes, it must exhibit orthotropic elastic symmetry. Recently, for isotropic solids, Ledbetter [1] described elastic constants and their interrelationships with other physical properties.

As described by Nowick and Berry [2], internal friction, or anelasticity, amounts to the imaginary part of either elastic stiffness or elastic compliance. Internal friction manifests itself in many ways: width of a resonance peak, amplitude decay of a stress wave, phase lag of strain behind stress, and area within an elastic-region stress-strain loop. Each of these manifestations provides a possible measurement method. As described below, we used resonance-peak width. In crystalline solids, internal friction usually arises from various relaxations: point defects, dislocations, grain boundaries, phonons, magnetoelastic couplings, and electron configurations. In amorphous polymers, the principal relaxation arises from the glass transition, attributed to large-scale rearrangements of the principal polymer chain. At lower temperatures, one observes secondary relaxations caused by side groups capable of independent hindered rotations. Adapted from Houwink and de Decker [3], Fig. 1 shows for four polymers the internal friction versus temperature, which we often call the mechanical-loss spectrum. Most polymers fit the general pattern suggested in Fig. 1.

Recently, Szwilski [4] described a method for determining the anisotropic elastic moduli of coal. He reported seven previous studies of coal's elastic constants. Besides these seven, at least six other experimental studies exist: Constantino and Trettennero [5] and Wert, Weller, and Völker [6-10].

Wert and Weller [6-10] used a torsional pendulum at frequencies near 1 Hz to measure between 10 and 450 K the temperature dependence of both the torsional modulus,  $G$ , and the internal friction,  $\tan \delta = Q^{-1}$ . These authors were first to report coal's internal-friction spectrum, which reveals mechanical-relaxation phenomena. See Fig. 2. Based on their experimental studies, Weller and Wert support a polymeric model for coal. In the above temperature range, these authors detected three peaks (denoted  $\alpha$ ,  $\beta$ ,  $\gamma$ ) and possible evidence for a low-temperature peak ( $\delta$ ) near 50 K. These peaks correspond closely to those observed in most polymers. Wert and Weller [7] ascribe the  $\alpha$ -peak to massive motion of macromolecules, related probably to the

glass transition. They ascribe the  $\beta$ -peak to reorientation under stress of side units, perhaps associated with water. They ascribe the  $\gamma$ -peak to twisting or other reorientation of segments of a linear section of  $\text{CH}_2$  units. They believe this peak decreases with coal's increasing carbon content (rank).

The present study relates closely to those of Wert and Weller [6-10]. The principal differences are three: (1) We used larger specimens by a factor of approximately 40 in volume. (2) We used higher frequencies: 45 kHz to their 1 Hz. (3) We studied a Young-modulus (extensional) deformation mode while they studied a torsional mode. Twisting induces no volume changes while uniaxial stress involves both shear and dilatation.

#### MATERIAL

We studied a high-volatile Eastern-Kentucky bituminous coal studied previously by Wert and Weller [7], who reported a composition of 81.8% carbon (wt. pct. daf). Specific gravity measured at 293 K by Archimedes's method was 1.316.

#### SPECIMENS

We prepared square-cross-section rod specimens, 0.48 cm by 2.43 cm, by sawing. The specimen reported on here lay in the coal's bedding plane and along the major cleat direction. We determined this orientation visually, based on easily discernible striae and longitudinal markings.

#### MEASUREMENTS

For measuring the Young modulus,  $E$ , and internal friction,  $Q^{-1}$ , we used a Marx-composite-oscillator method [11-14]. At  $T = 293$  K, the composite-oscillator resonance frequency was 45 kHz. Our version of this apparatus operates between 20 and 100 kHz in the fundamental mode. Using overtones permits higher frequencies. Cooling to liquid-nitrogen temperature (76 K) was achieved with a probe-and-dewar arrangement described elsewhere [13]. To obtain the Young modulus, one uses the relationship

$$E = 4\rho f_0^2 l^2 \quad (1)$$

where  $\rho$  denotes mass density,  $f_0$  specimen resonance frequency for the fundamental (half-wavelength) mode, and  $l$  specimen length. In a Young-modulus deformation mode, the rod cross-section is immaterial, if it is uniform along the specimen length. To obtain internal friction, one uses the relationship

$$Q^{-1} = (f_2 - f_1)/f_0 \quad (2)$$

where  $f_1$  and  $f_2$  denote the frequencies at the half-power points of the resonance peak and  $f_0$  denotes resonance frequency. Thus, versus frequency, one measures strain amplitude detected as the voltage generated in a piezoelectric quartz gage crystal. We did not correct for coal's contraction during cooling. Cooling rates were 2 K/min. A sweep over the resonance-frequency range required 40 s. Measurements made at lower cooling rates should show less scatter.

Concerning measurement uncertainties, our limited experience with this material precludes a precise statement. We guess that  $E$  is accurate within a few percent and  $Q^{-1}$  within about 20 percent. Scatter in Fig. 3 indicates the imprecisions.



## RESULTS

Figure 3 shows the principal results:  $E$  and  $Q^{-1}$  versus temperature between 293 and 76 K. We show  $E$  as a dimensionless ratio to the ambient-temperature value.

## DISCUSSION

Our ambient-temperature value,  $E = 6.4$  GPa, exceeds considerably the range for coal reported by Constantino and Trettenero [5], 3.0 to 4.5 GPa, measured perpendicular to the bedding plane. But it falls within the 2.1 to 9.5 GPa range reported by Szwilski [4] for the bedding plane. To minimize effects of microcracks, Szwilski applied a small confinement force, which would not affect the intrinsic elastic constant. Compared with polymers, this Young modulus is only slightly lower. For example, for four technical polymers, Athougies et al. [15] reported the dynamic Young modulus which showed a range of 7 to 9 GPa.

The extrapolated increase in  $E$  during cooling to zero temperature,  $E(0)/E(293) \cong 1.7$ , lies considerably below the torsional-modulus increase found by Wert and Weller [7],  $G(0)/G(293) \cong 2.6$ . For isotropic materials,  $E$  and  $G$  relate simply through the bulk modulus,  $B$ :

$$E = 9BG/(3B+G). \quad (3)$$

By differentiation

$$\frac{\Delta E}{E} = \frac{1}{(3B+G)} \left( G \frac{\Delta B}{B} + 3B \frac{\Delta G}{G} \right). \quad (4)$$

Taking the Poisson ratio to be 1/3, then [1]

$$\frac{\Delta E}{E} = \frac{1}{9} \left( 8 \frac{\Delta G}{G} + \frac{\Delta B}{B} \right). \quad (5)$$

Thus, the large  $\Delta G/G$  relative to  $\Delta E/E$  must arise from another source, not from a smaller  $\Delta B/B$  change, which contributes approximately one-ninth. One can identify four possible sources: measurement frequency, strain amplitude, temperature-dependent relaxation strength, and material anisotropy. Without further study, we can not comment on these possibilities.

Usually, one can describe the  $E(T)$  behavior by a relationship [16]

$$E(T) = E(0) - s/\exp(t/T) \quad (6)$$

where  $E(0)$  denotes zero-temperature Young modulus,  $s$  an adjustable parameter related to zero-point vibrations,  $t$  the Einstein temperature, and  $T$  temperature. This relationship fits the  $E(T)$  measurements only approximately because of the irregularities in  $E(T)$  that arise from cooling through some relaxation mechanisms, principally the  $\gamma$  peak. From a least-squares fit to the  $E(T)$  results shown in Fig. 3, we obtain  $t = 345$  K, a rough estimate of coal's effective Einstein temperature. In a preliminary study, Merrick [17] modeled coal's specific heat with an Einstein model. He made the usual Einstein-model interpretation: "the characteristic temperatures ... reflect the average properties of the bonds." For the temperature range 0-800°C, Merrick obtained  $t = 1200$  K. A second approach used a two-Einstein-temperature model with  $t_1 = 380$  K and  $t_2 = 1800$  K. This model recognizes anisotropic binding forces: strong forces within layers and weaker forces between layers. It gives a lower  $C_p(T)$  curvature and better agreement with measurement. We compare these

results with graphite where Komatsu [18] used a lattice-vibration model and the  $C_{44}$  elastic constant to predict that  $t_1 = 135$  K and  $t_2 = 1860$  K. We take this latter characteristic temperature as the upper bound of any "lattice" vibrations representing binding forces in coal. A better upper bound may arise from the  $t = 1680$  K Einstein temperature of diamond [1], where the carbon-carbon tetrahedral-covalent bond strength exceeds that of any other known material.

We turn now to internal friction. Figure 3 shows a broad peak centered near 240 K, which we interpret as the Wert-Weller  $\gamma$  peak detected at 130 K. From eq. (3.5-5) in Nowick and Berry

$$Q = k \ln (\omega_2/\omega_1) (T_{p1}^{-1} - T_{p2}^{-1})^{-1} \quad (7)$$

where  $k$  denotes Boltzmann's constant,  $Q$  denotes activation energy,  $\omega$  denotes angular frequency, and  $T_p$  denotes peak temperature, we obtain  $Q = 0.26$  eV compared with 0.18 eV obtained by Wert and Weller [10].

The upturn in Fig. 3 just above 76 K signifies a strong low-temperature ( $\delta$ ) peak only suggested in some of the Wert-Weller studies. This peak requires further study by cooling to lower temperatures. This  $\delta$  peak may appear stronger in our study because our higher measurement frequency (by a factor of  $5 \cdot 10^5$ ) approaches more closely the  $\delta$ -peak resonance frequency. From eq. (3.5-4) in Nowick and Berry

$$T_p = \frac{-Q}{k} \frac{1}{\ln \omega t_0} \quad (8)$$

where  $t_0 = \nu_0^{-1}$  denotes a fundamental relaxation time and  $\nu_0$  a fundamental frequency related to a mechanical-relaxation mechanism. Thus, a lower  $T_p$  corresponds to either lower  $Q$  or lower  $\nu_0$ . Lower  $T_p$  usually corresponds to a smaller vibrating unit.

#### CONCLUDING REMARKS

Given that coal is a polymer, then the enormous body of pre-existing polymer physics should transfer to coal. This physics includes measurement methods, mechanical models (Kelvin, Maxwell, etc.), molecular interpretations, structure geometry, viscoelasticity theory, and anisotropic phenomena. Many books summarize the state of polymer physics; several relate especially to dynamical-mechanical properties: Alfrey [19], Tobolsky [20], Ferry [21], Heijboer [22], McCrum, Read, and Williams [23], Christensen [24], Ward [25], Baer and Radcliffe [26], Nielsen [27], Read and Bean [28], and Murayama [29].

From the materials-science viewpoint, the most important relationships are those between structure and macroscopic properties. For polymers, Murayama [29] summarized the dynamical-mechanical studies:

The investigation of the dynamic modulus and internal friction over a wide range of temperatures and frequencies has proven to be very useful in studying the structure of high polymers and the variations of properties in relation to end-use performance. These dynamic parameters have been used to determine the glass transition region, relaxation spectra, degree of crystallinity, molecular orientation, crosslinking, phase separation, structural or morphological changes resulting from processing, and chemical composition in polyblends, graft polymers, and copolymers.

Thus, one expects similar possible results in applying dynamical-mechanical methods to coal.

Our preliminary measurements show that, by dynamic methods, one can measure coal's elastic constants and mechanical-relaxation spectrum in a Young-modulus mode at kilohertz frequencies.

Boyer [30] pointed out that in studying the relaxation spectra of polymers one can focus on five different aspects: (1) experimental methods; (2) individual spectra as a characterization; (3) spectra features common to many materials; (4) correlation of loss peaks with other physical and mechanical properties; (5) molecular mechanisms of loss peaks. The second aspect includes effects of thermal history, crystallinity, measurement frequency, external force field, molecular orientation, and other variables.

Further studies at NBS could include eight principal efforts: (1) refine our preliminary measurements and extend them to both lower and higher temperatures; (2) determine the complete nine-component elastic-constant tensor; (3) attempt to relate the mechanical-relaxation peaks to mechanisms; (4) determine by measurement the changes of these peaks produced by variables such as moisture, heating, aging; (5) possibly relate microstructure to physical properties; (6) model the macroscopic elastic constants in terms of those of constituents; (7) determine complete damping tensor; (8) focus especially on the low-temperature  $\delta$ -peak, which appears larger in our measurements than in previous ones.

#### ACKNOWLEDGMENT

Professor C.A. Wert (Urbana) helped us get started on this study by providing samples, reprints, and encouraging advice. Dr. M. Weller (Stuttgart) provided critical, useful comments.

#### REFERENCES

- [1] Ledbetter, H.M., in *Materials at Low Temperatures* (Amer. Soc. Metals, Metals Park, 1983), p. 1.
- [2] Nowick, A.S. and Berry, B.S., *Anelastic Relaxation in Crystalline Solids* (Academic, New York, 1972).
- [3] Houwink, R. and de Decker, H.K. (eds.), *Elasticity, Plasticity, and Structure of Matter* (Cambridge U.P., London, 1971), p. 161.
- [4] Szwilski, A.B., *Int. J. Rock Mech. Min. Sci. Geomech. Astr.* **21**, 3 (1984).
- [5] Constantino, M. and Trettenero, S., *J. Appl. Phys.* **54**, 76 (1983).
- [6] Wert, C.A. and Weller, M., *J. Physique* **42**, C5-581 (1981).
- [7] Wert, C.A. and Weller, M., *J. Appl. Phys.* **53**, 6505 (1982).
- [8] Weller, M., Völkl, J., and Wert, C., in *Proc. 1983 International Conference on Coal Science* (Pittsburgh, August 1983), p. 283.
- [9] Weller, M. and Wert, C.A., *J. Physique* **44**, C9-191 (1983).
- [10] Weller, M. and Wert, C., *Fuel* **63**, 891 (1984).
- [11] Marx, J., *Rev. Sci. Instrum.* **22**, 503 (1951).
- [12] Robinson, W.H. and Edgar, A., *IEEE Trans. Son. Ultrason.* **SU-21**, 98 (1974).
- [13] Weston, W.F., *J. Appl. Phys.* **46**, 4458 (1975).
- [14] Ledbetter, H.M., *Cryogenics* **20**, 637 (1980).
- [15] Athougies, A.D., Peterson, B. T., Salinger, G.L., and Swartz, C.D., *Cryogenics* **12**, 125 (1972).
- [16] Varshni, Y.D., *Phys. Rev.* **82**, 3952 (1970).
- [17] Merrick, D., *Fuel* **62**, 540 (1983).
- [18] Komatsu, K., *J. Phys. Soc. Japan* **10**, 346 (1955).
- [19] Alfrey, T., *Mechanical Behavior of High Polymers* (Interscience, New York, 1948).

- [20] Tobolsky, A.V., Properties and Structure of Polymers (Wiley, New York, 1960).
- [21] Ferry, J.D., Viscoelastic Properties of Polymers (Wiley, New York, 1961).
- [22] Heijboer, J., Physics of Noncrystalline Solids (North-Holland, Amsterdam, 1965).
- [23] McCrum, N.G., Read, B.E., and Williams, G., Anelastic and Dielectric Effects in Polymeric Solids (Wiley, London, 1967).
- [24] Christensen, R.M., Theory of Viscoelasticity (Academic, New York, 1971).
- [25] Ward, I.W., Mechanical Properties of Solid Polymers (Wiley, New York, 1971).
- [26] Baer, E. and Radcliffe, S.V., Polymeric Materials (Amer. Soc. Metals, Metals Park, 1974).
- [27] Nielsen, L.E., Mechanical Properties of Polymers and Composites (Dekker, New York, 1974).
- [28] Read, B.E. and Dean, G.O., The Determination of Dynamic Properties of Polymers and Composites (Wiley, New York, 1978).
- [29] Murayama, T., Dynamic Mechanical Analysis of Polymeric Material (Elsevier, Amsterdam, 1978).
- [30] Boyer, R.F., in ref. [26], p. 277.

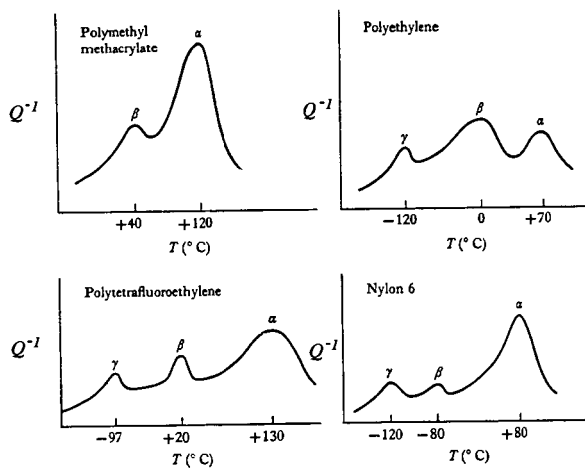


Fig. 1. Dynamic loss modulus versus temperature for four polymers; from Houwink and de Decker [3].

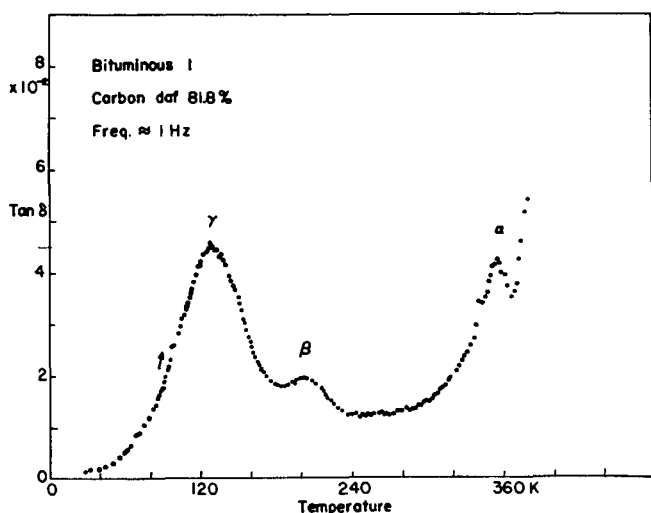


Fig. 2. Internal-friction spectrum of a bituminous coal; from Wert and Weller [7].

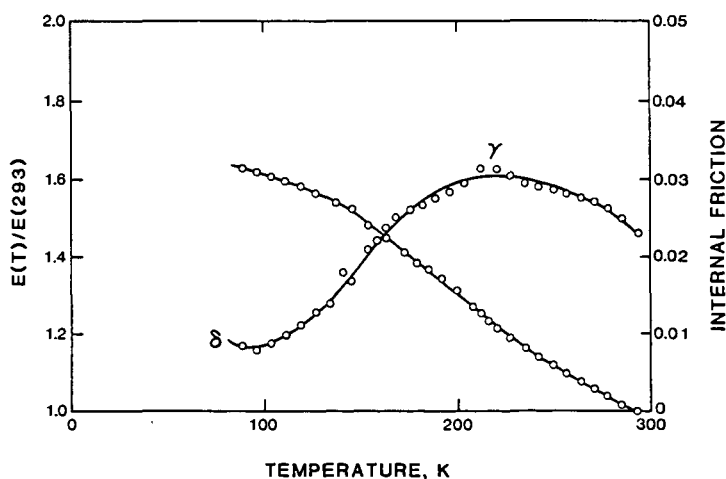


Fig. 3. Dynamic Young modulus and internal friction versus temperature measured near 50 kHz. A strong mechanical relaxation ( $\gamma$ ) occurs near 240 K. A strong low-temperature peak ( $\delta$ ) is suggested below 75 K.

## THE USES OF DIELECTRIC SPECTRA AND IMMERSIONAL CALORIMETRY IN THE CHARACTERIZATION OF LOW-RANK COALS

C. Tye, R. Neumann, and H.H. Schobert

University of North Dakota Energy Research Center  
Box 8213, University Station  
Grand Forks, North Dakota 58202

### Introduction

Moisture in low-rank coals is believed to involve at least two fundamentally different mechanisms for binding water to the coal matrix (1). The first type of moisture behaves as if were "free"; the vapor pressure versus temperature behavior is that of pure water. The second type occurs at sites where it is bound more tightly, resulting in a lowering of the vapor pressure relative to that of pure water at the same temperature. Such moisture may be hydrogen bonded to oxygen-containing functional groups or it may be incorporated as water of hydration of ion-exchangeable cations. There might also be tightly entrained moisture, in the pore structure, between the thermodynamically "free" moisture and the chemically bonded moisture. The objective of our work was to investigate the application of two experimental techniques, dielectric relaxation spectroscopy and immersional calorimetry, to the characterization of moisture content and pore structure of low-rank coals.

Dielectric techniques can sometimes prove valuable in studying bulk matter containing specific polar molecules (2, 3). From a theoretical standpoint, a parallel plate capacitor with a vacuum between its electrodes ceases to behave as a pure capacitance (at all frequencies) when a condensed matter dielectric is inserted. If an alternating voltage is applied to the capacitor containing a dielectric, the current and voltage will no longer be precisely  $\pi/2$  radians out of phase,  $\pi/2$  being the value for a vacuum-filled capacitor. The degree of departure from  $\pi/2$  radians as expressed by the angle  $\delta$ , depends on the "lossyness" of the dielectric.

The process of absorption (defined as the concentration of a substance on a surface where the substance, the absorbate, is in a gas or liquid form and the absorbent a solid) is spontaneous and is characterized by a fall in the entropy of the system and a decrease in surface free energy. This necessitates the absorption process to be exothermic, the resultant energy being referred to as the heat of immersion or heat of wetting. Therefore the exothermic heat liberated when a porous solid is immersed in a liquid is related to the surface energy of the solid and the measurement of it can be used to determine the surface area of various solid samples.

### Apparatus and Materials

#### (a) Dielectric Cell.

The dielectric cell was constructed from two stainless steel electrodes attached to corresponding outer stainless steel supports by means of a screw sandwiching a disk of insulating Teflon (see Figures 1 and 2). One electrode was 63 mm in diameter. The other, 50 mm in diameter, was surrounded by a 6 mm wide stainless steel annulus from which it was insulated by Teflon tape. This outer guard ring was kept at ground potential to eliminate fringing fields, edge effects and surface conduction across the dielectric being studied. The impedance measuring instrument used was a General Radio 1621 precision capacitance measuring system. This experimental setup enables the measurement of the equivalent parallel capacitance and resistance of the cell to be made at a given temperature and

frequency. For the subambient temperature measurements, the cell was placed in a styrofoam box and cooled with liquid nitrogen to the starting temperature.

(b) Differential Calorimeter.

The differential calorimeter consists, in essence, of two discrete units, each a calorimeter in its own right (see Figures 3 and 4). Each would have its own (identical to the other) paddle stirrer mechanism, heater circuit, temperature sensing circuit and Dewar flask. This twin calorimeter unit would then be operated in differential mode; i.e., a similar amount of wetting liquid would be put into each calorimeter Dewar, the calorimeters being imbedded in a metal heat sink for the thermal stability required, and the coal or carbon sample would be added to one Dewar. The temperature measuring circuit consists of a pair of matched thermistors, inserted into opposing arms of a Wheatstone bridge. Thus the heat liberated when the solid sample was added to the working Dewar would upset the balance conditions of the Wheatstone bridge due to the resistance change of the working Dewar's thermistor, with respect to the reference Dewar's thermistor resistance, and would produce an out-of-balance current that can be directly measured on a potentiometric chart recorder. This method of temperature measurement has the advantage that it is referenced to ambient conditions and not, for example, to the temperature of melting ice. The heat sink was fabricated from a 38 x 30 x 23 cm aluminum block. Two holes were bored in the heat sink of diameter slightly larger than the diameter of the Dewars, to enable them to be easily lowered inside. The stirring mechanism was designed to rapidly mix the material to be tested with the wetting liquid, producing a maximum dispersion of the material in the liquid with a minimum production of heat from the work of stirring. The work of stirring should ideally be constant. The rotating paddle type of stirrer was used, the glass paddle being mounted inside a guide tube which was in turn supported in a ground glass cone.

(c) Coal Samples.

Two coals were chosen for study: Gascoyne (North Dakota) lignite and Yampa (Colorado) subbituminous. The samples were obtained from the University of North Dakota Energy Research Center coal sample library. Composition data is given in Table I.

### Testing Procedures

(a) Dielectric Measurement.

Samples of several forms were used in the dielectric cell. Initial tests were performed with 63 mm diameter, 3 mm thick disks of coal sawn from solid blocks. Subsequent work involved 16, 30, 60, and -60 mesh powders. The connected and loaded cell was lowered into the styrofoam box and liquid nitrogen added to cool the cell and contents to around -190°C. The capacitance bridge was balanced and then the cell was allowed to warm up, during which time the measurements of T, temperature; F, frequency; C, capacitance, and G, conductance were performed. These variables would then subsequently be inserted into Equation 1 to determine the phase shift  $\tan \delta$  at a given frequency. The phase shift, expressed as the phase angle between voltage and current, is a function of the specific resistance of the coal, which in turn is dominated by the presence of its conductive phase, water.

$$\tan \delta = \frac{G}{2\pi FC} \quad 1)$$

A typical experiment involved taking data over a temperature range of -170° to 0°C at 0.1, 1.0 and 10.0 kHz. The temperature was measured by means of a chromel-alumel thermocouple attached to the guard ring. Plots of  $\tan \delta$  against temperature yielded the required dielectric spectra for that frequency.

Table I. ~ Characteristics of Coal Samples.

Sample	Gascoyne	Yampa
Rank	Lignite	Subbituminous
Mine Location	Bowman Co., North Dakota	Routt Co., Colorado
Heating Value (maf), Btu/lb	11677	13524
<u>Proximate Analysis, (As Rec'd); wt%:</u>		
Moisture	37.60	10.30
Volatile Matter	29.06	32.20
Fixed Carbon	0.00	44.00
Ash (ASTM)	9.70	13.50
<u>Ultimate Analysis (maf); wt%:</u>		
Carbon	69.05	80.81
Hydrogen	4.73	4.50
Nitrogen	1.04	2.53
Oxygen	23.15	11.30
Sulfur	2.03	0.79

## (b) Differential Calorimetry.

The technique used with the differential calorimeter was to add 75 ml of wetting fluid (methanol or tetralin) to each of the clean, dry Dewar vessels. The top sections, complete with sensing and stirring apparatus were then lowered into the Dewars. Two grams of sample in a stoppered bottle was placed on top of the heat sink so that it could attain the same temperature as the rest of the system. The chart recorder was started after the bridge had been adjusted to its optimum operating conditions (250 mV). When the temperature remained constant, shown by a straight horizontal line on the trace, the calibration heater was switched on for 60 seconds (A to B, Figure 5). During this time, the voltage across the heater and the current passing through it were determined. After a reasonable portion of the cooling curve had been recorded for extrapolation purposes (B to C, Figure 5), the weighed sample was introduced to the working Dewar by means of the funnel mounted in the cone (C to D, Figure 5). A reasonable portion of the cooling curve was again recorded (D to E, Figure 5) and later another application of the heater for a known time period was applied to the working Dewar with the resulting temperature rise (E to F, Figure 5).

The heat of wetting in calories per gram is given by:

$$H = \frac{VIT}{J\sigma_h} \times \frac{\sigma_w}{W} \quad 2)$$

where V is the heater voltage in volts.

I is the heater current in amps.

T is the time the heater was switched on for (in seconds)

which produced the corrected temperature deflection of  $\sigma_h$ .

$\sigma_w$  is the corrected temperature deflection when the sample was wetted with the wetting liquid.

J = A constant = 4.18 joules per calorie.

W = weight of sample in grams.



Note that the second application of the heater (after the addition of the sample) will always produce a lower deflection, due the contribution of the sample to the total specific heat capacity of the Dewar and contents. The expression for describing the thermal capacity of the system is:

$$C = C_F + M_L S_L + M_C S_C \quad 3)$$

where  $C$  = thermal capacity of system,  
 $C_F$  = thermal capacity of fixed apparatus in the Dewar  
 (heat supports, stirrer, Dewar, etc.),  
 $M_L$  = mass of liquid,  
 $S_L$  = specific heat capacity of wetting liquid,  
 $M_C$  = mass of sample,  
 $S_C$  = specific heat capacity of sample.

It should therefore be possible to get an idea of the heat capacity of the sample by the difference in deflections between the first and second applications of the calibration heater.

The heat of wetting per unit area for any given liquid on a particular surface is a constant for that liquid provided the liquid wets the surface of the solid perfectly. The value of this constant is given by Bond and Spencer (4) as 10.7 for methanol. In order to convert the heat of wetting results into surface areas, Bond and Spencer measured the heat of wetting of a non-porous carbon black having a surface area of 230 m<sup>2</sup>/gm. Thus, the heat of wetting per m<sup>2</sup> = 10.7/230 calories. Alternatively, 1 calorie of heat is liberated when 21.5 m<sup>2</sup> of carbon surface is wetted by methanol.

The corrected temperature rises were obtained (6) by extrapolating the cooling curve until it crossed the vertical line drawn from the point when the heater was initially switched on, or the point when the coal was added. In this way the effect of the cooling of the Dewar, which would occur during the time the heater was on, would be nullified. Therefore, each time the heater was turned on or the coal was added, enough time had to elapse afterwards for a representative amount of the cooling curve to be recorded for an accurate extrapolation to be made. This vertical distance would be measured and treated as the corrected temperature rise.

In most cases, the slope of the temperature against time curve before and after heat input was the same, making the actual time at which the corrected temperature rise was determined not critical.

## Results and Discussion

Figure 6 shows the  $\tan \delta$  versus temperature behavior for a Yampa (Colorado) subbituminous coal of 10% to 12% moisture; the coal had been stored under water and air-dried before insertion into the cell. No appreciable weight loss occurred during air drying. Between -60° and 0°C (not shown) the  $\tan \delta$  increases without bound; this is most likely caused by an ionic double layer formed by mobile ions present in the coal. The peaks show a simple Debye-like behavior in that they are relatively narrow and the temperature maxima shift to higher temperatures with increasing frequency. The solitary curve at the bottom of the figure is a 0.1 kHz  $\tan \delta$  plot for the same sample after it had been freeze-dried for two days at 10 microns pressure. The total loss of moisture was approximately 10% of the original weight of the coal. The complete loss of the large dispersion upon water removal is taken to be evidence that the dispersion is indeed caused by the relaxation of water molecules. When the coal sample was reconstituted with water after freeze-drying, there was no significant difference in dielectric spectra with the original spectra from the mine fresh sample. Figure 7 shows the dielectric characteristics of this Yampa coal on removing and replacing the moisture for one frequency.

Figure 8 is the resultant dielectric spectra of the Gascoyne lignite sample. Here there are two distinct sets of peaks; one set at  $-102^{\circ}$ ,  $-92^{\circ}$ , and  $-80^{\circ}\text{C}$ , the other set at  $-60^{\circ}$ ,  $-50^{\circ}$ , and  $-36^{\circ}\text{C}$ . The latter set is likely attributable to the presence of macroscopic crystals of ice. Accurate dielectric measurements on pure bulk ice have placed the spectrum in this vicinity (5). Figure 9 presents the spectrum of the same lignite after air drying for several days until a constant weight had been achieved. The upper set of peaks is missing and the lower set appears at  $-108^{\circ}$ ,  $-100^{\circ}$ , and  $-90^{\circ}\text{C}$ . The peak locations are virtually identical to those in the Colorado subbituminous coal. Finally, freeze-drying resulted in the loss of more water and produced the 1 kHz spectrum shown at the bottom of the Figure. Note again the evidence for associating the large relative maxima with the presence of water.

When the Gascoyne sample was reconstituted with water after freeze-drying, two distinct set of peaks were again apparent; the spectrum was not significantly different from that of Figure 8. These experiments indicate that this lignite incorporates 80% of its moisture in a loosely-bound form which freezes to ice below  $0^{\circ}\text{C}$  and that the remaining 20% is present in the coal possibly as water of hydration, which does not crystallize into ice. The Colorado subbituminous coal contains only the latter type of bound moisture. These results are consistent with the conclusion about two types of bound water, based on vapor pressure studies (3).

Samples of -60 mesh Yampa subbituminous and Gascoyne lignite were tested to see what effect powdering had on the dielectric spectral quality. The spectra displayed in Figures 10 and 11, respectively, show resolved  $\tan \delta$  peaks at approximately the same temperature locations observed for the solid disk experiments. This proves that the powdered coal samples show  $\tan \delta$  peaks of sufficient quality to alleviate the need for preparing solid disk samples.

A series of experiments were conducted to test the effect of different mesh sizes of coal granules on spectral peaks and spectral quality, to determine if particle size had an effect on the type or amount of water content of the coal. Yampa (Colorado) subbituminous was sieved into mesh sizes 16, 30, 60, and fines less than -60. The spectral quality for the first set of peaks (presumably corresponding to the tightly-bound water of hydration) improves as the size of the specimen particle decreases. The spectral peaks are much more clearly defined for the -60 mesh size than for those at 16 mesh.

The interpretation of the dielectric spectra and correlations of dielectric results with other measurable coal characteristics is still in progress. However, the size, location, and number of peaks in dielectric spectra provide a significant quantity of information on the state and behavior of the coal's intrinsic moisture. There are many ways in which water may be attached to the coal, either loosely as water in the pore structure or chemically bonded to the coal matrix as, for example, water of hydration. Measurement of dielectric properties of this water present in the coal has indicated the distinction between at least two of the mechanisms of the water bonding.

A sample of the Gascoyne lignite was tested in the immersion calorimeter with methanol. Its heat output (determined from Figure 12) was found to be 65.74 joules per gram (15.49 calories, per gram). Using a 10.7 conversion factor (4) gives a surface area of  $165.72 \text{ m}^2\text{gm}^{-1}$ . A similar sample of Yampa subbituminous coal was tested and gave rise to the output shown in Figure 13. It is interesting to note the key difference between these two figures, that of the nearly instantaneous heat output of the lignite (the exothermic heat of wetting was liberated in a few seconds) in comparison with that of the subbituminous coal. In the latter case, the heat output occurred over several hours, presumably as the methanol wetting liquid explored the system of micropores which were approaching molecular dimensions. The specific and corresponding surface area were not calculated due to the difficulty in obtaining a corrected temperature deflection  $\alpha_w$  from Figure 13.

Further testing was carried out on various mesh sizes of Gascoyne lignite to determine if the external or apparent surface area was a significant factor in the total (including internal pores) surface area value. Mesh sizes of 16, 30, 60, and

powder less than -60 were used without significant variation in the heat output. The total surface area of a coal is therefore very tolerant of sample powder size, the internal pore surface area term being dominant when compared to the external or apparent surface area term. This is the expected result if the pores are very small.

A probe liquid of larger molecular volume than methanol should not be so able to penetrate the porous structure, especially the micropore region which can account for up to 95% of the total surface area. Tetrahydronaphthalene (tetralin) was thus used because of its relatively large sized molecules and because of its interest as a hydrogen donor in liquefaction. Yampa subbituminous and Gascoyne lignite were then tested in the calorimeter using tetralin. The results of the surface area determinations are tabulated in Table II along with the corresponding results for the two coals in methanol.

Table II. Surface Area of Coals Using Different Wetting Liquids.

Coal Sample	Surface Area ( $\text{m}^2/\text{gm}$ )	
	Methanol	Tetralin
Colorado Subbituminous	>200	9.05
Gascoyne Red lignite	165.72	5.15

Since the tetrahydronaphthalene is a larger molecule than methanol, it is unable to penetrate the smallest pores in the coal. Heat is only liberated from the very large pores and the external or apparent surface as if the porous coal had transformed into a non-porous carbon black. In future experiments the use of probe liquids of intermediate molecular sizes between those of methanol and tetrahydronaphthalene will yield information on the relative amounts (distributions) of micro, transitional and macropores.

#### Acknowledgment

The authors are pleased to acknowledge the valuable assistance of Wayne Kinney in carrying out some of the experimental measurements of this project.

#### Literature Cited

1. Schobert, H.H. "Characterization of Low-Rank Coals Important in Their Utilization." Oral presentation at Penn State; short course on coal. November 1-5, 1982.
2. McCrum, N.G.; Read, B.E.; and Williams, G. "Anelastic and Dielectric Effects in Polymeric Solids." Wiley, New York, 1967.
3. Daniel, V.V. "Dielectric Relaxation", Academic Press, New York, 1967.
4. Bond, R.L. and Spencer, W.D. Proceedings of the 1957 conference on carbon (University of Buffalo), 1958, p. 357.
5. Mahajan, O.P. "Coal Structure." Meyers, R.A., Ed., Academic Press, New York, p. 65, 1982.
6. Tye, C. "Design, Building and Operation of a Differential Calorimeter." Final year project, University of Salford, U.K., April 1983.

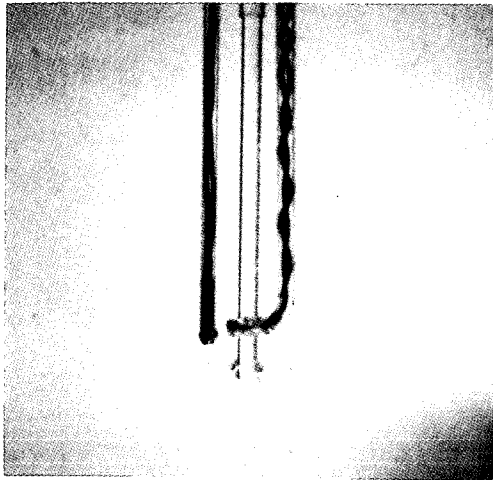


Figure 3. Shows details of one calorimeter.

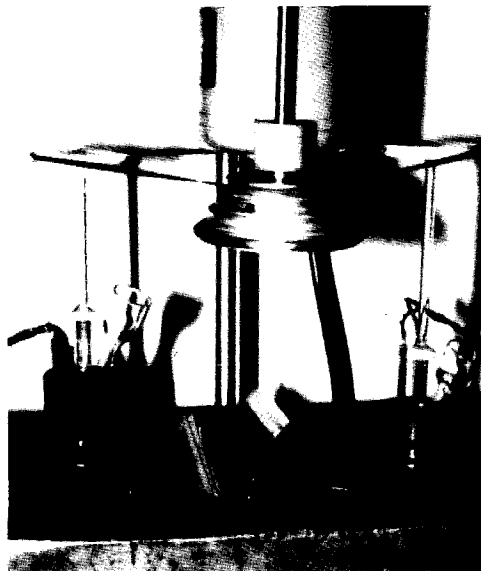


Figure 4. Shows overall differential calorimetry system.

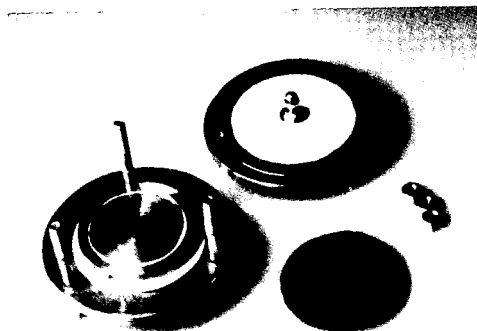


Figure 1. The disassembled cell and a water-saturated solid sample of Gascoyne Red lignite.

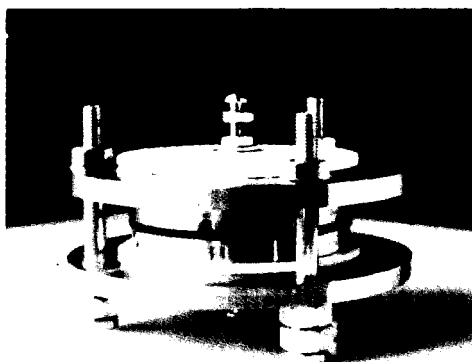


Figure 2. The assembled dielectric cell.

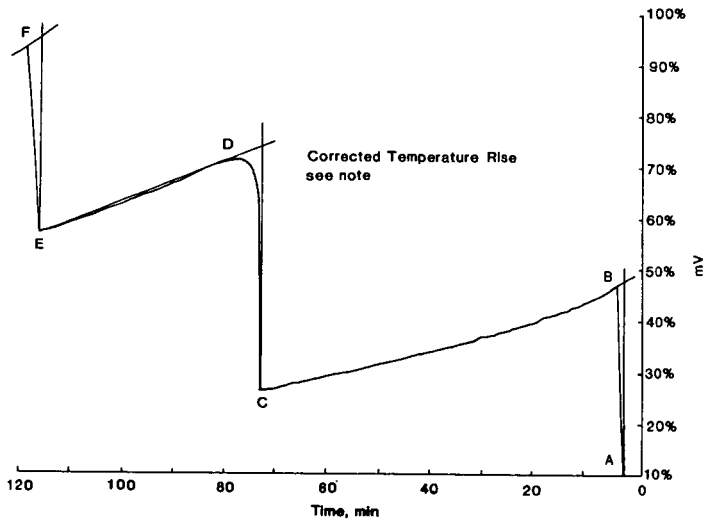


Figure 5. Trace for activated coconut shell carbon (2 mV full scale deflection 120 mm per hour).

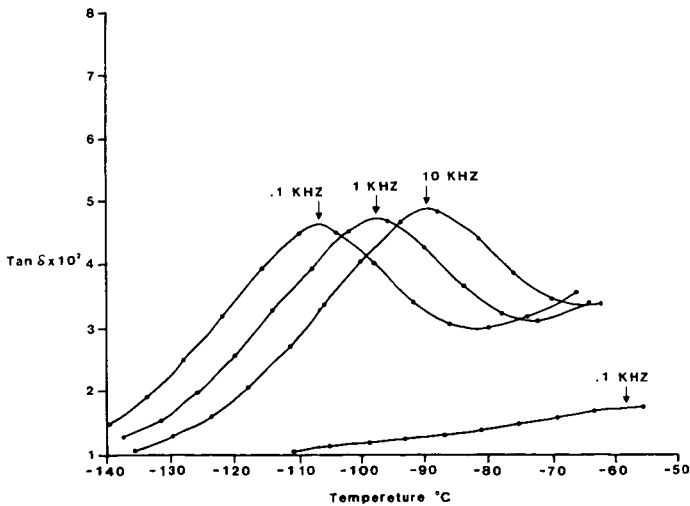


Figure 6. Phase shift vs. temperature for air-dried Yampa (Colorado) subbituminous coal.

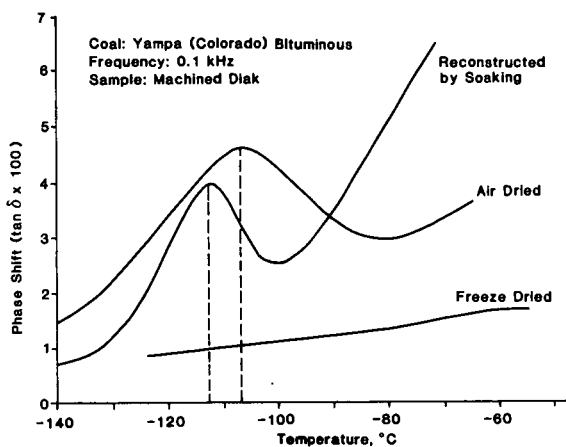


Figure 7. Dielectric characteristics of a subbituminous coal, showing effect of removal and replacement of tightly bound moisture.

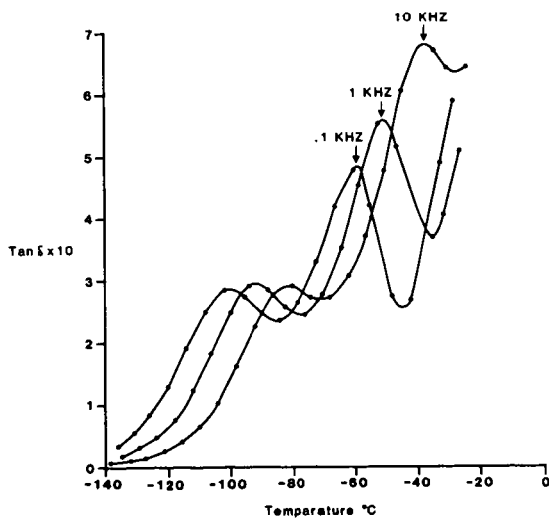


Figure 8. The temperature dependence of  $\tan \delta$  is depicted for the water-saturated Gascoyne Red lignite.

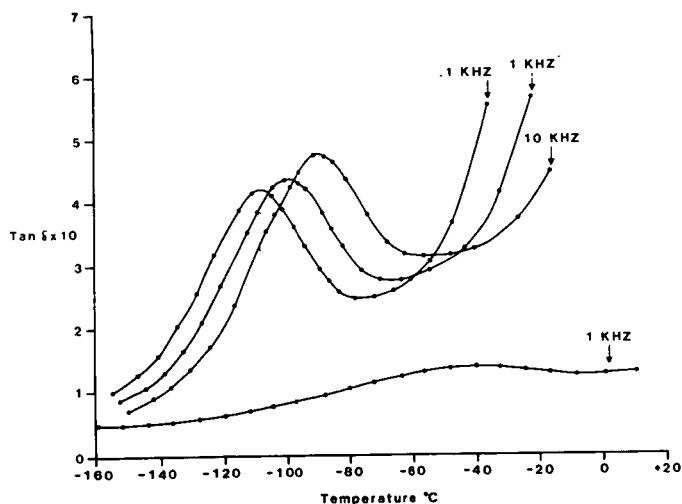


Figure 9. The temperature dependence of  $\tan \delta$  is depicted for the air-dried Gascoyne lignite. The lower (kHz) dispersion is for the freeze-dried coal.

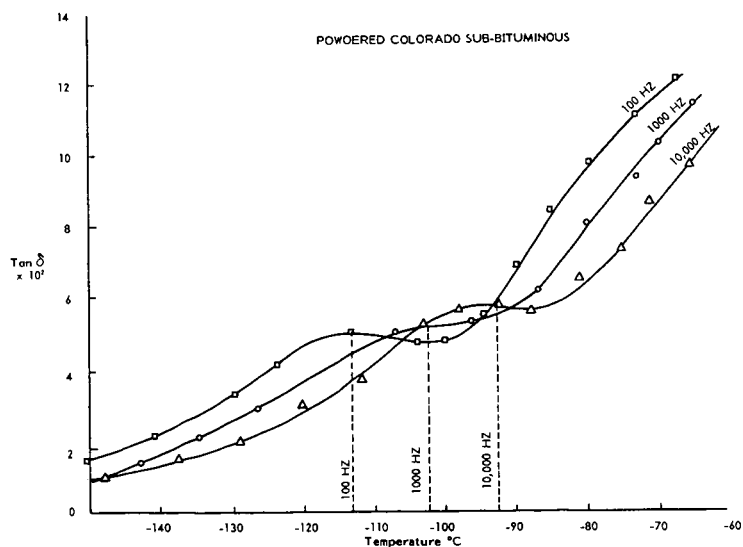


Figure 10. Spectra for powdered Yampa subbituminous.



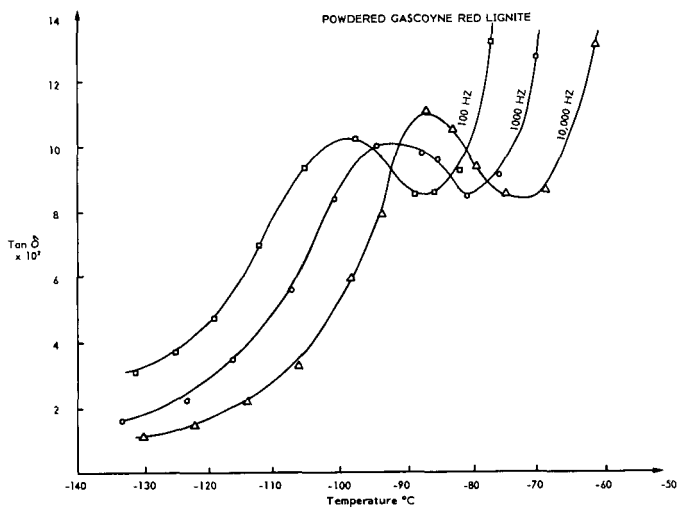


Figure 11. Spectra for powdered Gascoyne Red lignite.

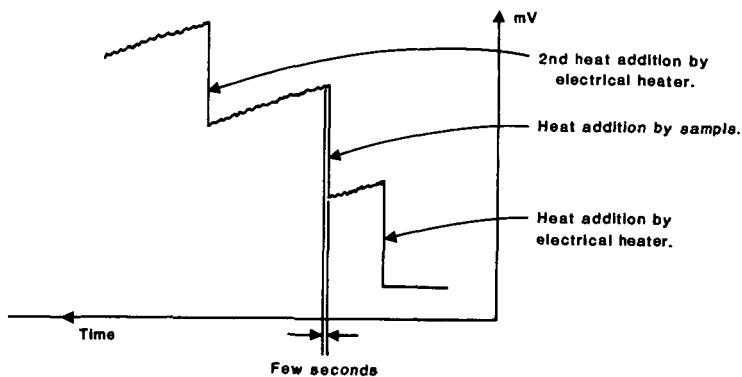


Figure 12. Characteristic of lignite type coals.

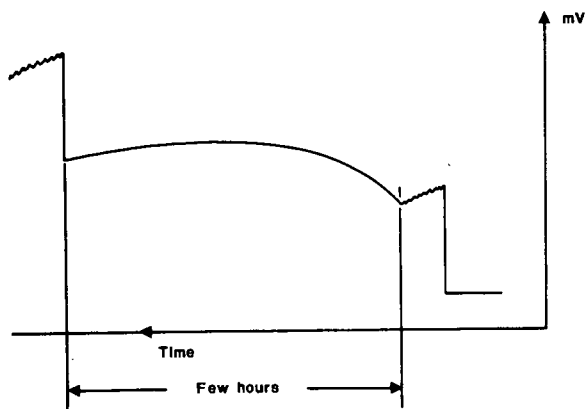


Figure 13. Characteristic of subbituminous type coals.

SEPARATION OF COAL LIQUIDS BY SIZE  
EXCLUSION CHROMATOGRAPHY - GAS CHROMATOGRAPHY (SEC-GC)

C.V. Philip and R.G. Anthony

Kinetic, Catalysis and Reaction Engineering Laboratory  
Dept. of Chemical Engineering, Texas A&M University  
College Station, Texas 77843

Introduction

The high efficiency gel columns packed with 5 $\mu$ m particles have increased the efficiency and decreased the analysis time of size exclusion chromatography (SEC). Since relatively large samples can be separated in a time as short as 20 minutes, SEC can be used as a preliminary separation technique prior to other analytical techniques such as gas chromatography (GC) and gas chromatography-mass spectroscopy (GC-MS). Such SEC separation of coal liquids, petroleum crudes and their distillation cuts into four or five fractions, followed by the analysis of the SEC fractions by GC and GC-MS have been reported elsewhere (1-14). The fraction collection and concentration of fractions were performed manually. This procedure was inefficient, and susceptible to human error. The Automated fraction collection followed by injection of the fraction into the GC reduces analysis time, and offers an option for collecting a desired number of fractions at predetermined time intervals.

The SEC separates coal liquids into fractions containing species with similar linear molecular sizes. Since similar molecular size species in coal liquid happened to have similar functionalities, the size separation enables the separation of fractions containing similar chemical species. When tetrahydrofuran (THF) is used as the mobil phase the coal liquid can be separated into four fractions containing heavy nonvolatiles, long chain alkanes mixed with light nonvolatile, phenols and aromatics. When the number of fractions are increased, less complex chromatograms with fewer peaks are obtained. The results of SEC-GC analysis of coal liquids indicate that the coal liquids are composed of a very large number of species but with similar structural blocks and functional groups. Lumping of similar components into four distinct groups such as nonvolatiles, alkanes (nonaromatic hydrocarbons) alkylated phenols and aromatics is seen as practical means of characterizing coal liquids. The instrumentation, analysis of coal liquid samples including recycle solvents are discussed in detail in this paper.

-----  
**Disclaimer:** This report was prepared as an account of work sponsored by an agency of the United States Government. Neither the United States Government nor any Agency thereof, nor any of their employees, makes any warranty, express or implied, or assumes any legal liability or responsibility for the accuracy, completeness, or usefulness of any information, apparatus, product, or process disclosed, or represents that its use would not infringe privately owned rights.

## Experimental

A Western Kentucky Synthoil and four recycle solvents from the Energy Research Center, University of North Dakota were the samples used for the analysis. Dry additive free tetrahydrofuran (THF) under helium atmosphere was used for preparing sample solutions and as the mobil phase in the size exclusion chromatograph (SEC). Although the synthoil could be injected without dilution, a 50% solution was preferred in order to reduce possible peak spreading and tailing. Since the recycle solvents were very viscous, 25% solutions were used. All the solutions were filtered through 0.5 Millipore filters using modest heat, but not high enough to boil THF, from a hot air gun and 30 psi Nitrogen pressure.

The instrumentation included a liquid chromatograph (LC, Waters ALC/GPC Model 202) equipped with a 60 cm, 5 $\mu$ m 100 Å PL gel column (Polymer Laboratories) and a refractive index detector (Waters Model R401) a Varian Chromatographic system (GC, VISTA 44) equipped with a 30 meter x 0.32 mm ID DB-5 capillary column (bonded phase fused silica column manufactured by J&W Scientific Co.) an autosampler (Varian 8000), a flame ionization detector (FID) and a nitrogen specific detector (thermionic ion specific - TSD) and a microcomputer system (IBM CS 9000) with 1000 K bytes RAM and dual 8" floppy disc drives for collecting raw chromatographic data.

The continuous sample separations on the gel column followed by the GC analysis of selected fractions was achieved by the operation of two sixport valves and a 3/4 port valve (All from Valco Instrument Company) as illustrated in figure 1. Sample injection into the LC was performed by a sixport valve ( $V_1$ ) with a 2 ml sample loop and fitted with a syringe-needleport for variable sample size injection. The combined operation of another sixport switching valve and the 3/4 port valve ( $V_2$ ) with 16 sample loops (100  $\mu$ l) enabled the linking of the liquid chromatograph with the autosampler of the gas chromatograph. The autosampler was modified to handle 100  $\mu$ l samples directly from the fraction collection loops of  $V_3$ . When  $V_2$  was turned clockwise, it kept  $V_3$  in line of LC effluents so that the fractions of separated sample could be collected and also the autosampler was bypassed.  $V_2$  at its counter clockwise position kept  $V_3$  in line with the autosampler for sample injection but bypassed the LC stream. Generally 0.1  $\mu$ l sample size was used for GC analysis. The stream from the capillary column was split (50/50) for the simultaneous monitoring by the FID and TSD. The real time monitoring of the GC was possible on both Varian and IBM systems and the raw chromatographic data were stored on the 8" floppy discs. The fraction collection, sample injection into the GC as well as the data collection was performed by the integrated system composed of a Varian Automation System (VISTA 401) and the IBM microcomputer (CS 9000). For each sample injection into the GPC column, up to 16 fractions were collected and analyzed by the GC using appropriate gas chromatographic programs stored in the memory without any manual interaction.

## Results and Discussions

The effluents from the GC capillary column are split into two streams and monitored by a flame ionization detector (FID) and a nitrogen specific detector (TSD). The analysis of a coal liquid derived naphtha (produced from western Kentucky coal-synthoil) is shown in Figure 2. The GC-MS analysis of coal liquid can miss several nitrogen compounds due to complex fragmentation pattern and low concentration. The FID output shows signs of overloading and most peaks are unresolved. Such overloading does not appear to affect the separation of nitrogen compounds. The use of a nitrogen specific detector in addition to FID enables one to identify the nitrogen species easily and GC-MS can be used for their structural identification.

Molecular size parameters such as molecular weight, molecular volume and hydrodynamic volume are used very effectively as the basis for SEC separation of polymers with identical building blocks or monomers (16-21). These molecular parameters need correction factors which vary depending on the individual structure of species (20), in order to use them as the basis for the SEC separation of mixtures of species especially the low molecular size compounds.

The SEC studies on a number of small molecular size species (5) such as alkanes, aromatics, phenols, amines and complex mixtures (15) such as coal liquids (1-11), petroleum crudes and their distillates (12,14), indicate that linear molecular size or the length of the molecule measured from its valance bond structure, is a better basis for explaining the mechanism of size separation by SEC (12). The effective linear molecular size of a species depends on its tendency to hydrogen bond with the solvent resulting in an increase of linear molecular size compared to nonhydrogen bonding species. Tetrahydrofuran, the SEC mobil phase, can increase the length of certain hydrogen bonding species such as phenols, amines and alcohols while the size of compounds such as benzene, pyridine, thiophene and alkanes are unaffected. This phenomenon enables the separation of phenols and aromatics in coal liquid into separate fractions.

SEC separation of recycle solvent obtained by the liquefaction of Wydak coal is illustrated in Figure 3a. The SEC effluents can be divided into four fractions based on elution time. The longer species appears first and are collected in Fraction 1. Since they are not volatile enough for GC-MS analysis, they are termed as heavy nonvolatiles. The second fraction is composed of volatiles, mostly straight chain alkanes ( $n\text{-C}_{14}\text{H}_{30}$  -  $n\text{-C}_{44}\text{H}_{90}$ ), and light nonvolatiles. Some olefins whose concentration may depend on the severity of liquefaction process, and branched alkanes such as pristane and phytane are also found in the second fraction. The third fraction is enriched mostly with alkylated phenols, indanols and naphthols. Some long structured aromatics such as biphenyls and binaphthyls may appear in this fraction. If the coal liquids are refined by cracking process resulting in naphthenic materials - a mixture of olefins and cyclic hydrocarbons, the third fraction may contain these materials also. The fourth fraction is composed of alkylated benzenes, indans, naphthalenes and heavy fused ring aromatics such as pyrenes and benzopyrenes.

When valve  $V_2$  and  $V_3$  are engaged the SEC Effluents (Figure 1) can be collected on the sample loops of  $V_3$  at specific intervals. The refractive index detector output shows the effect of such fraction collections as negative peaks (compare Figure 3a and 3b). Although sixteen is the maximum number of fractions, which can be collected at one time, more than sixteen fractions can be collected for a sample by repeating the procedure aimed at different elution times. Figure 4a shows SEC of a synthoil produced from western Kentucky coal. Twentythree fractions were collected. The FID output of 18 fractions, leaving the first three and the last two, are shown in Figure 5. The synthoil sample was analyzed by GC-MS prior to SEC-GC analysis and the major components were identified as alkanes ranging from  $n\text{-C}_{10}\text{H}_{22}$  to  $n\text{-C}_{44}\text{H}_{90}$ , phenols such as alkylated phenols, indanols and naphthols and aromatics such as alkylated benzenes, indans and naphthalenes. The first GC in Figure 5 shows the FID output of SEC fraction 4 of synthoil. All the peaks shown are straight chain alkanes. The next GC shows that the volatiles in fraction 5 are composed of relatively smaller alkanes. As the elution time increases the alkane chain length decreases. The fractions with short alkanes has overlap from heavy phenols (Fig. 5 GC, 6-9). The heavy phenols are not resolved but appear as a base line shift which is due to a large number of phenolic species eluting unresolved. As the fraction number increases smaller phenols appear as well resolved peaks (Fig. 5 GC, 9,14). When the molecular weight of phenolic species are increased by adding alkyl groups the probable number of isomers are increased and more isomers are possible for heavier phenols. The heavy and light aromatics appear in the last fractions (Fig. 5 GC 15-18). The fused ring aromatics such as pyrene and benzopyrenes appear after light aromatics (12).

At the Energy Research Center of the University of North Dakota, anthracene oil distillate was initially used as the solvent for coal liquefaction. The solvent along with dissolved liquefaction products were reused several times and solvent grade products mixed with the original solvents were supplied as recycle solvents. Four recycle solvents derived from four coals were analyzed by SEC-GC. The gas chromatograms of similar SEC fractions of these liquids are shown in Figures 3 and 4. Gas chromatograms of three similar fractions from each of the four solvents are presented in Figure 6. Examination of GCs indicate that these solvents contain similar volatile components.

### Conclusions

Although SEC and GC are two powerful chromatographic techniques, their combined use for analyzing complex mixtures has been limited due to the time consuming steps involved. The two valve interface which links the liquid chromatograph to gas chromatograph and the computer system which automate the system, reduce the analysis time as well as the frequency of manual interaction during the analysis which may take 8-10 hours for a coal liquid sample. By adding a mass spectrometer as a third detector to the GC, an extensive analysis of a rather complex sample such as coal liquid, petroleum crude and their refinery products is possible.

### Acknowledgements

The financial support of the U.S. Department of Energy, (Project Number DE-AC18-83FC10601) Texas A&M University Center for Energy and Mineral Resources and Texas Engineering Experiment Station is gratefully acknowledged. Energy Research Center at University of North Dakota furnished samples for the study.

### Literature Cited

1. Philip, C.V., Anthony, R.G., **Fuel Processing Technology**, 1980, 3, 285.
2. Philip, C.V., Anthony, R.G., **Proc. Coal Technology**, 1978, 2 p. 710.
3. Philip, C.V., Anthony, R.G., **Preprints ACS Org. Coat & Polym. Div.**, 1980 (August 20).
4. Zingaro, R.A., Philip, C.V., Anthony, R.G., Vindiola, A., **Fuel Processing Technology**, 1981, 4, 169.
5. Philip, C.V., Anthony, R.G., **Am. Chem. Soc. Div. Fuel Chem. Preprints**, (1979), 24, (3), 204.
6. Philip, C.V., Zingaro, R.A., Anthony, R.G., **Am. Chem. Soc. Fuel Chem. Preprints**, 1980, 25, (1), 47.
7. Philip, C.V., Zingaro, R.A., Anthony, R.G. in "Upgrading of Coal Liquids," Ed. Sullivan, R.F., **ACS Symposium Series No. 156**, 1981; p. 239.
8. Philip, C.V., Anthony, R.G., **Am. Chem. Soc. Div. Fuel Chem. Preprints**, 1977, 22, (5), 31.
9. Philip, C.V., Anthony, R.G. in "Organic Chemistry of Coal," Ed. Larsen, J.W., **ACS Symp. Series**, 1978, p. 258.
10. Philip, C.V., Anthony, R.G., **Fuel**, 1982, 61, 351.
11. Philip, C.V., Anthony, R.G., **Fuel**, 1982, 61, 357.
12. Philip, C.V. and Anthony, R.G., "Size Exclusion Chromatography", Ed. Proudler, T., **ACS Symp. Series**, 1984, 245, 257.
13. Philip, C.V., Anthony, R.G. and Cui, Z.D., "Chemistry of Low-Rank Coals, Ed. Schobert, H.H., **ACS Symp. Series**, 1984, 264, 287.
14. Philip, C.V., Bullin, J.A. and Anthony, R.G., **Fuel Processing Technology**, 1984, 9, 189.
15. Sheu, Y.H.E., Philip, C.V., Anthony, R.G. and Soltes, E.J., **Chromatographic Science**, 1984, 22, 497.
16. Hendrickson, J.G., **Anal. Chem.**, 1968, 40: 49.
17. Majors, R.E.J., **Chromatog. Sci.**, 1980, 18: 488.
18. Hendrickson, J.G. and Moore, J.C., **J. Polym. Sci. Part A-1**, 1966, 4: (1966).
19. Cazes, J. and Gaskill, D.R., **Sep. Sci.**, 1969 4: 15.
20. Krishen, A. and Tucker, R.G., **Anal. Chem.**, 1977 49: 898.
21. Snyder, R.L. and Kirkland, J.J., **Introduction to Modern Liquid Chromatography**, John Wiley and Sons, Inc., New York, 1974.

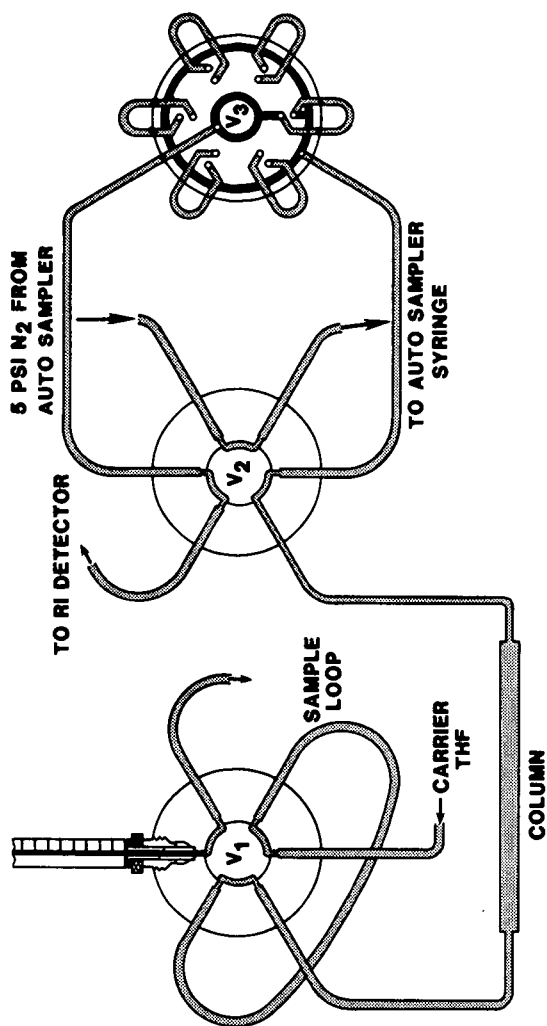


Figure 1. LC - GC interface. Note: V<sub>3</sub> has sixteen loops instead of six shown.



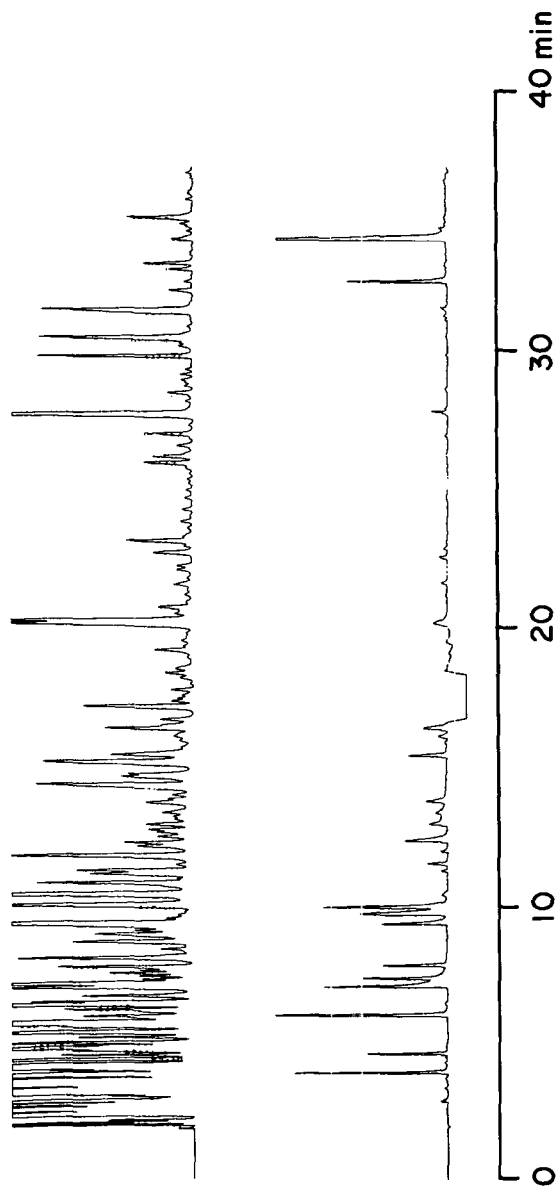


Figure 2. Gas chromatographic analysis of coal derived naphtha with duel detectors. The gas chromatograph is equipped with a bonded phase fused silica capillary column and an outlet stream splitter (1:1). Temperature program: 3 min hold at 40°C, 2°C/min to 80°C, 2°C/min to 120°C and 4 min hold at 120°C. One stream is monitored by an FID detector (top) and the other is monitored by a nitrogen specific detector (bottom).

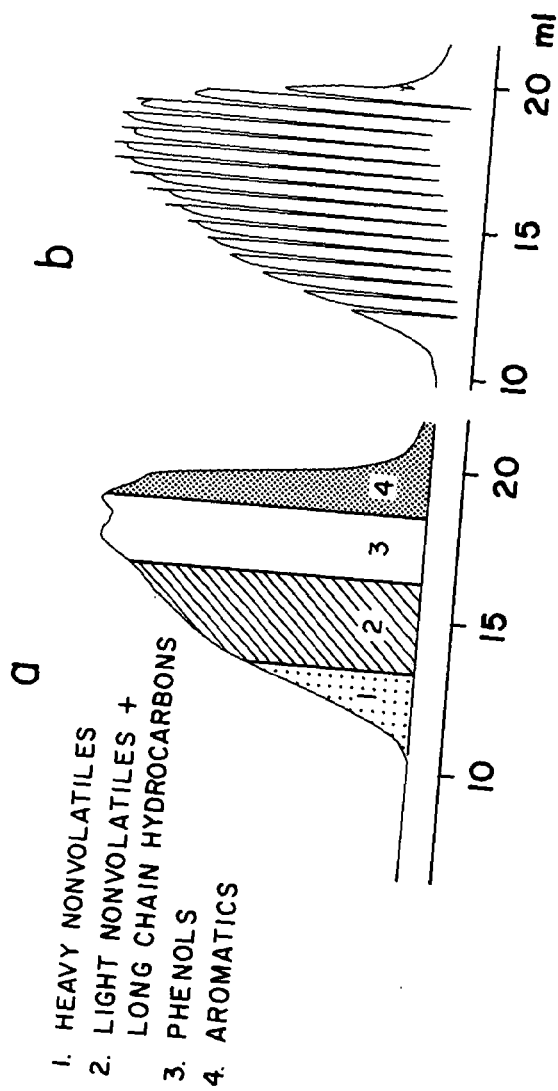


Figure 3. SEC separation of Wydak coal derived recycle solvent (a) LC-GC interface bypassed (b) 16 fraction were collected by LC-GC interface.

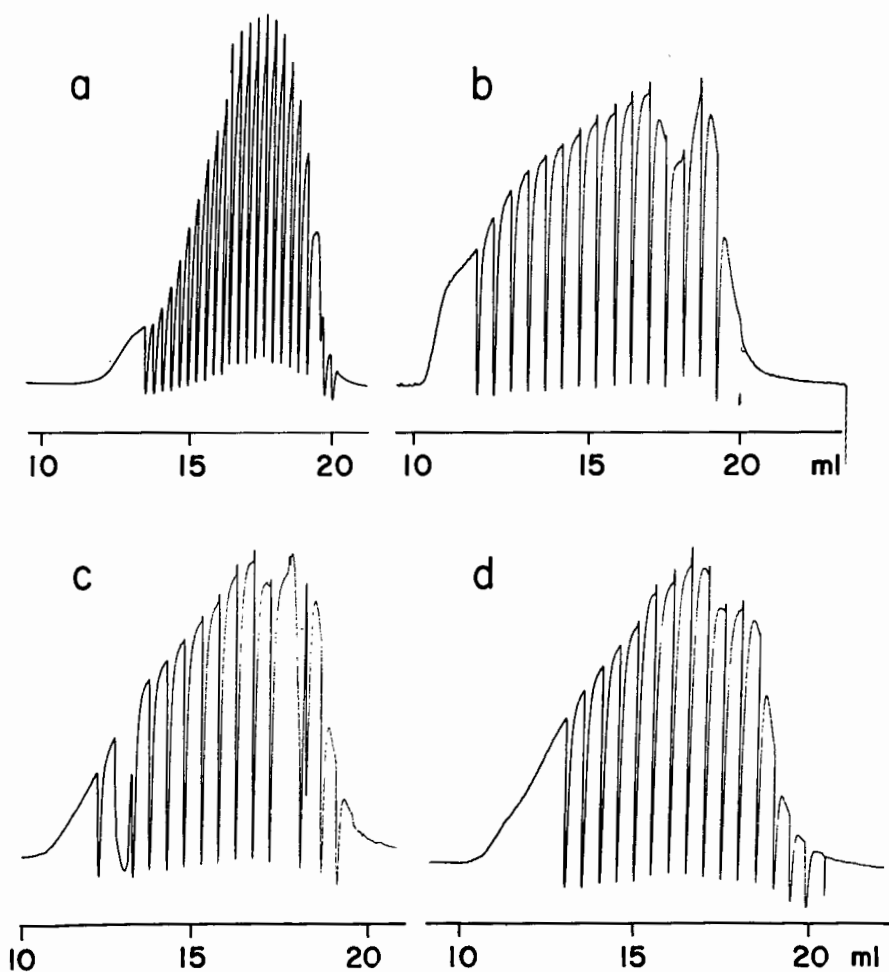


Figure 4. 100  $\mu$ l fractions are collected from the SEC effluents (a) Western Kentucky Synthoil. Recycle Solvents (b) Texas Big Brown (c) Beulah (d) Zap-2.

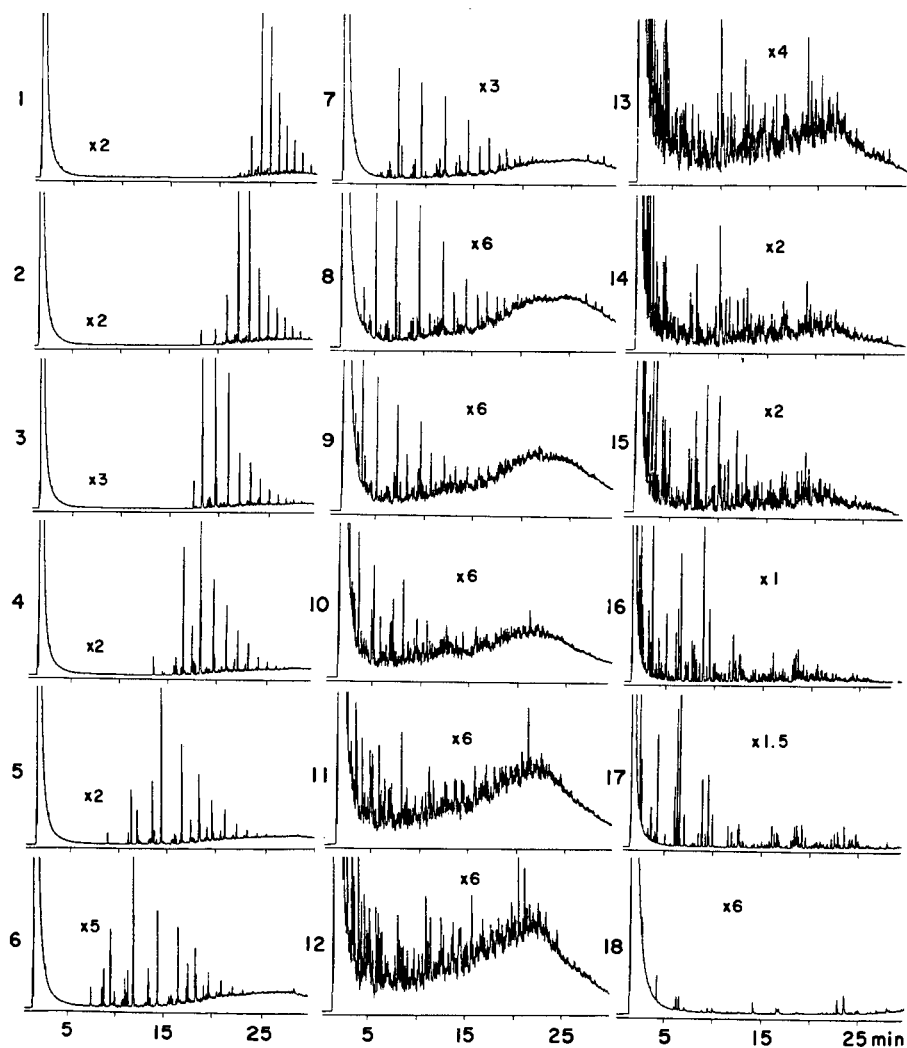


Figure 5. Gas Chromatograms of fractions from Western Kentucky Synthoil (Figure 4a) temperature program: 80-120°C at 4°C/min, 120-280°C at 10°C/min and 4 min. hold at 280°C.

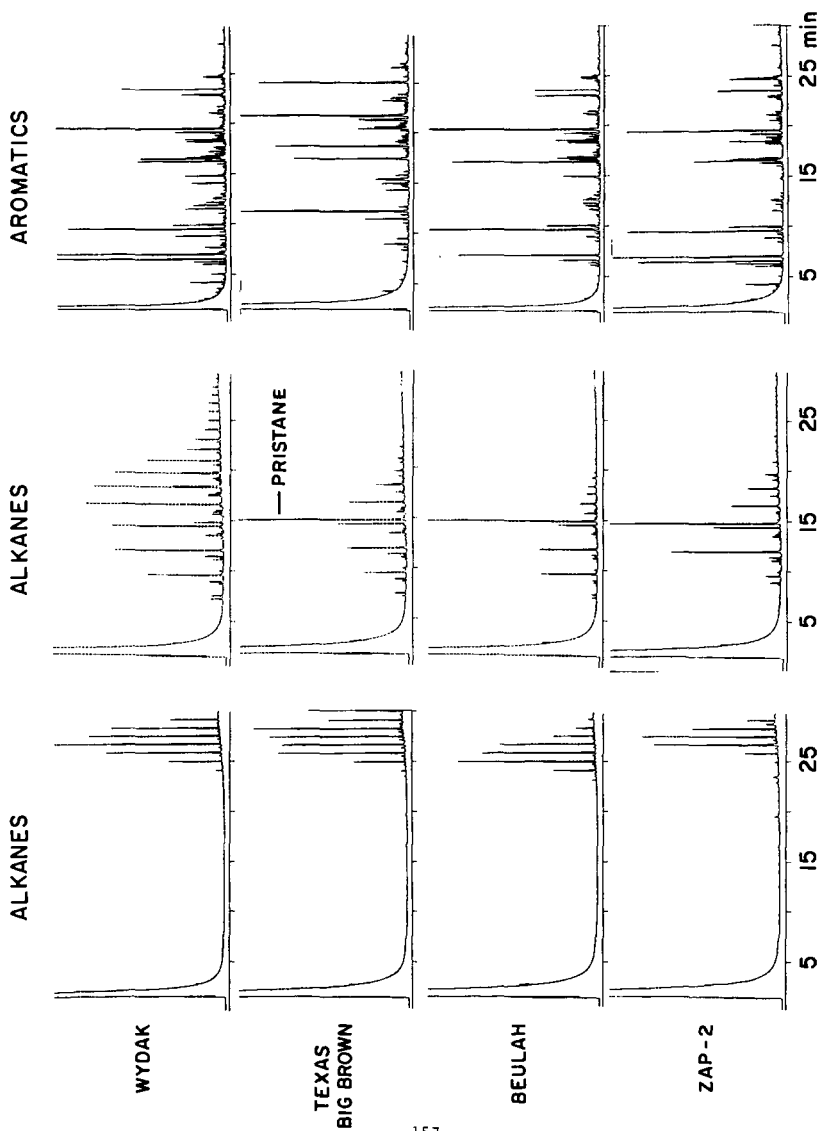


Figure 6. Gas chromatograms of similar fractions of four recycle solvents.  
GC conditions are same as in Figure 5.

UNDERSTANDING THE POUR POINT DEPRESSION MECHANISM-  
I. HPLC AND GPC ANALYSIS OF CRUDE OILS

C. A. Irani, D. S. Schuster, and R. T. Yin

Gulf Oil Research & Development, Production Research Center,  
P. O. Box 37048, Houston, TX 77236

SUMMARY

This study offers a preliminary explanation for the high pour point phenomena in waxy crudes, and attempts to differentiate between crude oils that do and do not respond to pour point depressants. Twelve internationally located crude oils were first subjected to a standard wax separation procedure, and the collected waxes were further analyzed by GPC and HPLC methods. The isolated wax fraction was found to be composed of aromatic, polar and hexane insoluble components in addition to the crystallizable saturate components. Based on GPC analysis of the molecular size distribution of the wax components isolated from the crudes, the 12 crudes could be categorized into three types. Regression analysis was successfully used to correlate pour point to the wax content and the saturates in the waxes. The saturates content gave the better correlation. GPC analysis of the saturate cuts was facilitated by the development of a saturates calibration curve to replace the existing polystyrene standard.

INTRODUCTION

Numerous problems occur during the production and transportation of waxy crudes. These crudes have high pour points (often over 100°F) and leave troublesome wax deposits in pipelines and production equipment. When cooled below the temperature for wax precipitation the precipitating waxes tend to form an interacting three-dimensional structure that can effectively tie up the lighter fractions of the crude and cause congealing to occur. A number of previous publications<sup>(1-10)</sup> have discussed the problems associated with the production and transportation of these crudes, and the methods that have been proposed for minimizing these problems.

Two approaches are commonly taken for handling these crudes. The obvious approach would be to always maintain the crude temperature above its pour point, but this is not always technically or economically feasible. The second approach is to use chemical pour point depressants to modify the interactions between the precipitating waxes, thus reducing the pour point and improving the flow characteristics. The problem arises in that the wax-additive interaction is extremely complex and very poorly understood, so that no prior judgement can be made as to the efficacy of a particular additive for depressing the pour point of a particular crude. The data presented in Table 1 serves to better demonstrate this point by comparing the properties of Cabinda (West Africa) and Handil (Kalimantan) crudes. Both crudes have similar API gravities and wax contents, yet their pour points are quite different. Additionally, Cabinda responds quite well to low concentrations of a

certain additive, yet Handil shows little response to most available additives.

Table 1  
Comparison of Two Waxy Crudes

Crude	API Gravity	Wax Content Wt. %	Pour Point °C (°F)	Depressed <sup>1</sup> Pour Point °C (°F)
Cabinda	32.1	16.3	21.1 (70)	-17.8 (0) <sup>2</sup>
Handil	32.1	16.5	32.2 (90)	21.1 (70) <sup>3</sup>

1. Maximum pour point depression seen with screening 50 pour point depressants.
2. 100 ppmw of Additive A.
3. 1000 ppmw of Additive B.

Based on the performance of these two crudes it was concluded that the wax-additive interaction is complex and poorly understood, and that a detailed analytical evaluation of at least the wax fractions in the crude oil would help in developing a better understanding of the interaction. More Specific questions that the study also attempted to address included: (1) The relationship between precipitated waxes and actual saturates; (2) The relationship between the pour point and the amount and composition of the wax fraction collected; (3) The nature of the waxes collected from different crudes; (4) An understanding of why there appeared to be a specific temperature for many crudes below which the pour point could not be chemically depressed.

Gel Permeation Chromatography (GPC) and High Pressure Liquid Chromatography (HPLC) were the major analytical tools used in this study to try and answer some of the questions raised above.

#### EXPERIMENTAL

Waxes were first isolated by an in-house procedure frequently used to determine the wax content of crudes and petroleum product. The procedure is a modification of ASTM D-721, and calls for diluting 1 gram of sample with 100 ml of methylethyl ketone. The solution is heated to 65.5°C (150°F) to dissolve the sample, and filtered at this temperature to remove the insoluble components (such as bulk asphaltenes). The solution is cooled to -17.8°C (0°F) and filtered through Whatman No. 50 filter paper to recover the wax precipitate. This fraction is referred to as the TOTAL waxes present in the crude oil.

HPLC was used to further separate this wax fraction into saturates, aromatic, polar, and hexane insoluble if present. The HPLC equipment and procedure has been discussed elsewhere.<sup>(11)</sup>

GPC was also used to classify the TOTAL waxes, as well as the saturates isolated from the TOTAL waxes by HPLC. The GPC consists of the following columns: 3-  $\mu$  styragel, ( $10^4$ ,  $10^3$ , 500 Å), and 2 $\mu$  spherogel (50 Å). Tetrahydrofuran solvent was used (20 mg/ml sample dilution). The injection volume was 100  $\mu$ l and a 2 ml/min flow rate was maintained. A differential refractometer detector was used. The elution of the sample was automatically monitored by a computer. At the end of the run, the computer integrates the chromatogram, calculates the molecular weight distribution, and prints out the results in digital and graphic form.

A special calibration curve was generated for the GPC analysis of the saturate fractions. For this purpose the saturates present in the wax fraction were separated by elution time in a preparative GPC. A Knauer Vapor Pressure Osmometer was used to determine their actual molecular weights, and their elution times on the analytical GPC were obtained. This molecular weight and elution time data was then combined to develop a calibration curve applicable to the saturate fractions.

## RESULTS AND DISCUSSIONS

Twelve waxy crude oils from fields around the world were analyzed in this study. Table 2 identifies the crude oils and presents some of their general properties (API gravity, pour point, wax content, HPLC analysis). Working on the premise that a difference in the composition of the wax fractions amongst these various crudes was responsible for the difference in behavior and response to chemical additives, the wax fractions were isolated and subject to further analysis.

GPC analysis of the wax precipitates provided molecular size distribution data based on which the crudes could be separated into three types. HPLC further indicated that what was being separated as a wax phase was actually a complex mixture of aromatic, polar, asphaltene and crystallizable saturate-type components. By employing a preparative HPLC method, large samples of the saturate fractions were collected and further analysed by GPC in order to identify distinguishing traits in the saturates present in the different crudes. Molecular weight distributions of the saturate components was facilitated by use of an in-house developed calibration curve specifically generated for this application to improve on the results available through the use of the existing polystyrene curve.

Even though the waxy components in a crude are directly responsible for the high pour point, previous attempts to correlate the pour point with the wax content of a crude have not proven very successful. For the 12 crudes used in this study, regression analysis showed a fair fit between the pour point and the wt. % waxes present, and a very good fit with the wt. % saturates present in the collected waxes. Details of this and other results are presented in the following sections.

### GPC Calibration Curve

GPC proved a valuable tool for both whole wax and saturates analysis. However, for pure saturates analysis the use of a polystyrene



based calibration curve was felt to give erroneous results. An attempt was made to correct this by developing a calibration curve specifically suited for saturates analysis. Both pure alkanes and saturate fractions isolated from a waxy crude were used to generate the necessary calibration curve. The waxes were first separated from the whole crude using the precipitation method described above, and preparative HPLC then used to isolate the saturates present in the wax cut. The saturates were further cut by preparative GPC into individual fractions, and the retention volume for each fraction established. The molecular weights of each saturate fraction were determined using vapor pressure osmometry. Molecular weight determinations were hampered by the low solubility of the saturates in the solvents used, and special handling procedures had to be used to overcome this problem. The calibration curves obtained are presented in Figure 1, which compares the polystyrene curve to the saturates curve and the pure alkane curve.

The pure alkane curve is limited in scope because pure alkanes were not available above a carbon number of 34, and yet it closely matches the saturates curve which could be taken to higher molecular weights. A substantial discrepancy exists between the saturates curve and the polystyrene curve, so that use of the saturates calibration curve gave a more reasonable molecular weight distribution of the saturates.

#### Composition of the Wax Fractions

Whereas pure saturates can be expected to be colorless or at most white, the actual wax fractions isolated were highly colored, leading to the conclusion that polar and/or aromatic type components were also present in the collected wax precipitates. Preparative HPLC was used to separate the wax fractions into saturates, aromatics, polars and asphaltenes, with the results shown in Table 2.

TABLE 2

#### HPLC ANALYSIS OF WAX FRACTIONS

Crude	API Grav.	Pour Point (°F)	Wax Content* Wt. %	Wt. % Sats.	Wt. % Arom.	Wt. % Polars	Wt. %* Asph.
Bentayan	22.6	110	36.4	55.0	14.2	28.1	2.7
Wasatch	41.8	105	37.1	90.0	8.2	1.7	0.1
Green River	30.3	95	26.8	61.4	16.5	14.9	6.6
Handil	32.3	90	16.5	88.8	6.0	4.0	1.6
Mibale	30.5	85	20.5	62.5	16.9	10.0	0.6
Cabinda	32.1	70	16.3	62.0	11.6	25.4	1.0
Lucina	39.6	60	12.2	73.0	12.5	9.4	5.1
Brega	43.1	50	6.4	73.5	9.7	13.3	3.5
Escravos	36.1	50	6.8	60.9	11.8	27.0	0.3
Mesa	30.4	50	7.3	62.9	15.6	21.0	0.5
Zaire GCO-4	30.4	50	14.2	39.3	11.7	36.0	13.0
Murban	39.7	15	4.8	72.9	17.5	8.6	1.0

\*Used in Regression Analysis

Clearly the wax precipitate is actually a very complex mixture of these crude oil components, a fact that compares well with field observations of paraffin deposits. Only in highly paraffinic and low asphaltic crudes do these deposits appear to have characteristics of pure saturates. Generally, depending on the composition of the crude, the deposits range from being high in saturates to almost asphaltic in nature. It is also generally recognized that successful chemical depression of the pour point requires that the additive modify the structure of the precipitating wax as the temperature is lowered. In untreated crude the precipitating waxes are capable of forming a complex, interacting three-dimensional structure which essentially ties up the lighter components of the crude thus reducing its fluidity. Consequently, for a chemical to successfully depress the pour point of a crude oil, it must first successfully destroy the interaction mechanism between these chemically complex species. Because no two crude oils have the same composition, no two wax precipitates can be expected to display a similar chemical interaction. Consequently a large discrepancy in performance between the response of various crudes to the same additive results. This also helps to explain why different crudes with similar saturate distributions show differing response, because the actual interaction is chemically more complex than a simple saturates interaction. For many refined streams, diesel oil for example, the pour point problem is more specific to the saturates present, and additives are capable of showing a much broader response. It is the complexity of the crude oil precipitates that limits the applicability of pour point depressants for their treatment.

#### Waxy Crude Classification

Review of the molecular size distribution data obtained by GPC for the 12 crudes under study indicated that it might be possible to use this information to classify the crudes. This was attempted, and three types were defined. Even though this classification may be considered loose, and has only been explored for the 12 crudes, the results are sufficiently encouraging to warrant extending this study to a larger number of crudes.

Type-1 crudes, as defined by the molecular size distribution of the total waxes, is shown in Figure 2. Many of the West African crudes fall in this category, which is characterized by a bimodal molecular size distribution. However, even though the C-25 and lower carbon numbers are well represented, the bulk of the wax components are in the higher molecular weight range. Extrapolation of this observation implies that the higher pour point crudes could perhaps fall in this type.

Type-2 crudes are presented in Figure 3. A bimodal distribution persists but there is a reversal in the relative contributions by the low and high carbon number fractions. The C-25 species are now more dominant, with the C-25+ species providing a hump at the tail end of the distribution. The remaining four crudes are classed together as Type-3 (Figure 4), but this is a weaker correlation. The primary trend for Type 3 crudes is towards a narrower distribution range as shown in Figure 4. Two of the crudes, Brega and Murban, show a continuation of this trend, with the two distinct peaks of the Type 2 crudes replaced by a single

peak in the C-25-30 range, and a declining contribution by the C-30+ fractions. Handil crude is an extreme example, in which almost the entire contribution is from the C-25-30 range material and only a limited contribution is from the C-30+ material. The one exception appears to be Escravos crude for which a distinct C-25-30 peak is present, but a very substantial contribution by components of very high carbon number is also observed.

Based on these noted differences in crude types it is now feasible to attempt to explain differences in crude responses to chemical additives. For example, the difference in behavior of Cabinda and Handil crudes can be attributed to the differences in the nature and distribution of the wax components in the two crudes, wherein a much narrower distribution of waxes is present in Handil relative to Cabinda. The response of these two crudes to additives would also be substantially different. Any additive in Handil crude would be swamped by a large amount of wax precipitating over a very narrow temperature range, whereas with Cabinda the effect would be much more gradual, with the additive capable of modifying the initial wax precipitate, which in turn could serve to modify the interaction between successive wax precipitates.

However, an intriguing question that remained unanswered was whether the differences in behavior of the two crudes could be attributed more to the differences in the saturate fractions present in the crudes, or to the more complex combination of material that represented the precipitated wax fraction. To this end preparative HPLC was used to isolate the pure saturate fractions from a number of crudes, and these saturate fractions analysed by GPC. The results, presented in Figure 5, indicated that the pure saturates are remarkably similar in size distribution, and consequently differences in behavior must be dependent on the chemical nature of the complexes formed between the saturates and aromatic, polar and asphaltene type components also present in the crudes.

#### Correlating Wax Content to the Pour Point

Numerous previous attempts to correlate the pour point to the wax content of a crude oil have not been very successful. Our studies have shown that the complex chemistry of the interactions involved would preclude any general correlation. Regression analysis was used to explore possible correlations between the pour point and the wax content of the crudes or the saturates present in the waxes. Table 3 presents the several variables ( $x_1 - x_{12}$ ) explicitly defined as functions of wax content and saturates in wax respectively.

TABLE 3

## Variables for Multiple Regression analysis

$x_1 = x$	$x_5 = x^2$	$x_9 = 1/e^x$
$x_2 = 1/x$	$x_6 = 1/x^2$	$x_{10} = \ln x/x^2$
$x_3 = \ln x$	$x_7 = 1/e^{\ln x}$	$x_{11} = (1-x)^2$
$x_4 = e^x$	$x_8 = e^{\ln x}$	$x_{12} = x(\ln x)$

$x$  = Wt. % Wax or Wt. % of Saturates in Wax

Functions  $x_4$ ,  $x_7$  and  $x_9$  were not used as they did not correlate well with the available data. Even though the remaining nine functions were used in multiple regression analysis, not all appear in the final regression equations, since the occurrence of singularities in the coefficient matrix indicated that the regression coefficient could not be solved simultaneously.

Equation 1 presents the relationship between the wax content and pour point.

$$\text{Pour Point (}^\circ\text{F)} = -44522.14 - 1333.95x_1 + 15754.08x_3 + 41954.46x_6 + 69462.51x_{10} + 226.71x_{12} \quad 1)$$

The correlation coefficient for this equation is .9423. A much higher correlation coefficient (0.9978) was obtained for the correlation between the pour point and the amount of saturates present in the wax fraction. Equation 2 is the necessary equation for this case.

$$\text{Pour Point (}^\circ\text{F)} = 49395.11 - 416.66x_1 + 50834.54x_2 - 14439.62x_3 - 2.78x_6 - 125575.07x_6 - 103337.73x_{10} \quad 2)$$

CONCLUSIONS

The pour point phenomena in waxy crudes is a complex chemical event which is influenced both by the amount of the saturates present in the crude and the chemical composition of the crude. GPC characterization of the wax precipitates allowed classifying the 12 crudes into three distinct types. HPLC analysis of the wax precipitates indicated that they are comprised of a complex mixture of saturate, aromatic, polar and asphaltic material. Differences in the behavior of the crudes and in their response to additives can be attributed to the differences in the distribution and composition of the wax fractions.

ACKNOWLEDGEMENTS

The assistance of the following Gulf personnel was greatly appreciated: J. Suatoni, R. Ruberto, and G. Chao for the GPC and HPLC analysis, and M. Greco for the VPO studies.

#### REFERENCES

1. Perkins, T. K. and J. B. Turner, "Starting Behavior of Gathering lines and Pipelines Filled with Gelled Prudhoe Bay Oil," Journal of Petroleum Technology, March, 1971, pp. 301-308.
2. Barry, E. G., "Pumping Non-Newtonian Waxy Crude Oils," Journal of the Institute of Petroleum, Vol., 57, No. 5534, March, 1971.
3. SPE Rocky Mountain Regional Meeting, May 23-25, 1983, "Paraffin Deposition and Rheological Evaluation of High Wax Content Altamont Crude Oils," by W. J. Matlach and M. E. Newberry.
4. Meyer, R. F. and C. T. Steel, ed., The Future of Heavy Crude Oils and Tar Sands, "Pipeline Transportation of Heavy Oils," A. Sloan, R. Ingham, and W. L. Mann, (Edmonton, Alberta, Canada, 1979), Chapter 86.
5. Rossemyr, L. I., "Cold Flow Properties and REsponse to Cold Flow Improver of Some Typical Fuel Oils," Ind. Eng. Chem. Prod. Res. Div., Vol. 18, No. 3, (1979).
6. SPE 55th Annual Fall Technical Conference and Exhibition, September 21-24, 1980, "Flow Properties of Utah Shale Oils," by W. H. Seitzer and P. F. Lovell, SPE 9500.
7. SPE Annual Technical Conference and Exhibition, October 5-7, 1981, "Pipeline Transportation of High Pour Handil Crude," by C. A. Irani and J. Zajac, SPE 10145.
8. Harvey, A. H., R. Briller, and M. D. Arnold, "Pipelining Oils Below Their Pour Point--Part I," Oil & Gas Journal, August 23, 1971, p. 96.
9. Harvey, A. H., R. Briller, and M. D. Arnold, "Pipelining Oils Below Their Pour Point--Part II," Oil & Gas Journal, August 30, 1971, p. 62.
10. Ford, P. E., J. W. Ells, and R. J. Russell, "What Pressure is Required for Restarting Gelled Line?" Oil & Gas Journal, May 17, 1965, pp. 134-136.
11. Suatoni, J. and R. E. Swab, "Preparative Hydrocarbon Type Analysis by High Performance Liquid Chromatography," Journal of Chromatography Science, Vol. 14, November 1976, pp. 535-537.

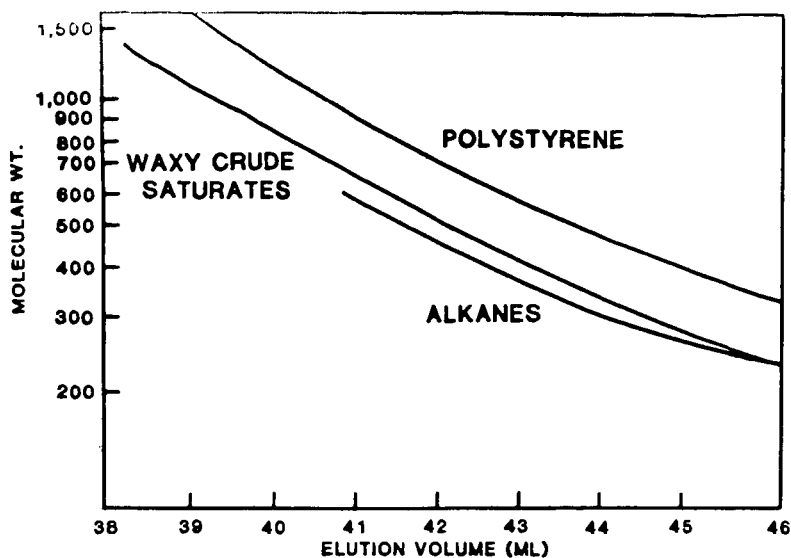


Fig. 1 WAXY CRUDE SATURATES CALIBRATION CURVES

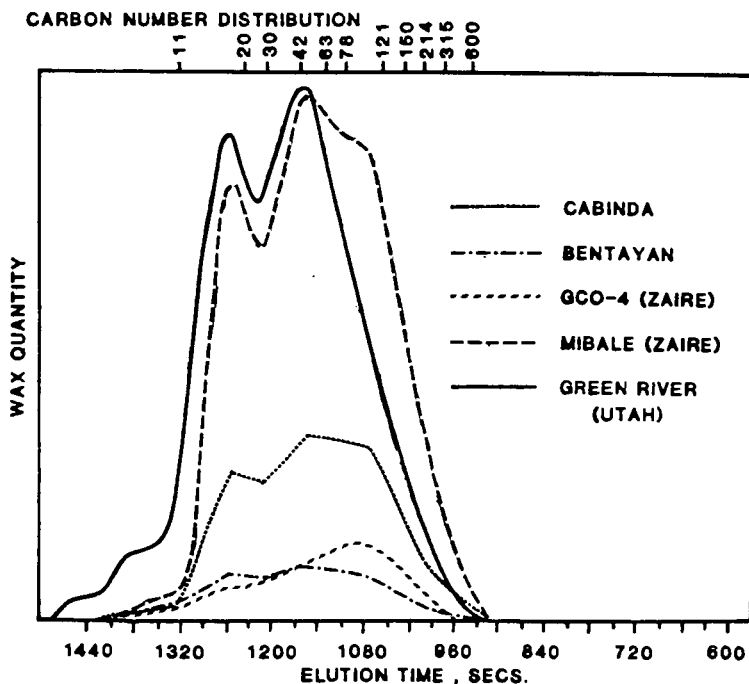


Fig.2 TYPE - I CRUDES

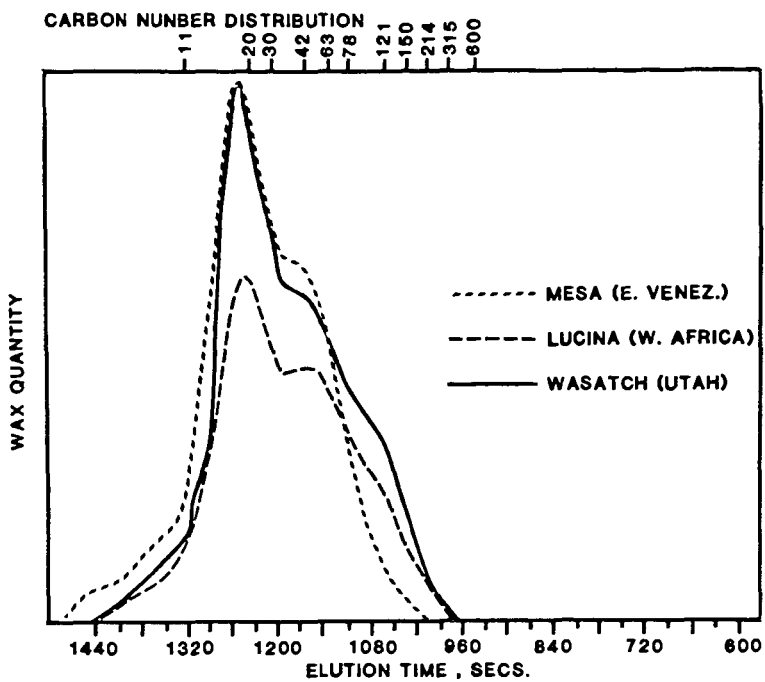


Fig.3 TYPE II CRUDES

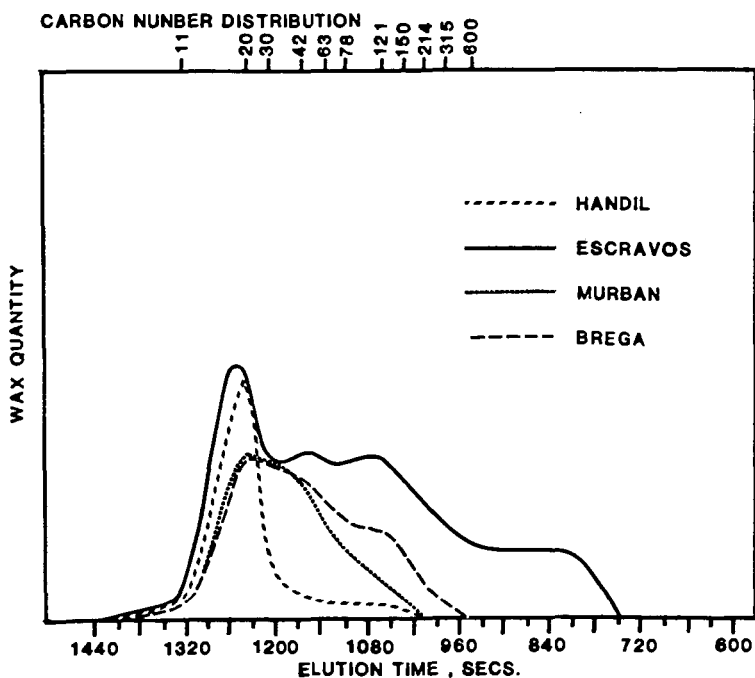


Fig.4 TYPE III CRUDES

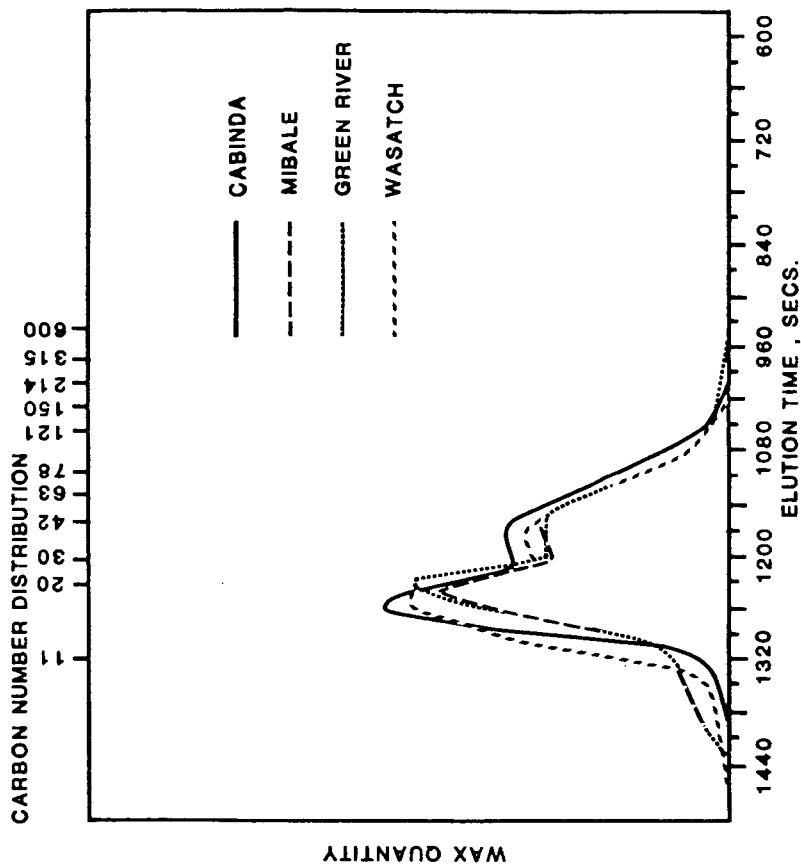


Fig.5 COMPARISON OF SATURATES FRACTIONS



## UNDERSTANDING THE POUR POINT DEPRESSION MECHANISM-II MICROFILTRATION ANALYSIS OF CRUDE OILS

D. S. Schuster and C. A. Irani

Gulf Oil Research & Development, Production Research Center,  
P. O. Box 37048, Houston, TX 77236

### SUMMARY

This study helps to explain the high pour point phenomena in waxy crudes and begins to explain differences in crude oils that do and do not respond to pour point depressants. Microfiltration was used to separate the waxes that precipitate out at the various temperatures in waxy crude oils. These waxes, which can be composed of saturates, aromatic, polars and asphaltenes, vary in molecular weight and composition with their temperature of precipitation in a waxy crude. Waxes that precipitate out of the crude oil solution at temperatures above the pour point are of higher molecular weight and have a high asphaltene content. The waxes that precipitate at lower temperatures have lower molecular weights and contain mostly saturates. Detailed chemical analysis showed that the temperature where asphaltenes are no longer associated with the waxes represents the maximum degree of pour point depression obtainable. This trend was verified for six waxy, high pour point crudes.

### INTRODUCTION

As pointed out in the preceding paper, treating waxy crudes with pour point depressants often offers a solution to high pour point problems. However, a major uncertainty with the chemical additive treatment for reducing the pour point is that many waxy crudes only show a limited response to the pour point depressant. Additionally, the mechanism of pour point reduction, while often hypothesized, still remains unknown.

Four questions concerning pour point depression were posed in the last paper. That paper demonstrated the answers to the first three questions and indicated that the pour point is a function of the amount of saturates in the wax fraction, the waxes are composed of aromatic, polar and asphaltic components in addition to the saturates, and that the waxes in different waxy crudes can be classified into three types. Thus, when dealing with waxy crudes, the polar, aromatic and asphaltic components must be considered.

This paper attempts to answer the remaining questions posed in the last paper, and a number of questions that follow from it. Specifically, 1) What happens at the pour point temperature? 2) Why can't the pour point of many crudes be depressed beyond a certain temperature? and 3) Why are pour point depressants effective on only certain crudes?

## EXPERIMENTAL

### Wax Fractionation

As presented in the previous paper, a method was defined to obtain the total amount of wax in a hydrocarbon fraction at a predetermined temperature of  $-17.8^{\circ}\text{C}$  ( $0^{\circ}\text{F}$ ). This procedure was modified to fractionate the waxes over distinct temperature ranges so that a more continuous analysis of the changing wax composition could be undertaken.

The crude was diluted (100:1) with methyl ethyl ketone and heated to  $150^{\circ}\text{F}$ . Bulk asphaltenes were removed by filtration at this temperature. The diluted sample was cooled through a series of  $5.5^{\circ}\text{C}$  ( $10^{\circ}\text{F}$ ) temperature intervals, with the precipitated wax being removed from the sample at each interval. The end results is a totally dewaxed oil at  $-17.8^{\circ}\text{C}$  ( $0^{\circ}\text{F}$ ) with the waxes separated out in successive  $5.5^{\circ}\text{C}$  ( $10^{\circ}\text{F}$ ) temperature ranges. The separated waxes were then further analyzed by the HPLC and GPC methods discussed in the previous paper.

### Centrifuge Study

Treatment with additives often does not reduce the crude's pour point to a sufficient degree. Indications are that the additive is successful with the initial range of waxes, but the either the additive is ineffective with the next range of waxes (which gives rise to the depressed pour point) or its effectiveness is inhibited by the deposition of waxes. The purpose of the centrifuge study was to separate the first precipitate of treated waxes, so that the succeeding wax fractions could be isolated for treatment and analysis. If a significant pour point reduction was obtained on this next set of waxes, the two treatments were then combined into a single treatment for the entire crude.

The basic experimental procedure was:

- 1) Treat the crude sample with the most successful additive package.
- 2) Remove the crude from the predetermined optimum oven cycle and transfer to centrifuge tubes at  $22.2^{\circ}\text{C}$  ( $40^{\circ}\text{F}$ ) above the treated crude's pour point.
- 3) Transfer the centrifuge tubes to a waterbath and cool the samples at  $1^{\circ}\text{C/hr.}$  ( $0.6^{\circ}\text{F/hr.}$ ) to  $11.1^{\circ}\text{C}$  ( $20^{\circ}\text{F}$ ) above the treated crude's pour point.
- 4) Preheat the centrifuge to the same temperature as in Step 3 above, and centrifuge the samples for five minutes.
- 5) Decant the top liquid phase from the settled waxes.

The top liquid phase was subjected to further treatment for pour point depression, and both the wax phase and the top liquid phase were further analyzed.

## RESULTS AND DISCUSSION

This study resulted in several interesting findings which are presented below. First, an analysis of the waxes obtained at different temperatures showed that the waxes precipitating above the pour point have a high molecular weight and contain significant amounts of asphaltenes. Another finding was that a strong association exists between asphaltenes and waxes that precipitate at various temperatures. The lowest temperatures at which asphaltenes are still present with the wax appears to indicate the maximum amount of pour point reduction achievable by the use of chemical additives. Further details are offered below.

### Wax-precipitation Temperature Trends

Analysis of the waxes separated at various temperatures from a crude indicates that the waxes that precipitate at temperatures above the 35°C (95°F) congealing temperature differ from those that precipitate at lower temperatures.

The first difference is shown by the GPC molecular size distribution curves (Figure 1) for Bu Attifel crude. The wax fractions isolated at 32.2°C (90°F) and 37.8°C (100°F) indicate that the waxes that precipitate below the congealing temperature is reached are composed of higher molecular weight components. Each size distribution curve represents a contribution from both higher and lower molecular weight species which show up as two distinct peaks. A reversal in the relative contributions from the two species takes place between 32.3°C and 37.8°C. At the higher temperatures (above the congealing temperature), the more sizeable contribution is from the higher molecular weight species (peak on the left), but at 32.2°C the major contribution is from the lower molecular weight components (peak on the right).

The second trend indicates that above the 35°C (95°F) congealing temperature, the wax fractions are primarily composed of asphaltenes, but at temperatures below the congealing temperature the waxes contain mostly saturates (Table I). Therefore, possible nucleating sites for wax crystal growth that precipitate at temperatures above the congealing temperature are primarily asphaltenes. These asphaltenes were initially removed by filtration during the wax separation. Apparently, some type of asphaltenes must be associated with the waxes, and they are not removed by bulk deasphalting.

TABLE I

HPLC ANALYSIS OF BU ATTIFEL WAXES SEPARATED BY MODIFIED G-281

TEMPERATURE- WAX REMOVAL	(G-281)	HPLC of the Waxes			
	WT. % WAXES	WT. % SATURATES	WT. % AROMATICS	WT. % POLARS	WT. % ASPHALTENES
100°F	1.8	4.7	0.3	---	95.0
100	1.1	24.0	0.7	0.3	75.0
95	1.0	95.5	2.1	0.4	2.0
90	0.4	95.9	2.8	0.7	0.6
80	1.7	89.7	1.7	0.2	8.4
70	1.6	89.0	2.5	0.2	8.3
60	5.6	95.9	3.5	0.1	0.4
50	2.3	94.6	4.4	0.6	0.4
40	2.4	96.6	3.0	0.4	---
30	3.6	97.2	2.7	0.1	---
20	4.1	95.7	3.6	0.7	---
0	5.0	96.8	2.7	0.5	---
-20	4.3	96.3	3.2	0.5	---

Aside from the uncertainty as to the source of the asphaltenes, it is understandable why the higher temperature waxes are composed of asphaltenes. Asphaltenes are high molecular weight species and can be viewed as being more peptized (less flocculated) at the higher temperatures. Therefore, asphaltenes would tend to associate with the higher temperature waxes. The presence of these asphaltenes with the higher temperature waxes could also explain why the GPC molecular size distribution contains two peaks. The peak on the left probably represents the asphaltenes, while the peak on the right might represent the saturates and associated polars and aromatics.

This reasoning does not, however, explain either how or why the asphaltenes are associated with any of these waxes, since a bulk deasphalting step should have removed them. Further analysis of this asphaltene association yielded some interesting results which are outlined below.

#### Asphaltene Effect

As noted, asphaltenes are associated with the waxes, even though they should have been removed by a bulk deasphalting step during the wax separation. This association was verified by determining the saturates, aromatics, polar, and asphaltene content of Bu Attifel in two different manners.

First, Bu Attifel crude was directly separated by group type into saturates, polars, aromatics, and asphaltenes and volatiles by HPLC. Conversely, by total wax separation at 0°F, the crude was separated into the total wax, oil and bulk asphaltene fractions. These fractions were then analyzed by HPLC to yield the group types contained in the fractions. The same total amounts of the saturates, aromatics, polars and asphaltenes should be obtained for both separation methods.

As can be seen in Table II, this does not appear to be true for the asphaltenes and saturates. Only when the saturates and asphaltenes are added together is conservation of mass satisfied. Apparently, the saturates and asphaltenes are associated with one another and do not totally separate from one another during the bulk deasphalting step. Asphaltenes have been reported to be associated with polar and aromatic components during deasphalting, but in this case, the deasphalting step is leaving asphaltenes behind.

TABLE II

BU ATTIFEL CRUDE COMPONENT ANALYSIS

HPLC Analysis After Separation Into Wax,  
Asphaltenes, and Oil By Gulf Method 281

Components	Wt. %	Saturates	Insolubles (asphaltenes)	Polars	Aromatics	Volatiles
Wax	29.5	= 27.317	+ 1.475	+ .059	+ .649	+ 0
Asphaltenes	3.9	= .17	+ 3.72	+ 0	+ 0	+ 0
Oil	41.0	= 36.018	+ 0	+ .241	+ 4.751	+ 0
Volatiles	25.6	= 0	+ 0	+ 0	+ 0	+ 25.6

---

Total	100.00	= 63.505	+ 5.195	+ .3	+ 6.40	+ 25.6
		68.7				

HPLC Analysis of the Total Crude

Total Crude	100.00	= 67.8	+ 0.9	+ .31	+ 5.79	+ 25.6
		68.7				

It is interesting to note the precipitation temperature at which the waxes no longer contain asphaltenes (Table I). No asphaltenes are found with the waxes that precipitate at temperatures below 10°C (50°F). It should be noted that Bu Attifel crude's pour point has never been depressed below this temperature.

Similar analysis of Cabinda Crude (Table III) verifies the Bu Attifel results. As with Bu Attifel crude, asphaltenes are associated with the saturates at higher precipitation temperatures. Asphaltenes are, however, found with all of the waxes that precipitate out to -17°C (0°F). This is especially interesting since this wax precipitation temperature also represents the maximum depressed pour point obtained for Cabinda crude by using chemical additives.

TABLE III

## HPLC ANALYSIS OF CABINDA WAXES SEPARATED BY MODIFIED G-281

TEMPERATURE- WAX REMOVAL (°F)	(G-281)	HPLC of the Waxes			
	WT. % WAXES	WT. % SATURATES	WT. % AROMATICS	WT. % POLARS	WT. % ASPHALTENES
100	2.1	12.4	4.1	8.3	75.2
90	0.3	20.4	7.2	28.8	43.6
80	3.1	57.0	13.6	24.4	1.7
70	2.0	70.5	11.6	17.5	0.4
60	1.4	70.3	12.2	17.4	0.1
50	2.2	70.3	12.7	16.6	0.4
40	3.7	60.0	16.4	23.3	0.3
20	4.4	66.7	16.3	16.9	0.1
0	3.3	66.2	18.5	15.1	0.2

Additional analysis of six crude oils confirms that asphaltenes are associated with the level of pour point depression. Table IV summarizes the maximum effect of pour point depressants on the crudes. Note that this temperature also represents the temperature at which the asphaltene-saturate association ends.

TABLE IV

## ASPHALTENE - POUR POINT DEPRESSION TREND

CRUDE	WASATCH	GREEN RIVER	HANDIL	GOBBS
Pour Point (°F)	105	95	90	85
Maximum Depressed Pour Point (°F)	105	60	70	30

Temperature-  
Wax Removal

## HPLC Indication of Asphaltene

110	*	*	*	*
100		*	*	*
95		*	*	*
90		*	*	*
80		*	*	*
70		*	*	*
60		*		*
50				*
40				*
30				*
20				
0				

\*Denotes presence of asphaltenes.

The treated and untreated waxes in Bu Attifel crude were isolated by the centrifuge method and analyzed with HPLC. This study indicated (Table V) that the untreated portion of Bu Attifel crude contained no asphaltenes.

TABLE V  
ANALYSIS OF UNTREATED, CENTRIFUGED BU ATTIFEL WAXES

(G-281)		HPLC OF THE WAXES				
TEMPERATURE- WAX REMOVAL (F°)	WT. % WAXES	WT. % SATURATES	WT. % AROMATICS	WT. % POLARS	WT. % VOLATILES	WT. % ASPHALTENES
0	33.9	70.9	6.5	0.4	22.2	0.0

Based on these results it appears that the presence of asphaltenes with waxes indicates that the waxes will be susceptible to wax crystal modification and subsequent pour point reduction induced by chemical additives. It is apparent that the asphaltenes are either a symptom of a wax crystalline form that is susceptible to modification, or themselves caused a weak link in the wax crystal and thus cause the wax to be susceptible to modification.

Past research has suggested that asphaltenes can aid or act as wax crystal modifiers (pour point depressants), but it was never possible to predict their effect on a given crude or distillate. Therefore, these results also begin to explain some of the ambiguities encountered with using asphaltenes as pour point depressants. Plain bulk asphaltenes may never be associated with or interfere with a given wax structure, but specific asphaltenes, such as those associated with the waxes in Cabinda crude may be necessary.

#### CONCLUSIONS

- 1) Waxes that precipitate at temperatures above the congealing temperature contain mainly asphaltenes. These waxes also are composed of higher molecular weight species than the waxes that precipitate at temperatures below the congealing temperature.
- 2) Asphaltenes appear to play an important role in pour point reduction. They either symptomize waxes that are susceptible to chemical additives, or else interfere with the congealing mechanism. The presence of asphaltenes with waxes indicates that the waxes will be modified by chemical additives.
- 3) Different high pour crudes have different wax precipitation temperature limits of the wax-asphaltene association. Therefore, the maximum pour point depression attainable with each crude appears to be a function of the precipitation temperature where asphaltenes are no longer associated with the waxes.

- 4) The bulk asphaltenes may be chemically different from the asphaltenes found associated with the Bu Attifel and Cabinda waxes.

#### ACKNOWLEDGEMENTS

The assistance of the following is greatly appreciated: R. Hutchison for the asphaltene separations and R. Ruberto for the GPC and HPLC analysis. Both were GR&DC employees at the time of this study.



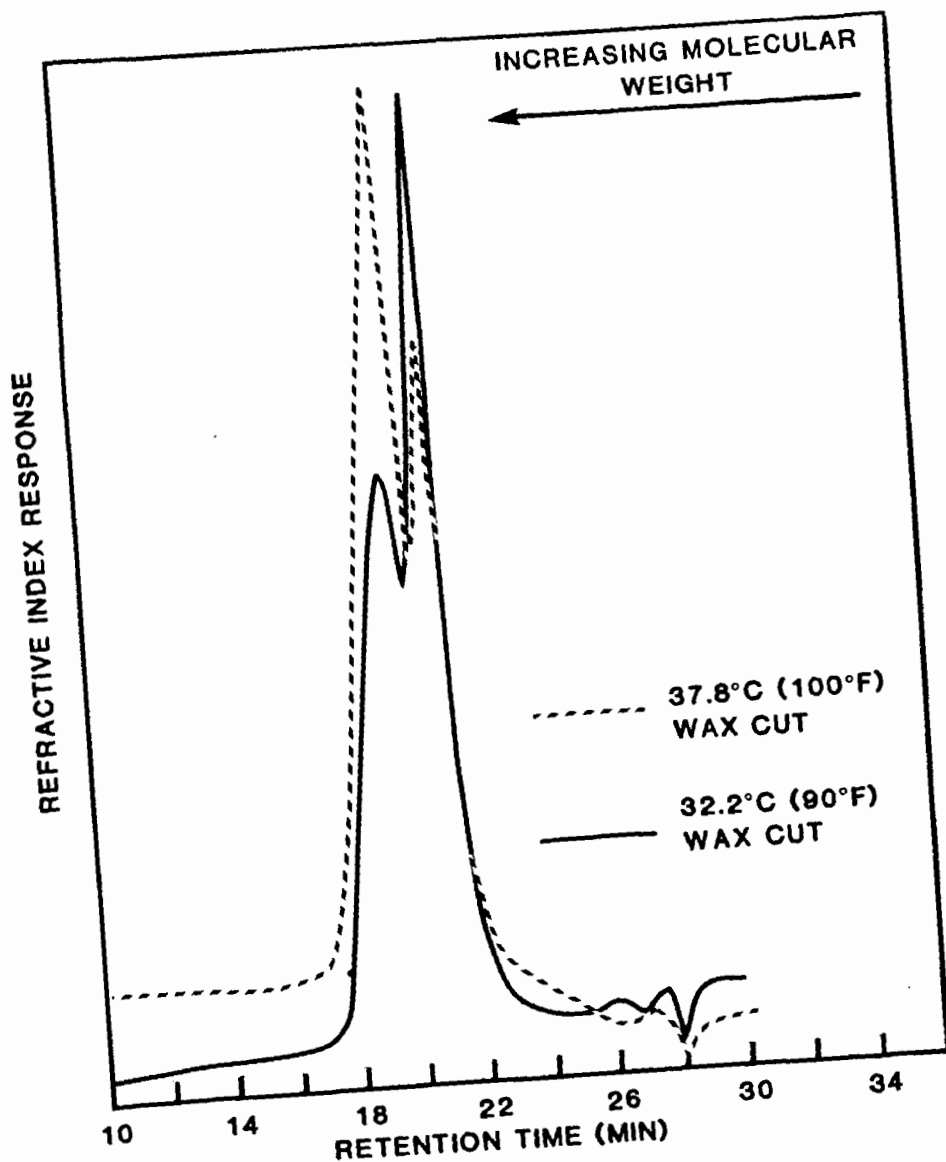


Fig.1 MOLECULAR WEIGHT DISTRIBUTION TREND  
CHANGE BETWEEN BUATTIFEL WAX FRACTIONS

## APPLICATIONS OF PERCOLATION THEORY TO THE ANALYSIS OF COAL GASIFICATION

Sebastián Reyes and Klavs F. Jensen

Department of Chemical Engineering and Materials Science  
University of Minnesota, Minneapolis, MN 55455

### INTRODUCTION

The changes in pore structure, internal surface area, and transport characteristics of porous carbonaceous materials play a major role in their gasification behavior. To describe the complex interactions of physical and transport properties during char gasification, it is essential to have a realistic model for the evolution of geometrical and topological features of the pore space. Several models for the structural changes during gas-solid reactions have been developed (1-11) resulting in important contributions to the understanding of char gasification reactions. Nevertheless, refinements are needed since available models can successfully predict only a subset of experimental observations. Even though available structural models include key features of pore branching, important topological effects are lost when the influence of closed porosity is not taken into account and effective diffusion coefficients are evaluated through tortuosity factors. Another key topologically dependent property is the eventual fragmentation of the particle at a critical porosity. The uniform development of porosity in the kinetic regime causes particle disintegration preferentially at high conversions. On the other hand, when diffusional resistances are important, the critical porosity of fragmentation is reached first at the particle surface, causing the continuous shrinkage of the particle from the early stages of conversion. Consequently, the overall conversion is not only determined by the conversion level of the shrinking particle but also by the history of released fragments. An interesting treatment of particle shrinkage during char particle combustion has been presented by Gavalas (9). However, more detailed analysis is required to relate the critical porosity of fragmentation to the topology of the internal structure.

The objective of this paper is to present an application of percolation theory to the analysis of coal gasification. It is well known that inorganic impurities naturally present in char particles can catalyze gasification reactions (12). However, our primary objective is to improve the structural models. Realistic extensions may then be made to include catalytic effects. The present particle description focuses on structural and topological features not included in previous models. The use of percolation theory provides a natural framework for understanding and evaluating the role of pore opening, pore enlargement and pore overlap in the evolution of porosity and internal surface area. Moreover, it accurately describes the fundamental influence of pore topology on transport characteristics of the internal structure, as well as particle fragmentation phenomena at high porosities.

### PERCOLATION CONCEPTS AND STRUCTURAL PROPERTIES

A general description of char gasification requires a model relating physical and transport properties to local structural changes. This model should accurately describe the accessible porosity ( $\phi^A$ ), accessible internal surface area per unit volume ( $\hat{a}^A$ ), and effective transport coefficients ( $\epsilon^B$ ) as functions of local carbon conversion. The potential contributions from closed pores to the total surface area ( $\hat{a}$ ) and total porosity ( $\phi$ ) can be locally described through the relations:

$$\phi^A = \phi - \phi^I \quad 1)$$

$$\hat{a}^A = \hat{a} - \hat{a}^I \quad 2)$$

where the superscript I on  $\phi$  and  $\hat{a}$  identify the isolated porosity and surface area. Equations 1 and 2 are necessary to account for pore opening by chemical reactions of the internal structure.

The effective transport coefficients are strongly dependent on the development of  $\phi^A$  as well as on the size and geometry of the pores. That is,  $\phi^A$  reflects the main topological features of the internal structure, such as dead ends and tortuous paths, which determine the extent of mass transport through the pore space. Moreover, if Knudsen diffusion is significant, the evolution of the pore size distribution also becomes a key factor in predicting transport.

Since a complete characterization of pore space morphology cannot be obtained by regular geometrical and topological simplifications, it is desirable to resort to some statistical description. This is supported by the observation that the majority of porous solids exhibit highly disordered structures. Consequently, the statistical means of percolation theory are ideally suited for evaluating  $\phi^A$ ,  $\hat{a}^A$  and  $\epsilon^E$  in terms of  $\phi$ . Percolation theory, first introduced by Broadbent and Hammersley (13), has been successfully applied to describe numerous physical and mechanical phenomena in disordered media. Key concepts and details of the theory can be found in available review papers (e.g. (14-16)).

Transport and reactions in porous solids can be modelled, in principle, by constructing large space filling random structures. However, the computational effort involved surpasses available resources even in large scale computing facilities. Fortunately, key features of these models are captured by simple networks. Reyes and Jensen (17) have recently demonstrated that a network model of pore topology, a so-called Bethe network may be used to evaluate  $\phi^A$  and  $\epsilon^E$  in porous solids. A Bethe network is an endlessly branching tree lacking reconnections and completely characterized by its coordination number  $z$ . The coordination number is the number of bonds connecting each site. If a fraction  $\phi$  of randomly selected bonds are labeled as "pores",  $\phi^A$  is a unique function of  $\phi$  and  $z$ . If  $\phi$  is less than a nonzero threshold value  $\phi_c$ , called the percolation threshold, the pore space consists of disconnected regions, i.e. isolated pores. The threshold value for Bethe networks is given by (18):

$$\phi_c = 1/(z-1) \quad 3)$$

The network thus defined can be conveniently used to simulate topological features in porous solids. Since its topological properties are preserved by increasing or decreasing the length and/or the cross-section of the bonds, the experimentally measured porosity,  $\phi^A$ , and pore size distribution,  $f(r)$ , can be readily matched to the network model by randomly removing a fraction  $1-\phi(\phi^A, z)$  of bonds and distributing sizes to a fraction  $\phi(\phi^A, z)$  according to  $f(r)$ . To completely specify the appropriate network model simulating the pore space of the porous solid, the coordination number of the Bethe network must be selected. This number is chosen to match the percolation threshold of the Bethe network and the porous solid.  $\phi_c$  for the solid can be determined from fragmentation studies (19) through the relation:

$$\phi_c = 1 - \phi^* \quad 4)$$

where  $\phi^*$  is the critical porosity of fragmentation. An alternative approach is to directly determine  $z$  from experimental data on effective diffusion coefficients (17). A schematic representation of accessible pore space simulated by a 3-coordinated Bethe network is shown in Figure 1 for arbitrary inputs of  $\phi^A$  and  $f(r)$ . The attractiveness of this approach is that effective transport coefficients can be exactly evaluated for binary mixtures without resorting to tortuosity factors while explicitly accounting for the influences of narrow necks, tortuous paths and dead ends. Close agreement has been found between predictions with this method and published experimental data on effective diffusion coefficients (17). As an example, Table 1 shows experimentally measured diffusion coefficients for the pair CO-CO<sub>2</sub> in porous

electrode graphite (20), and predicted values with a 5-coordinated Bethe network. Predicted values are in excellent agreement with measurements for a wide range of temperatures (18-900°C) and pressures (0.1-10 atm). Moreover, this approach allows a natural extension for evaluating  $\epsilon^E$  in changing structures, since input values of  $\phi$  and  $f(r)$ , characterizing the local morphology, can be determined from independent balance equations.

By using the present Bethe network representation of the pore space, particle fragmentation may be modelled by Equations 3 and 4. Once the appropriate coordination number has been selected, both  $\phi_c$  and  $\phi^*$  are determined. However, it should be emphasized that  $\phi^*$  is based solely on topological features of two-phase structures leading to particle breakup by reactions, and not to mechanical phenomena, such as abrasion. The mass distribution of released fragments may be estimated as (21):

$$g(r, z) = \frac{z((z-1)n)!}{(n-1)!((z-2)n+2)!} \cdot \frac{(z-2)^{(z-2)n+2}}{(z-1)^{(z-1)n+2}} \quad (5)$$

where  $n$  is an integer number representing the size of the cluster whose mass is  $m_f$ , with  $m_f$  being the mass of the smallest fractal unit characterizing the structure.

To complete the framework for a gasification model, the accessible internal surface area must be related to the local structure. Consistent with the Bethe network formulation, and based on probabilistic arguments,  $\hat{a}^A$  can be estimated as (21):

$$\hat{a}^A = K[\phi(1-\phi) - \phi I(\phi, z)[1 - \phi I(\phi, z)]] \quad (6)$$

The constant  $K$  is related to the mass per unit volume of a fractal unit, and can be obtained by matching  $\hat{a}^A$  to a single surface area determination. The important implications of this approach are that effects of pore enlargement and pore overlap become natural consequences of increasing  $\phi$  in a random fashion.

#### GASIFICATION MODEL

Gasification of a single char particle in  $\text{CO}_2$  is chosen to illustrate the percolation based approach outlined in the previous section. It is further assumed that there are no catalytically active mineral impurities in the char. The evaluation of physical, transport and fragmentation properties require initial data readily available by conventional characterization of porous solids (e.g.  $\phi_0^A$ ,  $\hat{a}_0^A$ ,  $f_0(r)$ ), except for the coordination number of the network. This number can be implied from experimental data on diffusion coefficients or fragmentation studies. However, here it is considered as a parameter to simulate gasification behavior of char particles with various levels of pore space connectivity. Typical values fall in the range 4 to 8 (17).

The reaction is considered to be first order in  $\text{CO}_2$ . Since this reaction leads to an increase in the number of moles, mass transfer contributions from both concentration and pressure gradients must be included in the model equations. The derivation of the appropriate equations describing the gasification behavior for the above conditions has been presented elsewhere (22). In dimensionless form, modelling equations may be summarized as:

Mass balances for gaseous components:  $i \neq j = \text{CO}, \text{CO}_2$

$$0 = \frac{1}{\eta} \frac{1}{\xi} \frac{\partial}{\partial \xi} \left[ \xi^2 \epsilon_{ij}^{ED} \lambda \frac{\partial X_i}{\partial \xi} + \xi^2 \epsilon_{ij}^{EP} X_i \frac{\partial \lambda}{\partial \xi} \right] + v_i \psi_0^2 S \lambda X_{\text{CO}_2} \quad (7)$$

$$X_i(\xi, 0) = 0 \quad (8)$$

$$\partial X_i(0, \tau) / \partial \xi = 0 \quad (9)$$

$$\left\{ \epsilon_{ij}^{ED} \lambda \frac{\partial X_i}{\partial \xi} + \epsilon_{ij}^{EP} X_i \frac{\partial \lambda}{\partial \xi} \right\} \Big|_{\xi=1} = \eta B_{m1} (X_{1b} - X_1(1, \tau)) \quad (10)$$

Mass balance for solid phase:

$$\frac{d\phi}{d\tau} = \sigma_0 S \lambda X_{CO_2} + \frac{\xi}{\eta} \frac{\partial \phi}{\partial \xi} \frac{d\eta}{d\tau} \quad (11)$$

$$\gamma(\xi, 0) = \phi_0 \quad (12)$$

Rate of particle shrinkage:

$$\frac{d\eta}{d\tau} = - \left\{ \lambda X_{CO_2} \right\} \Big|_{\xi=1} \quad \tau < \tau^* \quad (13)$$

$$\eta(0) = 1$$

$$\frac{d\eta}{d\tau} = - \eta \left\{ \frac{\sigma_0 S \lambda X_{CO_2}}{\partial \phi / \partial \xi} \right\} \Big|_{\xi=1} \quad \tau > \tau^* \quad (14)$$

$$\eta(\tau_+^*) = \eta(\tau_-^*)$$

Pore growth:

$$\zeta(\xi, \tau) = F(\xi, \tau) / S(\xi, \tau) \quad (15)$$

The dimensionless variables were chosen to facilitate the numerical solution of the modeling equations and expose time constants for key physicochemical processes involved.  $S$ ,  $\zeta$ ,  $\lambda$ ,  $X$  are dimensionless surface area, pore radius, pressure and gas concentration, respectively.  $\epsilon_{ij}^{ED}$  and  $\epsilon_{ij}^{EP}$  are dimensionless local effective diffusion and permeability coefficients, respectively. By defining  $\eta = r^*/r_{oc}$  and  $\xi = r/r^*$ , where  $r^*$  is the instantaneous particle radius, the moving boundary problem is transformed to a fixed one. The second term on the right hand side of Equation 11 accounts for the effect of the moving boundary arising from shrinking particle size. The external surface of the particle recedes by two major mechanisms: chemical reaction on the external surface and perimeter fragmentation, as described by Equations 13 and 14, respectively.  $\tau^*$  is the dimensionless time at which  $\phi$  in Equation 11 reaches the critical porosity of fragmentation  $\phi^*$ . The complete specification of the modelling equations requires working expressions for  $\phi^A(\phi, z)$  and  $\epsilon^E(z, \phi, f(r), L(r))$  developed in Reyes and Jensen (17).

#### GASIFICATION IN THE KINETIC REGIME

In the kinetic regime  $CO_2$  is uniformly distributed throughout the particle so only the rate of carbon consumption, according to Equation 11, is required to describe the gasification behavior. Furthermore, since only a negligible particle shrinkage occurs due to chemical reaction on the external surface, the second term on the right hand side of Equation 11 can be neglected. Because of the uniform porosity increase throughout the particle, Equation 14 predicts an instantaneous disintegration of the particle when  $\phi$  reaches  $\phi^*$ . For  $\phi > \phi^*$  it can be shown that (21):

$$\phi = \frac{\phi^*}{\phi^* + (1-\phi^*) \exp\{-Kr_{oc}[\tau-\tau^*]\}} \quad (16)$$

where  $r_{oc}$  is the initial particle radius, and  $\phi$  is now a pseudo-porosity whose complementary fraction  $(1-\phi)$  represents the remaining fraction of the initial solid

material. If conversion is related to  $\phi$  through the relation:

$$X_{cp} = \frac{\phi - \phi_0}{1 - \phi_0} \quad (17)$$

then the gasification rate is evaluated as:

$$\frac{dX_{cp}}{d\tau} = \frac{\{\sigma_0 \lambda X_{CO_2} / (1 - \phi_0)\} S}{K_{r_{oc}} \phi^* (1 - \phi^*) \exp\{-K_{r_{oc}}[\tau - \tau^*]\}} \quad , \tau < \tau^* \quad (18a)$$

$$\frac{dX_{cp}}{d\tau} = \frac{K_{r_{oc}} \phi^* (1 - \phi^*) \exp\{-K_{r_{oc}}[\tau - \tau^*]\}}{(1 - \phi_0) \{\phi^* + (1 - \phi^*) \exp\{-K_{r_{oc}}[\tau - \tau^*]\}\}^2} \quad , \tau > \tau^* \quad (18b)$$

Therefore, by using Equations 11, 16, 17 and 18 the complete gasification behavior of a char particle can be simulated. Typical kinetic and physical parameters chosen for this purpose are summarized in Table 2. It is assumed that micro- and mesopores are primarily responsible for the surface area and that they account for 2/3 and 1/3 of the pore volume, respectively. By using the general model equations it was verified that the parameter values in Table 2 correspond to gasification under kinetically controlled conditions. Figure 2 summarizes gasification behavior for porous char particles with different initial accessible porosities. A coordination number of  $z=7$  was chosen to simulate a complex random structure giving a critical porosity of fragmentation of approximately 5/6, similar to values observed by Dutta et al. (23) and Kerstein and Niksa (19). The solid lines describe the gasification before particle disintegration. As expected, the higher the initial porosity the lower the conversion at which particle disintegration takes place. Beyond this critical conversion, the gasification of fragments is described by the dashed lines, as evaluated by Equations 16, 17 and 18b. The shapes of the rate curves reflect competition between surface area enlargement due to pore growth at low conversion, and surface area decay due to pore coalescence at larger porosities. With increasing values of initial porosities the coalescence process becomes important at shorter times, causing the maximum rate to decrease and shift towards lower values of conversion. Further increases in porosity cause the maximum to disappear.

The existence of closed pores, a topological feature of the internal structure, also plays a role in the gasification. Their existence has been experimentally determined by several investigators (e.g. 20, 25). This effect can be readily illustrated by analyzing the behavior of char particles with different pore space connectivities. As observed from Figure 3, for a  $\phi_0^* = 0.20$ , the more connected the internal structure is the higher the conversion at which particle disintegration takes place. In addition, as the connectivity is increased, the maximum rates decrease in magnitude and shift toward higher values of conversion. These phenomena are readily explained by noting that the lower the connectivity of the pore space is, the greater the amount of closed pores that can be made accessible by chemical reactions of pore walls. This in turn causes the accessible surface area to increase but also makes the rate of pore coalescence dominant at low conversions.

#### GASIFICATION IN THE DIFFUSIONAL REGIME

To clearly focus on transport limitations caused by intraparticle phenomena, it will be assumed that there is no boundary layer resistance for mass transport to the external surface (i.e.  $B_{m1} \gg 1$ ). The existence of boundary layer resistance can readily be included in the numerical solution but the interpretation of the results become unnecessarily more complicated. The modelling equations 7-15 were solved numerically by using orthogonal collocation on finite elements (23).

Once the onset of perimeter fragmentation has been reached, the global conversion and gasification rate depend not only on the gasification behavior of the

shrinking particle but also on the gasification history of the released fragments. By integrating Equation 17 throughout the particle and dividing by the particle volume, the global particle conversion is evaluated as:

$$\hat{x}_{cp}(\tau) = 3 \int_0^1 \hat{x}_{cp}(\xi, \tau) \xi^2 d\xi \quad (19)$$

Since released fragments react in a kinetic regime (21), their conversions and gasification rates are obtained by Equations 16, 17 and 18b. The global conversion of the fragments released at time  $\tau_1$  is evaluated as:

$$\hat{x}_{cf}(\tau, \tau_1) = \frac{1 - \phi_0 \{1 + ((1 - \phi^*)/\phi^*) \exp[-K r_{oc}(\tau - \tau_1)]\}}{(1 - \phi_0) \{1 + ((1 - \phi^*)/\phi^*) \exp[-K r_{oc}(\tau - \tau_1)]\}} \quad , \quad \tau > \tau_1 > \tau^* \quad (20)$$

By weighting contributions from the shrinking particle and released fragments, the overall conversion behavior may be evaluated as:

$$\hat{x}_{cg}(\tau) = \eta^3(\tau) \hat{x}_{cp}(\tau) - \int_{\tau^*}^{\tau} \hat{x}_{cf}(\tau, \tau') \frac{dn^3(\tau')}{d\tau'} d\tau' \quad (21)$$

The corresponding overall gasification rate,  $d\hat{x}_{cg}(\tau)/d\tau$ , is obtained by taking the time derivative of  $\hat{x}_{cg}(\tau)$  in Equation 21.

In order to illustrate the model predictions, the gasification behavior of a char particle at 1000°C with  $\phi_0 = 0.20$  and simulated with  $z=7$  is presented. Other conditions as those in Table 2. Figure 4 shows CO<sub>2</sub> concentration profiles for different levels of carbon conversion. It is observed that as conversion increases, the profiles flatten out and approach the bulk concentration. This increase in concentration with burnoff is primarily caused by improved transport characteristics of the internal pore structure, as pore space is widened and made accessible. Since conversion increases most rapidly near the external surface, where the CO<sub>2</sub> concentration is high, the initial porosity for fragmentation is first reached at the particle surface when  $\hat{x}_{cg} = 0.65$ . While negligible particle shrinkage occurs because of chemical reaction on the particle surface, a rapid decrease in particle radius takes place by perimeter fragmentation.

The evolution of the dimensionless accessible surface area with carbon conversion is shown in Figure 5. In the early stages of conversion the surface area gradually grows due to pore enlargement as well as the contributions from closed pores. However, with increasing conversion, pore overlap between growing neighboring surfaces dominates over pore enlargement, causing the surface area to decrease. Because of the radially nonuniform conditions within the particle, the same qualitative surface area behavior occurs at each radial position but at different times. Even though this figure illustrates typical behavior during char gasification, it was previously shown that the surface area will not exhibit a maximum under conditions where pore overlap is already dominant from the beginning of the gasification.

The overall gasification curve for the above example is shown in Figure 6. This curve represents the often observed behavior where the rate goes through a maximum at some intermediate conversion. As intuitively expected, the conversion for maximum rate shifts toward higher values when the temperature is increased from a kinetic to a diffusional regime. Further temperature increase causes the critical conversion to decrease again, and eventually the maximum disappears, since in the limit of high temperature the particle reacts with a purely shrinking core behavior (SC). At  $\hat{x}_{cg} = 0.65$  the onset of perimeter fragmentation is observed. At this point the rate exhibits an increase in its slope, which indicates an acceleration in the gasification process due to fragmentation phenomena. This acceleration effect is small in the present example because the high surface area of the particle segregates the solid structure into very small fragments (21), whose concentration before their

release is not much different from the bulk concentration. In this case, the acceleration is primarily due to the higher rates in the shrinking particle because of increasing overall transport rates with decreasing particle size. A much stronger effect would have been observed if external mass transport resistances were significant (i.e.  $B_{mi} \ll 1$ ).

Figure 7 illustrates the change in particle size with particle conversion for different temperatures. At low temperatures the particle gasifies in the kinetic regime and disintegrates spontaneously when the critical porosity is reached. As diffusion resistance increases in importance with higher temperatures, perimeter fragmentation occurs at lower conversions. In the limit of very high temperatures (i.e. reaction rates) perimeter fragmentation takes place from the beginning and the particle then follows the classical shrinking core (SC) behavior.

#### CONCLUSION

The application of percolation theory concepts to modelling of a single particle char gasification has been summarized. Emphasis has been placed on the interpretation and evaluation of transport and fragmentation properties of the changing pore structure during gasification. The qualitative behavior of the model in both the kinetically and the diffusionally controlled regimes clearly reflect the strong influence of structural properties on gasification. Furthermore, the good agreement between these model predictions and reported experimental observations (11,20,24-33) are encouraging for further use of percolation theory in modelling changing coal structures.

#### REFERENCES

1. Petersen, E. E., *AIChE J.* 3, 443-448 (1957).
2. Szekely, J. and J.W. Evans, *Chem. Engng. Sci.* 25, 1091-1097 (1970).
3. Hashimoto, K. and P.L. Silveston, *AIChE J.* 19, 259-268 (1973).
4. Simons, G.A. and M.L. Finson, *Combust. Sci. Technol.* 19, 217-225 (1979).
5. Simons, G.A., *Combust. Sci. Technol.* 19, 227-235 (1979).
6. Bhatia, S.K. and Perlmutter, D.D., *AIChE J.* 26, 379-386 (1980).
7. Bhatia, S.K. and Perlmutter, D.D., *AIChE J.* 27, 247-254 (1980).
8. Gavallas, G.R., *AIChE J.* 26, 577-585 (1980).
9. Gavallas, G.R., *Combust. Sci. Technol.* 24, 197-210 (1981).
10. Zygourakis, K., L. Arri and N.R. Amundson, *Ind. Eng. Chem. Fundam.* 21, 1-12 (1982).
11. Tseng, H.P. and T.F. Edgar, *AIChE Annual Meeting*, Los Angeles, CA (1982).
12. Reyes, S. and K.F. Jensen, *Ind. Eng. Chem. Fundam.* 23, 223-229 (1984).
13. Broadbent, S.R. and J.M. Hammersley, *Proc. Camb. Phil. Soc.* E3, 629-641 (1957).
14. Frisch, H.L. and J.M. Hammersley, *J. SIAM*, 11, 894-918 (1963).
15. Shante, V.K.S. and S. Kirkpatrick, *Adv. Phys.* 20, 325-357 (1971).
16. Hughes, B.D. and S. Prager, "The Mathematics and Physics of Disordered Media," Springer-Verlag, New York, 1-108 (1983).
17. Reyes, S. and K.F. Jensen, *Annual AIChE Meeting*, San Francisco, CA, Paper 35a (1984).
18. Fisher, M.E. and J.W. Essam, *J. Math. Phys.* 2, 609-619 (1961).
19. Kerstein, A.R. and S. Niksa, *Int. Conference on Coal Science*, Pittsburgh, PA, 743-746 (1983).
20. Turkdogan, E.T., R.G. Olson and J.V. Vinters, *Carbon* 8, 545-564 (1970).
21. Reyes, S. and K.F. Jensen, submitted to *Chem. Engng. Sci.*
22. Reyes, S. and K.F. Jensen, submitted to *Chem. Engng. Sci.*
23. Carey, G.F. and B.A. Finlayson, *Chem. Engng. Sci.* 30, 587-596 (1975).
24. Dutta, S., C.Y. Wen and R. J. Belt, *Ind. Eng. Chem. Process Des. Dev.* 16, 20-30 (1977).
25. Kawahata, M. and P.L. Walker, Jr., *Proceedings 5th Carbon Conference*, Pergamon Press, London, 251-263 (1962).



26. Walker, P.L. Jr., R.J. Foresti, Jr. and C.C. Wright, Ind. Eng. Chem. 45, 1703-1710 (1953).
27. Petersen, E.E., P.L. Walker, Jr. and C.C. Wright, Ind. Eng. Chem. 47, 1629-1630 (1955).
28. Walker, P.L. Jr. and E. Raats, J. Phys. Chem. 60, 364-369 (1956).
29. Berger, J., T. Siemieniewska and K. Tomkow, Fuel 55, 9-15 (1976).
30. Tomkow, K., A. Jankowska, F. Czechowski and T. Siemieniewska, Fuel 56, 101-106 (1977).
31. Dutta, S. and C.Y. Wen, Ind. Eng. Chem. Process Des. Dev. 16, 31-37 (1977).
32. Hashimoto, K., K. Miura, F. Yoshikawa and I. Imai, Ind. Eng. Chem. Process Des. Dev. 18, 72-80 (1979).
33. Foster, M. and K.F. Jensen, Int. Conference on Coal Science, Pittsburgh, PA, 464-467 (1983).

#### ACKNOWLEDGEMENT

This work was supported by DOE (DE/FG22-82PC50806) and the Graduate School of the University of Minnesota.

Temperature	Pressure	$D_{CO-CO_2}^E$ (a)	$D_{CO-CO_2}^E$ (b)
$^{\circ}C$	atm.	$cm^2/s$	$cm^2/s$
18	1.0	0.0018	0.0014
500	1.0	0.0060	0.0069
600	1.0	0.0072	0.0083
700	0.1	0.043	0.041
700	0.2	0.035	0.032
700	0.5	0.018	0.019
700	1.0	0.0099	0.011
700	10.0	0.0012	0.0014
800	1.0	0.012	0.011
900	1.0	0.014	0.013

Table 1. Experimental and predicted effective diffusion coefficients in porous electrode graphite. (a) Experimental value, Turkdogan et al. (20), (b) Bethe network predictions ( $z=5$ ).

Preexponential factor	: $k = 5.0 \times 10^3$ (m/s)
Activation energy	: $E_a = 60.0$ (kcal/mol)
Specific surface area	: $S_o = 300.0$ (m <sup>2</sup> /gr)
Particle radius	: $r_{oc} = 200$ ( $\mu m$ )
Carbon density	: $\rho_p = 1500$ (kg/m <sup>3</sup> )
<u>Rayleigh distribution</u>	
smallest micropore radius	: $r_{\mu o} = 10A$
average micropore radius	: $r_{\mu a} = 20A$
smallest mesopore radius	: $r_{Mo} = 50A$
average mesopore radius	: $r_{Ma} = 200A$

Table 2. Kinetic and structural parameters used in the present simulations.

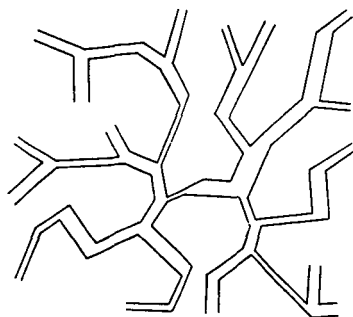


Figure 1. A schematic simulation of accessible pore space with a 3-coordinated Bethe network for arbitrary data of porosity and pore size distribution.

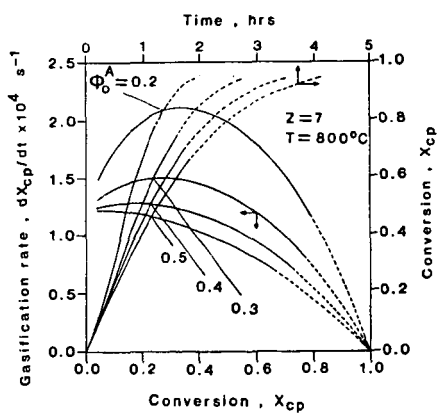


Figure 2. Conversion vs. time and gasification rate vs. conversion for a char particle for various initial porosities.

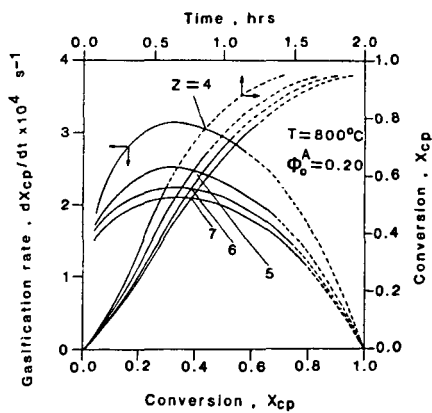


Figure 3. Conversion vs. time and gasification rate vs. conversion for a char particle with different pore space connectivities.

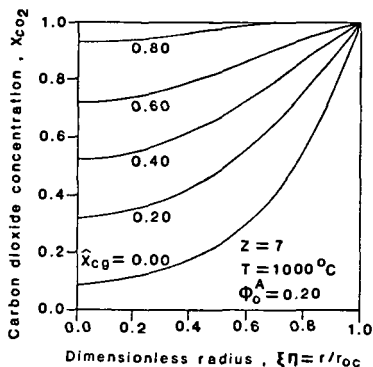


Figure 4. Carbon dioxide concentration profiles at various levels of overall conversion.

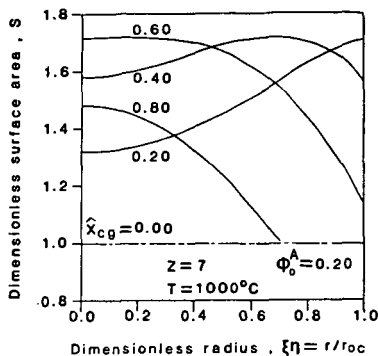


Figure 5. Dimensionless surface area profiles at various levels of overall conversion.

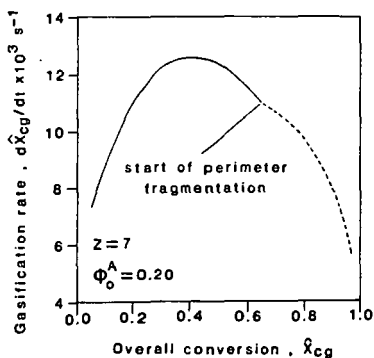


Figure 6. Gasification rate vs. conversion for a char particle at 1000^\circ C.

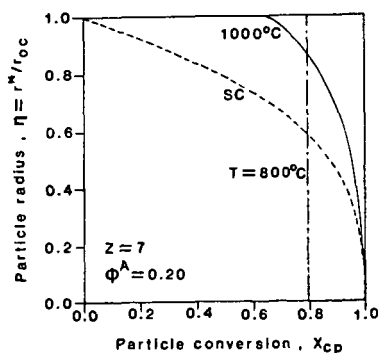


Figure 7. Particle radius as a function of particle conversion for a char particle for various reaction temperatures.

QUANTITATIVE ANALYSIS OF COALS AND COAL DERIVATIVES BY  
CP/MAS- $^{13}\text{C}$ -NMR SPECTROSCOPY

E. W. Hagaman and R. R. Chambers

Chemistry Division  
Oak Ridge National Laboratory  
P. O. Box X  
Oak Ridge, Tennessee 37831 USA

This paper reports experiments which are designed to ascertain the degree to which the CP/MAS- $^{13}\text{C}$ -nmr technique can be used in a quantitative sense in analysis of coal and coal derivatives. The quantitative capability of the experiment as applied to diamagnetic organic molecules is well documented (1). The uncertainty in the analysis of coals arises from the presence of a substantial organic-based free-electron spin density and from the uncertainty in the hydrogen distribution in these typically low H/C materials. The possibility exists that a fraction of the carbon in a coal experiences electron-nuclear interactions which render the signal invisible, broadened and/or paramagnetically shifted, or is in an environment depleted of hydrogen and unable to yield a  $^1\text{H}$ - $^{13}\text{C}$  CP signal.

To what extent are the carbons in coal detected with unit intensity response? The experiment selected to address this question entails introducing into the coal a known quantity of carbon designed to yield unit intensity response under the analysis conditions. The experimentally measured area ratio representing introduced carbon/native coal carbon from the CP/MAS- $^{13}\text{C}$ -spectrum is then compared with the same ratio determined in an unambiguous, independent experiment.

Chemical Modification of ILL. #6-Vitrain

The introduced carbon is incorporated by methylation of the heteroatoms of the coal which undergo base-catalyzed alkylation. In ILL. #6 vitrain these sites are predominantly (80-85%) phenolic residues. The balance of the introduced methyl groups are bonded to other functional groups. There is clear chemical shift evidence for methyl ester and aminomethyl groups and perhaps a small amount of sulfhydryl or select carbon methylation.

The methylation is performed with  $^{14}\text{C}$ ,  $^{13}\text{C}$ -double-labelled methyl iodide. The measure of introduced carbon is obtained by  $^{14}\text{C}$ -radioassay techniques, which, together with elemental analysis of the coal derivative, provides the benchmark ratio needed to evaluate the nmr integrations.

Large errors in the  $^{14}\text{C}$  and  $^{13}\text{C}$  ratio determinations can occur if solvents and/or reagents used in the derivitization contaminate the product. The extent of such unwanted incorporation in the present experiments have been measured by using  $^{14}\text{C}$ -labeled solvents and reagents in parallel experiments.

Initial methylations were performed using tetra-*n*-butyl ammonium hydroxide in aqueous THF following literature procedures (2). Repeated attempts to remove  $(\text{nBu})_4\text{N}^+\text{X}^-$  salts from the product using published methods were unsuccessful in our hands. The reagent can be removed by methanol washing, but a significant fraction of the coal is also solubilized by this solvent.

To prepare an O- $\text{CH}_3$  coal derivative free of carbon-containing reagents, a procedure for alkylation of coal using KOH in aqueous THF was developed. The methylation of ILL. #6 vitrain using this system introduced 4.6 methyl groups/100 coal carbons after 5 days reaction, ca. 10% fewer than obtained with the tetra-*n*-butylammonium

hydroxide/aqueous THF system. For the present purpose, complete alkylation is not required; the product, Ill. #6-OCH<sub>3</sub>, obtained following a single methylation step is analyzed in Table 1. Another product listed in Table 1, Ill. #6-XCH<sub>3</sub>, has been prepared by stirring Ill. #6 vitrain and methyl iodide (91.2% <sup>13</sup>C-enriched, 3-fold molar excess based on five acidic sites/100 coal carbons) in THF for five days. Under these conditions little aromatic methylether formed. The incorporation of methyl groups occurs predominantly on acid and amine functional groups.

THF retention in the coal products is minimal (<0.8 wt%) in all alkylation procedures.

#### CP/MAS-<sup>13</sup>C-NMR Analysis

The aromatic carbon fraction of coals,  $f_a$ , derived from CP/MAS-<sup>13</sup>C-nmr measurements are generally determined from aromatic and aliphatic carbon resonance area measurements taken from a single spectrum recorded under optimum or near optimum signal-to-noise conditions (cross polarization contact time = 1 ms). Reported  $f_a$  values determined in this fashion assume that the conditions for quantitative signal intensity response in this experiment, namely

$$T_{CH} \ll t_{cp} \ll T_{1\rho H}$$

are applicable.  $T_{CH}$  is the <sup>1</sup>H-<sup>13</sup>C cross polarization time constant under the Hartmann-Hahn condition,  $t_{cp}$  is the experimental cross polarization contact time, and  $T_{1\rho H}$  is the proton spin-lattice relaxation time in the rotating frame. Single spectrum analysis of  $f_a$  requires that a homogeneous  $T_{1\rho H}$  characterize the entire sample.

It has been shown that the aromatic and aliphatic resonance envelopes of coals generally display nearly homogeneous but different  $T_{1\rho H}$  behavior (3). The ratio  $T_{1\rho H}$  (aromatic)/ $T_{1\rho H}$  (aliphatic), with typical values of 0.8-1.2 for Ill. #6 vitrain derivatives, can be altered by chemical modification.

While the inequality  $T_{CH} \ll t_{cp} = 1$  ms is valid for protonated carbon sites in coals, it is only marginally met for the non-protonated aromatic carbon fraction of Ill. #6, which reveals an average  $T_{CH}$  of  $350 \pm 100$   $\mu$ s. This value should not differ significantly for other bituminous coals.

These considerations indicate that it is worthwhile to evaluate CP/MAS-<sup>13</sup>C-nmr data of coals more critically to assess the errors which may be introduced by single spectrum analysis.

The general expression given by Mehring (4) which describes the development of carbon signal intensity in the spin-lock, CP/MAS-<sup>13</sup>C-nmr experiment with non-negligible  $T_{1\rho H}$  relaxation is

$$A(t) = KN \frac{T_{1\rho H}}{T_{1\rho H} - T_{CH}} (e^{-t/T_{1\rho H}} - e^{-t/T_{CH}}) \quad 1)$$

where  $A(t)$  is <sup>13</sup>C signal intensity at  $t = t_{cp}$ ,  $N$  represents the number of acquisitions and  $K$  is a constant proportional to the number of <sup>13</sup>C spins and spectrometer sensitivity. By restricting the cross polarization contact time to values for which  $t_{cp} \gg T_{CH}$  and  $e^{-t_{cp}/T_{CH}} \ll e^{-t_{cp}/T_{1\rho H}}$ , Equation 1 reduces to

$$A(t) = KN \frac{T_{1\rho H}}{T_{1\rho H} - T_{CH}} (e^{-t/T_{1\rho H}}) \quad 2)$$

Examination of typical  $T_{1\rho H}$  and  $T_{CH}$  values for the coal derivatives under consideration shows that the use of cross polarization times  $> 2$  ms satisfy the restrictions which lead to Equation 2. To evaluate  $f_a$  the spectrum is recorded at five contact times  $> 2$  ms and the separate aromatic and aliphatic resonance areas are non-linear least-squares fit to Equation 2.  $K$  is evaluated at  $t_{cp} = 0$  as

$$K = A_0 \frac{T_{1\rho H} - T_{CH}}{T_{1\rho H}} \quad 3)$$

and  $f_a$  is given by  $K(\text{arom})/[K(\text{arom}) + K(\text{aliph})]$ .

The application of Equation 3 requires estimates of  $T_{CH}$  for several carbon types in coals. Previous studies of coals indicate that  $T_{CH}$  values of 35, 65 and 350  $\mu$ s for protonated carbons (aromatic and aliphatic), methyl carbons (methylether) and non-protonated aromatic carbons, respectively are acceptable estimates for the present analysis. The aliphatic resonance band is considered to have a negligible fraction of non-protonated carbons and 60% of the aromatic resonance band is considered to be non-protonated carbon (5).

Table 1 summarizes the aromaticity values for Ill. #6 vitrain calculated using Equation 3. Intensity data over the range of contact times 1.0-8.0 ms yields  $f_a$  of  $.660 \pm .003$ . The same data set, minus the intensity data for the 1 ms  $t_{cp}$ , yields a calculated  $f_a$  of  $.707 \pm .006$ . The 1 ms data strongly influences the calculation. Equation 3 is not an appropriate expression for analysis of the 1.0 - 8.0 ms data set since the inequality  $e^{-t_{cp}/T_{CH}} \ll t_{cp}/T_{CH}$  is not met for 1 ms data. Equation 1 should be used to treat this data. Note that the calculated  $f_a$  for the data for which  $t_{cp} > 2$  ms is in fair agreement with  $f_a$  determined from a single spectrum with  $t_{cp} = 1.0$  ms.

Table 1.  $f_a$  and Introduced CH<sub>3</sub>/100 Coal Carbons for Ill. #6 and Derivatives.

	$f_a$	Introduced CH <sub>3</sub> /100 Coal Carbons	
	Ill. #6	Ill. #6-OCH <sub>3</sub>	Ill. #6-XCH <sub>3</sub>
1.0-8.0ms $t_{cp}$ range	$0.660 \pm .003$	5.84	0.18
2.0-8.0ms $t_{cp}$ range	$0.707 \pm .006$	5.78	0.1
1.0ms $t_{cp}$ time	$0.697 \pm .02$	5.72	0.21

The number of methyl carbons introduced into the coal matrix is determined by assuming that  $f_a$  of Ill. #6 vitrain is valid for the original coal carbon of the products, i.e., interconversion of  $sp^2$  and  $sp^3$  carbons does not occur as a consequence of the derivitization. Hence,  $f_a$  of Ill. #6 vitrain and the aromatic resonance area of the product allow partitioning of the aliphatic resonance area into components representing native coal carbon and introduced carbon. This analysis is summarized in Table 1 for the two coal derivatives, Ill. #6-OCH<sub>3</sub> and Ill. #6-XCH<sub>3</sub>.

Note that the calculated value for the number of methyl groups introduced into Ill. #6-OCH<sub>3</sub> using the fitting procedure (Equation 3) is independent of the  $t_{cp}$  range and  $f_a$  assigned to the original coal, as long as the analysis of Ill. #6 vitrain and Ill. #6-OCH<sub>3</sub> is internally consistent. This is simply a statement that to within the error of the fit of the data to a single exponential, no detectable carbon intensity accrues in the spectrum between 1.0 and 2.0 ms. The fitting procedure simply corrects the measured areas for the differences in  $T_{1\rho H}$  between the coals and for the differences of  $T_{1\rho H}$  between the aromatic and aliphatic resonance bands of each coal.

The calculated values for the number of methyl groups introduced into the coal using single spectrum analysis with  $t_{cp} = 1.0, 2.0$  and  $3.0$  ms, is 5.72, 5.34 and 5.01, respectively, and indicate the magnitude of the error which is introduced by the  $T_{1\rho H}$  differentials between the coal and its derivative. Clearly the value at  $t_{cp} = 1.0$  ms is indistinguishable from the values obtained by the full fitting procedure. Thus a 1.0 ms cross polarization contact time is a judicious compromise value consistent with a nearly complete cross polarization signal from all carbons including detectable non-protonated carbons and minimum error introduced by differential  $T_{1\rho H}$  relaxation effects.

The methyl incorporation values shown in Table 1 for Ill. #6-XCH<sub>3</sub> show the same behavior but have larger relative error, a result of the small area changes in the product relative to Ill. #6 vitrain.

#### Comparison of <sup>13</sup>C-NMR and <sup>14</sup>C-Radioassay Analysis

The number of methyl groups found in Ill. #6-OCH<sub>3</sub> and Ill. #6-XCH<sub>3</sub> by the radioassay technique is 4.64/100 coal carbons and 0.20/100 coal carbons, respectively. The error in these values is largely determined by the error in elemental analyses and is <2%. The values determined by nmr analysis (1.0 ms CT) are  $5.72 \pm 1.1/100$  and  $0.21 \pm 0.04/100$  coal carbons, respectively. The 20% error associated with the nmr values is derived for the use of single spectrum analysis and is the worst case error calculated by allowing  $f_a$  of Ill. #6 vitrain and Ill. #6-OCH<sub>3</sub> to vary  $\pm .02$  from their measured values. We conclude that, within the estimated error of the nmr measurement, the CP/MAS-<sup>13</sup>C-nmr method does accurately monitor total carbon signal in the examined coals.

#### References

- 1a. Alemany, L. B.; Grant, D. M.; Pugmire, R. J.; Alger, T. D.; Zilm, K. W. *J. Amer. Chem. Soc.* **1983**, *105*, 2133.
- b. *Ibid* **1983**, *105*, 2142.
- 2a. Liotta, R. *Fuel* **1979**, *58*, 724.
- b. Liotta, R.; Rose, K.; Hippo, E. *J. Org. Chem.* **1981**, *46*, 277.
- c. Liotta, R.; Brons, G. *J. Amer. Chem. Soc.* **1981**, *103*, 1735.
3. Sullivan, M. T.; Maciel, G. E. *Anal. Chem.* **1982**, *54*, 1615.
4. Mehring, M. "High Resolution NMR Spectroscopy in Solids," Springer-Verlag, Berlin, **1976**, chapter 4.
5. Wilson, M. A.; Pugmire, R. J.; Karas, J.; Alemany, L. B.; Woolfenden, W. R.; Grant, D. M.; Given, P. H. *Anal. Chem.* **1984**, *56*, 933.

**Acknowledgment.** Research sponsored by the Division of Chemical Sciences/Office of Basic Energy Sciences, US Department of Energy under contract DE-AC05-84OR21400 with the Martin Marietta Energy Systems, Inc.

ANALYSIS OF MIDDLE DISTILLATE FUELS BY HIGH RESOLUTION  
FIELD IONIZATION MASS SPECTROMETRY

Ripudaman Malhotra, Michael J. Coggiola, Steven E. Young,  
Doris Tse, and S. E. Buttrill Jr.

Mass Spectrometry Program, Chemical Physics Laboratory  
SRI International, Menlo Park, CA 94025

INTRODUCTION AND BACKGROUND

During the decade following the Arab oil embargo, there has been an increase in both the variety and variability of petroleum feedstocks for the production of middle distillate fuels. As a result, the variability and the chemical constitution of the currently used middle distillate fuels are different from those used before 1970. Problems have arisen in the use of specifications developed empirically from experience with fuels of the older composition. There have even been a few instances in which a fuel which met specification on delivery quickly became so unstable in storage as to become unusable. Therefore, new fuel specifications based more directly upon the chemical constitution of the fuel are needed. This will require the development of new methods for distillate fuel analysis capable of providing rapid and detailed information on the chemical composition of the distillate fuels.

A number of methods for the analysis of fossil fuels by mass spectrometry have been reported. Many of them, including the ASTM standard, D2425-67 (1978), use electron-impact (EI) ionization. This mode of ionization causes extensive fragmentation and precludes obtaining any information on the molecular-weight distribution of the sample. To circumvent this problem, many investigators have used low-energy electron-impact ionization, and other softer modes of ionization, such as field ionization (1,2) and field desorption (3). Both field desorption, and low-energy EI display a wide range of response factors for different classes of compounds and field ionization appears to be a method of choice, at least for distillate fuels (4).

For the past several years, SRI International's unique Field Ionization Mass Spectrometer (FIMS) has provided detailed quantitative information on the composition of diesel and jet fuels derived from oil-shale, coal, and petroleum. Complete and quantitative molecular-weight distributions on all of the types of hydrocarbon compounds present in these fuels previously required a time-consuming chromatographic separation of the fuel into several fractions followed by FIMS analysis of each of these fractions. In this paper we describe the development of a high-resolution FIMS facility capable of providing a rapid and complete quantitative analysis of distillate fuels without the need for a chromatographic separation step.

By using high resolution, it will be possible to distinguish between molecular ions belonging to different hydrocarbon classes that share the same nominal mass. To resolve pairs of hydrocarbons differing by a  $C-H_{12}$  doublet, e.g., nonane and naphthalene, a resolving power of 3,200 is sufficient for all molecules of molecular weight 300 amu or less.



## DESCRIPTION OF EQUIPMENT AND SOFTWARE

### Field Ionization Mass Spectrometer

A vintage MS-9 mass spectrometer (AEI, Ltd.) was completely disassembled, cleaned, and reworked to bring it into good operating condition. In the EI ionization mode using the original ion source, a mass resolution of 30,000 was eventually obtained. The spectrometer has been interfaced with a Kratos DS-55C data system.

In order to install an SRI volcano-style field ionization (FI) source on the MS-9, the original source and mounting flange were removed along with the original solid sample probe and reentrant connection for the batch inlet system. To make room for the field ionization source and some new ion lenses, an extension of the original source housing was designed and built (5). Figure 1 shows a scale drawing of a cross-section through the modified MS-9 source housing.

The volcano-style FI source used in this work was designed at SRI by Aberth and Spindt (6). Ions produced by the field ionization of fuel molecules are accelerated to 6 kV and focused into a small diameter, round beam. The ions then pass through a dual electrostatic quadrupole lens assembly that provides: (1) focusing of the ion beam on to the entrance slit of the MS-9 mass spectrometer, and (2) a means of transforming the round ion beam into a more nearly ribbon-shaped beam that better matches the shape of the entrance slit to the mass spectrometer.

The resolution of the MS-9 equipped with the FI-source was tested with a mixture of hydrocarbons containing both saturates and naphthalenes in the molecular weight range 128 to 156. The instrument could easily resolve the molecular ions of these two classes of compounds indicating a resolution of greater than 1600. Furthermore, with a mixture of benzene and pyridine, it was possible to resolve besides the molecular ions of pyridine and benzene containing a single carbon-13 atom the doublet due to the latter ion and the 1% of protonated benzene that is present in this system. The separation of this minor ion from the molecular ion of benzene with one carbon-13 requires a resolving power of 18,800; as shown in the inset of Figure 1, this power has been slightly exceeded.

### Software for Generating z-Tables

Distillate fuels are likely to contain anywhere between 50 and 150 constituents. A list of masses and their intensities would be a very cumbersome way to present the information on the composition of these fuels. A more manageable representation would be a matrix in which homologous series of different compound classes were sorted into different columns. Since most of the fuel components are hydrocarbons, the obvious choice of compound classification is that according to the z-number, where z is defined by expressing the molecular formula of the hydrocarbon as  $C_nH_{2n+z}$ .

A mass scale which defines the  $CH_2$  unit as 14.0000 can be used to sort the different compound classes, since in this scale the mass defect of any given class will be the same throughout the mass range (7). Rather than writing a new computer code to generate a z-table from the raw data, an existing DS-55C program was modified. The original program was designed to calculate the elemental composition corresponding to each peak in the spectrum. An added advantage of this approach is that the intensities of  $^{13}C$  satellite peaks can also be easily added to the intensity of the parent peak.

Once all of the entries in the table have been computed, their intensities are summed, and renormalized to a total intensity of 100.0. The resulting table of percentages can then be printed, plotted or stored for future reference. In addition, a second program has been written that could retrieve the stored z-tables from different runs, and compute the average and standard deviation for each entry. This procedure is useful in evaluating the reproducibility of the analysis method, and any fuel composition-property correlations.

## **ANALYTICAL PROCEDURE**

### Sample Introduction

Approximately 1-2  $\mu\text{L}$  of liquid fuel together with 0.5-1  $\mu\text{L}$  of a mixture of benzene, toluene, and isooctane, which serve as mass markers, are introduced into a high temperature, glass batch-inlet system attached to the high resolution FIMS instrument. To minimize loss of volatile components during sample introduction, the fuel and the standard mass-marker mixtures are taken in micro-pipettes (Microcaps, Drummond Scientific Company, Broomall, PA) and placed inside the sample holder. Inside the evacuated glass batch-inlet system, the fuel sample vaporizes completely. A portion of the fuel sample vapor flows into the ion source of the mass spectrometer. Because all of the fuel sample is vaporized at the same time, the number of molecules of a specific type flowing into the ion source is directly proportional to the number of molecules of that type present in the original fuel.

### Ionization and Data Acquisition

The field ionization source in the mass spectrometer ionizes sample molecules into molecular ions. The molecular ions are separated according to their mass by the spectrometer, which is operated at a mass resolution of 3000 or greater, sufficient to completely separate the molecular ions of the different hydrocarbon types present in the original fuel. The mass spectrometer is scanned at a speed of 120 seconds per decade. A scan time of 110 seconds plus a magnet settling time of ten seconds allows one scan to be completed every two minutes. Typically, 10 to 15 scans are collected although the amount of sample used is sufficient to allow two to three times as many scans if so desired.

The Kratos DS-55C data system requires the presence of a large number of reference peaks in the high-resolution mass spectrum. These reference peaks are normally produced by introducing perfluorokerosene (PFK) into the electron impact ion source together with the sample. Because of their negative mass defect, the numerous fragmentation peaks of PFK are easily resolved from most of the sample peaks and provide good mass calibration. However, field ionization produces little fragmentation, and most of the commonly used reference compounds including PFK are unsuitable for use as internal mass references for our purpose. We have solved this problem by using added compounds and the common fuel components as references. A mixture of benzene, toluene, and isooctane is added together with the fuel sample. Isooctane is one of the few compounds which even under field ionization undergoes complete fragmentation to give t-butyl ions. This is advantageous since the molecular ion of isooctane would be in the mass range of interest. At the same time, isooctane is sufficiently high boiling to allow easy handling. The fragment t-butyl ion produced from isooctane and the molecular ions of benzene and toluene serve as the autostart masses for the time-to-mass conversion software. A combination of saturated hydrocarbon and alkybenzene peaks are used as reference masses for the rest of the mass range. Several sets

of reference peak masses have been tabulated and different ones are used for different types of fuels.

Time centroid data are usually collected because they can be conveniently reprocessed in the event of an incomplete or unsatisfactory time-to-mass conversion. This can sometimes be a problem because of the highly variable fuel composition of distillate fuels from different sources. Reprocessing of the time-centroid data with a different set of reference peaks is necessary in such cases.

#### Data Processing

Each of the scans of ion peak intensity is stored in a computerized high-resolution mass spectrometer data system, which averages these individual scans and calculates the accurate masses and the elemental composition (chemical formulas) of each of the peaks in the field ionization mass spectrum of the fuel sample. This information enables the peak intensities to be sorted by compound type (z-series) and the number of carbons present in the molecule. The final result of the analysis is a table showing the relative amounts of the various compounds present in the fuel mixture organized by z-series and carbon number. The relative field ionization signals of each component of the fuel can be converted into mole-fraction of that component present in the original fuel sample by using measured relative field ionization efficiency data for known compounds.

### **RESULTS AND DISCUSSION**

#### Determination of Response Factors

Relative ionization efficiencies were determined by using a number of test mixes containing up to 30 components. The various test mixes were designed to study possible matrix effects and to determine the efficiencies of isomeric compounds. These studies also helped in developing the analytical technique. Ionization efficiencies of the various compounds were measured relative to 1-phenylheptane. Response factors were determined for several homologs within a compound class. We observed that ionization efficiencies for the various classes of compounds varies only slightly over the molecular weight range encountered with distillate fuels; 100 to 300 amu. Branching lowers the observed intensity of the molecular ion because of some fragmentation, but this effect is serious only in the case of molecules containing quaternary carbons. Polycyclic aromatics have the highest ionization efficiency and straight chain aliphatics the least.

For the purposes of analyzing fuel samples we used an average of the response factors of the various homologs belonging to that class. We had not expected compounds more unsaturated than biphenyls in diesel and jet fuels and therefore had not determined the response factors of phenanthrenes and dihydrophenanthrenes. However, we did encounter them and have used the same response factors for them as naphthalenes. The response factors used for the various classes are given in Table 1.

#### Analysis of Some Distillate Fuel Samples

We had earlier reported on the analysis of a stable and unstable fuel sample and shown that the unstable fuel had a substantially greater amount of naphthalenes (5). This result is in concert with the findings of Mayo and Lan (8).

Several other diesel fuel marine and experimental jet fuel samples have been analyzed by HR-FIMS. Results of the analysis of a very stable fuel (NRL-83-14) are shown in Table 2. The table gives the mole percent of the various constitu-

ents by their carbon number and z-series. The fuel contains 27.8% acyclic and 14.4% monocyclic saturates. No bicyclic or tricyclics were detected. This fuel is also very rich in alkyl benzenes and tetralins. It is interesting to note that the distribution of the compounds within any z-series is fairly uniform for all compound classes except naphthalenes. The compound at  $m/z$  212.0712, identified as  $C_{17}H_8$  ( $z = -26$ , M.W. 212.0626) is most likely ethyl (or dimethyl-) dibenzthiophene (M.W. 212.0660). Composition of a model fuel used for engine tests, NRL-82-15, is given in Table 3. The fuel is less stable relative to NRL-83-14 and has somewhat of a higher naphthalene content.

### CONCLUSIONS

This work demonstrates the applicability of high-resolution FIMS as a powerful technique for rapid chemical characterization of middle distillate fuels. We have fixed most of the problems with the spectrometer, and the instrument is now operating on a routine basis. The only weak point in the entire system appears to be the heated batch inlet system. Preliminary results have shown that this technique provides accurate and reproducible data. Data analyzed thus far are too scant to make definitive fuel composition-property correlations; such studies are currently underway.

**ACKNOWLEDGMENT:** Support for this work by the Naval Research Laboratory (Contract No. N00014-81-K-2032) is greatly acknowledged.

### References

- (1) S. E. Scheppele, C. S. Hsu, T. D. Marriott, P. A. Benson, K. N. Detwiler, and N. B. Perreia, Int. J. Mass Spectrom., 1978, **28**, 335.
- (2) G. A. St. John, S. E. Buttrill, Jr., and M. Anbar, in Organic Chemistry of Coal, J. W. Larsen, Ed., ACS Symposium Series 71, Washington, DC, 1978, p. 223.
- (3) T. Aczel, J. A. Laramée, and G. T. Hansen, ASMS Proceedings, 1982, 808.
- (4) G. A. St. John and S. E. Buttrill, Jr., unpublished results.
- (5) S. E. Young and S. E. Buttrill, Jr., ASMS Proceedings, 1982, 534.
- (6) W. Aberth and C. A. Spindt, Int. J. Mass Spectrom. Ion Phys. 1977, **25**, 183.
- (7) E. Kendrick, Anal. Chem. 1963, **35**, 2146.
- (8) F. R. Mayo and B. Y. Lan, Division of Petroleum Chemistry, Preprints 1983, **28(5)**, 1209.

Table 1  
RELATIVE FIELD IONIZATION EFFICIENCIES OF VARIOUS HYDROCARBONS

<u>Compound Class</u>	<u>Z</u>	<u>Relative Response</u> <sup>*</sup>
Alkanes	2	0.34
Monocyclic alkanes	0	0.54
Bicyclic alkanes	-2	0.63
Tricyclicalkanes	-4	0.56
Benzenes	-6	0.91
Tetralins	-8	0.86
Octahydrophenanthrenes	-10	1.03
Naphthalenes	-12	1.03
Biphenyls or Tetrahydro-		
phenanthrenes	-14	1.44
Dihydrophenanthrenes	-16	1.44
Phenanthrenes or		
Anthracenes	-18	1.44

<sup>\*</sup>Relative to 1-phenylheptane.

Table 2

## COMPOSITION OF FUEL NRL-83-14\* BY CARBON NUMBER AND Z-SERIES

n/z	2	0	-2	-4	-6	-8	-10	-12	-14	-16	-18	-26
10					2.58							
11					2.91	1.84		1.53				
12					2.08	2.47		5.15				
13					2.02	2.58		6.96	0.77			
14		4.89										
15		5.16	2.30		2.14							
16		5.34	2.87		1.59	2.11		1.54	1.26	0.79	0.98	
17		4.00	2.19		2.07	1.73		1.35	1.26		0.84	1.01
18		4.74	1.31		2.04	1.94			0.86			
19		3.65	2.20		1.42							
20					1.94							
SUM	27.8	14.4			20.8	12.7		16.5	4.2	0.8	1.8	1.0 †

\*A very stable fuel sample.

†The compound is most likely ethyl (or dimethyl-) dibenzthiophene.

Table 3

## COMPOSITION OF FUEL NRL-82-15\* BY CARBON NUMBER AND Z-SERIES

n/z	2	0	-2	-4	-6	-8	-10	-12	-14	-16	-18
8					0.63						
9					1.00						
10					0.89						
11	1.67	0.89			0.83	1.17		4.08			
12	6.95	1.52	1.96		1.30	2.02		6.54			
13		2.75			1.69	2.50		6.55			
14	4.60										
15	3.74	2.21	2.62	0.92	1.26						
16	3.61		2.09		1.04	1.55	1.23	1.57	0.89		
17	4.64	1.48	1.24	1.32	1.43	1.24	0.80	0.78	0.47		
18	3.07	2.16	0.70		0.62	1.07	0.69				
19	2.57	2.11	0.96		0.53			0.44			
SUM	30.9	12.5	9.6	2.2	11.2	9.6	2.7	20.0	1.4		

\*Relatively unstable fuel, but not the worst.

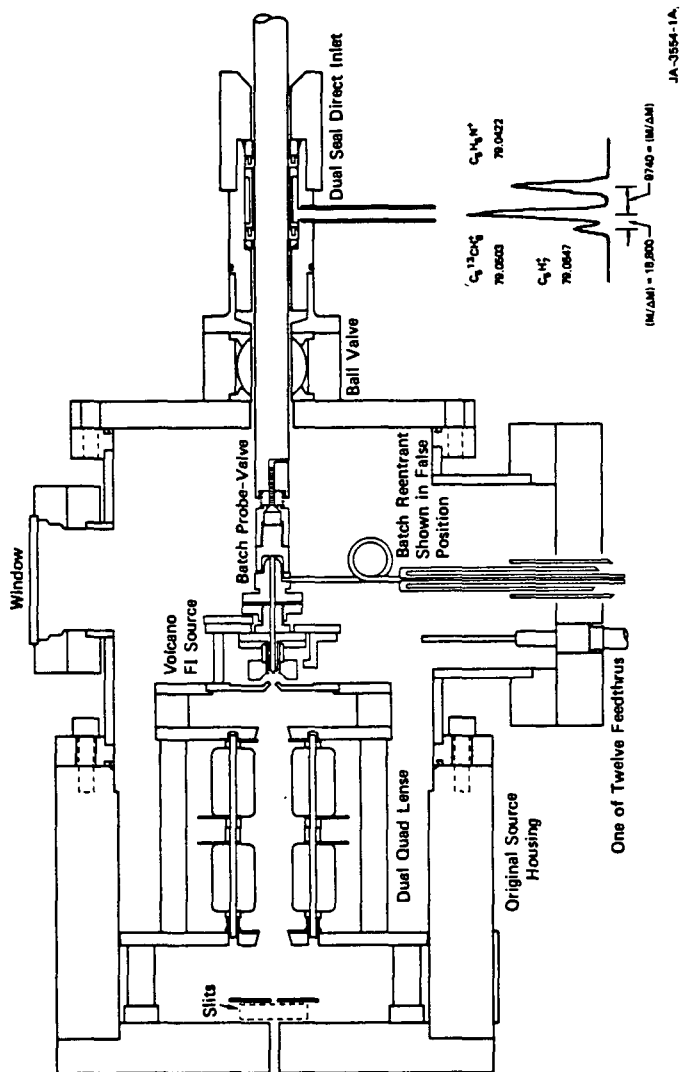


FIGURE 1 CROSS SECTION OF SOURCE HOUSING FOR MS-9

## NUMERICAL EXTRACTION OF CHEMICAL COMPONENT PATTERNS FROM PYROLYSIS MASS SPECTRA OF U.S. LIGNITES

Henk L.C. Meuzelaar, Willem Windig and G. Steven Metcalf

Biomaterials Profiling Center, University of Utah  
391 South Chipeta Way, Suite F  
Salt Lake City, Utah 84108

### INTRODUCTION

Structural characterization of lignites presents a major challenge because of the extreme complexity and heterogeneity of these low rank coals. Whereas most peats still contain macroscopically and microscopically identifiable plant remains, morphological analysis of lignites is much less straightforward. Moreover, routine coal characterization tests such as Free Swelling Index or Vitrinite Reflectance, are less readily applicable to lignites whereas sophisticated spectroscopic techniques such as IR, NMR or MS tend to give highly complex spectra due to the presence of multiple, overlapping chemical components. Although combined analytical methods such as MS/MS, GC/MS or GC/FTIR are capable of resolving and identifying many of these overlapping components, such "hyphenated" techniques tend to be costly and require time-consuming data evaluation and interpretation steps thus making it impractical to apply these methods to large sample series.

A novel approach capable of resolving overlapping signals in spectra of complex mixtures involves numerical extraction of component patterns by means of factor and discriminant analysis (1). Thus far, this numerical extraction approach has been applied especially to pyrolysis mass spectrometry (Py-MS) patterns of coals and other fossil fuels, because of the relative ease of numerical conversion of mass spectra (compared to the continuous curves obtained by IR, NMR or chromatographic techniques).

The main advantages of combining single stage analytical techniques with numerical extraction methods rather than using "hyphenated" physicochemical techniques are: high speed and relatively low cost. Moreover, numerical extraction methods are especially powerful when relatively large series of samples need to be studied. Meuzelaar *et al.* (2) demonstrated the applicability of the combined Py-MS/numerical extraction approach to a series of over 100 coal samples from the Rocky Mountain Coal Province obtained from the Penn State Coal Sample Bank. Other, smaller Py-MS studies of coals have been published by Van Graas *et al.* (3), De Leeuw *et al.* (4) and Larter (5). As listed in Table I, the Py-MS study reported here involves a selection of samples representing both U.S. coal provinces with major lignite reserves, namely the Northern Plains Province (6 samples) and the Gulf Province (16 samples).

### EXPERIMENTAL

Lignite samples were obtained from the Penn State Coal sample bank in hermetically sealed metal cans containing 500 g, 20 mesh aliquots under Argon. All further grinding and splitting operations were performed under N<sub>2</sub>, finally resulting in 10 mg, 300 mesh aliquots which were subsequently suspended in 2 1/2 ml of Spectrograde methanol. Two 5  $\mu$ l drops of these suspensions were applied to ferromagnetic wires (Curie-point temperature 610°C) and air-dried at room temperature under continuous rotation, resulting in a sample size of approx. 40  $\mu$ g. Within one hour after preparation, all coated wires were analyzed by Curie-point pyrolysis mass spectrometry using an Extranuclear 5000-1 quadrupole MS system described elsewhere (6). Py-MS conditions were as follows: temp. rise time 5 s, equilibrium temp. 610°C, total heating time 10 s, electron energy setting 11 eV, mass range scanned m/z 20-



260, scanning rate 2000 amu/s, total scanning time 20 s. Each lignite sample was analyzed in triplicate and the resulting 66 spectra were normalized using the NORMA program (7). Subsequent multivariate analysis was carried out with the SPSS program package (8) and consisted of factor analysis followed by discriminant analysis using the 11 most significant factors (eigenvalue >1), according to a procedure described previously by Windig *et al.* (9). It should be noted that each set of three duplicate analysis was assigned a separate category number in the discriminant analysis procedure, thus avoiding the creation of artificial clusters and divisions in the data set. Finally, the five most significant discriminant functions were analyzed with the aid of the variance diagram (VARDIA) procedure developed by Windig *et al.* (10). This resulted in the localization of at least six individual component axis which were then evaluated further by means of discriminant loading and spectrum plot procedures, as described by Windig *et al.* (9).

## RESULTS AND DISCUSSION

The pyrolysis mass spectra of three of the twenty two lignite samples are shown in Figure 1, demonstrating marked differences in the bulk composition of the pyrolyzates, e.g., with regard to hydroxyaromatic compound series, aliphatic hydrocarbon series and sulfur signals. Moreover, arrows in Figure 1 point to minor "biomarker" peaks at  $m/z$  234 (retene) and  $m/z$  194 (unknown biomarker) which were found to be quite characteristic for lignite samples from the Northern Plains and Gulf provinces respectively.

Before describing a more detailed chemical interpretation of the Py-MS findings, it should be pointed out that chemical labels assigned to peak series or individual peaks in Figure 1 (as well as throughout this paper) are tentative only. Generally these interpretations are based on literature data although some of the chemical identities are backed up by Py-GC/MS studies on the same lignites (11). Another factor to consider when interpreting Py-MS data on coals is the incomplete pyrolytic conversion. Under the experimental conditions employed in our study, estimated tar yields for high volatile bituminous coals are in the 50-60% range (12) whereas lignite conversion yields are basically unknown but may well fall in the same range. Moreover, not all the tar products will be detected by our mass spectrometric procedures. Ultimately, perhaps only 20-30% of the (dry) bulk of the original lignite sample contributes directly to the mass spectrum.

In view of the large number of spectra obtained and the hundreds of mass peaks in each spectrum, the use of sophisticated data reduction and correlation methods is indispensable. As described under "Experimental", factor analysis followed by discriminant analysis was applied to the Py-MS data set. This resulted in seven "significant" discriminant functions (see Table II). The scores of the first two functions are plotted in Figure 2, revealing a relatively good separation between lignites from the two different coal provinces (on DI) as well as a definite separation between lignites from different seams, fields or regions (on DII).

The nature of the underlying chemical components responsible for the clustering behavior in Figure 2 was examined by means of a novel, interactive method known as the Variance Diagram (VARDIA) technique (10), which enables us to determine the optimal location of each major chemical component in discriminant space. The VARDIA method has proven to be capable of extracting numerical components from mass spectra of complex mixtures, including fossil fuel pyrolyzates (10).

Two VARDIA plots, representing discriminant functions I and II as well as III and IV respectively, are shown in Figure 3, revealing the presence of at least six major component axes (labeled A-F) in the space spanned by these four functions. The mass spectral patterns associated with these component axes are shown in Figures 4 and 5. Component axes A and B (Figure 4a, b) obviously represent

the two bulk components seen in the lignite spectra, namely hydroxyaromatic compounds and aliphatic hydrocarbon moieties.

The nature and origin of the hydroxyaromatic compound series becomes clear when comparing the spectral pattern of component axis A (Figure 4a) with that of a softwood lignin model compound (Figure 4c). Although obvious quantitative differences exist between the two spectral patterns, the qualitative similarities strongly suggest a direct chemical relationship. That lignin-like patterns can be preserved in pyrolysis mass spectra of fossil organic matter  $10^7$  to  $10^8$  years old has also been reported in several other studies (4,6,13).

The chemical nature and origin of the aliphatic hydrocarbon pattern in Figure 4b presents a more difficult problem. Nevertheless, an intriguing qualitative match was obtained with the Py-MS pattern of Apiezon L, a high MW petroleum distillate consisting of 67% aliphatic, 28% naphthenic and 5% aromatic hydrocarbons (14). Since the petrographic analysis data available from the Penn State Coal data bank did not reveal major contributions of liptinite macerals (see Table I), it may be assumed that the hydrocarbon moieties observed by Py-MS represent maceral types easily overlooked by routine petrographic analysis, e.g., from exsudatinite or bituminite (15). An interesting speculation is that we may be dealing with hydrocarbons derived from algal precursors although major contributions from bacterial lipids (16) cannot be ruled out either.

The spectral patterns of the component axes shown in Figure 5a-c are interpreted to represent terpenoid resins (Figure 4a; e.g. retene signal at  $m/z$  234), unknown biomarker compounds (Figure 5b; e.g., signals at  $m/z$  194, 179 and 168) and sulfur moieties as well as related marine-influenced peak series (Figure 5c), respectively.

Comparison of the VARDIA plots in Figure 3 with the discriminant score plot in Figure 2 shows that component axis F (representing reduced sulfur forms such as  $H_2S$  and  $CH_3SH$ ) correlates most strongly with the Wildcat seam lignites from South-Central Texas which are known to have been deposited in marine-influenced, lagoonal environments (17). However, component axis E (representing more oxidized sulfur forms such as  $SO_2$  and  $CS_2$ ) also correlates with the Fort Union Bed lignites of Montana, which lack an obvious marine depositional influence. In these lignites, the oxidized sulfur forms may well represent the relatively high inertinite content since similar correlations were noted in previous Py-MS studies of purified coal macerals (18).

That the two biomarker signals at  $m/z$  234 and  $m/z$  194 are very characteristic, indeed, for the two coal provinces (as also indicated by a comparison of Figures 2 and 3) is confirmed by the bivariate plot in Figure 6. Apparently, the biomarker precursors (conifer resins?) of the Northern Plains province were not present in the ancient depositional environment of the Gulf province; and *vice versa*.

Finally, it should be mentioned that the above discussed interpretations of the Py-MS data were further supported by a systematic correlation with conventional coal characterization data (e.g., petrographic analysis, ultimate analysis, proximate analysis, calorific value and and vitrinite reflectance) obtained from the Penn State Coal Data Bank. The results of these data correlation efforts, e.g., using canonical variate analysis techniques (19), will be reported elsewhere (20).

In conclusion, the data analysis results presented here confirm the feasibility of numerical extraction of chemical components from the low voltage mass spectra of extremely complex lignite pyrolyzates.

#### ACKNOWLEDGEMENTS

The authors are indebted to the Penn State Coal Sample Bank for providing lignite samples and especially to Dr. Peter Given for his help and advice in selecting the particular set of lignites used in this study.

The research reported here was supported by a development grant from Phillips Petroleum Company, by U.S. Department of Energy Contract #DE FG22-82PC50970 and by matching funds from the State of Utah.

#### REFERENCES

1. Meuzelaar, H.L.C., Windig, W., Harper, A.M., Huff, S.M., McClennen, W.H., Richards, J.M., *Science* 226, 268 (1984).
2. Meuzelaar, H.L.C., Harper, A.M., Hill, G.R., Given, P.H., *Fuel* 63, 640 (1984).
3. G. Van Graas, J.W. De Leeuw, P.A. Schenck, in *Advances in Organic Geochemistry* A.G. Douglas and J.R. Maxwell, Eds. (Pergamon Press, Oxford, UK, 1979), pp. 485-494.
4. P.A. Schenck, J.W. De Leeuw, T.C. Viets, J. Haverkamp, in *Petroleum Geochemistry and Exploration of Europe*, J. Brooks, Ed. (Blackwell Scientific Publications, 1984), pp. 267-274.
5. S.R. Larter, in *Analytical Pyrolysis-Techniques and Applications*, K.J. Voorhees, Ed. (Butterworth, London, 1984), pp. 212-275.
6. H.L.C. Meuzelaar, J. Haverkamp, F.D. Hileman, *Pyrolysis Mass Spectrometry of Recent and Fossil Biomaterials-Compendium and Atlas* (Elsevier, Amsterdam, 1982).
7. A.M. Harper, H.L.C. Meuzelaar, G.S. Metcalf, D.L. Pope, in *Analytical Pyrolysis-Techniques and Applications* (Butterworth, London, 1984), pp. 157-195.
8. *Statistical Package for the Social Sciences (SPSS)*, N.H. Nie et al., Eds. (McGraw-Hill, New York, ed. 2, 1975).
9. W. Windig, P.G. Kistemaker, J. Haverkamp, *J. Anal. Appl. Pyrol.* 3, 199 (1981).
10. Windig, W., Meuzelaar, H.L.C., *Anal. Chem.* 56, 2297 (1984).
11. Nip, M., De Leeuw, J.W., Schenck, P.A., Meuzelaar, H.L.C., Stout, S.A., Given, P.H., Boon, J.J., *J. Anal. Appl. Pyrol.*, in press.
12. Meuzelaar, H.L.C. McClennen, W.H., Cady, C.C., Metcalf, G.S., Windig, W., Thurgood, J.R., Hill, G.R., *ACS Preprints (Div. of Fuel Chem.)*, Vol. 29, No. 5, 1984, pp. 166-177.
13. W.L. Maters, D. Van de Meent, P.J.W., Schuyt, J.W. De Leeuw, P.A. Schenck, H.L.C. Meuzelaar, in *Analytical Pyrolysis*, C.E.R. Jones and C.A. Cramers, Eds. (Elsevier, Amsterdam, 1977), pp. 203-216.
14. Personal communication by Biddle Instruments Inc., Blue Bell, PA.
15. M. Teichmüller, in *Stach's Textbook of Coal Petrology*, E. Stach et al. Eds. (Gebrüder Borntraeger, Berlin, 1982), pp. 219-294.
16. Ourisson, G., Albrecht, P. Rohmer, M., *Sci. Am.* 251, 44 (1984).
17. Kaiser, W.R., Johnston, J.E., Bach, W.N., *Geological Circular 78-4*, Bureau of Economic Geology, The University of Texas at Austin (Austin, TX), 1978.
18. Meuzelaar, H.L.C., Harper, A.M., Pugmire, R.J., Karas, J., *Coal Geology* 4, 143 (1984).

19. Halma, G., Van Dam, D., Haverkamp, J., Windig, W., Meuzelaar, H.L.C., *J. Anal. Appl. Pyrol.*, in press.
20. Metcalf, G.S., Windig, W., Hill, G.R., Meuzelaar, H.L.C., to be published.

TABLE I  
CONVENTIONAL LIGNITE CHARACTERIZATION DATA

No. 1	PSOC Code 2	Seam Name (State) 3	Maceral Conc. (%)			Ultimate Anal. (%)				% S (tot) 11
			Vit. 4	Inert. 5	Exin. 6	C 7	H 8	N 9	O 10	
1	833	Fort Union Bed (MT)	74.1	23.2	1.4	70.0	4.60	1.29	23.7	0.64
2	838	Fort Union Bed (MT)	81.7	16.9	1.4	71.3	4.74	1.08	22.3	1.34
3	1084	Sawyer (MT)	88.9	10.8	0.3	71.5	4.84	1.01	22.2	0.60
4	1087	Sawyer (MT)	82.5	16.3	1.2	71.0	4.75	1.00	23.0	0.23
5	1090	Sawyer (MT)	89.1	10.2	0.7	71.9	4.66	0.99	22.1	0.35
6	975	Anderson (WY)	79.6	8.0	12.3	73.0	5.18	0.99	20.3	0.48
7	791	A-Pit (TX)	90.7	8.4	0.9	72.3	5.39	1.20	20.2	0.99
8	792	A-Pit (TX)	94.7	4.5	0.8	72.7	5.61	1.18	19.6	0.97
9	414	Darco (TX)	80.6	17.5	1.9	73.0	5.31	1.37	19.3	1.14
10	415	Darco (TX)	83.4	14.1	2.5	73.6	5.66	1.45	18.4	0.89
11	623	Darco (TX)	81.0	17.2	1.8	74.8	5.26	1.32	17.6	1.35
12	625	Darco (TX)	83.3	15.2	1.5	74.1	4.89	1.30	18.1	2.38
13	1037	Unnamed (TX)	86.5	13.1	0.4	73.1	5.31	1.62	18.9	1.16
14	1038	Unnamed (TX)	88.1	10.8	1.1	73.6	5.02	1.65	18.5	1.39
15	427	Unnamed (TX)	90.6	8.1	1.3	72.9	5.37	1.24	19.2	1.61
16	428	Unnamed (TX)	94.5	3.7	1.8	73.3	6.02	1.28	18.0	1.78
17	786	Unnamed (TX)	87.0	12.0	1.0	73.4	5.12	1.34	18.9	1.44
18	788	Unnamed (TX)	91.6	7.9	0.5	73.5	5.46	1.20	18.7	1.15
19	421	Wildcat (TX)	87.7	10.9	1.4	71.6	5.83	1.34	19.4	2.63
20	422	Wildcat (TX)	88.7	10.1	1.2	75.5	5.86	1.39	15.6	2.03
21	424	Wildcat (TX)	90.7	6.1	3.2	73.7	6.05	1.22	17.6	2.08
22	637	Wildcat (TX)	83.8	14.6	1.6	74.8	5.28	1.32	16.6	2.75

<sup>7,8,9,10</sup>-modif. Parr dmmf (<sup>10</sup> calculated by diff.); <sup>11</sup>-daf

TABLE II  
DISCRIMINANT ANALYSIS RESULTS

Discriminant Function	Eigenvalue	Relative Percentage	Canonical* Correlation
I	341.0	61.3	.999
II	124.0	22.3	.996
III	38.2	6.9	.987
IV	23.6	4.3	.979
V	16.1	2.9	.970
VI	8.8	1.6	.948
VII	2.5	0.5	.845

\* with 11 original factors

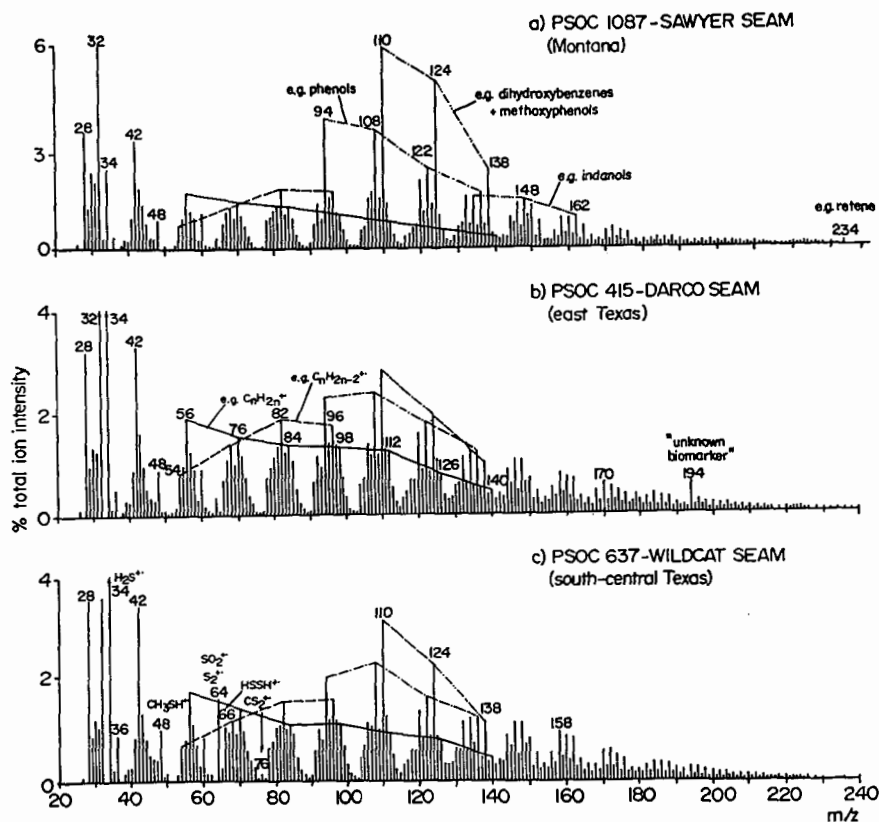


Figure 1. Low voltage pyrolysis mass spectra of three selected lignites representing the Northern Plains province (a) and the Gulf province (b and c). Note the relatively high abundance of hydroxyaromatic series in (a) compared to the more prominent aliphatic hydrocarbon series in (b) and (d). Further note the marked sulfur compounds in (c) and the small biomarker signals (arrows at  $m/z$  234 and 194 in (a) and (b), respectively).

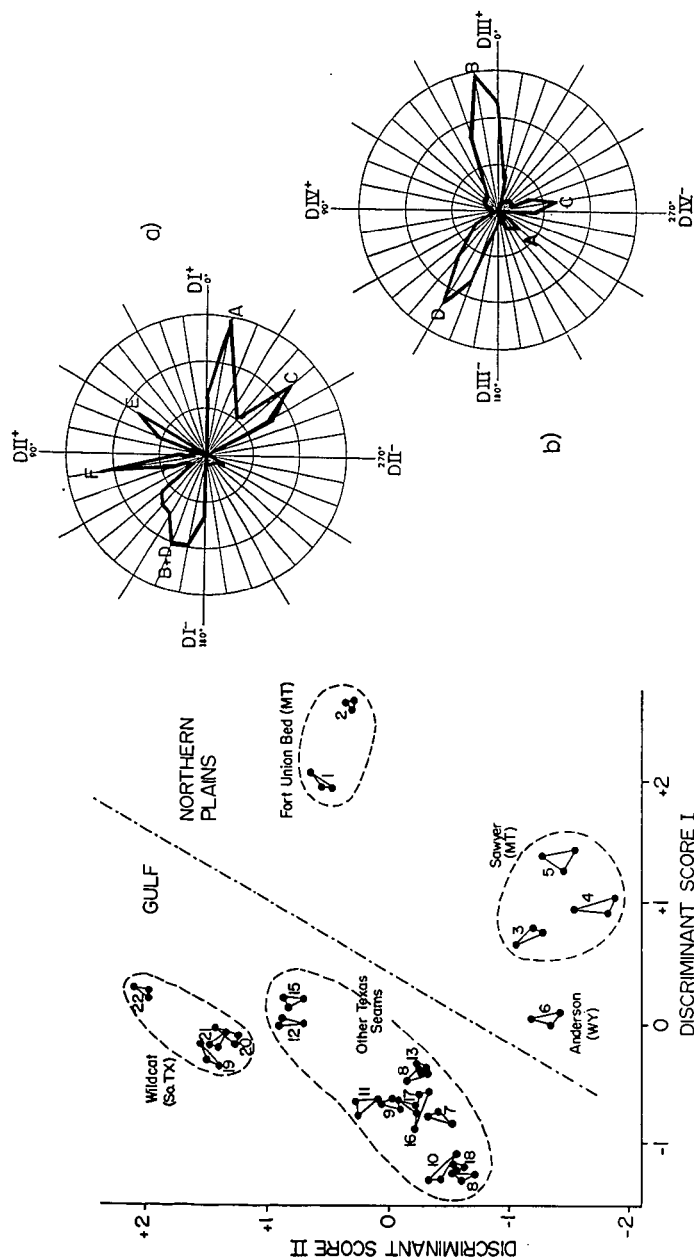


Figure 2. Scatter plot of the scores of the first two discriminant functions showing the clustering behavior of the 22 lignite samples. Triplicate analyses of the same sample are connected by solid lines. Dashed lines indicate coal seam or field relationships. For sample codes, see Table 1.

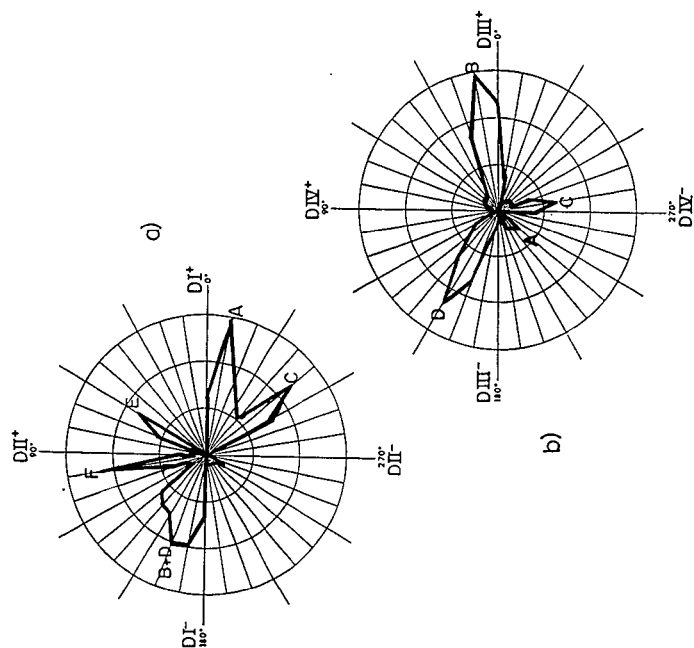


Figure 3. Variance diagrams showing the presence of six major component axes (A-F) in the space spanned by discriminant functions I, II (a) and III, IV (b), respectively.

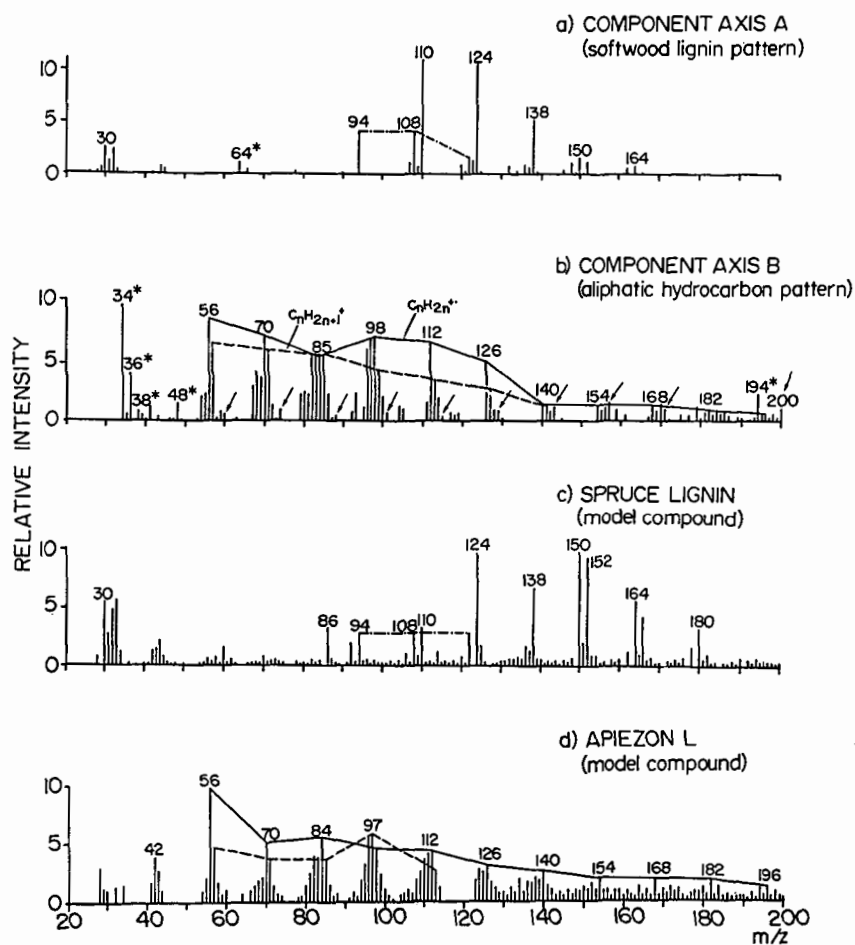


Figure 4. Comparison of the numerically extracted discriminant "spectra" of components A (a) and B (b) with the pyrolysis mass spectra of two model compounds (c and d). Mass peak intensities not optimally represented on the component axes are indicated by asterisks. Arrows point to an aliphatic carboxylic acid series in (b).

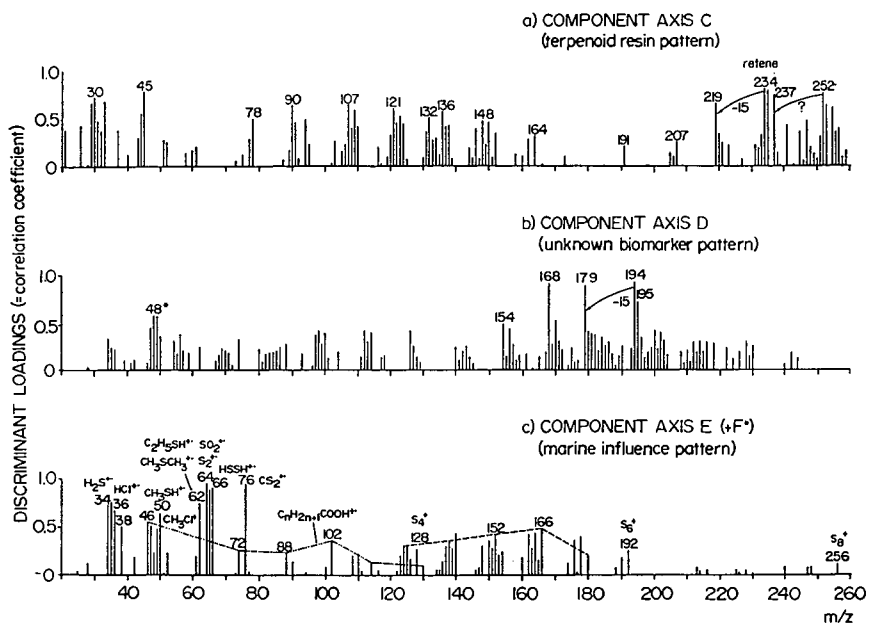


Figure 5. Loading (correlation coefficient) plots representing components C-F in Figure 3. For explanation, see text.

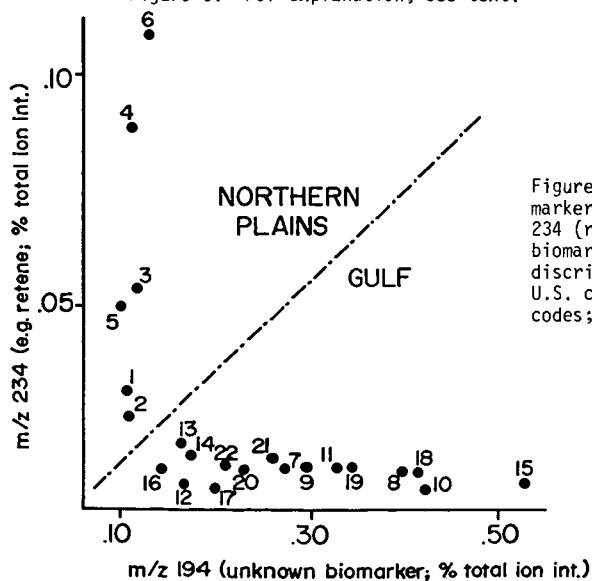


Figure 6. Scatter plot of biomarker peak intensities at  $m/z$  234 (retene) and  $m/z$  194 (unknown biomarker) showing the perfect discrimination between the two U.S. coal provinces. For sample codes; see Table I.



## HIGH RESOLUTION MASS SPECTROMETRIC ANALYSIS OF COAL LIQUIDS

Thomas Aczel, Steve G. Colgrove, and Stephen D. Reynolds

Exxon Research and Engineering Company  
Baytown Research and Development Division  
P. O. Box 4255  
Baytown, TX 77522-4255

### INTRODUCTION

Development of new industrial technologies requires meaningful cooperation among many scientific disciplines, including several branches of chemistry, physics, engineering, economics, and others. This is particularly true for coal liquefaction technology, that involves complex operations, deals with rather refractory materials, and represents a potentially large impact on overall consumption patterns.

Analytical chemistry is a key player in this team effort. It seeks and obtains, to an extent commensurate with effort and circumstances, information on the composition of feed, product and intermediate streams. This information is utilized for fundamental understanding of the reactions involved in coal liquefaction and the upgrading of coal liquids, for monitoring day-to-day pilot plant operations, for evaluating end-products quality and for assessing process and product impact on the environment.

This paper reviews some of the analytical approaches we use in our laboratories for the in-depth characterization of coal liquids. Emphasis will be placed on methods determining organic composition. Issues discussed will include the overall nature of coal liquids, analytical strategy and methodology, the scope of the analyses, the role of separation, mass spectrometric and other techniques, and on the calculation and/or prediction of useful physical parameters from compositional data.

### DISCUSSION

#### Overall Nature of Coal Liquids

Coal liquids are very complex liquids that contain a large variety of chemical classes and compounds. A non-exhaustive list is given in Table I. In-depth analysis generally requires the use of a variety of analytical tools, although, as we will see, these can be often reduced to mass spectrometry alone, provided that one is willing to use some assumptions and clearly understands the limitations of the short-cut method selected.

Composition is a function of both coal origin and liquefaction and/or upgrading conditions. Liquids from some western coals contain significantly lower concentrations of sulfur compounds than those from some eastern coals; while the type and severity of the upgrading process changes significantly the ratios between saturate, hydroaromatic, aromatic, and polar components. Gross composition of end-products in most cases is more affected by the type of upgrading than by coal origin.

#### Analytical Strategy

Selection of the best analytical strategy for the analysis of coal liquids depends on the nature of the information needed, the availability of analytical tools, funding for a particular project, and time. Information content and time/cost restraints are most often balanced with a compromise. A typical analytical scheme that is often used in our laboratories is shown on Figure 1. This scheme provides the user with a

very large body of information that is generally sufficient for most studies involving reaction kinetics, process behavior, end-product quality. The main roles of the various steps are summarized in the following paragraphs.

Separation into saturates, aromatics and polars yields valuable information on the overall amounts of these classes of compounds. It also facilitates the subsequent analysis. For example, saturates are difficult to characterize in detail in the presence of aromatics; and separation of aromatics and polars reduces the mass spectrometric resolving power requirements for the analysis of most nitrogen and oxygen compounds. Separation also eliminates structural uncertainties between furanic and phenolic oxygen types that even high resolution MS can not cope with in complex mixtures. Furans are concentrated in the aromatic fraction, phenolics in the polar fraction; separation thus allows a reliable structural assignment.

Low resolution, high voltage compound type analysis of the saturates determines total paraffins and one to six ring naphthenes. GC distillation and subsequent analysis of trapped cuts yields this type of information as a function of boiling range.

The main feature of the overall analysis is the high resolution, low voltage characterization of the aromatic, polar aromatic, and asphaltene fractions. As will be shown in the remainder of this presentation, this approach yields detailed information of several thousands of individual components and provides the user with a number of physical parameters that are related to composition.

Time and funding constraints might restrict the scope of the analytical scheme. If the separation step is not carried out, total saturates, aromatics and polars can be determined with reasonable accuracy from high voltage, low resolution MS data (Table II), while the aromatic and polar components can be measured accurately from the high resolution, low voltage analysis of the total stream. The decrease in information content will affect only the saturate type distribution, the relationship between saturate composition and boiling range, and the specific identification of some of the oxygenated types. This reduced approach is the only one feasible for materials in the gasoline range; separation of these streams would involve unacceptable losses of volatiles.

A further simplification consists of the substitution of a low resolution, low voltage analysis to the high resolution procedure. This approach is generally applicable to only rather severely hydrogenated coal liquids, as it determines only a few heteroatomic components, such as phenols. Separation of more and less condensed aromatics, that usually requires a resolving power of at least 1000 per 100 MW units, is accomplished through computerized deconvolution of the interfering homologous series, for example alkyltetralins and alkylpyrenes. The deconvolution calculations are based on a large number of high resolution analyses. The low resolution approach, using high voltage for determining saturates/aromatics/polars and low voltage for the determination of aromatic types and carbon number homologs, yields fast and highly reproducible analyses. The method was used extensively in monitoring the large coal liquefaction pilot plant at Baytown, Texas, with an average of two analyses every four to six hours each day, and with a response time of about one hour (1980-1982).

Special nature of some samples and research projects requires occasionally a more extensive analytical treatment than that outlined in Figure 1. These include separation of the aromatics into one, two, three, and four ring concentrates; separation of the polars into weak and strong acids, weak and strong bases, and neutral polars; and analysis of all the fractions by GC/MS,  $^{13}\text{C}$  NMR, and proton NMR. The more specific separations facilitate interpretation and yield information on components in the parts per billion range (Table III); GC/MS yields important information on individual isomers; NMR corroborates and extends the structure assignments made by MS.

### High Resolution, Low Voltage MS Analysis

This method is the cornerstone of our procedures. It has the unique ability to give both detailed quantitative data on a very large number of components and to summarize and sort these into process and/or product quality related parameters.

The underlying principle of the method is the simultaneous use of high resolution and low voltage. High resolution separates the very large number of hydrocarbons and heterocompounds that have the same nominal molecular weight but possess different formulas and thus slightly different precise masses. Such multiplets consist of six to eight peaks on the average at every mass from about mass 150 to mass 500 or 600 in coal liquids. Examples are given in Table IV. Low voltage greatly simplifies the spectra of complex mixtures by ionizing only aromatic and polar aromatic molecular ions. Low voltage is an open-ended approach that allows one to analyze as many components as are present in a sample; and calibration sets can be set up based on theoretical considerations and extrapolations. This is particularly important in complex natural products, that contain thousands of components that are not available in pure form for calibration.

The procedures involved in high resolution, low voltage analysis can be summarized as follows:

- The sample and a blend of halogenated aromatic mass reference standards are charged to a high resolution mass spectrometer, in our case a Kratos MS50, and are run at an effective voltage of 10-11 electron volts (measured by a ratio of 50 to 100 between the molecular ion, 106, and a strong fragment, 91, in m-xylene).
- A computerized data acquisition system, Kratos DS55 plus Exxon proprietary programs determines the mass and intensity of each component, assigns formulas, and sorts the components according to formula or compound type and carbon number.
- A second set of Exxon proprietary computer programs quantitates all individual concentrations and also summarizes the data into overall structural parameters. The scope of the analysis is shown in Table V; typical summary parameters calculated are listed in Table VI.

A very useful feature of the analysis is the calculation of physical and process related parameters from composition (Table VI). For samples available only in very small amounts, this is often the only means to obtain these parameters. Most of the calculations use simple stoichiometric equations; distillation is calculated by assigning each component a boiling range derived either from the literature or extrapolations; carbon and hydrogen types are expressed in NMR terms by assigning theoretical values to each component. In all cases, total sample values are obtained by weighing the theoretical values of all components by the corresponding concentrations in a particular stream and by compositing the data.

The physical parameters calculated are generally quite accurate. Table VII shows typical data for elemental analysis, Table VIII for distillation, Table IX for NMR type parameters.

### DEVELOPMENTS IN PROGRESS

While mass spectrometry is certainly the technique that yields the most detailed information on coal liquids, it also has some limitations. The major ones are the need to heat and volatilize the materials to be analyzed, and the difficulty of identifying specific isomers in complex mixtures. The volatility limitation applies to heavy ends boiling above approximately 1100°F; specific isomer identification is a

problem mainly in total coal liquids. Work is continuing in our laboratories to reduce or eliminate the impact of these factors.

The volatility requirement can be eliminated by using field desorption or fast atom bombardment for ionization. Preliminary data obtained in our laboratories show that field desorption can be used to reproducibly analyze heavy ends with molecular weights as high as 3000 for coal liquids and 4000 for petroleum liquids. The approach requires use of a high-field magnet for mass measurements up to 6000+ molecular weight and very careful standardization of the numerous experimental steps involved, including preparation of the special emitters, sample loading, source alignment, scanning and computerized data acquisition. Recognition of individual isomers can be accomplished through the use of GC/MS, in particular for the lighter components up to  $C_{12}$ , and the more outstanding ones beyond that range. GC/MS data in our labs are generally normalized to high resolution MS data on the corresponding homologs in order to account for the components that can only be identified non-specifically. We are now working on methods to interpret GC/MS data in the absence of pure compound calibrants.

#### CONCLUSION

The analytical methodology discussed above was used for literally hundreds of thousands of samples in the past decade. Many were run with the standard approach outlined in Figure 1; more with the simplified, "MS only" alternative; and several with the extended technology that included GC/MS and NMR.

Availability of the very detailed and summarizable data was demonstrably of great use in the planning, development, and evaluation of coal liquefaction and upgrading processes including very small to large scale efforts.

Table I

MAJOR COMPOUND CLASSES IN COAL LIQUIDS

<u>Class</u>	<u>Type</u>
● SATURATES	● n-paraffins, iso-paraffins, cyclopentanes, cyclohexanes, 1-8 ring condensed cycloparaffins; biological residuals (biomarkers) such as isoprenoid paraffins, steranes, hopanes, etc.
● AROMATICS	● One to eight ring aromatics, such as benzenes, naphthalenes, acenaphthenes, fluorenes, phenanthrenes, pyrenes, chrysenes, benz-pyrenes, benz-perylenes, coronenes, etc.; and the corresponding aromatic thiophenes, dithiophenes, furans, difurans, thiophenfurans.
● NAPHTHENOAROMATICS	● One to eight ring aromatics as above associated with one or more six membered naphthenic rings (hydroaromatics) and/or one or more five membered naphthenic rings. Typical hydroaromatics are tetralins, tetra and octa hydrophenanthrenes, the various hydropyrenes; typical naphtheno-aromatics are indans, benzindans, etc.
● POLAR AROMATICS	● Mono, di- and trihydroxyl-aromatics and naphtheno-aromatics; pyrroles and pyridines associated with aromatics; dinitrogen compounds (probably dipyridine types); nitrogen-oxygen compounds such as hydroxy pyridines and hydroxy pyrroles.
● ASPHALTENES	● Polar aromatics with increased amounts of poly-functional types, such as di-oxygen compounds.

Table II

MS TYPE ANALYSES ARE IN GOOD AGREEMENT WITH CHROMATOGRAPHIC SEPARATIONSA. Accuracy

<u>Sample</u>	<u>Weight Percent</u>					
	<u>Saturates</u>		<u>Aromatics</u>		<u>Polars</u>	
	<u>MS</u>	<u>Sepn.</u>	<u>MS</u>	<u>Sepn.</u>	<u>MS</u>	<u>Sepn.</u>
A	17	19	44	47	39	34
B	8	8	65	63	27	29
C	4	4	51	55	39	36

B. Reproducibility

<u>Replicate runs</u>	<u>Weight Percent</u>	
	<u>Saturates</u>	<u>Aromatics &amp; Polars</u>
1	27.69	72.31
2	27.66	72.34
3	27.71	72.29
4	27.92	72.08
5	27.68	72.32
6	27.54	72.46

Average standard deviation  
on 16 runs in one month

0.081

0.081

Table III

SEPARATION PLUS HIGH RES MS DETECTS PPB COMPONENTS

Example: Acidic Fraction of a Coal Liquid

<u>Carbon No.</u>	<u>Concentration, parts per billion</u>			
	<u>Phenols</u>	<u>Indanols</u>	<u>Hydroxy-Indenes</u>	<u>Naphthols</u>
6	4389	---	---	---
7	28400	---	---	---
8	16875	---	---	---
9	1715	301	62	---
10	450	142	43	0
11	287	58	35	15
12	21	44	30	5
13	8	49	14	0
14	0	36	0	0
15	34	18	3	0

- Separation enrichment : ~4,200-fold
- Dynamic range in high res MS run : ~18,000

Table IV  
TYPICAL MULTIPLET SITUATIONS IN COAL LIQUIDS

<u>Component Class</u>	<u>Example</u>	<u>Delta Mass</u>	<u>Resolving Power Required</u>	
			<u>Mass 300</u>	<u>Mass 600</u>
Non Condensed/Condensed Hydrocarbons	$C_{22}H_{36}/C_{23}H_{24}$	0.0939	3200	6400
Non Condensed Hydrocarbons/ Aromatic Thiophenes	$C_{22}H_{36}/C_{20}H_{28}S$	0.0905	3300	6600
Non Condensed Hydrocarbons/ Mono-Oxygen Compounds	$C_{22}H_{36}/C_{21}H_{32}O$	0.0364	8300	16600
$^{13}C$ isotopes of Hydro- carbons/N compounds	$^{13}C^{12}C_{21}H_{36}/C_{21}H_{35}N$	0.0082	37000	64000
Aromatic Thiophenes/ condensed Hydrocarbons	$C_{20}H_{28}S/C_{23}H_{24}$	0.0034	88000	176000

Table VI

PARAMETERS CALCULATED BY HIGH RESOLUTION, LOW VOLTAGE MS ANALYSISComposition

- Each component (carbon no. homolog) + weight percent
- Each homologous series
  - + weight percent
  - + Avg. C no.
  - + Avg. MW
- Overall sample
  - + Aromatic ring distribution by chemical class
  - + Avg. MW
  - + Avg. carbon no.
  - + Avg. hydrogen deficiency
  - + Weight fraction in aromatic nuclei, sidechains, saturate rings

Physical Properties

- Overall sample
  - + Atomic C, H, O, N, S, H/C
  - + C, H types as measured by NMR
- Selected classes, homologous series for suitable properties
  - + Distillation curve
  - + Density, refractive index
  - + Predicted composition of potential distillation cuts

Process Related Parameters

- Overall sample
  - + Solvent quality index in Exxon Donor Solvent process
  - + Several others



Table V

MS ANALYSIS DETERMINES VERY LARGE NUMBER OF COMPONENTS

<u>Chemical Class</u>	<u>List of Components Determined Range in Homologous Series</u>		<u>Appr. No. of Components</u>
Hydrocarbons	$C_nH_{2n+2}$	through $C_nH_{2n-50}$	700
Thiophenes	$C_nH_{2n-2}S$	" $C_nH_{2n-50}S$	550
Dithiophenes	$C_nH_{2n-6}S_2$	" $C_nH_{2n-44}S_2$	550
Furans/Phenolics	$C_nH_{2n-2}O$	" $C_nH_{2n-50}O$	1100
	$C_nH_{2n-6}O_2$	" $C_nH_{2n-40}O_2$	650
	$C_nH_{2n-6}O_3$	" $C_nH_{2n-28}O_3$	600
	$C_nH_{2n-6}O_4$	" $C_nH_{2n-28}O_4$	600
Nitrogen Cpds	$C_nH_{2n-3}N$	" $C_nH_{2n-41}N$	500
Nitrogen Oxygen Cpds	$C_nH_{2n-3}NO$	" $C_nH_{2n-41}NO$	500
Sulfur-Oxygen, Sulfur-dioxygen Cpds	$C_nH_{2n-10}SO_x$	" $C_nH_{2n-40}SO_x$	1000
DiNitrogen, Nitrogen Di-oxygen Cpds	$C_nH_{2n-6}N_xO_x$	" $C_nH_{2n-40}N_xO_x$	500
Miscellaneous highly condensed, poly- functional compounds	-----		<u>600</u>
	Total		7250

Table VII  
COMPARISON OF ELEMENTAL ANALYSES BY MS AND CHEMICAL TECHNIQUES

A. Individual Samples

Weight Percent					
Atomic H/C		Elemental N		Elemental O	
MS	Chem.	MS	Chem.	MS	Chem.
0.93	0.96	0.10	0.12	0.02	0.10
1.12	1.14	0.90	0.70	0.71	0.76
1.70	1.69	2.30	2.52	2.40	2.63
2.17	2.17	5.92	6.00	3.68	3.22

B. Composite Data on Separated Classes

Element	MS on Separated Classes			MS Composite	Chemical
	Saturates	Aromatics	Polars		
C	86.10	91.34	84.68	88.60	88.84
H	13.90	7.68	7.37	7.84	7.82
O	---	0.40	5.43	2.28	1.83
N	---	---	2.52	0.95	1.17
S	---	0.58	---	0.33	0.33

Table VIII  
COMPARISON OF MS AND GC DISTILLATIONS

Temperature, °F	Percent Off			
	Sample A		Sample B	
	MS	GCD	MS	GCD
400	0.9	0.1	13.4	12.8
500	5.5	3.6	52.5	48.3
600	15.0	14.0	83.6	86.5
700	37.0	34.4	96.7	98.2
800	63.1	65.8	99.2	99.8
900	86.0	88.5	99.7	100.0
1000	76.8	98.3	99.9	100.0

Table IX  
COMPARISON OF CARBON TYPES BY MS AND NMR

Carbon Type	Mole Percent	
	MS	NMR
Saturate	37.1	38.7
Naphthenic	18.2	19.5
Linear	18.9	19.2
Olefinic	0.0	0.0
Aromatic	62.9	61.3

Figure 1

# ANALYTICAL PROCEDURE FOR COAL LIQUIDS

